Functional methods for cosmic structure formation

Alaric Alexander Erschfeld

DISSERTATION

Put forward by

Alaric Alexander Erschfeld

born in the Free and Hanseatic City of Hamburg

in the Federal Republic of Germany

Disputation 15 December 2021

FUNCTIONAL METHODS FOR COSMIC STRUCTURE FORMATION

INSTITUTE FOR THEORETICAL PHYSICS

DEPARTMENT OF PHYSICS AND ASTRONOMY

RUPRECHT-KARLS-UNIVERSITY HEIDELBERG

Referees: **Priv.-Doz. Dr. rer. nat. Stefan Flörchinger**
Prof. Dr. rer. nat. Matthias Bartelmann

Funktionale Methoden für kosmische Strukturentstehung

Kurzreferat

Diese Dissertation befasst sich mit der Untersuchung kosmischer Strukturentstehung zu späten Zeiten und auf großen Längenskalen, unter der Anwendung von nicht-störungstheoretischen funktionalen Methoden auf eine feldtheoretische Beschreibung von Dunkler Materie. Um Phänomene beschreiben zu können, die sich nicht mit der herkömmlichen Näherung einer idealen Flüssigkeit erklären lassen, wird die Beschreibung der Dunklen Materie mittels kinetischer Theorie um Geschwindigkeitsdispersions-Freiheitsgrade erweitert. Als effektive Theorie erlaubt diese es, die Dynamik von Dunkler Materie über das sich Kreuzen von Teilchen-Trajektorien hinaus zu beschreiben, wohingegen die Näherung einer idealen Flüssigkeit scheitert. Um nichtlineare Skalen zu untersuchen, bei denen gewöhnliche störungstheoretische Methoden versagen, werden die Dyson-Schwinger-Gleichung und die funktionale Renormierungsgruppe genutzt. Diese erlauben es auf natürliche Weise in nicht-störungstheoretischen Näherungen zu arbeiten, die notwendig sind, um die physikalischen Prozesse auf nichtlinearen Skalen zu beschreiben. Die funktionale Renormierungsgruppe wird genutzt, um den Sektor der großen Wellenzahlen mittels Ward-Identitäten zu lösen, welche auf eine erweiterte Version von Galilei-Invarianz zurückzuführen sind. Ebenso wird die funktionale Renormierungsgruppe auf eine effektive Beschreibung von Dunkler Materie angewendet, die Dynamiken beschreibt, die lokal in der Zeit sind. Weiterhin wird die Entstehung und Fortentwicklung von Vortizität und Geschwindigkeitsdispersion von Dunkler Materie mit der Dyson-Schwinger-Gleichung untersucht, was zu einer nicht-störungstheoretischen Vorhersage von Korrelationen führt.

Functional methods for cosmic structure formation

Abstract

This thesis is concerned with the investigation of late-time large-scale cosmic structure formation by applying non-perturbative functional methods to a field-theoretic description of dark matter. To account for phenomena beyond the standard perfect fluid approximation, the kinetic theory description of dark matter is extended by including velocity dispersion degrees of freedom. As an effective theory description, this naturally allows to describe the evolution of dark matter after shell-crossing where the perfect fluid approximation breaks down. To probe the non-linear regime of cosmic structure formation where standard perturbative methods fail, the Dyson–Schwinger equation and the functional renormalisation group are employed. These naturally allow for non-perturbative approximation schemes that are necessary to capture the relevant physics at non-linear scales. The functional renormalisation group is used to solve the large wave number sector using Ward identities related to an extended version of Galilean invariance as well as to investigate time-local dynamics for an effective fluid description of dark matter. Moreover, the emergence and evolution of dark matter vorticity and velocity dispersion are studied with the Dyson–Schwinger equation, leading to the non-perturbative prediction of correlations from first principles.

Publications

This thesis contains results from collaborative research which is published, submitted or in preparation at the time of completion of this thesis. The jointly authored publications are:

- A. Erschfeld & S. Floerchinger, *Evolution of dark matter velocity dispersion*, J. Cosmol. Astropart. Phys. **06** (2019) 039.

- A. Erschfeld, S. Floerchinger & M. Rupprecht, *General relativistic nonideal fluid equations for dark matter from a truncated cumulant expansion*, Phys. Rev. D **102** (2020) 063520.

- A. Erschfeld & S. Floerchinger, *Cosmological functional renormalization group, extended Galilean invariance, and approximate solutions to the flow equations* (submitted to Phys. Rev. D).

- A. Erschfeld & S. Floerchinger, *Dark matter vorticity and velocity dispersion from truncated Dyson–Schwinger equations* (in preparation).

- A. Erschfeld & S. Floerchinger, *Time-local effective dynamics for dark matter from the functional renormalisation group* (in preparation).

Especially the chapters 5, 6 and 7 contain significant overlap with the last three listed publications. In all of these I performed the analytical and numerical investigations, sometimes based on earlier work of the co-author S. Floerchinger.

Contents

Contents

1 General introduction

One of the main objectives of contemporary cosmology is to understand the formation and evolution of the large-scale structure of the Universe. Observations show a rich variety of objects, from starts to galaxies, galaxy groups to clusters, organised into even larger structures forming filaments separated by immense voids that permeate the Universe to form the so-called *cosmic web*. Surveys of the cosmos indicate that the large-scale structure of the Universe appears to be statistically homogeneous and isotropic in space, a notion also known as the *cosmological principle.*

In the cosmological concordance model it is assumed that the energy content of the late-time Universe is dominated by two contributions. The larger part is made up of an unknown form of energy that is responsible for the accelerated expansion of the Universe and is dubbed *dark energy* [1]. The remaining energy is almost entirely made up of matter, the dominant part of which interacts only weakly, if at all, with three of the four fundamental interactions of nature. The hypothetical form of *dark matter* interacts only gravitationally, at least to leading-order approximation, and is responsible for the observed large-scale structure of the Universe. It is believed that quantum fluctuations in the energy density of the primordial Universe seed matter perturbations which grow under the influence of gravity over the course of time to form the structures which are observed today [2,3].

The key to a description of late-time cosmic structure formation therefore lies within understanding the gravitational dynamics of dark matter. To this end, a rather useful tool are *N*-body simulations which compute numerical solutions for the dynamics of gravitationally interacting particles. While *N*-body simulations can give a profound knowledge of the large-scale structure of the Universe [4], they are necessarily subject to spurious effects such as the finite simulation volume or the amount of simulated particles. Moreover, they give very little insight into the physical processes responsible for structure formation. Ideally, one would like to have an effective description of dark matter that can capture the process of structure formation without tracing the microscopic degrees of freedom but rather describes dark matter gravitational dynamics in terms of a coarse-gained model that accounts for the relevant physical phenomena.

Such a description can be given in a kinetic theory approach which describes an ensemble of self-gravitating classical point particles. By coarse-gaining the microscopic degrees of freedom, dark matter can be described in terms of macroscopic degrees of freedom that quantify the energy density, pressure, heat current, stress and other properties of an effective dark matter description. Typically, one is interested in a finite amount of these properties, rendering an effective hydrodynamical description of dark matter, sometimes called the *cosmological fluid.*

In a kinetic theory description of dark matter the state of the theory is described by a phase-space distribution function which obeys the Vlasov–Poisson equations [5]. In the *single-stream approximation* dark matter is modelled by a perfect pressureless fluid which is preserved by the Vlasov–Poisson equations, in the sense that no other degrees of freedom are sourced if initially absent. However, it is an apparent self-consistency due to the phenomenon of *shell-crossing*. During gravitational collapse, dark matter particles meet in position space and generate a non-trivial velocity dispersion tensor which indicates the break down of the single-stream approximation. While the perfect pressureless fluid description provides a surprisingly good account of the early stages of gravitational instabilities, one naturally longs for a description that is capable to capture the physics of a multi-stream flow. Ultimately, this relies on including some notion of velocity dispersion. To this end, various approaches have been developed, ranging from a description including the velocity dispersion tensor [6–11] through effective terms parametrising the effect of velocity dispersion [12], through functional approaches, either over the phase-space distribution function [13] or the Lagrangian displacement field [14], to using the Schrödinger method [15, 16], to name only a few.

Since it is believed that the large-scale structure of the Universe is the outcome of primordial quantum fluctuations, one often adopts a statistical description for dark matter. This can be understood as describing an ensemble of cosmic histories, only one realisation of which is the Universe that is observed. Due to the stochastic nature of the initial conditions, one is typically interested in correlation functions that quantify the properties of cosmic structure on different length scales. A major obstacle for a prediction of the correlation functions is that dark matter gravitational dynamics is non-linear. In such a setting it is in general not possible to straightforwardly calculate correlation functions. Typically, the linear part of the dynamics can be solved while non-linearities are taken *perturbatively* into account [17]. Formally, this is understood as expanding the theory around the linear solutions which is naturally only sensible as long as the deviations from linear theory are small. This is only the case for the largest of cosmic scales where the deviation from a homogeneous and isotropic background are small. To also describe smaller scales, different methods have been proposed. These include various resummation schemes [18–26], two-particle irreducible methods [27–30], direct interaction approximations [31–33], the renormalisation group [34–38], effective theories [39–42], higher-order perturbation theory and extensions thereof [43–45] and kinetic field theory [46–48], to name only a few.

In the light of future surveys, such as the Euclid mission, which are probing ever increasingly smaller scales, it is necessary to have a description of cosmic structure formation that can go beyond the limitations of the single-stream approximation and standard perturbation theory. To this end, dark matter gravitational dynamics in the kinetic picture can be formulated as a statistical field theory [27]. This allows to make use of a lot of the methods that have been developed for quantum field theories [49]. Although being a classical field theory, the formal analogies allow to apply a large part of the machinery to the case of non-linear structure

formation. In particular this includes *non-perturbative* functional methods that do not rely on an expansion around linear theory. Most important in the following are the *Dyson–Schwinger equation* [50–52] and the *functional renormalisation group* [53]. These provide a framework in which the correlation functions characterising the statistical properties of dark matter can be computed in a generically non-perturbative manner and have been proven to be very useful for various phenomena in quantum field theories and statistical mechanics [54, 55]. Both methods rely on studying the effective action of the theory which in principle encodes all physical information. While both methods in practice cannot be solved exactly, they allow for approximation schemes that are generically non-perturbative.

In this thesis the gravitational dynamics of dark matter is investigated in a description beyond the single-stream approximation using non-perturbative functional methods to probe the non-linear regime of cosmic structure formation with non-perturbative methods. In chapter 2 the description of dark matter gravitational dynamics in terms of general relativistic kinetic theory is reviewed and its Newtonian limit is derived. To model dark matter in terms of an effective description that goes beyond the single-stream approximation, truncations of the phase-space distribution function's cumulant expansion that include the velocity dispersion tensor are discussed. In chapter 3 the statistical description of dark matter motivated from inflation is discussed and the relevant statistical concepts needed in the subsequent chapters are introduced. In chapter 4 the statistical field theory for dark matter gravitational dynamics is formulated and various perturbative and non-perturbative approximation schemes are discussed. These include in particular the Dyson–Schwinger equation and the functional renormalisation group which are used in the following chapters to investigate the non-linear regime of cosmic structure formation. In chapter 5 the large wave number sector of the functional renormalisation group is solved for the two-point correlation functions using Ward identities that are related to an extended version of Galilean invariance. In chapter 6 the Dyson–Schwinger equations are truncated in a self-consistent one-loop approximation that allows for a non-perturbative calculation of one- and two-point correlation functions. These are computed for a dark matter description that includes velocity dispersion degrees of freedom to overcome the limitations of the perfect fluid description. In chapter 7 the functional renormalisation group is investigated with an ansatz for the effective action that corresponds to time-local effective dynamics. The two-point correlation functions are computed with this ansatz and compared to results obtained in other approximation schemes. Finally, in chapter 8 the insights obtained throughout this thesis are discussed and an outlook for future directions is given.

2 Gravitational dynamics of dark matter

In this chapter the description of dark matter in terms of general relativistic kinetic theory is reviewed. Starting from first principles, the Vlasov–Einstein equations are derived describing the dynamics of matter and metric degrees of freedom. These are studied for Friedmann–Lemaître–Robertson–Walker space-times that describe a homogeneous and isotropic background cosmology. Following, a perturbed space-time is considered and the Vlasov–Einstein equations are investigated to first order in perturbations. Finally, the Newtonian limit leading to the Vlasov–Poisson equations is discussed and the cumulant expansion of the kinetic theory phase-space distribution function is investigated. Truncations thereof are discussed and the perfect fluid approximation is extended to include velocity dispersion degrees of freedom.

2.1 General relativistic kinetic theory

In the current understanding of nature, gravity is a geometrical property of space-time which warps in the presence of energy. This is formalised in the general theory of relativity which describes how space-time bends in the presence of energy and momentum. In general, there are a rather large amount of contributions to the energy content of the Universe. Although the underlying microscopic physics of all these contributions is in itself interesting, it can be sufficient to describe the different contributions by means of effective theories.

A rather good developed theory is the kinetic theory of classical point particles, being able to describe a wide range of physical phenomena. Kinetic theory relies on the assumption that there is a hierarchy of scale such that one can distinguish between short and long ranged forces, meaning that the mean free path between short ranged interactions is much larger than the range of those interactions, in some way saying the system is dilute. The short range interactions can then be treated as point particle collisions while the large range interactions are described as an external force due to a potential field. Keeping track of the dynamics of single particles is rather complicated and it is questionable whether this is even wanted. Rather, one studies the average dynamics of an ensemble of states in the sense of an effective theory as a macroscopic state. The state of the theory can be described by an (average) phase-space distribution function, where the underlying microscopic nature of the state and internal degrees of freedom such as spin are disregarded, in the sense that they are already integrated out.

2.1.1 General relativity

Mathematically, space-time is modelled by a four-dimensional Lorentzian manifold which is characterised by its metric tensor. In local coordinates x the components of the metric tensor are denoted $g_{\mu\nu}(x)$ which locally describes the geometry of space-time.[1] In local coordinates the metric tensor can be specified by its line element,

$$\mathrm{d}s^2 = g_{\mu\nu}\,\mathrm{d}x^\mu\,\mathrm{d}x^\nu =: -c^2\,\mathrm{d}\tau_*^2 \;, \tag{2.1}$$

where τ_* is the proper time as measured by an observer at rest.[2] In the absence of any forces except for gravity, observers are said to be in free fall and according to Einstein's equivalence principle follow geodesics. Geodesics can be parametrised in terms of an affine parameter which is particularly convenient chosen to be proper time, at least for a massive observer. The world line $x(\tau_*)$ of a freely falling observer is then given by the solution of the geodesic equation,

$$\frac{\mathrm{d}^2 x^\mu}{\mathrm{d}\tau_*^2} + \Gamma^\mu_{\rho\sigma}\frac{\mathrm{d}x^\rho}{\mathrm{d}\tau_*}\frac{\mathrm{d}x^\sigma}{\mathrm{d}\tau_*} = 0 \;. \tag{2.2}$$

Here, $\Gamma^\mu_{\rho\sigma}(x)$ are the components of the Levi–Civita connection in coordinates x, giving a notation of how tangent spaces at different points in space-time are connected. The so-called Christoffel symbols of the second kind are defined by

$$\Gamma^\rho_{\mu\nu} := \frac{g^{\rho\sigma}}{2}\left(\frac{\partial g_{\sigma\mu}}{\partial x^\nu} + \frac{\partial g_{\nu\sigma}}{\partial x^\mu} - \frac{\partial g_{\mu\nu}}{\partial x^\sigma}\right) \;. \tag{2.3}$$

The central equations governing how the curvature of space-time is related to the energy content are Einstein's field equations [57],

$$G_{\mu\nu} + \Lambda g_{\mu\nu} = \kappa\, T_{\mu\nu} \;, \tag{2.4}$$

where Λ the cosmological constant and $\kappa := 8\pi G_{\mathrm{N}}/c^4$ is given in terms of the speed of light c and Newton's gravitational constant G_{N}. The left-hand side of Einstein's field equations (2.4) describes the geometry of space-time in terms of the Einstein tensor $G_{\mu\nu}(x)$ while the right-hand side specifies the energy content of space-time in terms of the energy-momentum tensor $T^{\mu\nu}(x)$. The Einstein tensor is a non-linear function of the metric tensor and its components are defined as

$$G_{\mu\nu} := R_{\mu\nu} - \tfrac{1}{2}R g_{\mu\nu} \;, \tag{2.5}$$

which in turn are defined in terms of the Ricci curvature tensor,

$$R_{\mu\nu} := \Gamma^\rho_{\mu\nu,\rho} - \Gamma^\rho_{\rho\mu,\nu} + \Gamma^\rho_{\mu\nu}\Gamma^\sigma_{\rho\sigma} - \Gamma^\rho_{\sigma\mu}\Gamma^\sigma_{\nu\rho} \;, \tag{2.6}$$

---

[1] Greek indices run from zero to three whereas Latin indices from the middle of the alphabet run from one to three and Einstein's summation convention is employed where repeated indices within the same term are summed over.

[2] The metric signature convention $(-,+,+,+)$ is used and the MTW sign convention $(+,+,+)$ is adopted [56].

and scalar curvature,

$$R := g^{\mu\nu} R_{\mu\nu} \, . \tag{2.7}$$

The Einstein field equations are a system of ten coupled non-linear hyperbolic-elliptic partial differential equations which describe the dynamics the metric degrees of freedom.

For an empty space-time the Einstein field equations can be solved given suitable initial data. Naturally, the Universe is not empty but rather filled with all sorts of energy. Although local energy-momentum conservation is incorporated in general relativity due to the Bianchi identities, it is not sufficient to describe the dynamics of a general energy content since the energy-momentum tensor has ten degrees of freedom and energy-momentum conservation only supplies four equations.

2.1.2 Kinetic theory

In the following it is assumed that space-time is filled exclusively with an ensemble of classical point particles of rest mass m which admit a kinetic theory description.[3] The four-momentum of a particle of rest mass m is given by the tangent vector $p^\mu = m \, \mathrm{d}x^\mu / \mathrm{d}\tau_*$ fulfilling the on-shell constraint

$$g_{\mu\nu} p^\mu p^\nu + m^2 c^2 = 0 \, , \qquad -p^\mu u_\mu > 0 \, , \tag{2.8}$$

where u^μ is a future-directed time-like vector field that is normalised to $u^\mu u_\mu = -1$.[4] The phase-space can be given canonical local coordinates $(x^\mu, \, p_\mu)$ in terms of the conjugate momentum p_μ.[5] The state of the theory is described by a one-particle phase-space distribution function $f(x, p)$ defined on the mass hyperboloid (2.8) of phase-space. Define the hypersurface element

$$\mathrm{d}\Sigma_\mu(x) := \frac{|g|^{\frac{1}{2}}}{3!} \, \epsilon_{\mu\nu\rho\sigma} \, \mathrm{d}x^\nu \wedge \mathrm{d}x^\rho \wedge \mathrm{d}x^\sigma \, , \tag{2.9}$$

and the on-shell momentum range

$$\begin{aligned}
\mathrm{d}\Pi_x &:= \frac{4\pi}{|g|^{\frac{1}{2}}} \, \theta(-u^\alpha p_\alpha) \, \delta\big(g^{\mu\nu} p_\mu p_\nu + m^2 c^2\big) \, \frac{\mathrm{d}p_0 \wedge \mathrm{d}p_1 \wedge \mathrm{d}p_2 \wedge \mathrm{d}p_3}{(2\pi)^4} \\
&= \frac{1}{|g|^{\frac{1}{2}}} \frac{1}{p_+^0} \frac{\mathrm{d}p_1 \wedge \mathrm{d}p_2 \wedge \mathrm{d}p_3}{(2\pi)^3} \, ,
\end{aligned} \tag{2.10}$$

---

[3]For simplicity the absence of corresponding anti-particles is assumed.

[4]Space-time is assumed to be time-orientable and connected such that the future mass hyperboloid (2.8) is unambiguously defined through the whole manifold [58]. Moreover, it is assumed that space-time is globally hyperbolic such that it can be foliated by space-like Cauchy surfaces which are assumed to be orientable and thus parallelisable.

[5]From a mathematical point of view, phase-space is the cotangent bundle of the space-time manifold and the future mass hyperboloid (2.8) is the submanifold of on-shell states. The conjugate momentum is defined to be the tautological one-form providing a bridge between Lagrangian and Hamiltonian dynamics.

on the future mass hyperboloid, where $|g|$ is the determinant's absolute value of the metric tensor's matrix representation and

$$p_+^0(x, \boldsymbol{p}) := \sqrt{(g^{0i}p_i)^2 - g^{00}(g^{ij}p_ip_j + m^2c^2)} \, , \tag{2.11}$$

where $\boldsymbol{p} = (p_1, p_2, p_3)$ are local coordinates on the mass shell. The number of particles flowing through the hypersurface element $\mathrm{d}\Sigma_\mu(x)$ which are in the (on-shell) momentum range $\mathrm{d}\Pi_x$ at position x is then given by

$$\mathrm{d}N = f(x, p) \, g^{\mu\nu}p_\mu \, \mathrm{d}\Sigma_\nu(x) \, \mathrm{d}\Pi_x \, . \tag{2.12}$$

The particle number current density and energy-momentum tensor are obtained as

$$N_\mu(x) = c \int_{P_x} p_\mu \, f(x, p) \, \mathrm{d}\Pi_x \, , \tag{2.13}$$

and

$$T_{\mu\nu}(x) = c \int_{P_x} p_\mu p_\nu \, f(x, p) \, \mathrm{d}\Pi_x \, , \tag{2.14}$$

respectively, where P_x is the mass fiber over x. More generally, one can define moments with respect to the conjugate momentum argument of the distribution function,

$$M_{\mu_1 \dots \mu_n}(x) := c \int_{P_x} p_{\mu_1} \dots p_{\mu_n} \, f(x, p) \, \mathrm{d}\Pi_x \, , \tag{2.15}$$

the full set of which completely characterise the distribution function, assuming the distribution function is sufficiently regular and all moments exist. In terms of moments, the particle number density and energy-momentum tensor are the first and second moment.

To write the integrals over the mass hyperboloid (2.8) more explicitly, it is useful to introduce the concept of frame fields, also called tetrad or vierbein formalism in physics. These can be understood as (local) transformations to a laboratory frame where the metric is flat,

$$g_{\mu\nu}(x) \, e^\mu{}_a(x) \, e^\nu{}_b(x) = \eta_{ab} \, , \tag{2.16}$$

where $\eta_{ab} = \mathrm{diag}(-1, 1, 1, 1)$ is the Minkowski metric. The dual one-form is the coframe field $e^a{}_\mu(x)$, such that

$$e^a{}_\mu(x) \, e^\mu{}_b(x) = \delta^a{}_b \, , \qquad e^\mu{}_a(x) \, e^a{}_\nu(x) = \delta^\mu{}_\nu \, . \tag{2.17}$$

In terms of the frame fields the momentum can be written as $p_\mu = p_a \, e^a{}_\mu$ and moments of the distribution function read

$$M_{a_1 \dots a_n}(x) = c \int_{\boldsymbol{p}'} \frac{\bar{p}_{a_1} \dots \bar{p}_{a_n}}{\left[m^2c^2 + \delta^{ij}p_i'p_j' \right]^{\frac{1}{2}}} \, f(x, \boldsymbol{p}') \, , \tag{2.18}$$

where three-vectors expressed in the laboratory frame are denoted with a prime. Here $f(x, \boldsymbol{p})$ denotes the restriction of the distribution function to the mass hyperboloid with momenta $\bar{p} = (p_0^+, \boldsymbol{p})$ and p_0^+ is the corresponding conjugate momentum to the four-momentum (2.11).[6]

2.1.3 Vlasov–Einstein equations

The geodesic equation (2.2) implies Hamilton's equations

$$\frac{\mathrm{d}x^\mu}{\mathrm{d}\tau_*} = \frac{g^{\mu\nu}p_\nu}{m} \,, \qquad \frac{\mathrm{d}p_\mu}{\mathrm{d}\tau_*} = -\frac{\partial g^{\rho\sigma}}{\partial x^\mu}\frac{p_\rho p_\sigma}{2m} \,, \tag{2.20}$$

along which the distribution function is conserved according to Liouville's theorem. In the absence of collision, the distribution function thus obeys the Vlasov equation [59]

$$\left[g^{\mu\nu}p_\nu \frac{\partial}{\partial x^\mu} - \frac{1}{2}\frac{\partial g^{\rho\sigma}}{\partial x^\mu} p_\rho p_\sigma \frac{\partial}{\partial p_\mu} \right] f(x,p) = 0 \,, \tag{2.21}$$

also known as Liouville's equation or the collisionless Boltzmann equation.[7] The Vlasov equations can be naturally restricted to the mass hyperboloid (2.8) which can be realised by using the relations

$$\begin{aligned}
\frac{\partial}{\partial x^\mu} f(x, \boldsymbol{p}) &= \left[\frac{\partial}{\partial x^\mu} - \frac{1}{2p_+^0}\frac{\partial g^{\rho\sigma}}{\partial x^\mu} \bar{p}_\rho \bar{p}_\sigma \frac{\partial}{\partial p_0} \right] f(x,p)\Big|_{p=\bar{p}} \,, \\
\frac{\partial}{\partial p_i} f(x, \boldsymbol{p}) &= \left[\frac{\partial}{\partial p_i} - \frac{g^{i\mu}\bar{p}_\mu}{p_+^0}\frac{\partial}{\partial p_0} \right] f(x,p)\Big|_{p=\bar{p}} \,.
\end{aligned} \tag{2.22}$$

Doing so, one obtains the one-shell Vlasov equation

$$\left[g^{\mu\nu}\bar{p}_\nu \frac{\partial}{\partial x^\mu} - \frac{1}{2}\frac{\partial g^{\rho\sigma}}{\partial x^i} \bar{p}_\rho \bar{p}_\sigma \frac{\partial}{\partial p_i} \right] f(x,\boldsymbol{p}) = 0 \,. \tag{2.23}$$

---

[6]The (co)frame fields form an orthonormal basis of the (co)tangent space and can be globally defined if and only if the space-time manifold is parallisable which was assumed earlier. In the following three-dimensional momentum space integrals are abbreviated as

$$\int_{\boldsymbol{p}} = \int_{\mathbb{R}^3} \frac{\mathrm{d}^3 p}{(2\pi)^3} \,. \tag{2.19}$$

[7]More generally, for collisional systems a collision term is present giving the Boltzmann equation. This term depends on the two-particle phase-space distribution function which in turn can only be solved for by knowing the three-particle phase-space distribution function and so on, creating the so-called Bogoliubov–Born–Green–Kirkwood–Yvon hierarchy. To obtain a closed system of equations which can be solved, one needs to resort to approximation schemes such as the Stoßzahlansatz where the collision term is approximation in terms of one-particle distribution functions. Although it would most be interesting to include a collision term to account for dark matter self-interaction, this is not further pursued here.

The Vlasov equation can be straight forwardly integrated to give the covariant conservation of all moments

$$\nabla_\nu M^{\nu\mu_1\cdots\mu_n}(x) = 0 \,, \tag{2.24}$$

where ∇_ν denotes to covariant derivative associated with the Levi–Civita connection. The first two of these conservation equations then correspond to the conservation of particle number and energy-momentum. Moments of the distribution function are studied in much more detail in the Newtonian limit in section 2.4 although most of these considerations can be similarly transferred to the relativistic setting.

The Vlasov equation (2.23) and Einstein's field equations (2.4) form a set of closed non-linear integro-differential equations that describe the dynamics of the energy content as well as geometry of space-time. When solving these in terms of moments of the distribution function one usually needs to resort so some sort of truncation scheme. Usual approximations include the method of moments [60] and the Müller–Israel–Stewart theory [61–64] or more modern truncations schemes which keep moments to infinite order [65–67].

2.2 The homogeneous and isotropic Universe

On the largest observable scales the Universe appears to be spatially homogeneous and isotropic, a notion also referred to as the *cosmological principle*. To understand the dynamics of the Universe at these scales one has to solve the Einstein field equations (2.4) for a space-time geometry respecting the symmetries of the cosmological principle.

The class of manifolds that respect the symmetries of the cosmological principle are Friedmann–Lemaître–Robertson–Walker space-times. They are characterised by a line element of the form

$$\mathrm{d}s^2 = a(\tau)^2\big[-c^2\,\mathrm{d}\tau^2 + \mathrm{d}\sigma^2\big] \,, \tag{2.25}$$

where $a(\tau)$ is a positive warp function, in cosmology called scale factor, and $\mathrm{d}\sigma^2$ is the line element of a three-dimensional manifold with constant sectional curvature K.[8] The spatial part of the Universe is modelled by a three-dimensional space form and is distinguished for vanishing, positive and negative curvature corresponding to spherical or elliptical, Euclidean and hyperbolic geometries, respectively.[9]

---

[8]Mathematically speaking, the four-dimensional space-time manifold factorises, at least locally, into the warped product of an interval (time) and a maximally symmetric three-dimensional Riemannian manifold (space).

[9]Usually one restricts to globally homogeneous and isotropic manifolds that are simply connected. These are isometric to three-dimensional Euclidean space, the three-sphere and hyperbolic three-space, respectively. More generally, other topologies can be allowed by loosening the condition of simply connectedness and allowing for only locally homogeneous and isotropic manifolds, which seems reasonable since the Universe cannot be probed globally. In this case there exist an infinite amount of manifolds all of which have one of the simply connected cases as their universal covering [68].

In local coordinates (χ, θ, φ) the spatial line element may be written as

$$\mathrm{d}\sigma^2 = \mathrm{d}\chi^2 + S_K(\chi)^2 [\mathrm{d}\theta^2 + \sin(\theta)^2 \, \mathrm{d}\varphi^2] \,, \tag{2.26}$$

with

$$S_K(\chi) = \begin{cases} K^{-\frac{1}{2}} \sin(K^{\frac{1}{2}}\chi) & \text{for } K > 0 \\ \chi & \text{for } K = 0 \\ |K|^{-\frac{1}{2}} \sinh(|K|^{\frac{1}{2}}\chi) & \text{for } K < 0 \end{cases} \,. \tag{2.27}$$

Spatial hypersurfaces have (spatially) constant sectional curvature K/a^2 and the coordinate χ is chosen to carry the units of length such that the curvature K has the units of length^{-2}. For simply connected space-times these coordinates are particularly convenient since the whole manifold is covered by $\chi \in [0, \pi/K^{\frac{1}{2}})$ for $K > 0$ and $\chi \in [0, \infty)$ for $K \le 0$ and $\theta \in [0, \pi)$ and $\varphi \in [0, 2\pi)$.

2.2.1 Friedmann's equations

Having specified the type of space-times allowed by the symmetries of the cosmological principle one can proceed to solve the Einstein field equations. For the following investigations τ is called conformal time and it is convenient to work in the comoving quasi-Cartesian coordinates $\boldsymbol{x} = (x^1, x^2, x^3)$ with spatial line element

$$\mathrm{d}\sigma^2 = \gamma_{ij}(\boldsymbol{x}) \, \mathrm{d}x^i \, \mathrm{d}x^j \,, \tag{2.28}$$

where the metric is diagonal,

$$\gamma_{ij}(\boldsymbol{x}) = \left(1 + \frac{K}{4} \delta_{kl} x^k x^l\right)^{-2} \delta_{ij} \,, \tag{2.29}$$

and δ_{ij} is the Kronecker delta. The Einstein tensor in these coordinates is given by

$$G_{00} = \frac{3(\mathcal{H}^2 + Kc^2)}{c^2} \,, \qquad G_{0i} = 0 \,, \qquad G_{ij} = -\frac{2\dot{\mathcal{H}} + \mathcal{H}^2 + Kc^2}{c^2} \gamma_{ij} \,, \tag{2.30}$$

where $\mathcal{H} = \dot{a}/a$ is the conformal Hubble function parametrising the expansion or contraction rate of space-time. The energy-momentum tensor allowed by the cosmological principle is of the form

$$T_{\mu\nu} = \epsilon u_\mu u_\mu + P(g_{\mu\nu} + u_\mu u_\nu) \,, \tag{2.31}$$

which in a kinetic picture can be identified as a perfect fluid with volumetric energy density ϵ and kinetic pressure P as measured by a freely falling observer with (normalised) four-velocity $u^\mu = \delta^\mu{}_0/a$. More generally, the energy-momentum tensor (2.31) can describe any type of energy contained in the Universe, irrespective whether it admits a kinetic theory description.

In terms of the Einstein tensor (2.30) and the energy-momentum tensor (2.31) the Einstein field equations reduce to the celebrated Friedmann equations [69],

$$\frac{\mathcal{H}^2 + Kc^2}{a^2} = \frac{\kappa c^2}{3}\,\epsilon + \frac{\Lambda c^2}{3}\,, \qquad \frac{\dot{\mathcal{H}}}{a^2} = -\frac{\kappa c^2}{6}\,(\epsilon + 3P) + \frac{\Lambda c^2}{3}\,. \qquad (2.32)$$

These govern the dynamics of the homogeneous and isotropic Universe and allow for expanding and contracting solutions of the scale factor a depending on the type energy content. Since general relativity incorporates local energy-momentum conservation, the Friedmann equations can be combined to give

$$\dot{\epsilon} + 3\mathcal{H}(\epsilon + P) = 0\,, \qquad (2.33)$$

describing the dilution of energy with the expansion of space-time. For a constant equation of state $\omega := P/\epsilon$ one finds $\epsilon \propto a^{-3(1+\omega)}$ and typical examples include non-relativistic matter (cold dust) with $\omega_{\mathrm{m}} = 0$ and ultra-relativistic radiation with $\omega_{\mathrm{r}} = 1/3$. For a Universe where the energy content is made up of contributions which are characterised by a constant equation of state the Friedmann equations (2.32) can be written as

$$\sum_X \Omega_X + \Omega_K + \Omega_\Lambda = 1\,, \qquad \frac{\dot{\mathcal{H}}}{\mathcal{H}^2} = 1 - \Omega_K - \tfrac{3}{2}\sum_X (1 + \omega_X)\Omega_X\,, \qquad (2.34)$$

where the sum runs over all contributions X to the energy content and the (time-dependent) density parameters are given by

$$\Omega_X = \frac{8\pi G_{\mathrm{N}} a^2 \epsilon_X}{3\mathcal{H}^2 c^2}\,, \qquad \Omega_\Lambda = \frac{\Lambda c^2 a^2}{3\mathcal{H}^2}\,, \qquad \Omega_K = -\frac{Kc^2}{\mathcal{H}^2}\,. \qquad (2.35)$$

In the Λ cold dark matter (ΛCDM) model one usually assumes the energy content to be made up of radiation, baryonic matter, cold dark matter, curvature and dark energy. In the minimal six-parameter model curvature is neglected and dark energy is assumed to be a cosmological constant, such that the Friedmann equations can be written as

$$H^2 = H_0^2\big[\Omega_{\mathrm{r},0}\,a^{-4} + \Omega_{\mathrm{m},0}\,a^{-3} + \Omega_{\Lambda,0}\big]\,, \qquad (2.36)$$

where $H = \mathcal{H}/a$ is the usual Hubble function and subscripted objects with a 0 are the values at $a = 1$, corresponding to today.

Current observations [162] indicate, that the Universe is almost flat and the to-day's contributions are roughly $\Omega_{\mathrm{m},0} \approx 0.3$, $\Omega_{\Lambda,0} \approx 0.7$, $\Omega_{\mathrm{r},0} \approx 10^{-4}$ and $h \approx 0.7$ is the reduced Hubble parameter and defined by $H_0 = h \cdot 100$ km/(s Mpc). Since the scale factor grows in time, there are eras of the Universe in which the different contributions entering (2.36) dominate the energy content. Due to the scaling these are chronologically given by a radiation dominated era, to a matter dominated era and finally a dark energy dominated era. This naturally only holds as long as there are no other contributions to the energy content such as believed for a very early epoch of the Universe where the energy content is dominated by an inflaton field leading to an exponential growth of the Universe. This is discussed in more detail in chapter 3.

2.2.2 Distribution function

The Ehlers–Geren–Sachs theorem [70] shows that if all freely falling observers measure an isotropic cosmic background radiation relative to their four-velocity, the Universe is a Friedmann–Lemaître–Robertson–Walker space-time, at least if one adopts a kinetic picture without collision or in detailed balance.[10] For a particle species admitting a kinetic description one can now make the connection to the phase-space distribution function. To this end it is convenient to use the coframe fields

$$e^a{}_\mu(\boldsymbol{x}) = \begin{pmatrix} 1 & 0 \\ 0 & |\gamma(\boldsymbol{x})|^{\frac{1}{2}} \, \delta^i{}_j \end{pmatrix} , \tag{2.37}$$

where it should be noted that the lab frame is only conformally flat and still expanding such that momentum in this frame is still comoving. One then obtains $\boldsymbol{p}^2 = \gamma^{ij} p_i p_j = \delta^{ij} p'_i p'_j = \boldsymbol{p}'^2$ and defines $E_{\boldsymbol{p}}(\tau) := c\sqrt{(mc)^2 + \boldsymbol{p}^2/a^2}$. The most general distribution function obeying the symmetries of homogeneity and isotropy which solves the Vlasov equation is given by a (physically sensible) positive function $f(\boldsymbol{p}^2)$ [70, 73, 74]. The particle number current is then given by

$$N_a = n u_a , \tag{2.38}$$

and the particle number density as measured by the rest frame observer moving with $u^a = \delta^a{}_0/a$ is given by

$$n(\tau) = \frac{c}{a^3} \int_{\boldsymbol{p}'} f(\boldsymbol{p}'^2) . \tag{2.39}$$

Similarly, the energy-momentum tensor is given by

$$T_{ab} = \epsilon u_a u_b + P(g_{ab} + u_a u_b) , \tag{2.40}$$

where the mean volumetric energy density is

$$\epsilon(\tau) = \frac{1}{a^3} \int_{\boldsymbol{p}'} E_{\boldsymbol{p}'} \, f(\boldsymbol{p}'^2) , \tag{2.41}$$

and the mean (kinetic) pressure is

$$P(\tau) = \frac{c^2}{a^5} \int_{\boldsymbol{p}'} \frac{\boldsymbol{p}'^2}{3 E_{\boldsymbol{p}'}} \, f(\boldsymbol{p}'^2) . \tag{2.42}$$

Given these formulas, one can now consider the case of non-relativistic (dust) matter where $E_{\boldsymbol{p}} \to mc^2$ and of ultra-relativistic radiation where $E_{\boldsymbol{p}} \to |\boldsymbol{p}|c/a$ and $|\boldsymbol{p}|$ denotes the modulus of three-momentum. From equation (2.41) one obtains $\epsilon_\mathrm{m} \propto a^{-3}$ and $\epsilon_\mathrm{r} \propto a^{-4}$ corresponding to the equations of state $\omega_\mathrm{m} = 0$ and $\omega_\mathrm{r} = 1/3$ discussed earlier.

---

[10]This result generalises to the case with collisions [71] and even applies to the more realistic case of a nearly isotropic cosmic background radiation [72], showing the stability of the theorem.

2.3 Relativistic cosmology

Having introduced the foundations to describe a Universe filled with collisionless classical point particles in the previous section, the goal here is to establish some standard results from relativistic cosmology. In particular, a homogeneous and isotropic background cosmology as well as first-order perturbations around that background are studied.

The above considerations describe a homogeneous and isotropic expanding Universe and as such no structures can form. To describe structure formation, one naturally needs deviations from the homogeneous and isotropic background cosmology. Generally this is most certainly a very complex process which is naturally difficult to solve.

To get a grip on structure formation one solves the Einstein field equations perturbatively on the homogenous and isotropic background cosmology. This is justified as long as the deviations from the background are small which is typically the case through the Universe, when not probing the extremest of gravitational phenomena such as black holes or neutron stars. In the following, the Vlasov–Einstein equations are solved up to first order in deviations from the background cosmology.

2.3.1 Perturbed metric

To study deviations from the a Friedmann–Lemaître–Robertson–Walker background cosmology a metric corresponding to the line element

$$\mathrm{d}s^2 = -a^2(1 + 2\psi)\,\mathrm{d}\tau^2 + 2a^2 w_i\,\mathrm{d}\tau\,\mathrm{d}x^i + a^2\big[(1 - 2\phi)\gamma_{ij} + 2h_{ij}\big]\,\mathrm{d}x^i\,\mathrm{d}x^j\ , \quad (2.43)$$

is considered, where h_{ij} is a symmetric second-order three-tensor field with $\gamma^{ij}h_{ij} = 0$ since the trace is already parametrised in terms of the potential ϕ. In the following, the speed of light is set to unity to clear up notation and only when explicitly needed it is restored. The scalar potentials can be identified with the Newtonian gravitational potential as is shown in the next section. In the following the deviation from the background metric is assumed to be small, $\delta g_{\mu\nu} \ll 1$, allowing for a perturbative treatment of the otherwise highly non-linear Einstein field equations.

Generally the metric has ten degrees of freedom although due to the freedom of choosing a coordinate frame only six of them are physical. Although is can be sensible to work with gauge-invariant perturbations [75–77] here a gauge is chosen where $\nabla^i w_i = 0$ and $\nabla^i h_{ij} = 0$ such that the vector field is solenoidal [78]. When neglecting the metric vector and tensor perturbations this gauge reduces to the common conformal Newtonian gauge [79, 80]. Here ∇_i denotes the Levi–Civita connection associated to the spatial metric γ_{ij} which is used to raise and lower indices on w_i and h_{ij} and partial derivatives are denoted as ∂_i.

Generally, a vector field V_i and symmetric tensor field S_{ij} defined on the three-space with metric γ_{ij} can be decomposed as [81]

$$V_i = \nabla_i V + V_i^\perp\ , \qquad S_{ij} = (\nabla_i\nabla_j - \tfrac{1}{3}\gamma_{ij}\nabla^2)S + \nabla_{(i}S_{j)}^\perp + S_{ij}^{\mathrm{tt}}\ , \qquad (2.44)$$

where $\nabla^2 := \nabla_i \nabla^i$ is the connection Laplacian which acts differently for scalar, vector and tensor fields and reduces to the Laplace–Beltrami operator for scalar functions. Here $\nabla_i V$ is called the longitudinal part and $\nabla^i V_i^{\perp} = 0$ the transverse part. Similarly one has the transverse part $\nabla^i S_i^{\perp} = 0$ and $\nabla^i S_{ij}^{\text{tt}} = 0$ is called the traceless and transverse part.[11] As such, also the Einstein field equations can be decomposed into different parts [82].

The Einstein tensor is then given to first order in the perturbations [83] by the (00)-component

$$\delta G_{00} = 2\nabla^2 \phi + 6K(\psi + \phi) - 6\mathcal{H}\dot{\phi} \, , \tag{2.45}$$

the longitudinal $(0i)$-component

$$\delta G_{0i} = 2\nabla_i(\dot{\phi} + \mathcal{H}\psi) \, , \tag{2.46}$$

the transverse $(0i)$-component

$$\delta G_{0i} = -(2\dot{\mathcal{H}} + \mathcal{H}^2 + 2K)w_i - \tfrac{1}{2}\nabla^2 w_i \, , \tag{2.47}$$

and the longitudinal (ij)-component

$$\delta G_{ij} = \left[2(2\dot{\mathcal{H}} + \mathcal{H}^2)(\psi + \phi) + 2\mathcal{H}(\dot{\psi} + 2\dot{\phi}) + 2\ddot{\phi} + \nabla^2(\psi - \phi)\right]\gamma_{ij} \\ + \nabla_i \nabla_j(\phi - \psi) \, , \tag{2.48}$$

and the transverse (ij)-component

$$\delta G_{ij} = -(\partial_\tau + 2\mathcal{H})\nabla_{(i} w_{j)} \, . \tag{2.49}$$

and the traceless and transverse (ij)-component

$$\delta G_{ij} = -2(2\dot{\mathcal{H}} + \mathcal{H}^2)h_{ij} + 2\mathcal{H}\dot{h}_{ij} + \ddot{h}_{ij} - \nabla^2 h_{ij} \, . \tag{2.50}$$

To close the Einstein field equations also the matter part needs to be perturbed which is done in the following.

2.3.2 Perturbed matter

Since working perturbatively, the distribution function is split into a background and perturbation, $f(\tau, \boldsymbol{x}, \boldsymbol{p}) = \bar{f}(\boldsymbol{p}^2) + \delta f(\tau, \boldsymbol{x}, \boldsymbol{p})$. To express the energy-momentum tensor in terms of the distribution function, it is convenient to work in the coframe

$$e^a{}_\mu = \begin{pmatrix} 1 + \psi & -w_j \\ 0 & (1-\phi)|\gamma|^{\frac{1}{2}}\delta^i{}_j + |\gamma|^{\frac{1}{2}}h^i{}_j \end{pmatrix} \, , \tag{2.51}$$

such that the particle number current can be written as

$$N_a = nu_a + a\nu_a \, , \tag{2.52}$$

---

[11]Such decompositions are discussed in greater detail for Euclidean space in appendix A

and the energy momentum tensor is

$$T_{ab} = \epsilon u_a u_b + P(g_{ab} + u_a u_b) + 2a q_{(a} u_{b)} + a^2 \pi_{ab} \ . \tag{2.53}$$

with respect to the rest frame observer with four-velocity $u^a = \delta^a{}_0/a$. The diffusion current $\nu_a = (0, \nu'_i)$ and momentum flux density $q_a = (0, q'_i)$ are orthogonal to the fluid four-velocity as well as the shear stress tensor which has only spatial components.[12] These are given in terms of the particle number density

$$\delta n(\tau, \boldsymbol{x}) = \frac{c}{a^3} \int_{\boldsymbol{p}'} \delta f(\tau, \boldsymbol{x}, \boldsymbol{p}') \ , \tag{2.54}$$

the diffusion current

$$\nu'_i(\tau, \boldsymbol{x}) = \frac{c^2}{a^4} \int_{\boldsymbol{p}'} \frac{p'_i}{E_{\boldsymbol{p}'}} \delta f(\tau, \boldsymbol{x}, \boldsymbol{p}') \ , \tag{2.55}$$

the perturbed energy density

$$\delta \epsilon(\tau, \boldsymbol{x}) = \frac{1}{a^3} \int_{\boldsymbol{p}'} E_{\boldsymbol{p}'} \delta f(\tau, \boldsymbol{x}, \boldsymbol{p}') \ , \tag{2.56}$$

the perturbed pressure

$$\delta P(\tau, \boldsymbol{x}) = \frac{c^2}{a^5} \int_{\boldsymbol{p}'} \frac{\boldsymbol{p}'^2}{3 E_{\boldsymbol{p}'}} \delta f(\tau, \boldsymbol{x}, \boldsymbol{p}') \ , \tag{2.57}$$

the momentum flux density across the hypersurface normal to i

$$q'_i(\tau, \boldsymbol{x}) = -\frac{c}{a^4} \int_{\boldsymbol{p}'} p'_i \, \delta f(\tau, \boldsymbol{x}, \boldsymbol{p}') \ , \tag{2.58}$$

and the shear stress tensor

$$\pi'_{ij}(\tau, \boldsymbol{x}) = \frac{c^2}{a^5} \int_{\boldsymbol{p}'} \frac{p'_i p'_j - \delta_{ij} \boldsymbol{p}'^2/3}{E_{\boldsymbol{p}'}} \delta f(\tau, \boldsymbol{x}, \boldsymbol{p}') \ . \tag{2.59}$$

For the sake of completeness let us discuss another way to define the fluid velocity often done is cosmology and more generally in relativistic fluid dynamics. There are two rather obvious ways to define the fluid velocity, the first being in the direction of the particle number current, the particle or so-called Eckart frame [84] where the diffusion current vanishes,

$$N_\mu = n u_\mu^{\mathrm{E}} \ . \tag{2.60}$$

With the three-velocity $u^i = v^i/a$ this corresponds to defining the spatial velocity as pointing in the direction of the diffusion current, $v_i^{\mathrm{E}} = \nu_i/\bar{n}$. Secondly, the energy

---

[12]The prime is to denote that the three-vectors are expressed in the coframe (2.51).

16

or so-called Landau frame [85] in which the fluid velocity is the time-like eigenvector of the energy-momentum tensor such that the momentum density flux vanishes,

$$T_{\mu\nu} = \epsilon u_\mu^{\mathrm{L}} u_\nu^{\mathrm{L}} + P(g_{\mu\nu} + u_\mu^{\mathrm{L}} u_\nu^{\mathrm{L}}) + a^2 \pi_{\mu\nu} , \qquad (2.61)$$

implying that one has $v_i^{\mathrm{L}} = q_i/(\bar{\epsilon} + \bar{P})$. In either of these cases, the fluid three-velocity is pointing in the direction of the dissipation current or energy flux, respectively. Especially the Landau frame is most commonly used in perturbation theory, such that instead of the energy flux the fluid three-velocity is used as a perturbative variable. Since this is just a choice of convention, here the momentum density flux is kept.

2.3.3 Vlasov–Einstein equation

Combining the results obtained from the perturbed metric and energy-momentum tensor one can now find Einstein's field equations in these variables. These are given by the (00)-component

$$(\nabla^2 + 3K)\phi = \tfrac{1}{2}\kappa a^2[\delta\epsilon - 3\mathcal{H}q] , \qquad (2.62)$$

the longitudinal (0i)-component

$$\dot{\phi} + \mathcal{H}\psi = -\tfrac{1}{2}\kappa a^2 q , \qquad (2.63)$$

the transverse (0i)-component

$$(\nabla^2 + 2K)w_i = 2\kappa a^2 \left[(\bar{\epsilon} + \bar{P})\, w_i + q_i^\perp\right] , \qquad (2.64)$$

the trace (ij)-component

$$\ddot{\phi} + \mathcal{H}(\dot{\psi} + 2\dot{\phi}) + (2\dot{\mathcal{H}} + \mathcal{H}^2)\psi + \tfrac{1}{3}\nabla^2(\psi - \phi) - K\phi = \tfrac{1}{2}\kappa a^2 \delta P , \qquad (2.65)$$

the longitudinal (ij)-component

$$\phi - \psi = \kappa a^2 \pi , \qquad (2.66)$$

the transverse (ij)-component

$$(\partial_\tau + 2\mathcal{H})w_i = -\kappa a^2 \pi_i^\perp , \qquad (2.67)$$

and finally the transverse traceless (ij)-component

$$(\partial_\tau^2 + 2\mathcal{H}\partial_\tau - \nabla^2 + 2K)h_{ij} = \kappa a^2 \pi_{ij}^{\mathrm{tt}} . \qquad (2.68)$$

One can now realise that the six equations (2.63), (2.65), (2.67) and (2.68) describe the time evolution of the metric perturbations corresponding to the six physical degrees of freedom while the other four equation (2.62), (2.64) and (2.66) are constraint equations.

While the Einstein field equation describe the evolution of the metric perturbations, the dynamics of the matter perturbations are determined by the Vlasov equation (2.23). Since $\partial_\mu f$ is already of first order in perturbations, the coefficient in front can be set to the background value. In contrast $\partial f / \partial p_i$ has a background contribution such. With the metric (2.43) one then obtains the Vlasov equation

$$\partial_\tau f + \frac{p_i}{aE_{\boldsymbol{p}}/c^2}\,\partial^i f - \left[\frac{aE_{\boldsymbol{p}}}{c^2}\,\partial_i\psi + \frac{\boldsymbol{p}^2}{aE_{\boldsymbol{p}}}\,\partial_i\phi - \frac{p_j}{c}\,\partial_i w^j - \frac{p_j p_k}{aE_{\boldsymbol{p}}}\,\partial_i h^{jk}\right]\frac{\partial f}{\partial p_i} = 0\,, \quad (2.69)$$

where the speed of light is explicitly reinstalled in order take the non-relativistic limit in the next section.

In principal one could now solve the perturbed Einstein–Vlasov equations for a general relativistic treatment of structure formation. Since these in general involves solving for the full distribution function and the six metric degrees of freedom it is a rather involving problem. One could turn to truncation schemes that describe the phase-space distribution function in terms of its moments to reduce the complexity although a truncation of such an expansion is also problematic in the general relativistic setting [67]. Before turning to such truncation schemes it is convenient to additionally reduce the complexity by considering the Newtonian limit of the perturbed Einstein–Vlasov equations as applicable for non-relativistic dark matter. This is pursued in the next section.

2.4 Newtonian cosmology

Often the full general relativistic Vlasov–Einstein equations can be reduced to a much simpler system of equations. The requirements for such a simplification are discussed in the following.

2.4.1 Newtonian limit

Typical gravitational fields throughout the Universe are relatively small in magnitude and quasi-stationary, at least when not probing the extremest of gravitational phenomena such as black holes or neutron stars. Additionally, the currently favoured candidate accounting for the dominant contribution to the matter content of the Universe is *cold dark matter*. In the kinetic theory picture this corresponds to a phase-space distribution function which is centred around velocities much smaller than the speed of light. With these assumptions the dynamics of dark matter gravitational instabilities greatly simplify as shown in the following.

The *Newtonian limit* is defined by the requirements:

- Gravitational fields are weak, $|\delta g_{\mu\nu}| \ll 1$.

- Gravitational fields are quasi-stationary, $|\partial_\tau \delta g_{\mu\nu}\,/\,\mathcal{H}| \ll 1$.

- Particle velocities are non-relativistic, $|v^i| \ll c$.

Note that while the gravitational fields are assumed to be small in magnitude, this does not necessary imply that deviations from the background distribution function are small.

The assumption of weak gravitational fields justifies the perturbative treatment of Einstein's field equations resulting in Friedmann's equations and the first-order deviations from them. When studying late-time cosmic structure formation it is additionally convenient to work in a spatially flat geometry and neglect the radiative contribution to the energy content of the Universe.[13] This is well justified since the curvature and radiation densities contribute below the per mille level to the energy content of the Universe sufficiently deep within the matter dominated era. With these assumptions, the Friedmann equations (2.34) reduce to

$$\Omega_{\mathrm{m}} + \Omega_{\Lambda} = 1 \;, \qquad \frac{\dot{\mathcal{H}}}{\mathcal{H}^2} = 1 - \frac{3}{2}\,\Omega_{\mathrm{m}} \;. \tag{2.70}$$

To leading order one obtains $E_{\boldsymbol{p}} \to mc^2$ in the non-relativistic limit such that the Vlasov equation (2.69) simplifies to

$$\partial_\tau f + \frac{p_i}{am}\,\partial_i f - am\,\partial_i\psi\,\frac{\partial f}{\partial p_i} = 0 \;, \tag{2.71}$$

in the Newtonian limit. Therefore, the only relevant equations needed to obtain a closed system of equations are the non-relativistic limit of the constraint equations (2.62) and (2.66). These yield Poisson's equation

$$\partial_i\partial_i\phi = \frac{3}{2}\,\mathcal{H}^2\Omega_{\mathrm{m}}\,\frac{\delta\epsilon}{\bar{\epsilon}} \;, \tag{2.72}$$

and $\psi = \phi$, respectively. In the following, it is chosen to work in terms of the gravitational potential ϕ such that effectively the metric in the Newtonian limit is given by

$$\mathrm{d}s^2 = a^2\big[-(1+2\phi)\,\mathrm{d}\tau^2 + (1-2\phi)\,\delta_{ij}\,\mathrm{d}x^i\,\mathrm{d}x^j\big] \;, \tag{2.73}$$

also known as conformal Newtonian gauge.[14]

2.4.2 Vlasov–Poisson equations

In the following, it is sensible to define the non-relativistic analogue of the components of the particle number current (2.13) and energy-momentum tensor (2.14). These are related to the non-relativistic moments of the phase-space distribution

---

[13]In Euclidean space, vectors and covectors are no longer distinguished as they are canonically related and all vectors are denoted with subscripts in the following.

[14]In principal, one could engineer the limit such that it also includes vector and tensor metric perturbations. These are absent in the presented derivation since it is assumed that all metric perturbations are of the same dimension, $[\psi] = [\phi] = [w_i] = [h_{ij}]$. In this case the vector and tensor perturbations drop out of the non-relativistic limit of the Vlasov equation (2.69) since they are suppressed by the speed of light.

function and studied in the next section. The proper dark matter mass density field is defined as

$$\rho(\tau, \boldsymbol{x}) := \frac{m}{a^3} \int_{\boldsymbol{p}} f(\tau, \boldsymbol{x}, \boldsymbol{p}) \,, \tag{2.74}$$

the proper momentum flux reads

$$\rho(\tau, \boldsymbol{x}) \, u_i(\tau, \boldsymbol{x}) := \frac{m}{a^3} \int_{\boldsymbol{p}} \frac{p_i}{am} \, f(\tau, \boldsymbol{x}, \boldsymbol{p}) \,, \tag{2.75}$$

and the proper stress tensor is

$$\rho(\tau, \boldsymbol{x}) \big[u_i(\tau, \boldsymbol{x}) \, u_j(\tau, \boldsymbol{x}) + \sigma_{ij}(\tau, \boldsymbol{x}) \big] := \frac{m}{a^3} \int_{\boldsymbol{p}} \frac{p_i}{am} \frac{p_j}{am} \, f(\tau, \boldsymbol{x}, \boldsymbol{p}) \,. \tag{2.76}$$

The momentum flux (2.75) and stress tensor (2.76) have already been expressed in terms of the velocity field $u_i(\tau, \boldsymbol{x})$ and velocity dispersion tensor $\sigma_{ij}(\tau, \boldsymbol{x})$ which are the connected part of the corresponding moments and play a central role in the subsequent sections and chapters.

The non-relativistic limit of the components of the particle number current and energy-momentum tensor are given by

$$n \to \frac{\rho c}{m} \,, \quad \nu_i \to \frac{\rho u_i}{m} \,, \quad \epsilon \to \rho c^2 \,, \quad q_i \to \rho c u_i \,, \quad \delta_{ij} P + \pi_{ij} \to \rho \sigma_{ij} \,, \tag{2.77}$$

where the particle and energy flow are pointed into the direction of the mass flow such that the Eckart and Landau frame coincide in this limit, at least to leading order.

Since the gravitational potential is sourced by the relative deviation from the background energy density it is convenient to also split the mass density field into a homogeneous background and a local fluctuation,

$$\rho(\tau, \boldsymbol{x}) =: \bar{\rho}(\tau) \big[1 + \delta(\tau, \boldsymbol{x}) \big] \,. \tag{2.78}$$

The background density decays with the expansion of space $\bar{\rho} \propto a^{-3}$ as was already discussed in section 2.2.[15] It is convenient to redefine the distribution function as

$$\tilde{f}(\tau, \boldsymbol{x}, \boldsymbol{p}) := \frac{1}{\bar{\rho}} \frac{m}{a^3} \, f(\tau, \boldsymbol{x}, \boldsymbol{p}) \,, \tag{2.79}$$

such that it is normalised to unity with respect to the momentum argument at the level of the homogeneous and isotropic background cosmology. Since the time-dependence is the same as for the standard distribution function, it obeys the same

---

[15]For non-vanishing velocity dispersion this is only true to leading order since the equation of state is of the order $\mathcal{O}(\bar{\sigma}_{ii}/c^2)$. In the following it is assumed that this contribution is small enough to not significantly contribute to the evolution of the background cosmology.

Vlasov equation (2.71). Dropping the tilde in the following, the Vlasov–Poisson equations [5] take the form

$$\partial_\tau f + \frac{p_i}{am}\,\partial_i f - am\,\partial_i \phi\,\frac{\partial f}{\partial p_i} = 0\ ,$$

$$\partial_i \partial_i \phi = \tfrac{3}{2}\mathcal{H}^2 \Omega_{\mathrm{m}}\left[\int_{\boldsymbol{p}} f - 1\right]. \tag{2.80}$$

Together with Friedmann's equations (2.70) they form a closed system of equations.

2.4.3 Moments, cumulants and the Vlasov hierarchy

While it would in principal be desirable to know the full phase-space distribution function, the main problem lies in the complexity when supplying random initial conditions. In the study of late-time large-scale cosmic structure formation one usually adopts a statistical description in which the phase-space distribution function itself is random.[16] In this case the Vlasov–Poisson equations (2.80) are stochastic partial differential equations in seven variables that are quite challenging to investigate with analytical methods. Therefore, one is often not interested in the full phase-space distribution function but rather in velocity moments thereof. The full set of moments completely characterise the distribution function and parametrise the degrees of freedom of the dark matter particle ensemble.

To investigate the moments of the phase-space distribution function with respect to the momentum argument in a systematic manner, it is convenient to introduce the moment-generating function

$$M(\tau,\boldsymbol{x};\boldsymbol{l}) := \int_{\boldsymbol{p}} \mathrm{e}^{\frac{\boldsymbol{l}\cdot\boldsymbol{p}}{am}}\,f(\tau,\boldsymbol{x},\boldsymbol{p})\ . \tag{2.81}$$

The *proper velocity moments* of the distribution function are obtained by taking derivatives with respect to the source vector $\boldsymbol{l}$ and evaluating at vanishing value,

$$m_{i_1\dots i_n}^{(n)}(\tau,\boldsymbol{x}) := \left.\frac{\partial^n M}{\partial l_{i_1}\dots\partial l_{i_n}}\right|_{\boldsymbol{l}=\boldsymbol{0}}. \tag{2.82}$$

The first few moments were already defined in equations (2.74), (2.75) and (2.76). In terms of the redefined distribution function (2.79) these reads

$$m^{(0)} = 1+\delta\ ,\qquad m_i^{(1)} = (1+\delta)u_i\ ,\quad m_{ij}^{(2)} = (1+\delta)(u_i u_j + \sigma_{ij})\ . \tag{2.83}$$

The time evolution of the moments is determined by the Vlasov equation and obtained by an appropriately weighted integration over momentum space,

$$\partial_\tau m_{i_1\dots i_n}^{(n)} + n\mathcal{H}\,m_{i_1\dots i_n}^{(n)} + \partial_{i_{n+1}} m_{i_1\dots i_n i_{n+1}}^{(n+1)} + n\,m_{i_1\dots i_{n-1}}^{(n-1)}\partial_{i_n}\phi = 0\ . \tag{2.84}$$

---

[16]The statistical description of dark matter is discussed in chapter 3 and at the heart of the field-theoretic formulation introduced in chapter 4.

To obtain a closed system of equations Poisson's equation needs to be supplied,

$$\partial_i \partial_i \phi = \tfrac{3}{2} \mathcal{H}^2 \Omega_\mathrm{m} \delta \ . \tag{2.85}$$

While the second term on the left-hand side of the evolution equation (2.84) represents the Hubble drag term of the corresponding moment, the third and fourth term couple to the next lower- and (more importantly) next higher-order moment. This creates an infinite tower of coupled non-linear evolution equations sometimes called the *Vlasov hierarchy* [86].

From a practical point of view it is rather pointless to keep the full (infinite) set of moments. To obtain a finite and closed (and thereby solvable) system of equations one usually needs to resort to approximations.

To find an appropriate approximation scheme for the description of dark matter gravitational dynamics it is useful to introduce another type of object that equivalently well characterises the distribution function. The *proper velocity cumulants* are the connected part of the moments and are derived from the cumulant-generating function $C(\tau, \boldsymbol{x}; \boldsymbol{l}) := \ln(M)$ in the same manner as moments are obtained from the moment-generating function M,

$$c_{i_1 \dots i_n}^{(n)}(\tau, \boldsymbol{x}) := \left. \frac{\partial^n C}{\partial l_{i_1} \dots \partial l_{i_n}} \right|_{\boldsymbol{l} = \boldsymbol{0}} \ . \tag{2.86}$$

The first few cumulants are then given by

$$c^{(0)} = \ln(1 + \delta) \ , \qquad c_i^{(1)} = u_i \ , \qquad c_{ij}^{(2)} = \sigma_{ij} \ . \tag{2.87}$$

Although being two sides of the same coin, it is often preferential to work in terms of cumulants rather than moments, one of the reasons being that the degenerate and normal distribution are fully characterised in terms of a finite amount of cumulants.

The time evolution of the cumulants is determined by the Vlasov equation and obtained in a similar manner as for the moments. The corresponding evolution equations read [87]

$$\partial_\tau c_{i_1 \dots i_n}^{(n)} + n\mathcal{H} c_{i_1 \dots i_n}^{(n)} + \partial_{i_{n+1}} c_{i_1 \dots i_{n+1}}^{(n+1)} + \sum_S c_{j_1 \dots j_{|S|} i_{n+1}}^{(|S|+1)} \partial_{i_{n+1}} c_{j_{|S|+1} \dots j_n}^{(n-|S|)} \\ + \delta_{n1} \partial_{i_1} \phi = 0 \ , \tag{2.88}$$

where the sum runs over all combinations of picking indices $\{j_1, \dots, j_n\}$ out of $\{i_1, \dots, i_n\}$.[17] The cumulant evolution equations are non-linear and create an infinite hierarchy of coupled equations, very similar to the equations (2.84).

Although the general structure is discussed in the next section, the applications studied in later chapters only involve the first few of the evolution equations explicitly. These are given by the continuity equation

$$\partial_\tau \delta + \partial_i [(1 + \delta) u_i] = 0 \ , \tag{2.89}$$

---

[17]More formally, the sum runs through all 2^n sets S in the power set $\mathcal{P}(\{i_1, \dots, i_n\})$ with $\{j_1, \dots, j_{|S|}\} \in S$ and $\{j_{|S|+1}, \dots, j_n\} \in \{i_1, \dots, i_n\} \backslash S$.

Cauchy's momentum equation

$$\partial_\tau u_i + \mathcal{H} u_i + \partial_j \sigma_{ij} + u_j \partial_j u_i + \sigma_{ij} \partial_j \ln(1+\delta) + \partial_i \phi = 0 \ , \qquad (2.90)$$

and the velocity dispersion equation

$$\partial_\tau \sigma_{ij} + 2\mathcal{H} \sigma_{ij} + \partial_k c_{ijk}^{(3)} + u_k \partial_k \sigma_{ij} + \sigma_{jk} \partial_k u_i + \sigma_{ik} \partial_k u_j + c_{ijk}^{(3)} \partial_k \ln(1+\delta) = 0 \ . \ (2.91)$$

The continuity equation (2.89) is expressed in terms of the density contrast field rather than in the zeroth-order cumulant because δ is the natural physical field variable and enters Poisson's equation (2.85). At the same time it is emphasised that the non-linear terms in the higher-order evolution equations (2.90) and (2.91) couple to the logarithmic density field.

Cauchy's momentum equation (2.90) describes the momentum transport of the dark matter particle ensemble and is as such rather general. By specifying a constitutive relation, the stress tensor can be expressed in terms of viscosity and the velocity field such that one obtains the Navier–Stokes equation describing the dynamics of a viscid fluid. Similarly, one obtains Euler's equations for a vanishing velocity dispersion tensor describing the dynamics of a perfect fluid.

These limits are related to approximations in which the phase-space distribution function is described in terms of finite cumulants only. General truncation schemes of the cumulant expansion are investigated in the next section in order to find a viable description for the dynamics of dark matter gravitational instabilities. These should be understood as coarse-gaining the microscopic dynamics such that one is left with a finite set of macroscopic quantities describing the dark matter particle ensemble in an effective theory description also referred to as the *cosmological fluid.*

2.4.4 Truncations of the cumulant expansion

Since keeping the full cumulant expansion of the phase-space distribution function is impractical for applications, this section is concerned with approximations. To this end it is sensible to analyse the different terms for the nth-order cumulant evolution equation (2.88):

- The second term is the Hubble drag term of the nth-order cumulant.

- The third term depends on the $(n+1)$th-order cumulant creating the Vlasov hierarchy.

- The fourth term is non-linear in cumulants and couples the $(k+1)$th- and $(n-k)$th-order for all $k \in \{0, \dots, n\}$.

- The fifth term only contributes for $n = 1$ and depends on the gravitational potential.

The main issue in finding a self-consistent truncation of the cumulant expansion that does not generate any other cumulants lies within the non-linear terms. One can

easily verify that any truncation of the cumulant expansion that includes cumulants of order $n > 1$ naturally generates all higher-order cumulants due to the non-linear terms [88].

The only apparent self-consistent truncation of the cumulant expansion is obtained by only keeping the zeroth and first order. The so-called *single-stream approximation* corresponds to a degenerate distribution function

$$f(\tau, \boldsymbol{x}, \boldsymbol{p}) = (1 + \delta)(2\pi)^3 \, \delta(\boldsymbol{p} - am\boldsymbol{u}) \,, \tag{2.92}$$

where momentum is directly related to the velocity field at each instant in time and point in space. The distribution function (2.92) is described in terms of four degrees of freedom only, namely the density contrast and velocity field. The corresponding evolution equations are the continuity and Euler's equations describing the dynamics of a perfect pressureless fluid.

While the single-stream approximation is mathematically self-consistent it cannot capture the exact physical dynamics. During gravitational collapse dark matter particle trajectories cross in positions space and the velocity field is multi-valued, a phenomenon known as *shell-crossing*. By construction the single-stream approximation cannot account for the multiple streams coexisting in the same region of space at shell-crossing. The superposition of streams naturally generate a non-trivial velocity dispersion tensor which in turn sources all higher-order cumulants and thus the single-stream approximation breaks down [88].

To go beyond the shell-crossing regime one generally needs to include higher-order cumulants. By the above presented arguments it is clear that one would actually need to include all higher-order cumulants since even if initially absent the Vlasov hierarchy would generate them. Naturally the question arises whether all cumulants are needed for a viable description that can capture the relevant physical processes of cosmic structure formation.

For non-relativistic dark matter that decouples thermally in the early Universe one would expect the background distribution function to be Maxwellian [2],

$$\bar{f}(\boldsymbol{p}^2) = \left(\frac{2\pi}{mk_{\mathrm{B}}T}\right)^{\frac{3}{2}} \exp\left(-\frac{\boldsymbol{p}^2}{2mk_{\mathrm{B}}T}\right) \,, \tag{2.93}$$

where T is the dark matter temperature and k_{B} the Boltzmann constant. Equation (2.93) corresponds to a normal distribution that is described in terms of the three cumulants (2.87) only. The zeroth- and first-order cumulants vanishes due to the normalisation (2.79) and isotropy, respectively, while the second-order cumulant is given by $\bar{\sigma}_{ij} = \delta_{ij}k_{\mathrm{B}}T/(ma^2)$. At the level of the background the distribution function is naturally conserved since the Vlasov equation reduces to $\partial_\tau \bar{f}(\boldsymbol{p}^2) = 0$.

A simple extension of the single-stream approximation is achieved by including the velocity dispersion tensor and truncating the cumulant expansion thereafter [6–8]. In this case the momenta are normal distributed,

$$f(\tau, \boldsymbol{x}, \boldsymbol{p}) = \frac{(1 + \delta)\,(2\pi)^{\frac{3}{2}}}{a^3 m^3 \det(\sigma)^{\frac{1}{2}}} \exp\left(-\frac{1}{2}\left[\frac{p_i}{am} - u_i\right](\sigma^{-1})_{ij}\left[\frac{p_j}{am} - u_j\right]\right) \,, \tag{2.94}$$

and $\sigma_{ij}(\tau, \boldsymbol{x})$ is the covariance matrix.[18] The non-trivial velocity dispersion tensor regularises the momentum delta function of the single-stream approximation (2.92) which is recovered in the limit $\sigma_{ij} \to 0$. Although the distribution function (2.94) cannot capture shell-crossing microscopically, it supports the average motion of a multi-stream flow.

The distribution function (2.94) naturally supports a Maxwell–Boltzmann distribution of momenta (2.93), such as expected for thermal relics [2] or virialised clumps of dark matter, at least in simple halo models [89], but is more general in the sense that it can describe local deviations from the background. Although the subsequent evolution in time naturally deforms the distribution function away from its initial shape, the first three cumulants can provide a good approximation of the full distribution function as long as the other cumulants are relatively small.

More generally, one could include higher-order cumulants up to some desired order n and truncate the expansion thereafter. For truncations with $n > 2$ the distribution function can no longer be explicitly reconstructed.[19] Nonetheless, one would expect that any finite cumulant expansion has a natural range of scales where it is applicable, but eventually breaks down due to small scale effects that are not captured by the truncation.

2.4.5 Galilean invariance

In the Newtonian limit Hamilton's equations (2.20) take the form

$$\frac{\mathrm{d}x_i}{\mathrm{d}\tau} = \frac{p_i}{am}, \qquad \frac{\mathrm{d}p_i}{\mathrm{d}\tau} = -am\, \partial_i \phi\,. \tag{2.95}$$

A standard symmetry of the Newtonian limit of general relativity is Galilean invariance [90]. A Galilean transformation relates two inertial frames of reference and is given by the coordinate transformation $\boldsymbol{r} \mapsto \boldsymbol{r} + \boldsymbol{v}t$ for any constant velocity $\boldsymbol{v}$ in terms of proper cosmic time $\mathrm{d}t := a(\tau)\,\mathrm{d}\tau$ and proper physical coordinates $\boldsymbol{r} := a(\tau)\,\boldsymbol{x}$.[20] The corresponding transformation of the comoving coordinates and conjugate momenta take the time-dependent form [92]

$$\boldsymbol{x} \mapsto \boldsymbol{x} + \boldsymbol{v}\,T\,, \qquad \boldsymbol{p} \mapsto \boldsymbol{p} + am\boldsymbol{v}\,\dot{T}\,, \tag{2.96}$$

where

$$T(\tau) := \frac{1}{a(\tau)} \int_{\tau_{\mathrm{in}}}^{\tau} \mathrm{d}\tau'\, a(\tau')\,. \tag{2.97}$$

The phase-space distribution function is invariant under Galilean transformations and transforms as

$$f(\tau, \boldsymbol{x}, \boldsymbol{p}) \mapsto f(\tau, \boldsymbol{x} - \boldsymbol{v}\,T, \boldsymbol{p} - am\boldsymbol{v}\,\dot{T})\,. \tag{2.98}$$

---

[18]By construction the velocity dispersion tensor is positive definite such that the distribution function exists, except for trivial degenerate cases.

[19]The only distribution functions that have a finite amount of cumulants are the degenerate and normal distribution.

[20]Naturally the velocity $\boldsymbol{v}$ should be much smaller than the speed of light to justify the Newtonian limit.

For the moment-generating function one then obtains

$$M(\tau, \boldsymbol{x}; \boldsymbol{l}) \mapsto M(\tau, \boldsymbol{x} - \boldsymbol{v}\,T; \boldsymbol{l})\,\mathrm{e}^{\boldsymbol{l}\cdot\boldsymbol{v}\dot{T}}\;,\tag{2.99}$$

and as such all velocity moments are affected by a Galilean transformation. In terms of the cumulant-generating function one has

$$C(\tau, \boldsymbol{x}; \boldsymbol{l}) \mapsto C(\tau, \boldsymbol{x} - \boldsymbol{v}\,T; \boldsymbol{l}) + \boldsymbol{l}\cdot\boldsymbol{v}\dot{T}\;,\tag{2.100}$$

implying that only the first-order cumulant transforms non-trivially under a Galilean transformation,

$$c^{(n)}_{i_1\dots i_n}(\tau, \boldsymbol{x}) \mapsto c^{(n)}_{i_1\dots i_n}(\tau, \boldsymbol{x} - \boldsymbol{v}\,T) + \delta_{n1}v_{i_1}\dot{T}\;.\tag{2.101}$$

The presence of the self-gravitating cosmological fluid spontaneously breaks Galilean invariance since there exists a preferred frame in which the fluid is at rest [93]. This is immediately evident when considering the transformation of the gravitational potential [90] under the Galilean transformation (2.96),

$$\partial_i\phi(\tau, \boldsymbol{x}) \mapsto \partial_i\phi(\tau, \boldsymbol{x} - \boldsymbol{v}\,T) + \boldsymbol{v}\,\dot{\mathcal{H}}T\;,\tag{2.102}$$

as demanded by the equations of motion (2.95). While Galilean invariance is no longer manifest it corresponds to an extended symmetry and is related to the large wave number sector of the theory studied in chapter 5.

3 Statistical cosmology

In this chapter the statistical description of dark matter, which is at the heart of the field theory formulated in chapter 4, is introduced. In section 3.1 the description of dark matter in terms of random fields and correlation functions is introduced. In section 3.2 the theory of inflation as the initial condition for large-scale cosmic structure formation is discussed. In section 3.3 the decomposition into irreducible representations of the translation and rotation group of dark matter degrees of freedom is performed. Finally, in section 3.4 linear perturbation theory is reviewed.

Fourier transform

In the following, it is often convenient to work in terms of the Fourier transform taking position vectors $\boldsymbol{x}$ to their reciprocal wave vectors $\boldsymbol{k}$. For any suitable function or distribution $f(\boldsymbol{x})$ the convention

$$f(\boldsymbol{k}) = \int_{\boldsymbol{x}} \mathrm{e}^{-\mathrm{i}\boldsymbol{k}\cdot\boldsymbol{x}} f(\boldsymbol{x}) \ , \qquad f(\boldsymbol{x}) = \int_{\boldsymbol{k}} \mathrm{e}^{\mathrm{i}\boldsymbol{k}\cdot\boldsymbol{x}} f(\boldsymbol{k}) \ , \tag{3.1}$$

is employed. The Fourier transform is denoted by the same symbol and distinguished by its argument if not clear from the context. The three-dimensional Euclidean inner product is written as $\boldsymbol{k}\cdot\boldsymbol{x} = k_i x_i$ and the modulus of three-vectors is abbreviated as the corresponding lightface symbol, such as for the wave number $k = |\boldsymbol{k}|$. Integrals over the entire domain are abbreviated as

$$\int_{\boldsymbol{x}} := \int_{\mathbb{R}^3} \mathrm{d}^3 x \ , \qquad \int_{\boldsymbol{k}} := \int_{\mathbb{R}^3} \frac{\mathrm{d}^3 k}{(2\pi)^3} \ , \tag{3.2}$$

and wave vector delta functions are often denoted as $\bar{\delta}(\boldsymbol{k}) := (2\pi)^3 \, \delta(\boldsymbol{k})$.

3.1 Statistical description of dark matter

To study late-time large-scale cosmic structure formation, one usually adopts a statistical description of dark matter. This is most often motivated from the assumption that the very early Universe goes through a period of rapid expansion inflating quantum fluctuations in the energy density to macroscopic perturbations. The most common type of such inflation models predict these perturbations to be very close to statistically homogeneous and isotropic Gaussian random fields [94] and is discussed in more detail in the next section.

   The employed statistical field theory can be understood as describing an ensemble of cosmic histories or, equivalently for this purpose, a sample corresponding to a large

but finite spatial volume of the Universe. The *fair sample hypothesis* conjectures that ensemble averages over cosmic histories can be treated as samples averages for large enough spatial domains [95]. The closely related concept of *ergodicity* asserts that ensemble averages are equal to sample averages over an infinite volume. Since the fair sample hypothesis assumes this property to also hold for finite patches of the Universe, it is a much stronger assumption.

To characterise the statistical properties of random fields, one usually studies expectation values of composite field operators which are most often taken to be monomials in the fields. These so-called *correlation functions* are the natural generalisation of the moments of a multivariate random variable. The cosmological principle corresponds to the assumption that spatial homogeneity and isotropy are realised statistically such that the correlation functions transform trivially under the action of the translation and rotation group [96].

In a kinetic theory description, one is interested in correlation functions of the phase-space distribution function $f(\tau, \boldsymbol{x}, \boldsymbol{p})$ or the velocity moments and cumulants thereof. The simplest type of correlation functions has already been encountered in chapter 2, namely the dark matter background mass density

$$\bar{\rho}(\tau) = \langle \rho(\tau, \boldsymbol{x}) \rangle \,, \tag{3.3}$$

and background pressure

$$\delta_{ij} \bar{P}(\tau) = \langle \rho(\tau, \boldsymbol{x}) \, \sigma_{ij}(\tau, \boldsymbol{x}) \rangle \,, \tag{3.4}$$

where $\langle ... \rangle$ denotes the ensemble average.

One-point correlation functions are *mean fields*, such as background density (3.3), which are constant throughout space due to statistical homogeneity. The density contrast field (2.78) has a vanishing mean field as it is defined as the relative deviation from the density mean field (3.3). Due to statistical isotropy the velocity field cannot obtain a mean field and in fact all moments and cumulants of odd order have vanishing mean fields. In contrast, moments and cumulants of even order in general have non-vanishing mean fields, such as the stress tensor (3.4). Of the cumulants discussed in chapter 2 only the trace of the velocity dispersion tensor can obtain a mean field,

$$\delta_{ij} \bar{\sigma}(\tau) \coloneqq \langle \sigma_{ij}(\tau, \boldsymbol{x}) \rangle \,. \tag{3.5}$$

It is emphasised that the pressure mean field (3.4) is not given by the product of the density and velocity dispersion mean fields but also includes cross-correlations of density and velocity dispersion fields due to the non-linear splitting (3.4).

To study higher-order correlation functions, it is useful to introduce *connected correlation functions* as the natural generalisation of the cumulants of a multivariate random variable. The connected two-point correlation functions are expectation values of two fields and correspond to auto- and cross-covariance functions. Since inflation predicts the initial state of the theory to be very near to a Gaussian random field, the covariance functions together with the mean fields fully characterise the initial state of the theory.

The cross-covariance function of two scalar fields ϕ and ψ is denoted as

$$C_{\phi\psi}(|\boldsymbol{x} - \boldsymbol{x}'|) = \langle \phi(\boldsymbol{x})\,\psi(\boldsymbol{x}')\rangle_{\mathrm{c}} := \langle \phi(\boldsymbol{x})\,\psi(\boldsymbol{x}')\rangle - \langle\phi(\boldsymbol{x})\rangle\langle\psi(\boldsymbol{x}')\rangle \,, \qquad (3.6)$$

where $\langle...\rangle_{\mathrm{c}}$ is the connected part of the expectation value. Due to statistical homogeneity and isotropy, the two-point correlation functions only depend on the distance, at least for scalar fields.

In cosmology, one is mostly concerned with the density contrast equal-time auto-covariance function although in general also unequal-time and cross-covariance functions are necessary to understand all the physics at play.[1]

In general, one can also study higher-order (connected) correlation functions which quantify the deviation from a Gaussian random field similar to the skewness and kurtosis of a random variable. Since the dynamics of dark matter gravitational instabilities is non-linear, the late-time statistical properties of dark matter are naturally non-Gaussian. However, one expects the covariance functions to be the dominant correlations on cosmically large scales where deviations from the homogeneous and isotropic background are small and gravitational dynamics is almost linear.

It is often convenient to work with the Fourier transform of correlation functions. Since the mean fields are spatially constant, they consist of a zero mode only. The Fourier transform of a connected two-point correlation function is the *power spectral density*

$$P_{\phi\psi}(k) := \int_{\boldsymbol{x}} \mathrm{e}^{\mathrm{i}\boldsymbol{k}\cdot(\boldsymbol{x}-\boldsymbol{x}')}\, C_{\phi\psi}(|\boldsymbol{x} - \boldsymbol{x}'|) \,, \qquad (3.7)$$

one of the central objects studied in cosmology. It quantifies the distribution of 'power' into Fourier modes and is also called the power spectrum. Simple examples include a constant power spectral density corresponding to Gaussian white noise and the reciprocal of a pure quadratic polynomial corresponding to an Ornstein–Uhlenbeck process [97].

Another useful quantity is the dimensionless power spectrum

$$\Delta_{\phi\psi}(k) := \frac{k^3}{2\pi^2}\, P_{\phi\psi}(k) \,. \qquad (3.8)$$

The coincidence limit of the covariance function, provided it exists and is finite, can then be written as

$$C_{\phi\psi}(0) = \int_{\boldsymbol{k}} P_{\phi\psi}(k) = \int_{-\infty}^{\infty} \mathrm{d}\ln(k/k_*)\, \Delta_{\phi\psi}(k) \,, \qquad (3.9)$$

where the last equality implies that the dimensionless power spectrum quantifies the contribution to the covariance in a logarithmic interval at k/k_* for some arbitrary wave number k_*.

---

[1]The density contrast equal-time auto-covariance function is in cosmology often called *the* correlation function and denoted by $\xi(|\boldsymbol{x} - \boldsymbol{x}'|)$.

Although the two-point correlation functions have been introduced for scalar fields only, the definition can be straight forwardly extended to fields that transform non-trivially under the rotation group. This is discussed in section 3.3, where degrees of freedom are classified according to their transformation properties.

Higher-order correlation functions can be Fourier transformed in a similar fashion. The corresponding spectral densities are the natural generalisations of the power spectrum and are also frequently studied in cosmology in terms of the bi- and trispectrum [98].

3.2 Inflation

It is believed that shortly after the Big Bang the Universe underwent an inflationary phase of rapid expansion. Typical models assume the energy content to be dominated by an inflaton field driving the exponential growth of the Universe [99–101].[2] Quantum fluctuations of the inflaton field are stretched to macroscopic length scales during inflation forming the seeds for late-time cosmic structure formation.

Metric perturbations are induced by the inflaton field due to the warping of spacetime by its energy content. These are most conveniently described in terms of the comoving curvature perturbation $\mathcal{R}$ which is essentially the gravitational potential ϕ in Poisson gauge. Most inflation models predict the comoving curvature perturbation to be described by a near to scale-free Gaussian random field. The corresponding dimensionless power spectrum is usually parametrised in terms of an amplitude A_s and a spectral index n_s at some arbitrary pivot scale k_*,

$$\Delta_\mathcal{R}(k) = A_\mathrm{s} \left(\frac{k}{k_*} \right)^{n_\mathrm{s}-1} . \tag{3.10}$$

In the case $n_\mathrm{s} = 1$ one obtains the scale-free Harrison–Zeldovich power spectrum [102, 103] describing Gaussian white noise.

Since the gravitational potential couples to the dark matter density perturbations via Poisson's equations (2.85), the primordial dimensionless power spectrum of dark matter density perturbations is

$$\Delta_{\delta\delta}^\mathrm{prim}(k) \propto k^4 \Delta_\mathcal{R}(k) \propto k^{n_\mathrm{s}+3} , \tag{3.11}$$

such that induced primordial matter density perturbations are expected to be near to scale-free and Gaussian [104–107].

During inflation the comoving Hubble horizon $c/\mathcal{H}$ is shrinking and perturbations with a larger wave length are said to be superhorizon. After inflation ends and during the subsequent radiation and matter dominated eras of the Universe, perturbations re-enter the growing Hubble horizon and become subhorizon. Since the dark matter density perturbations evolve differently on sub- and superhorizon scales in

---

[2]There is a vast landscape of inflation models, covering single- to multi-scalar field models or even more exotic theories.
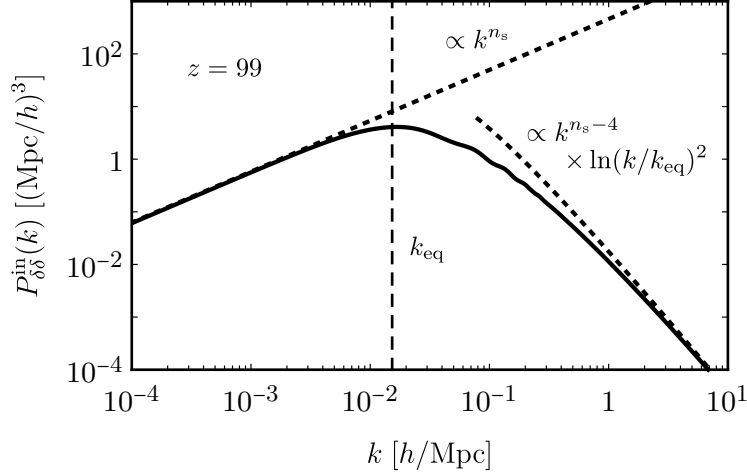
Figure 3.1: Typical density contrast power spectrum used as an initial condition for late-time cosmic structure formation. The infrared and ultraviolet limits (3.12) are shown as dotted curves. The power spectrum is generated at redshift $z = 99$ for a ΛCDM cosmology with parameters from Planck 2018 [162] using the CLASS code [157]. The equality scale $k_{\rm eq} \approx 0.015$ h/Mpc is computed for a cosmic microwave background temperature $T_{\rm CMB} \approx 2.73$ K [158].

the radiation dominated era of the Universe, the near to scale-free power spectrum (3.11) is altered. The matter perturbations inside the horizon are suppressed during radiation domination while outside the horizon continue to grow [3]. During matter domination, the matter perturbations grow equally on all scales and thus the characteristic scale of suppression is set by the radiation-matter equality wave number $k_{\rm eq} = \mathcal{H}_{\rm eq}/c$.[3] This leads to a characteristic shape of the density contrast power spectrum deep within the matter dominated era of the Universe which is given by

$$P_{\delta\delta}^{\rm in}(k) \propto \begin{cases} k^{n_{\rm s}} & \text{for } k \ll k_{\rm eq} \\ k^{n_{\rm s}-4}\ln(k/k_{\rm eq})^2 & \text{for } k \gg k_{\rm eq} \end{cases} . \tag{3.12}$$

A typical density contrast power spectrum used as an initial condition for late-time large-scale cosmic structure formation is shown in figure 3.1.

3.3 Scalar-vector-tensor decomposition

Due to statistical homogeneity and isotropy, it is sensible to classify the degrees of freedom under study according to their transformation properties with respect to the

---

[3]The subhorizon evolution of perturbations in the radiation and matter dominated eras of the Universe is described by the Mészáros equation [108].

three-dimensional Euclidean translation and rotation group. From a group-theoretic point of view this is understood as the decomposition into irreducible representations and is discussed in greater detail in appendix A.

Since the following chapters mainly deal with the velocity cumulants of the phase-space distribution function, they are classified in the following. The decomposition into irreducible unitary representations of the translation group is given by the decomposition into Fourier modes,

$$c_{i_1 \ldots i_n}^{(n)}(\boldsymbol{x}) = \int_{\boldsymbol{k}} \mathrm{e}^{\mathrm{i}\boldsymbol{k}\cdot\boldsymbol{x}}\, c_{i_1 \ldots i_n}^{(n)}(\boldsymbol{k}) \,, \tag{3.13}$$

where time arguments are suppressed in the remainder of this section.

For a fixed wave vector $\boldsymbol{k}$ the Fourier modes are symmetric nth-order three-tensors and as such transform in the nth symmetric power of the defining representation of the rotation group, denoted as $\mathrm{Sym}^n(\mathbf{3})$. The symmetric power can be decomposed into a direct sum of irreducible representations very similar to the Clebsch–Gordan decomposition,

$$\mathrm{Sym}^n(\mathbf{3}) \cong \bigoplus_{j=0}^{\lfloor n/2 \rfloor} (\mathbf{2n - 4j + 1}) \,, \tag{3.14}$$

where the boldfaced right-hand side denotes the irreducible representations in terms of their dimension and $\lfloor \ldots \rfloor$ is the floor function.

Since $\boldsymbol{k}$ singles out a direction, the representations further break up into irreducible representations of the circle group describing rotations in the plane perpendicular to $\boldsymbol{k}$. More explicitly, the odd dimensional irreducible representations of the rotation group break up as

$$(\mathbf{2\ell + 1}) \cong \bigoplus_{j=1}^{\ell} \mathbf{2}_j \oplus \mathbf{1}_0 \,, \tag{3.15}$$

where $\mathbf{2}_j$ are two-dimensional representations and $\mathbf{1}_0$ is the trivial representation of the circle group.[4] The former correspond to spin-j modes that are transverse to $\boldsymbol{k}$ while the latter are spin-0 modes parallel to $\boldsymbol{k}$. In the following, the spin-0 modes are called scalar, the spin-1 modes are called vector and the spin-2 modes are called tensor as is common in cosmology.[5]

Combining the decompositions (3.14) and (3.15) one finally obtains the splitting

$$\mathrm{Sym}^n(\mathbf{3}) \cong \bigoplus_{j=0}^{n} \mathbf{2}_j^{\oplus m_{n,j}} \oplus \mathbf{1}_0^{\oplus m_{n,0}} \,, \tag{3.16}$$

where the multiplicities are given by

$$m_{n,j} = \left\lfloor \frac{n + 2 - j}{2} \right\rfloor \,. \tag{3.17}$$

---

[4]Since the circle group is abelian, its complex irreducible representations are one-dimensional. As such, the two-dimensional real irreducible representation $\mathbf{2}_j$ corresponds to two one-dimensional conjugate complex representations.

[5]Notice that by this nomenclature the vector and tensor modes only have two degrees of freedom.

From a practical point of view the decomposition corresponds to splitting a symmetric nth-order three-tensor into transverse, traceless and symmetric nth-order three-tensors.[6]

Velocity cumulants

Returning to the phase-space distribution function, one finds that a truncation of the cumulant expansion after order n corresponds to a description which includes $(n+3)(n+2)(n+1)/6$ degrees of freedom which can be decomposed into

$$\sum_{k=j}^{n} \left\lfloor \frac{k+2-j}{2} \right\rfloor , \tag{3.18}$$

Fourier modes of spin j.

In the following, this decomposition is used to explicitly decompose the first- and second-order velocity cumulant. While equation (3.16) straight forwardly implies that the velocity field decomposes as $\mathbf{3} \cong \mathbf{2}_1 \oplus \mathbf{1}_0$ and the velocity dispersion tensor as $\mathrm{Sym}^2(\mathbf{3}) \cong \mathbf{2}_2 \oplus \mathbf{2}_1 \oplus \mathbf{1}_0 \oplus \mathbf{1}_0$, one has the freedom to choose a normalisation. To this end, it is convenient to define the the velocity-divergence and vorticity field,

$$\theta(\boldsymbol{x}) := \partial_i u_i(\boldsymbol{x}) , \qquad \omega_i(\boldsymbol{x}) := \epsilon_{ijk}\partial_j u_k(\boldsymbol{x}) , \tag{3.19}$$

quantifying the momentum flux through an infinitesimally small surface enclosing $\boldsymbol{x}$ and the local rotation of fluid elements at $\boldsymbol{x}$, respectively.[7] In terms of these, the decomposition of the velocity field reads

$$u_i(\boldsymbol{x}) = \int_{\boldsymbol{k}} \mathrm{e}^{\mathrm{i}\boldsymbol{k}\cdot\boldsymbol{x}} \left[\epsilon_{ijl} \frac{\mathrm{i}\,k_j}{k^2} \omega_l(\boldsymbol{k}) - \frac{\mathrm{i}\,k_i}{k^2} \theta(\boldsymbol{k}) \right] . \tag{3.20}$$

For the velocity dispersion tensor, the scalar modes are parametrised as

$$\sigma(\boldsymbol{k}) := \tfrac{1}{3}\,\delta_{ij}\sigma_{ij}(\boldsymbol{k}) , \qquad \vartheta(\boldsymbol{k}) := \left(\hat{k}_i\hat{k}_j - \tfrac{1}{3}\,\delta_{ij} \right) \sigma_{ij}(\boldsymbol{k}) , \tag{3.21}$$

where $\hat{k}_i := k_i/k$. These correspond to isotropic and anisotropic velocity dispersion degrees of freedom, respectively. The vector and tensor modes are anisotropic velocity dispersion degrees of freedom and are defined as the projections

$$\vartheta_i(\boldsymbol{k}) := \mathrm{P}_{il}(\boldsymbol{k})\,\hat{k}_j\,\sigma_{lj}(\boldsymbol{k}) , \qquad \vartheta_{ij}(\boldsymbol{k}) := \mathrm{P}_{ijkl}(\boldsymbol{k})\,\sigma_{kl}(\boldsymbol{k}) . \tag{3.22}$$

The transverse projector is $\mathrm{P}_{ij}(\boldsymbol{k}) := \delta_{ij} - \hat{k}_i\hat{k}_j$ and the transverse, traceless and symmetric projector reads

$$\mathrm{P}_{ijlm}(\boldsymbol{k}) := \tfrac{1}{2} \left[\mathrm{P}_{il}(\boldsymbol{k})\,\mathrm{P}_{jm}(\boldsymbol{k}) + \mathrm{P}_{im}(\boldsymbol{k})\,\mathrm{P}_{jl}(\boldsymbol{k}) - \mathrm{P}_{ij}(\boldsymbol{k})\,\mathrm{P}_{lm}(\boldsymbol{k}) \right] . \tag{3.23}$$

---

[6]An explicit formula for the full decomposition is derived in appendix A.

[7]It is noted that the vorticity field is a pseudovector transforming trivially under parity transformations. In terms of the velocity-divergence and vorticity field, the decomposition of the velocity field is the Helmholtz decomposition.

The decomposition of the velocity dispersion tensor then takes the form

$$\sigma_{ij}(\boldsymbol{x}) = \int_{\boldsymbol{k}} \mathrm{e}^{\mathrm{i}\boldsymbol{k}\cdot\boldsymbol{x}} \left[\vartheta_{ij}(\boldsymbol{k}) + 2\widehat{k}_{(i}\vartheta_{j)}(\boldsymbol{k}) + \tfrac{3}{2}\left(\widehat{k}_i\widehat{k}_j - \tfrac{1}{3}\delta_{ij}\right)\vartheta(\boldsymbol{k}) + \delta_{ij}\sigma(\boldsymbol{k}) \right] . \quad (3.24)$$

Similarly, one can decompose the higher-order velocity cumulants using the splitting (3.16) but this is not further pursued here.

Correlation functions

Having classified the matter degrees of freedom, one might ask about correlation functions of scalar, vector and tensor modes. Due to statistical isotropy only the scalar modes can obtain a non-vanishing mean field although one should be careful to correctly take the physical degrees of freedom into account. For example the velocity-divergence $\theta(\boldsymbol{k})$ can in principal obtain a non-vanishing mean field, while the physical velocity field cannot. From the decomposition (3.20), one can realise that a zero-mode of the velocity-divergence field leads to an unbounded growth of the corresponding velocity field rendering it unphysical.[8] Similarly, one can realise that the isotropic velocity dispersion field $\sigma(\boldsymbol{k})$ can feature a mean field while the anisotropic velocity dispersion field $\vartheta(\boldsymbol{k})$ in general cannot.

More generally, only those scalar modes $\mathbf{1}_0$ can obtain a non-vanishing mean field that also correspond to the trivial representation $\mathbf{1}$ of the rotation group. The scalar modes which are obtained from non-trivial representations due to the decomposition (3.15) in general have a vanishing mean field in order to ensure statistical isotropy of the corresponding physical degrees of freedom.

Turning to the two-point correlation functions, the statistical isotropy symmetry guarantees that only modes of the same spin have a non-vanishing covariance function. Naturally, one also deals with vector power spectra such as e.g.

$$P_{\omega_i\omega_j}(\boldsymbol{k}) = \int_{\boldsymbol{x}} \mathrm{e}^{\mathrm{i}\boldsymbol{k}\cdot(\boldsymbol{x}-\boldsymbol{x}')} C_{\omega_i\omega_j}(\boldsymbol{x}-\boldsymbol{x}') , \quad (3.25)$$

for which the trace $C_{\omega_i\omega_i}(|\boldsymbol{x}-\boldsymbol{x}'|)$ only depends on the distance of the two position vectors. The vector power spectrum is invariant under parity transformations, $P_{\omega_i\omega_j}(-\boldsymbol{k}) = P_{\omega_i\omega_j}(\boldsymbol{k})$, since it is proportional to the projector $\mathrm{P}_{ij}(\boldsymbol{k})$.[9] The power spectrum can be reduced to

$$P_{\omega\omega}(k) := \tfrac{1}{2}\mathrm{P}_{ij}(\boldsymbol{k})\, P_{\omega_i\omega_j}(\boldsymbol{k}) , \quad (3.26)$$

where the factor one half is due to the identity $\mathrm{P}_{ij}\mathrm{P}_{ij} = 2$.

When working in terms of the power spectrum, one is often interested in the scaling of it in certain regimes such that it is useful to define the spectral index, e.g.

$$n_{\omega}(k) := \frac{\mathrm{d}\ln(P_{\omega\omega}(k))}{\mathrm{d}\ln(k)} , \quad (3.27)$$

---

[8] From the point of view of the Helmholtz decomposition, one would argue that boundary conditions need to be imposed for a unique reconstruction of the velocity field.

[9] This is true irrespective of whether the transverse vector mode is a true- or pseudovector.

which is constant for a pure power law power spectrum.

Very similarly, one can proceed for the power spectrum of tensor modes although not needed in the following and therefore not explicitly treated here.

3.4 Standard perturbation theory

Having introduced the dynamics of gravitational instabilities, the nature and statistical description of the initial conditions and the decomposition of the matter degrees of freedom into irreducible components, one can now turn to actually calculate late-time statistical properties of dark matter. In this section, this is presented in terms of standard perturbation theory of the single-stream approximation before constructing a much more complete framework in the next chapter in terms of a functional formalism for the underlying statistical field theory.

In the framework of standard perturbation theory of the single-stream approximation, dark matter is described in terms of the density contrast and velocity-divergence fields while the vorticity field is neglected [17].[10] The Fourier transform of the continuity equation (2.89) is given by

$$\partial_\tau \delta(\boldsymbol{k}) + \theta(\boldsymbol{k}) + \int_{\boldsymbol{k}'} \alpha(\boldsymbol{k}', \boldsymbol{k} - \boldsymbol{k}')\,\theta(\boldsymbol{k}')\,\delta(\boldsymbol{k} - \boldsymbol{k}') = 0 \;, \qquad (3.28)$$

and Euler's equation (2.90) for the velocity-divergence reads

$$\partial_\tau \theta(\boldsymbol{k}) + \mathcal{H}\theta(\boldsymbol{k}) - \tfrac{3}{2}\,\Omega_{\mathrm{m}}\mathcal{H}^2\,\delta(\boldsymbol{k}) + \int_{\boldsymbol{k}'} \beta(\boldsymbol{k}', \boldsymbol{k} - \boldsymbol{k}')\,\theta(\boldsymbol{k}')\,\theta(\boldsymbol{k} - \boldsymbol{k}') = 0 \;, \qquad (3.29)$$

where Poisson's equation (2.85) has been used to eliminate the gravitational potential. The mode coupling functions are determined by the non-linear terms and are given by [17]

$$\alpha(\boldsymbol{k}_1, \boldsymbol{k}_2) := \frac{(\boldsymbol{k}_1 + \boldsymbol{k}_2) \cdot \boldsymbol{k}_1}{k_1^2} \;, \qquad \beta(\boldsymbol{k}_1, \boldsymbol{k}_2) := \frac{(\boldsymbol{k}_1 + \boldsymbol{k}_2)^2 (\boldsymbol{k}_1 \cdot \boldsymbol{k}_2)}{2 k_1^2 k_2^2} \;. \qquad (3.30)$$

The density contrast and velocity-divergence are assumed to be Gaussian random fields at some initial time deep within the matter dominated era of the Universe and are as such fully characterised in terms of their respective power spectra which are predicted by inflation and the early Universe physics discussed in section 3.2.

3.4.1 Linear perturbation theory

The linear parts of the continuity equation (3.28) and Euler's equation (3.29) can be combined to the second-order differential equation

$$\partial_\tau^2 \delta^{\mathrm{L}}(\tau, \boldsymbol{k}) + \mathcal{H}(\tau)\,\partial_\tau \delta^{\mathrm{L}}(\tau, \boldsymbol{k}) - \tfrac{3}{2}\,\Omega_{\mathrm{m}}(\tau)\,\mathcal{H}(\tau)^2\,\delta^{\mathrm{L}}(\tau, \boldsymbol{k}) = 0 \;, \qquad (3.31)$$

---

[10]This is well justified since in the absence of velocity dispersion vorticity is not sourced and decays with the expansion of the Universe.

which together with Friedmann's equations (2.70) determine the linear growth of density fluctuations. Since each Fourier mode involves independently, the general solution is given by the superposition of its two independent solutions which may be written as

$$\delta^{\mathrm{L}}(\tau, \boldsymbol{k}) = D_+(\tau)\, A(\boldsymbol{k}) + D_-(\tau)\, B(\boldsymbol{k}) \,, \tag{3.32}$$

where the functions $A(\boldsymbol{k})$ and $B(\boldsymbol{k})$ are determined by the initial density contrast field. The linear growth functions $D_+(\tau)$ and $D_-(\tau)$ denote the fastest and slowest growing solution, respectively, and are chosen to be normalised to unity at $a = 1$. The continuity equation (3.28) then determines the linear velocity-divergence field,

$$\theta^{\mathrm{L}}(\tau, \boldsymbol{k}) = -\mathcal{H}(\tau)\Big[f(\tau)\, D_+(\tau)\, A(\boldsymbol{k}) + g(\tau)\, D_-(\tau)\, B(\boldsymbol{k}) \Big] \,, \tag{3.33}$$

where $f = \partial \ln(D_+)/\partial \ln(a)$ and $g = \partial \ln(D_-)/\partial \ln(a)$.

In the linear growing mode, the fields obey the relation $\delta^{\mathrm{L}} = -\theta^{\mathrm{L}}/(f\mathcal{H})$ and therefore the linear power spectra

$$P^{\mathrm{L}}_{\delta\delta} = -P^{\mathrm{L}}_{\delta\theta/(f\mathcal{H})} = P^{\mathrm{L}}_{\theta\theta/(f\mathcal{H})^2} \,, \tag{3.34}$$

are all equal and given by

$$P^{\mathrm{L}}_{\delta\delta}(\tau, \tau', k) = \frac{D_+(\tau)}{D_+(\tau_{\mathrm{in}})} \frac{D_+(\tau')}{D_+(\tau_{\mathrm{in}})}\, P^{\mathrm{in}}_{\delta\delta}(k) \,. \tag{3.35}$$

In an Einstein–de Sitter cosmology the energy content is dominated by matter with $\Omega_{\mathrm{m}} = 1$ and the linear growth functions are

$$D_+ = a \,, \qquad D_- = a^{-3/2} \,. \tag{3.36}$$

In a ΛCDM cosmology without a radiative component, which is applicable in the late-time Universe where the radiation density is small compared to the matter and cosmological constant densities, one obtains [109]

$$D_+ = a\, \frac{{}_2F_1\left(\frac{1}{3}, 1; \frac{11}{6}; -a^3\omega\right)}{{}_2F_1\left(\frac{1}{3}, 1; \frac{11}{6}; -\omega\right)} \,, \qquad D_- = a^{-\frac{3}{2}}\, \frac{{}_2F_1\left(-\frac{1}{2}, \frac{1}{6}; \frac{1}{6}; -a^3\omega\right)}{{}_2F_1\left(-\frac{1}{2}, \frac{1}{6}; \frac{1}{6}; -\omega\right)} \,, \tag{3.37}$$

where ${}_2F_1$ is the Gaussian hypergeometric function and $\omega = (1 - \Omega_{\mathrm{m},0})/\Omega_{\mathrm{m},0}$ is today's relative energy density fraction due to matter.

Since it is much easier to work in an Einstein–de Sitter cosmology, the approximation $\Omega_{\mathrm{m}}/f^2 = 1$ mapping a ΛCDM onto an Einstein–de Sitter cosmology is frequently employed. The approximation essentially assumes that the slowest growing solution is given by $D_- = (D_+)^{-\frac{3}{2}}$ which is strictly speaking only true for the growth functions (3.36). The approximation is frequently employed in perturbation theory since the equations become separable in this case [110].

3.4.2 Non-linear perturbation theory

In order to compute non-linear corrections to the linear power spectrum (3.35), the continuity equation (3.28) and Euler's equation (3.29) can be solved order by order using the perturbative expansions

$$\delta(\tau, \boldsymbol{k}) = \sum_{n=1}^{\infty} \delta^{(n)}(\tau, \boldsymbol{k}) , \qquad \theta(\tau, \boldsymbol{k}) = \sum_{n=1}^{\infty} \theta^{(n)}(\tau, \boldsymbol{k}) . \tag{3.38}$$

The $n = 1$ terms are then the linear solutions (3.32) and (3.33) such that the higher-order terms correspond to an expansion in the linear or initial fields.

The corrections to linear theory should be small in order to obtain predictive results from a truncation of the perturbative series. This is only justified on cosmically large scales where the Universe becomes homogeneous and isotropic. Going to smaller scales, the non-linear coupling of modes become larger and perturbation theory naturally breaks down such that the expansion (3.38) should be understood as an asymptotic series.

Using the perturbative expansion (3.38) one can find an expansion for the density contrast power spectrum [17]

$$P_{\delta\delta}(\tau, \tau', k) = \sum_{\ell=0}^{\infty} P_{\delta\delta}^{(\ell)}(\tau, \tau', k) , \tag{3.39}$$

and similarly for the other power spectra. One obtains for the zeroth loop order the linear power spectrum,

$$P_{\delta\delta}^{(0)}(\tau, \tau', k) = P_{\delta\delta}^{\mathrm{L}}(\tau, \tau', k) , \tag{3.40}$$

while the one-loop contribution is usually expressed as [111, 112]

$$P_{\delta\delta}^{(1)}(\tau, \tau', k) = P_{\delta\delta}^{(2,2)}(\tau, \tau', k) + 2P_{\delta\delta}^{(1,3)}(\tau, \tau', k) . \tag{3.41}$$

Truncating the expansion (3.39) after $\ell = 1$ one obtains the one-loop power spectrum

$$P_{\delta\delta}^{\text{1-loop}}(\tau, \tau', k) = P_{\delta\delta}^{(0)}(\tau, \tau', k) + P_{\delta\delta}^{(1)}(\tau, \tau', k) . \tag{3.42}$$

Similarly one can proceed for the velocity-divergence auto-power spectrum and velocity-divergence-density contrast cross-power spectrum [113, 114].

The basic idea is to expand the fields in powers of their initial conditions, such that expectation values such as the power spectrum can be computed from the statistics of the initial state alone. Using a generalisation of Isserlis' theorem [115], in physics often called Wick's theorem [116], one can then express all expectation values in terms of initial power spectra only.

Standard perturbation theory is again reviewed in chapter 4 embedded into the larger functional formalism presented there.

The performance of the standard perturbation theory one-loop power spectrum computed in the single-stream approximation is shown in figure 3.2. As one can
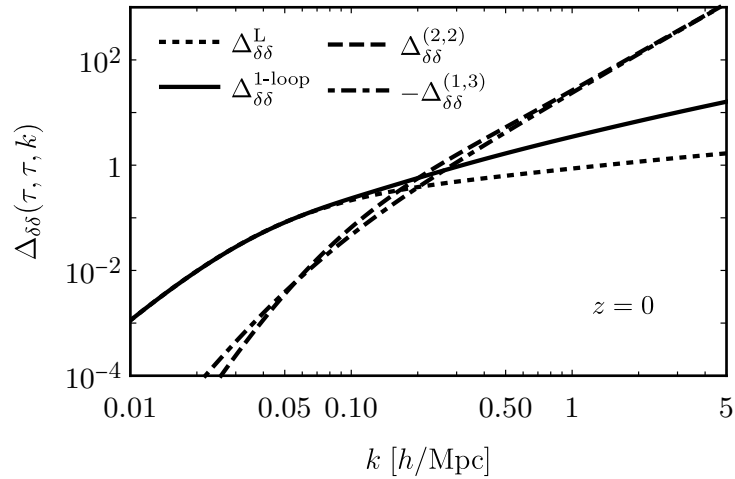
Figure 3.2: Dimensionless density contrast equal-time power spectrum as predicted from one-loop standard perturbation theory at redshift $z = 0$. It is computed from an initial power spectrum ΛCDM cosmology with parameters from Planck 2018 [162] using the Eisenstein & Hu fitting formula [177].

clearly see, the one-loop correction leads to an enhancement of the power spectrum at small scales. The enhancement is a result of a rather accurate cancellation of the two contributions $P_{ab}^{(2,2)}$ and $P_{ab}^{(1,3)}$. In fact, the correction strongly overestimates the power at small scales when compared to data from *N*-body simulations or observations, which is due to the fact that at small scales the theory is no longer perturbative. Although some improvement can be achieved on mildly non-linear scales by including higher loop orders, the perturbative expansion ultimately breaks down due to its nature as an asymptotic series [117].

4 Cosmological field theory

In this chapter the basic formalism used in the following chapters is established. In section 4.1 the dynamics of dark matter gravitational instabilities is formulated as an action based statistical field theory. Generalised correlation functions such as the mean linear response and covariance function are discussed and the corresponding generating functional is introduced. The one-particle irreducible effective action is defined and a diagrammatic representation for correlation functions is introduced. In section 4.2 standard perturbation theory is discussed within the functional framework and the usual one-loop results of the single-stream approximation are derived. In section 4.3 the loop expansion of the effective action and its relation to the one-particle irreducible resummation scheme is discussed and computed to one-loop order. In sections 4.4 and 4.5 the Dyson–Schwinger equation and the functional renormalisation group are derived and discussed, which are the main methods used in the following chapters to study late-time cosmic structure formation. Finally, in section 4.6 the symmetries of the theory are studied and related Ward identities are derived.

4.1 Statistical field theory formulation

Having introduced the dynamics of dark matter gravitational instabilities and the statistical nature of the corresponding initial conditions, one can understand late-time cosmic structure formation from a field-theoretic point of view [118].

In the following, the matter degrees of freedom are chosen to be a set of velocity cumulants of the phase-space distribution function and the desired field content is assembled into the multiplet

$$\psi_a(\tau, \boldsymbol{x}) = \begin{pmatrix} \delta, & u_i, & \sigma_{ij}, & ... \end{pmatrix} , \tag{4.1}$$

where the index a carries any additional substructure of the fields, such as tensorial indices, and is summed over if appearing twice in a single term. The equations of motion (2.88) can then be written as

$$\partial_\tau \psi_a(\tau, \boldsymbol{x}) + \int_{\boldsymbol{x}'} \Omega_{ab}(\tau, \boldsymbol{x} - \boldsymbol{x}') \, \psi_b(\tau, \boldsymbol{x}')$$
$$+ \int_{\boldsymbol{x}', \boldsymbol{x}''} \gamma_{abc}(\boldsymbol{x} - \boldsymbol{x}', \boldsymbol{x} - \boldsymbol{x}'') \, \psi_b(\tau, \boldsymbol{x}') \, \psi_c(\tau, \boldsymbol{x}'') = 0 , \tag{4.2}$$

where the gravitational potential has already been eliminated by formally solving

Poisson's equation (2.85).[1] The linear part is characterised by the matrix

$$
\Omega(\tau, \boldsymbol{x} - \boldsymbol{x}') = \begin{matrix} & \delta & u_j & \sigma_{kl} & \\ \delta & & & & \\ u_i & \\ \sigma_{ij} & \end{matrix} \begin{pmatrix} 0 & \partial_j \delta(\boldsymbol{x} - \boldsymbol{x}') & 0 & \cdots \\ O_i(\tau, \boldsymbol{x} - \boldsymbol{x}') & \mathcal{H} \delta_{ij} & \delta_{ik} \partial_l \delta(\boldsymbol{x} - \boldsymbol{x}') & \cdots \\ 0 & 0 & 2\mathcal{H} \delta_{ik} \delta_{jl} & \cdots \\ \vdots & \vdots & \vdots & \ddots \end{pmatrix} , \quad (4.3)
$$

where the fields above and to the left of the matrix are displayed as an orientation and indicate which field (above) enters into which equation of motion (left). The matrix Ω_{ab} is local and of upper triangular form except for the velocity-density component that is determined by the solution of Poisson's equation. It is given by the operator

$$
O_i(\tau, \boldsymbol{x} - \boldsymbol{x}') = \frac{3}{2} \mathcal{H}^2 \Omega_{\mathrm{m}} \frac{1}{4\pi} \frac{x_i - x_i'}{|\boldsymbol{x} - \boldsymbol{x}'|^3} , \quad (4.4)
$$

together with an appropriate boundary condition which is discussed in more detail in section 4.6.3. The diagonal entries of Ω_{ab} are the Hubble drag terms of the corresponding cumulants while the entries above the diagonal are derivatives coupling to the next higher-order cumulant.

The vertices γ_{abc} are symmetrised with respect to the two fields they couple and their spatial dependence is through gradients. The first few that are relevant in the following chapters are listed in appendix C.

4.1.1 Response and correlation functions

Before turning to the functional formulation it is necessary to discuss the type of correlation functions one has to deal with in a field-theoretic description. Besides statistical correlation functions one naturally obtains another type of correlation functions that are related to the response functions characterising the dynamics of the system.

The linear part of the equations of motion (4.2) can be formally solved by a Green's function that is in cosmology most often called the linear retarded propagator [119]. The Green's function obeys the equation

$$
\partial_\tau g_{ac}^{\mathrm{R}}(\tau, \tau', \boldsymbol{x} - \boldsymbol{x}') + \int_{\boldsymbol{x}''} \Omega_{ab}(\tau, \boldsymbol{x} - \boldsymbol{x}'') \, g_{bc}^{\mathrm{R}}(\tau, \tau', \boldsymbol{x}'' - \boldsymbol{x}')
$$
$$
= \delta_{ac} \, \delta(\tau - \tau') \, \delta(\boldsymbol{x} - \boldsymbol{x}') , \quad (4.5)
$$

is spatially translation invariant and subject to the boundary conditions

$$
g_{ab}^{\mathrm{R}}(\tau, \tau', \boldsymbol{x} - \boldsymbol{x}') = 0 \ \text{ for } \ \tau' > \tau , \quad g_{ab}^{\mathrm{R}}(\tau, \tau', \boldsymbol{x} - \boldsymbol{x}') = \delta_{ab} \ \text{ for } \ \tau' \to \tau^- , \quad (4.6)
$$

---

[1] Equation (4.2) cannot capture the equations of motion (2.88) exactly, since they contain non-linear terms of the form $c^{(n+1)} \partial_{\boldsymbol{x}} \ln(1 + \delta)$. These are non-polynomial in the field content (4.1) and are in the following approximated as $c^{(n+1)} \partial_{\boldsymbol{x}} \delta$ for $n > 1$. This can be understood as a vertex expansion around the (vanishing) density contrast mean field. Similarly, one could chose to include the logarithmic density contrast in the field content (4.1), although in this case Poisson's equation (2.85) is non-polynomial in the field content leading to a similar problem.

rendering it causal.[2]

The linear retarded propagator can be interpreted as the linear impulse response to an ultra-local source. This notion can be generalised to higher-order response functions to which end one supplies a source current $K_a(\tau, \boldsymbol{x})$ to the right-hand side of equation (4.2). The general solution $\psi_a^{\mathrm{sol}}(\tau, \boldsymbol{x})$ is then source-dependent and the nth-order response function is defined as

$$R_{ab_1\ldots b_n}^{(n)}(\tau, \boldsymbol{x}; \tau_1, \boldsymbol{x}_1; \ldots; \tau_n, \boldsymbol{x}_n) := \left. \frac{\delta^n \psi_a^{\mathrm{sol}}(\tau, \boldsymbol{x})}{\delta K_{b_1}(\tau_1, \boldsymbol{x}_1) \ldots \delta K_{b_n}(\tau_n, \boldsymbol{x}_n)} \right|_{K_a=0}, \qquad (4.7)$$

which in general depends on the initial conditions $\psi_a^{\mathrm{in}}(\boldsymbol{x})$. The zeroth-order response function is the solution of the equations of motion in the absence of a source current and vanishes for vanishing initial conditions. The linear retarded propagator is obtained as the first-order response function for vanishing initial conditions,

$$\left. R_{ab}^{(1)}(\tau, \boldsymbol{x}; \tau', \boldsymbol{x}') \right|_{\psi_a^{\mathrm{in}}=0} = g_{ab}^{\mathrm{R}}(\tau, \tau', \boldsymbol{x} - \boldsymbol{x}'), \qquad (4.8)$$

although more generally carrying non-linear information for non-vanishing initial data.[3]

For random initial conditions $\psi_a^{\mathrm{in}}(\boldsymbol{x})$ the response functions are in general also random and as such one is rather interested in the *mean response functions*, obtained by averaging the response functions (4.7) over the initial state. One of the central objects studied in the subsequent chapters is the retarded propagator which is defined as the mean linear response function,

$$G_{ab}^{\mathrm{R}}(\tau, \tau', \boldsymbol{x} - \boldsymbol{x}') := \left\langle R_{ab}^{(1)}(\tau, \boldsymbol{x}; \tau', \boldsymbol{x}') \right\rangle_{\mathrm{in}}, \qquad (4.9)$$

where $\langle \ldots \rangle_{\mathrm{in}}$ denotes the expectation value over the initial state.

Besides mean response functions one is mainly interested in the statistical correlation functions of the fields (4.1). Since these are subject to the equations of motion (4.2) the relevant expectation values are the mean fields

$$\Psi_a(\tau) := \left. \left\langle \psi_a^{\mathrm{sol}}(\tau, \boldsymbol{x}) \right\rangle_{\mathrm{in}} \right|_{K_a=0}, \qquad (4.10)$$

---

[2]More rigorously, in the limit $\tau' \to \tau$ one obtains $g_{ab}^{\mathrm{R}}(\tau, \tau', \boldsymbol{x} - \boldsymbol{x}') \to \delta_{ab}\theta(0)$ where $\theta(0)$ is the Heaviside unit step function at vanishing argument. In the functional formalism introduced in the next section the value of $\theta(0)$ is fixed by the discretisation procedure for stochastic differential equations. The convention equivalent of Itô calculus is employed, leading to $\theta(0) = 0$ which is discussed in more detail in appendix B.

[3]Similarly, one could define the non-linear response function (4.7) at vanishing initial conditions such that the the first-order response function is the linear retarded propagator. In this case initial conditions can be supplied by the time-localised shift $\delta(\tau - \tau_{\mathrm{in}})\psi_a^{\mathrm{in}}(\boldsymbol{x})$ of the source current. Using this convention, it is evident that the linear response function as defined in equation (4.7) carries non-linear information for non-vanishing initial conditions.

covariance functions,

$$C_{ab}(\tau, \tau', \boldsymbol{x} - \boldsymbol{x}') := \left\langle \psi_a^{\text{sol}}(\tau, \boldsymbol{x})\, \psi_b^{\text{sol}}(\tau', \boldsymbol{x}') \right\rangle_{\text{in,c}} \Big|_{K_a = 0} , \qquad (4.11)$$

and generally higher-order correlation functions.

Equations (4.10) and (4.11) give a concrete prescription how to calculate the correlation functions introduced in chapter 3, namely by averaging products of the fields that solve the equations of motion over the initial state.

A note on rigour

It seems quite natural to ask under which conditions the afore mentioned mean response and correlation functions are well-defined. Usually this requires the equations of motion to admit sufficiently well behaved solutions that are globally existent and unique. From a mathematical point of view this is a rather delicate assumption even for the perfect fluid case, not to mention extensions thereof. Despite the mathematical subtleties one should understand the following investigations from an effective theory point of view in the sense that any blow up is expected to be regularised due to small scale physics.

In appendix B a scalar toy model with cubic interaction, which is structurally speaking the closest to the equations of motion (4.2), is discussed in more detail. Since there exist solutions with finite escape time for this model, the mean response and correlation functions are ill-defined.[4] For a physically viable theory one would expect some mechanism which renders the correlation functions finite, such as a quartic interaction term with very small coupling coming to rescue at large field values.

4.1.2 Generating functionals

One would like to have a systematic way to obtain expectation values such as the mean linear response function (4.9), the mean field (4.10) and the covariance function (4.11). To this end, the Martin–Siggia–Rose/Janssen–de Dominicis formalism [120–123] allows to construct a generating functional from which all type of correlation functions can be obtained.[5] The explicit construction is performed in appendix B for a (1+0)-dimensional toy model, although it is straight forwardly generalised to include spatial dimensions. Although not including mean fields and constructed in slightly different ways, similar field theory constructions have already been studied in cosmology [9, 27–30, 35, 37].

The relevant generating functional is given by

$$Z[J, \hat{J}] := \left\langle \exp\left\{ \int_{\tau, \boldsymbol{x}} J_a(\tau, \boldsymbol{x})\, \psi_a^{\text{sol}}(\tau, \boldsymbol{x}) \right\} \right\rangle_{\text{in}} , \qquad (4.12)$$

---

[4]From a quantum field-theoretic point of view this corresponds to the absence of a stable vacuum state due to an unbounded Lagrangian.

[5]It can be viewed as the classical statistical field theory equivalent to the Schwinger–Keldysh formalism [124, 125].

where $\psi_a^{\mathrm{sol}}(\tau, \boldsymbol{x})$ is understood to solve the equations of motion (4.2) in the presence of a source current $\mathrm{i}\,\hat{J}_a(\tau, \boldsymbol{x})$ and for Gaussian distributed random initial conditions.[6] Applying functional derivatives with respect to the source current $J_a(\tau, \boldsymbol{x})$ to $Z[J, \hat{J}]$ allows to calculate correlation functions such as the mean field (4.10) and the covariance function (4.11) while functional derivatives with respect to the source current $\hat{J}_a(\tau, \boldsymbol{x})$ are related to mean response functions such as the retarded propagator (4.9).

Following the Martin–Siggia–Rose formalism [120] one introduces a set of so-called response fields $\hat{\psi}_a(\tau, \boldsymbol{x})$ which are utilised in the Janssen–de Dominicis formalism [121–123] to obtain the functional integral representation

$$Z[J, \hat{J}] = \int \mathcal{D}\psi \int \mathcal{D}\hat{\psi}\; \mathrm{e}^{-S + J_A \psi_A + \hat{J}_A \hat{\psi}_A}\; . \tag{4.13}$$

The measures $\mathcal{D}\psi$ and $\mathcal{D}\hat{\psi}$ are understood as the continuum limit of integrals on a lattice in time and space and the bare action is given by

$$
\begin{aligned}
S[\psi, \hat{\psi}] = -\mathrm{i} \int_{\tau, \boldsymbol{x}, \boldsymbol{x}'} & \hat{\psi}_a(\tau, \boldsymbol{x}) \Big[\partial_\tau \delta_{ab}\, \delta(\boldsymbol{x} - \boldsymbol{x}') + \Omega_{ab}(\tau, \boldsymbol{x} - \boldsymbol{x}') \Big] \psi_b(\tau, \boldsymbol{x}') \\
& -\mathrm{i} \int_{\tau, \boldsymbol{x}, \boldsymbol{x}', \boldsymbol{x}''} \hat{\psi}_a(\tau, \boldsymbol{x})\, \gamma_{abc}(\boldsymbol{x} - \boldsymbol{x}', \boldsymbol{x} - \boldsymbol{x}'')\, \psi_b(\tau, \boldsymbol{x}')\, \psi_c(\tau, \boldsymbol{x}'') \\
& + \int_{\boldsymbol{x}, \boldsymbol{x}'} \hat{\psi}_a(\tau_{\mathrm{in}}, \boldsymbol{x}) \Big[\mathrm{i}\, \delta(\boldsymbol{x} - \boldsymbol{x}')\, \Psi_a^{\mathrm{in}} + \tfrac{1}{2}\, C_{ab}^{\mathrm{in}}(\boldsymbol{x} - \boldsymbol{x}')\, \hat{\psi}_b(\tau_{\mathrm{in}}, \boldsymbol{x}') \Big]\, ,
\end{aligned}
\tag{4.14}
$$

where Ψ_a^{in} and $C_{ab}^{\mathrm{in}}(\boldsymbol{x} - \boldsymbol{x}')$ are the mean field and covariance function which fully characterise the Gaussian initial state.[7]

Capital letters from the beginning of the Latin alphabet denote DeWitt indices, e.g. $A = (a, \tau, \boldsymbol{x})$, which are summed and integrated over when appearing twice in a single term for discrete and continuous variables respectively, while boldface indices additionally comprise the physical-response field structure, e.g. $\psi_{\boldsymbol{A}} = (\psi_A, \hat{\psi}_A)$.

From the generating function (4.13) it is clear that J_a and $\hat{J}_a$ serve as source currents for the physical and response fields, respectively.[8] Functional derivatives

---

[6]The imaginary unit in front of the source current is inserted for later convenience and related to the one used in equation (4.7) by $K_a = \mathrm{i}\,\hat{J}_a$.

[7]The construction assumes the existence of a unique solution $\psi_a^{\mathrm{sol}}(\tau, \boldsymbol{x})$ in some time interval τ_{in} to τ_{fi} and depends on the method of discretisation for stochastic differential equations. To this end the convention equivalent to Itô calculus is employed, which is particular convenient since it does not need the introduction of additional ghost fields [126]. Integrals over the whole time interval are abbreviated as

$$\int_\tau = \int_{\tau_{\mathrm{in}}}^{\tau_{\mathrm{fi}}} \mathrm{d}\tau\; ,$$

while spatially periodic boundary conditions are imposed.

[8]Notice that the initial mean field can be absorbed into the response field source current. In the following it is chosen to keep the initial mean field explicit such that physical correlation functions are obtained at vanishing source currents.

with respect to the source currents are abbreviated as

$$Z^{(n)}_{\boldsymbol{A}_1 \dots \boldsymbol{A}_n} := \frac{\delta^n Z}{\delta J_{\boldsymbol{A}_1} \dots \delta J_{\boldsymbol{A}_n}} \quad , \qquad Z^{(m,n)}_{A_1 \dots B_n} := \frac{\delta^{m+n} Z}{\delta J_{A_1} \dots J_{A_m} \hat{J}_{B_1} \dots \delta \hat{J}_{B_n}} \quad , \qquad (4.15)$$

where the two notations are related by

$$Z^{(1)}_{\boldsymbol{A}} = \begin{pmatrix} Z^{(1,0)}_A \\ Z^{(0,1)}_A \end{pmatrix} \quad , \qquad Z^{(2)}_{\boldsymbol{A}\boldsymbol{B}} = \begin{pmatrix} Z^{(2,0)}_{AB} & Z^{(1,1)}_{AB} \\ Z^{(1,1)}_{BA} & Z^{(0,2)}_{AB} \end{pmatrix} \quad , \qquad (4.16)$$

for first- and second-order derivatives and similarly for higher orders. Due to general properties of the construction the generating functional is normalised to $Z[0, \hat{J}] = 1$ [127] which immediately implies

$$Z^{(0,n)}_{B_1 \dots B_n} = 0 \quad , \qquad (4.17)$$

for all $n > 0$ at vanishing source currents. Correlation functions are defined as

$$\left\langle \psi_{\boldsymbol{A}_1} \dots \psi_{\boldsymbol{A}_n} \right\rangle := \frac{Z^{(n)}_{\boldsymbol{A}_1 \dots \boldsymbol{A}_n}}{Z} \quad , \qquad (4.18)$$

which naturally include mean response as well as statistical correlation functions. Physical correlation functions are obtained at vanishing source currents and are said to be 'on the equations of motion'.

It is convenient to also introduce the generating functional $W := \ln(Z)$ from which one obtains connected correlation functions as

$$\left\langle \psi_{\boldsymbol{A}_1} \dots \psi_{\boldsymbol{A}_n} \right\rangle_{\mathrm{c}} = W^{(n)}_{\boldsymbol{A}_1 \dots \boldsymbol{A}_n} \quad . \qquad (4.19)$$

At vanishing source currents the first-order functional derivatives give

$$W^{(1)}_{\boldsymbol{A}} = \begin{pmatrix} \Psi_a(\tau) \\ 0 \end{pmatrix} \quad . \qquad (4.20)$$

while the second-order derivatives are

$$W^{(2)}_{\boldsymbol{A}\boldsymbol{B}} = \begin{pmatrix} C_{ab}(\tau, \tau', \boldsymbol{x} - \boldsymbol{x}') & \mathrm{i}\, G^{\mathrm{R}}_{ab}(\tau, \tau', \boldsymbol{x} - \boldsymbol{x}') \\ \mathrm{i}\, G^{\mathrm{A}}_{ab}(\tau, \tau', \boldsymbol{x} - \boldsymbol{x}') & 0 \end{pmatrix} \quad . \qquad (4.21)$$

Here the advanced propagator is defined as the 'transpose' of the retarded and obeys the relation

$$G^{\mathrm{A}}_{ab}(\tau, \tau', \boldsymbol{x} - \boldsymbol{x}') = G^{\mathrm{R}}_{ba}(\tau', \tau, \boldsymbol{x}' - \boldsymbol{x}) \quad . \qquad (4.22)$$

From these expressions it becomes clear that expectation values involving the response field are naturally related to response functions and generalisations thereof.

In a formal analogy to probability distributions, the expectation values $\langle \dots \rangle$ are understood as being taken as averages weighted with e^{-S}, although this does not

allow for a probabilistic interpretation since the bare action (4.14) is in general complex and the response fields are not physical degrees of freedom.[9]

To get a hand on the formalism it is enlightening to study two limits in which the generating function can be explicitly computed. It is obvious that these limits are rather trivial since for non-linear dynamics and a non-trivial random initial state the generating functional is in general not explicitly computable.

Linear limit

Conceptually the easiest case in which one can explicitly calculate the generating functional is the linear limit $\gamma_{abc} \to 0$. In this case the bare action (4.14) is quadratic in the fields and the functional integrals in the generating functional 4.13 are Gaussian. Performing the integrations one obtains

$$
\begin{aligned}
W^{\mathrm{L}} = \int_{\tau, \boldsymbol{x}} & J_a(\tau, \boldsymbol{x})\, \Psi_b^{\mathrm{L}}(\tau) \\
& + \mathrm{i} \int_{\substack{\tau, \tau' \\ \boldsymbol{x}, \boldsymbol{x}'}} J_a(\tau, \boldsymbol{x})\, g_{ab}^{\mathrm{R}}(\tau, \tau', \boldsymbol{x} - \boldsymbol{x}')\, \hat{J}_b(\tau', \boldsymbol{x}') \\
& + \tfrac{1}{2} \int_{\substack{\tau, \tau' \\ \boldsymbol{x}, \boldsymbol{x}'}} J_a(\tau, \boldsymbol{x})\, C_{ab}^{\mathrm{L}}(\tau, \tau', \boldsymbol{x} - \boldsymbol{x}')\, J_b(\tau', \boldsymbol{x}')\,,
\end{aligned}
\tag{4.24}
$$

where the linear mean field,

$$
\Psi_a^{\mathrm{L}}(\tau) = \int_{\boldsymbol{x}} g_{ab}^{\mathrm{R}}(\tau, \tau_{\mathrm{in}}, \boldsymbol{x})\, \Psi_b^{\mathrm{in}}\,,
\tag{4.25}
$$

and the linear covariance function,

$$
C_{ab}^{\mathrm{L}}(\tau, \tau', \boldsymbol{x} - \boldsymbol{x}') = \int_{\boldsymbol{y}, \boldsymbol{y}'} g_{ab}^{\mathrm{R}}(\tau, \tau_{\mathrm{in}}, \boldsymbol{x} - \boldsymbol{y})\, C_{ab}^{\mathrm{in}}(\boldsymbol{y} - \boldsymbol{y}')\, g_{ab}^{\mathrm{A}}(\tau_{\mathrm{in}}, \tau', \boldsymbol{y}' - \boldsymbol{x}')\,, \tag{4.26}
$$

are build from the linear propagator and initial mean field or covariance function only. Consequently one has

$$
W_{\boldsymbol{A}_1 \dots \boldsymbol{A}_n}^{\mathrm{L}\,(n)} = 0\,,
\tag{4.27}
$$

for $n > 2$ and the theory is described by Gaussian random fields at all times.

---

[9]Even though e^{-S} does not allow for a probabilistic interpretation, the functional

$$
P[\psi] = \int \mathcal{D}\hat{\psi}\, \mathrm{e}^{-S}\,,
\tag{4.23}
$$

is real and can be interpreted as a 'probability density functional' for the fields ψ_a.

Deterministic limit

Another case in which the generating functional can be calculated explicitly is the deterministic limit $C_{ab}^{\mathrm{in}} \to 0$. In this case the initial state is fixed to the mean field Ψ_a^{in} and not fluctuations are present. The generating functional is then given by

$$W^{\mathrm{D}} = \int_{\tau,\boldsymbol{x}} J_a(\tau,\boldsymbol{x})\, \Psi_a^{\mathrm{sol}}(\tau,\boldsymbol{x}) \;, \tag{4.28}$$

where $\Psi_a^{\mathrm{sol}}(\tau,\boldsymbol{x})$ is the solution to the equations of motion (4.2) in the presence of a source current $\mathrm{i}\,\hat{J}_a(\tau,\boldsymbol{x})$, given the initial condition Ψ_a^{in}. Very similar to equation (4.7) the solution is made up of all the response functions of the system which no longer depend on the random initial conditions but rather on the initial mean field Ψ_a^{in}. Since the initial distribution is degenerate in the deterministic limit these can be replaced by the mean fields when averaging. From this one can immediately infer that the connected expectation values

$$W_{A_1\dots B_n}^{\mathrm{D}\,(m,n)} = 0 \;, \tag{4.29}$$

for all $m > 1$. This especially implies that all correlation functions of physical fields vanish, as to be expected since the theory features no fluctuations. The non-vanishing correlation functions are given by the mean response functions

$$W_{ab_1\dots b_n}^{\mathrm{D}\,(1,n)}(\tau,\boldsymbol{x};\tau_1,\boldsymbol{x}_1;\dots;\tau_n,\boldsymbol{x}_n) = R_{ab_1\dots b_n}^{(n)}(\tau,\boldsymbol{x};\tau_1,\boldsymbol{x}_1;\dots;\tau_n,\boldsymbol{x}_n) \;, \tag{4.30}$$

which depend on the initial mean field Ψ_a^{in}.

4.1.3 The one-particle irreducible effective action

In the following, it is useful to introduce yet another generating functional. The one-particle irreducible (1PI) effective action Γ is defined as the Legendre transform of the generating functional W with respect to both source currents,

$$\Gamma[\Psi,\hat{\Psi}] := \sup_{J,\hat{J}}\left[J_A\Psi_A + \hat{J}_A\hat{\Psi}_A - W[J,\hat{J}] \right] \;, \tag{4.31}$$

and can be regarded as the natural generalisation of the bare action S which includes all statistical information.[10]

One-particle irreducible correlation functions are defined as the functional derivatives of the effective action with respect to the mean fields $\psi_{\boldsymbol{A}}$ and are denoted in analogy to equation (4.15) as $\Gamma_{\boldsymbol{A}_1\dots\boldsymbol{A}_n}^{(n)}$. The normalisation $W[0,\hat{J}] = 0$ implies that $\Gamma[\Psi,0] = 0$ and as such all 1PI correlation functions involving only physical fields vanish on the equations of motion [128].

---

[10]From a formal point of view Z and W are moment- and cumulant-generating functionals of the 'distribution functional' e^{-S}. The 1PI effective action Γ is related to a rate function which quantifies fluctuations away from the expected (mean field) behaviour, decaying asymptotically with $\mathrm{e}^{-\Gamma}$ for an infinite sample, at least in the standard ergodic paradigm.

The 1PI one-point function by construction obeys

$$\Gamma_{\boldsymbol{A}}^{(1)} = J_{\boldsymbol{A}} \,, \tag{4.32}$$

assuming that the supremum on the right-hand side of equation (4.31) is attained at some maximising (field-dependent) source current $J_{\boldsymbol{A}} = J_{\boldsymbol{A}}^{\mathrm{sup}}[\Psi, \widehat{\Psi}]$. On the equations of motion the 1PI one-point function is given by

$$\Gamma_{\boldsymbol{A}}^{(1)} = \begin{pmatrix} 0 \\ -\mathrm{i}\, E_a(\tau) \end{pmatrix} \,, \tag{4.33}$$

where $E_a(\tau)$ are the effective equations of motion determining the dynamics of the physical mean fields.

Due to general properties of the Legendre transform the 1PI and connected two-point correlation functions are inverse to each other,

$$\Gamma_{\boldsymbol{AB}}^{(2)} \, W_{\boldsymbol{BC}}^{(2)} = \delta_{\boldsymbol{AC}} \,, \tag{4.34}$$

where the left-hand side is taken to depend on the source currents or equivalently on the mean fields via equation (4.32). On the equations of motion the 1PI two-point functions are given by

$$\Gamma_{\boldsymbol{AB}}^{(2)} = \begin{pmatrix} 0 & -\mathrm{i}\, D_{ab}^{\mathrm{A}}(\tau, \tau', \boldsymbol{x} - \boldsymbol{x}') \\ -\mathrm{i}\, D_{ab}^{\mathrm{R}}(\tau, \tau', \boldsymbol{x} - \boldsymbol{x}') & H_{ab}(\tau, \tau', \boldsymbol{x} - \boldsymbol{x}') \end{pmatrix} \,, \tag{4.35}$$

where the inverse retarded propagator $D_{ab}^{\mathrm{R}}(\tau, \tau', \boldsymbol{x} - \boldsymbol{x}')$ is defined by the relation

$$\int_{\tau', \boldsymbol{x}'} D_{ab}^{\mathrm{R}}(\tau, \tau', \boldsymbol{x} - \boldsymbol{x}') \, G_{bc}^{\mathrm{R}}(\tau', \tau'', \boldsymbol{x}' - \boldsymbol{x}'') = \delta_{ac} \, \delta(\tau - \tau'') \, \delta(\boldsymbol{x} - \boldsymbol{x}'') \,, \tag{4.36}$$

and the statistical 1PI two-point correlation function $H_{ab}(\tau, \tau', \boldsymbol{x} - \boldsymbol{x}')$ is defined by

$$\begin{aligned} \int_{\tau', \boldsymbol{x}'} D_{a\bar{a}}^{\mathrm{R}}(\tau, \tau', \boldsymbol{x} - \boldsymbol{x}') \, C_{\bar{a}b}(\tau', \tau'', \boldsymbol{x}' - \boldsymbol{x}'') \\ = \int_{\tau', \boldsymbol{x}'} H_{a\bar{b}}(\tau, \tau', \boldsymbol{x} - \boldsymbol{x}') \, G_{\bar{b}b}^{\mathrm{A}}(\tau', \tau'', \boldsymbol{x}' - \boldsymbol{x}'') \,. \end{aligned} \tag{4.37}$$

Notice that equation (4.36) reduces to the linear retarded propagator equation (4.5) in the linear limit. More generally, the equations (4.36) and (4.37) are evolution equations for the retarded propagator and covariance function, respectively. As such they allow to obtain the connected two-point correlation functions as the solution to these equations, provided one can supply the corresponding 1PI correlation functions.

Due to the translational invariance of the correlation functions it is convenient to work also with the Fourier transform. Here the convolution integrals becomes simple products and in the following both representations are used interchangeably and the DeWitt indices may include position or wave vector arguments.

Equation (4.37) can be formally inverted to give the power spectrum

$$P_{ab}(\tau, \tau', \boldsymbol{k}) = \int_{\tau'', \tau'''} G_{a\bar{a}}^{\mathrm{R}}(\tau, \tau'', \boldsymbol{k}) \, H_{\bar{a}\bar{b}}(\tau'', \tau''', \boldsymbol{k}) \, G_{\bar{b}b}^{\mathrm{A}}(\tau''', \tau', \boldsymbol{k}) \,. \qquad (4.38)$$

To study approximation schemes, it is convenient to split correlation functions into a linear and a non-linear contribution. In terms of the 1PI correlation functions this corresponds to identifying the linear parts of the bare action (4.14). For the effective equations of motion one then finds

$$E_a(\tau) = \partial_\tau \Psi_a(\tau) + n\mathcal{H}\Psi_a(\tau) - Q_a(\tau) - \delta(\tau - \tau_{\mathrm{in}}) \Psi_a^{\mathrm{in}} \,, \qquad (4.39)$$

where n denotes the number of tensorial indices carried by the field Ψ_a and corresponds to the corresponding term is the Hubble drag term. The function $Q_a(\tau)$ is the mean field *source term* and parametrises the back-reaction effect of non-linear corrections to the linearly decaying mean field.

Similarly, the 1PI two-point functions can be decomposed into a linear part and a *self-energy*. For the inverse propagator this is parametrised as

$$D_{ab}^{\mathrm{R}}(\tau, \tau', \boldsymbol{k}) = [\partial_\tau \delta_{ab} + \Omega_{ab}(\tau, \boldsymbol{k})]\delta(\tau - \tau') - \Sigma_{ab}^{\mathrm{R}}(\tau, \tau', \boldsymbol{k}) \,, \qquad (4.40)$$

while for the statistical 1PI two-point function

$$H_{ab}(\tau, \tau', \boldsymbol{k}) = \delta(\tau - \tau_{\mathrm{in}}) \, \delta(\tau' - \tau_{\mathrm{in}}) \, P_{ab}^{\mathrm{in}}(\boldsymbol{k}) + \Pi_{ab}(\tau, \tau', \boldsymbol{k}) \,. \qquad (4.41)$$

In the following it is convenient to further split the retarded self-energy into a local and non-local contribution

$$\Sigma_{ab}^{\mathrm{R}}(\tau, \tau', \boldsymbol{k}) = \delta(\tau - \tau') \, \Sigma_{ab}^{\mathrm{H}}(\tau, \boldsymbol{k}) + \Sigma_{ab}^{\mathrm{F}}(\tau, \tau', \boldsymbol{k}) \,, \qquad (4.42)$$

which are called the Hartree and Fock self-energy in analogy to the corresponding approximation in quantum field theory. While the Hartree self-energy describes time-local corrections which do not account for correlations, the Fock self-energy is in general non-local in time and corresponds to memory effects due to correlations. In this sense the statistical self energy (4.41) is also of Fock-type. Physically, one would expect the effective dynamics to be local in time although it is not clear whether this can really be realised in terms of the macroscopic description studied here. In chapter 7 local and non-local dynamics are discussed in detail in order to find an appropriate ansatz for the effective action.

It is emphasised that up to here only formal manipulations have been performed and no approximations have been made. As such all the objects and equations are still exact.

4.1.4 Diagrammatic representation

To investigate expansion and approximation schemes it is convenient to introduce diagrammatic rules for the computation of correlation functions. To this end, connected and 1PI correlation functions are represented by

$$W_{A_1 \ldots A_m B_1 \ldots B_n}^{(m,n)} = m \ \substack{\diagup \\ \bigcirc \\ \diagdown} \ n \quad , \qquad \Gamma_{A_1 \ldots A_m B_1 \ldots B_n}^{(m,n)} = m \ \substack{\diagup \\ \bullet \\ \diagdown} \ n \quad . \qquad (4.43)$$

External solid (dashed) edges correspond to physical (response) source currents or fields, respectively. Edges can be appropriately connected such that the corresponding DeWitt indices are summed and integrate over, while loops are cycle diagrams and imply a trace over the corresponding indices.

The equations (4.36) and (4.37) can then be written as

$$-\!\bullet\!-\!\!\circ\!\cdots = 1 \quad , \qquad -\cdot\,\bullet\!-\!\!\circ\!- \;=\; -\,-\cdot\bullet\cdot\!\circ\!- \quad . \tag{4.44}$$

For the following investigations it is necessary to also introduce a diagrammatic representation for the *linear* connected and *bare* 1PI correlation functions,

$$W^{\mathrm{L}\,(m,n)}_{A_1\ldots A_m B_1\ldots B_n} = m \;\Yleft\!\!\circ\!\!\Yright\; n \quad , \qquad S^{(m,n)}_{A_1\ldots A_m B_1\ldots B_n} = m \;\Yleft\!\!\bullet\!\!\Yright\; n \quad . \tag{4.45}$$

From the linear generating functional (4.24) and the bare action (4.14) it is evident that only linear one- and two-point connected and bare 1PI one-, two- and three-point correlation functions exist.

Notice that the linear and bare correlation functions are in general different as the latter include non-linearities to some extend. Consider e.g. the bare inverse retarded propagator which is given by

$$-\cdot\,\bullet\!- \;=\; -\,\mathrm{i}\,\tilde\delta(\boldsymbol{k}+\boldsymbol{k}')[\partial_\tau\delta_{ab} + \Omega_{ab}(\tau,\boldsymbol{k}) + 2\gamma_{abc}(\boldsymbol{k},\boldsymbol{0})\,\Psi_c(\tau)]\,\delta(\tau-\tau') \,, \tag{4.46}$$

on the equations of motion. As such, the bare inverse retarded propagator already features a non-vanishing Hartree self-energy which quantifies the coupling of the mean field to the fluctuations.

Since one typically deals with connected two-point functions in expansion schemes it is sensible to define the connected two-point functions solving the evolution equations (4.36) and (4.37) for the bare 1PI two-point functions. Diagrammatically these are denoted as

$$-\cdot\,\bullet\!-\!\!\bullet\!\cdots = 1 \quad , \qquad -\cdot\,\bullet\!-\!\!\bullet\!- \;=\; -\,-\cdot\bullet\cdot\!-\!\!\bullet\!- \quad , \tag{4.47}$$

and play a role in the 1PI resummation schemes studied in section 4.3.

4.2 Standard perturbation theory

In standard perturbation theory the generating functional (4.13) is formally expanded as

$$Z[J,\hat{J}] = \sum_{n=0}^{\infty} \frac{1}{n!}\left[-\frac{1}{2}\,S^{(2,1)}_{ABC}\,\frac{\delta}{\delta J_A}\frac{\delta}{\delta J_B}\frac{\delta}{\delta \hat{J}_C}\right]^n Z^{\mathrm{L}}[J,\hat{J}] \,, \tag{4.48}$$

where $S^{(2,1)}_{ABC}$ is proportional to the bare vertex.

This should be understood as an asymptotic series as the series expansion of the interaction operator is exchanged with the functional integration, formally only possible if the perturbative series converges absolutely. In general such perturbative

series do not converge and in cosmology the perturbative expansion shows clear signals of being asymptotic, namely corrections start to grow beyond some finite order and do not further improve results by including higher orders [117].

Since the bare vertex γ_{abc} couples two physical to one response field, the series (4.48) is also an expansion in the linear (or initial) mean field and covariance function. As such, it is organised in orders of Ψ_a^{L} and C_{ab}^{L} where by dimensional arguments the the $(2n)$th-order in Ψ_a^{L} corresponds to the nth-order in C_{ab}^{L}.

While it is straight forward to derive correlation functions from the generating functional (4.48), it is quite tedious to do so explicitly. Diagrammatically, this can be done in a much more convenient and systematic matter and is in the following done for the first non-trivial order.

Including the terms up to $n = 1$ of the perturbative series (4.48) gives the mean field

$$\text{—◉} = \text{—◦} - \tfrac{1}{2} \text{—◦--●} \bigcirc + \dots \quad , \tag{4.49}$$

where the second diagram on the right-hand side is the one-loop contribution and indicates the back-reaction of fluctuations onto the mean field. In principal there is also the diagram proportional to

$$\text{—◦--●}\!\!\!< \quad , \tag{4.50}$$

which vanishes due to the derivative nature of the bare vertices and spatial homogeneity of the mean field.

For the connected two-point functions one can proceed similarly. Although one also obtains corrections for the $n = 1$ term of the perturbative series, at least in the presence of a non-vanishing mean field, the fist loop corrections appear at order $n = 2$. For the retarded propagator the expansion up to order $n = 2$ reads

$$\text{—◉--} = \text{—◦--} + \tfrac{1}{2} \text{—◦--●}\bigcirc\text{●--◦--} + \tfrac{1}{2} \text{—◦--●}\bigcirc\text{●--◦--} + \dots \; , \tag{4.51}$$

where only the contributions for a vanishing mean field are displayed. The additional contributions due to a non-vanishing mean field are of the type

$$\text{—◦--●--◦--} \quad , \quad \text{—◦--●--◦--●--◦--} \quad , \quad \dots \tag{4.52}$$

where the expansion (4.49) is used to substitute the full mean field, in order to reduce the amount of diagrams, which should only be taken into account to the

appropriate order. Similarly one obtains for the power spectrum

$$\tag{4.53}$$

which, similar to the propagator, has additional contributions due to a non-vanishing mean field not shown explicitly here.

In terms of the formal solution (4.38) and the self-energy splitting (4.41), one can identify the loop diagram in the first line of equation (4.53) as the self-energy correction while the loops in the second and third line are corrections due to the propagator. These can be identified with the standard perturbation theory one-loop expansion which is usually written as

$$P_{ab}^{\text{1-loop}}(\tau, \tau', k) = P_{ab}^{\text{L}}(\tau, \tau', k) + P_{ab}^{(2,2)}(\tau, \tau', k) + 2P_{ab}^{(1,3)}(\tau, \tau', k) , \tag{4.54}$$

where the $P_{ab}^{(2,2)}$ contribution is the loop diagram in the first line while the $2P_{ab}^{(1,3)}$ contribution is given by the loop diagrams in the second and third line of equation (4.53).

Besides the problem that the method is perturbative, one should also be aware that at smaller scales the phenomenon of shell-crossing naturally generates higher-order velocity cumulants and thus invalidates the single-stream approximation. That is, even if one could compute the power spectrum exactly with some non-perturbative method, one would expect the true physical power spectrum to carry the signature of other small scale effects. These must not necessarily be all encoded in the density contrast equal-time auto-spectrum, but could be encoded in the general set of auto- and cross-spectra or higher-order correlation functions. In chapter 6 various two-point correlation functions are computed in an approximation which goes beyond the single-stream approximation with a non-perturbative method in order to take care of the above discussed issues.

4.3 Effective action loop expansion

Another in field theory often employed approximation is the loop expansion of the effective action. It is related to the 1PI resummation scheme which naturally leads to results corresponding to an infinite, but partial, resummation of the perturbative series (4.48). The basic idea of one-partial irreducible resummation schemes is to directly work with 1PI correlation functions rather than with (connected) correlation functions. These can be expanded in a similar fashion and truncated. To do so, one is interested in an expansion of the corresponding generating functional, namely

the effective action Γ. The advantage of such an expansion scheme is that a finite truncation of the effective action naturally corresponds to resummed two-point connected correlation functions when solving the evolution equations (4.36) and (4.37). This is also known as the 1PI resummation scheme.

From the definition of the effective action (4.31) one finds

$$\mathrm{e}^{-\Gamma[\Psi]+J_A\Psi_A} = \int \mathcal{D}\psi \; \mathrm{e}^{-S[\psi]+J_A\psi_A} \; , \tag{4.55}$$

where the source currents should be understood as being field-dependent here though the Legendre transform (4.32). To find an approximation where the right-hand side can be explicitly computed use can use the method of steepest decent. To do so, the bare action is expanded around the bare solution ψ_A^{sol}, solving the bare equations of motion $S_A^{(1)} = J_A$. For the physical field this simply implies that the bare solution solves the equations of motion (4.2) in the presence of a source current while the response field vanishes on the equations of motion. It is emphasised that the bare solution is taken to not be on the equations of motion, meaning the solutions are source dependent which in turn via the Legendre transform implies that the bare solution depends on the mean fields $\psi_A^{\mathrm{sol}}[\Psi]$. Doing so up to quadratic order gives

$$\begin{aligned} S[\psi] = S[\psi^{\mathrm{sol}}] &+ S_A^{(1)}[\psi^{\mathrm{sol}}] \, (\psi_A - \psi_A^{\mathrm{sol}}) \\ &+ \tfrac{1}{2} \, S_{AB}^{(2)}[\psi^{\mathrm{sol}}] \, (\psi_A - \psi_A^{\mathrm{sol}})(\psi_B - \psi_B^{\mathrm{sol}}) + \mathcal{O}\!\left[(\psi - \psi^{\mathrm{sol}})^3\right] , \end{aligned} \tag{4.56}$$

where by construction $S_A^{(1)}[\psi^{\mathrm{sol}}] = J_A$. Keeping only the terms up to quadratic order in the fields renders the functional integral on the right-hand side of equation (4.55) Gaussian. Using that the mean field by definition obeys the effective equations of motion $\Gamma_A^{(1)}[\Psi] = J_A$ one finds that the difference to the bare solution needs to be a correction of higher order contained in the last term of the right-hand side of equation (4.56), such that one can set $\psi_A^{\mathrm{sol}} = \Psi_A$ up to the indicated order. Doing so one is finally left with the one-loop effective action

$$\Gamma = S + \tfrac{1}{2}\,\mathrm{Tr}\!\left[\ln\!\big(S^{(2)}\big)\right] + \dots \; , \tag{4.57}$$

where the logarithm should be understood as the functional series expansion of the operator $S_{AB}^{(2)}$ and the trace operator is understood to run over the physical and response field content, time and space.[11]

Having an expression for the effective action one can now obtain explicit expressions for the 1PI correlation functions. Applying first-order derivative to the one-loop effective action (4.57) on obtains the 1PI one-point function

$$\Gamma_A^{(1)} = S_A^{(1)} + \tfrac{1}{2}\,\mathrm{Tr}\!\left[\left[S^{(2)}\right]^{-1} \cdot S_A^{(3)}\right] , \tag{4.58}$$

and similar for second-order derivatives which yield the 1PI two-point functions

$$\Gamma_{AB}^{(2)} = S_{AB}^{(2)} - \tfrac{1}{2}\,\mathrm{Tr}\!\left[\left[S^{(2)}\right]^{-1} \cdot S_A^{(3)} \cdot \left[S^{(2)}\right]^{-1} \cdot S_B^{(3)}\right] , \tag{4.59}$$

---

[11]In the last step the identity $\ln(\det(A)) = \mathrm{tr}(\ln(A))$ was used.

where the dot product runs over all internal structures similar to the trace.

On the equations of motion these can be expressed diagrammatically. The effective equations of motion read

$$
\text{--}\bullet \;=\; \text{--}\bullet \;+\; \tfrac{1}{2}\,\text{--}\bullet\!\bigcirc \quad , \tag{4.60}
$$

while the corresponding response field part vanishes on the equations of motion. The inverse propagator takes the form

$$
\text{--}\bullet\!\text{--} \;=\; \text{--}\bullet\!\text{--} \;-\; \tfrac{1}{2}\,\text{--}\bigcirc\!\bullet\!\text{--} \;-\; \tfrac{1}{2}\,\text{--}\bigcirc\!\bullet\!\text{--} \quad . \tag{4.61}
$$

while the statistical 1PI two-point correlation function is

$$
\text{--}\bullet\text{--} \;=\; \text{--}\bullet\text{--} \;-\; \tfrac{1}{2}\,\text{--}\bullet\!\bigcirc\!\bullet\text{--} \quad . \tag{4.62}
$$

Using these expression to solve the propagator and power spectrum evolution equations (4.44), results in an infinite partial resummation of the full perturbative series. This can be seen as a first step towards a non-perturbative method and it is seen in the next section that this approximation scheme is a truncation of the Dyson–Schwinger equation.

4.4 The Dyson–Schwinger equation

The Dyson–Schwinger equation provides a non-perturbative method to compute correlation functions and is derived in the following. In chapter 6 the Dyson–Schwinger equation is employed to studied large-scale cosmic structure formation.

Essentially, the Dyson–Schwinger equation is a consequence of the identity

$$
\int \mathcal{D}\psi \int \mathcal{D}\hat{\psi}\, \frac{\delta}{\delta\psi_{\boldsymbol{A}}}\, \mathrm{e}^{-S+J_{\boldsymbol{A}}\psi_{\boldsymbol{A}}} = 0 \,, \tag{4.63}
$$

from which one obtains

$$
\Gamma^{(1)}_{\boldsymbol{A}}[\Psi] = \left\langle S^{(1)}_{\boldsymbol{A}}[\psi] \right\rangle , \tag{4.64}
$$

using the Legendre transform (4.32).[12] Additionally, from definition (4.18) one can realise that source-dependent expectation values can be written as

$$
\left\langle \psi_{\boldsymbol{A}_1} \dots \psi_{\boldsymbol{A}_n} \right\rangle = \left(\Psi_{\boldsymbol{A}_1} + \frac{\delta}{\delta J_{\boldsymbol{A}_1}} \right) \left\langle \psi_{\boldsymbol{A}_2} \dots \psi_{\boldsymbol{A}_n} \right\rangle , \tag{4.65}
$$

---

[12]Remember that boundary terms vanish due to imposing periodic boundary conditions when taking the continuum limit.

where $\Psi_{\boldsymbol{A}}[J, \hat{J}]$ is the source-dependent mean field. Here, the first term compensates for the normalisation $1/Z$ while the second term generates a field. By iteration one obtains

$$\left\langle \psi_{\boldsymbol{A}_1} ... \psi_{\boldsymbol{A}_n} \right\rangle = \prod_{m=1}^{n} \left(\Psi_{\boldsymbol{A}_m} + W^{(2)}_{\boldsymbol{A}_m \boldsymbol{B}} \frac{\delta}{\delta \Psi_{\boldsymbol{B}}} \right) , \tag{4.66}$$

where the equation is understood to depend on the mean fields through the Legendre transform (4.32). Using the inverse relation of the connected and 1PI two-point functions (4.34), one can express the expectation value of any operator $\mathcal{O}[\psi]$ which has a well-defined series expansion in the fields as

$$\langle \mathcal{O}[\psi] \rangle = \mathcal{O}\left[\psi = \Psi + \left[\Gamma^{(2)} \right]^{-1} \cdot \frac{\delta}{\delta \Psi} \right] . \tag{4.67}$$

Finally, combining equations (4.64) and (4.67) one obtains the celebrated Dyson–Schwinger equation [50–52]

$$\Gamma^{(1)}_{\boldsymbol{A}}[\Psi] = S^{(1)}_{\boldsymbol{A}}\left[\psi = \Psi + \left[\Gamma^{(2)} \right]^{-1} \cdot \frac{\delta}{\delta \Psi} \right] . \tag{4.68}$$

Applying field derivatives one obtains Dyson–Schwinger equations for the 1PI n-point correlation functions. The one-point function reads

$$\Gamma^{(1)}_{\boldsymbol{A}} = S^{(1)}_{\boldsymbol{A}} + \tfrac{1}{2} \operatorname{Tr}\left[W^{(2)} \cdot S^{(3)}_{\boldsymbol{A}} \right] , \tag{4.69}$$

while the two-point function is given by

$$\Gamma^{(2)}_{\boldsymbol{AB}} = S^{(2)}_{\boldsymbol{AB}} - \tfrac{1}{2} \operatorname{Tr}\left[W^{(2)} \cdot S^{(3)}_{\boldsymbol{A}} \cdot W^{(2)} \cdot \Gamma^{(3)}_{\boldsymbol{B}} \right] , \tag{4.70}$$

and the three-point function is

$$\begin{aligned} \Gamma^{(3)}_{\boldsymbol{ABC}} = S^{(3)}_{\boldsymbol{ABC}} &+ \tfrac{1}{2} \operatorname{Tr}\left[W^{(2)} \cdot S^{(3)}_{\boldsymbol{A}} \cdot W^{(2)} \cdot \Gamma^{(3)}_{\boldsymbol{B}} \cdot W^{(2)} \cdot \Gamma^{(3)}_{\boldsymbol{C}} \right] + (\boldsymbol{B} \leftrightarrow \boldsymbol{C}) \\ &- \tfrac{1}{2} \operatorname{Tr}\left[W^{(2)} \cdot S^{(3)}_{\boldsymbol{A}} \cdot W^{(2)} \cdot \Gamma^{(4)}_{\boldsymbol{BC}} \right] , \end{aligned} \tag{4.71}$$

where the inverse of the second-order functional derivative of the effective action is expressed using the inverse relation (4.34).

Similarly, equations for higher-order 1PI correlation functions are obtained by applying more functional derivatives with respect to the mean fields. For the type of bare action (4.14) the Dyson–Schwinger equation for the n-point function involves the $(n+1)$-point function generating an infinite tower of coupled equations. For practical applications one needs to truncate this hierarchy to obtain a finite solvable system of equations.

It is interesting to notice the relation between the one-loop effective action expressions (4.58) and (4.59) and the Dyson–Schwinger equations (4.69) and (4.70). The former are approximations obtained from a loop expansion of the effective action while the latter are exact. From this point of view the one-loop 1PI expansion scheme can be seen as a truncation of the Dyson–Schwinger equations.

The Dyson–Schwinger equations can be used to find explicit expressions for the non-linear parts of correlation functions. The mean field source term is obtained from the second term on the right-hand side of equation (4.69). On the equations of motion it is given by

$$Q_a(\tau) = -\int_{\boldsymbol{q}} \gamma_{abc}(\boldsymbol{q}, -\boldsymbol{q})\, P_{bc}(\tau, \tau, \boldsymbol{q})\,, \tag{4.72}$$

which is proportional to the equal-time coincidence limit of the covariance function. Similarly, the self-energies of the 1PI two-point functions are obtained from equation (4.70). The Hartree self-energy is contained in the non-linear part of $S^{(2)}_{\boldsymbol{AB}}$ and reads on the equations of motion

$$\Sigma^{\mathrm{H}}_{ab}(\tau, \boldsymbol{k}) = -2\,\gamma_{abc}(\boldsymbol{k}, \boldsymbol{0})\, \Psi_c(\tau)\,. \tag{4.73}$$

Diagrammatically, these are represented by

$$\mathrm{i}\,Q_a = \tfrac{1}{2}\; \text{---}\!\!\bigcirc\!\!\circ \;, \qquad \mathrm{i}\,\Sigma^{\mathrm{H}}_{ab} = \;\text{---}\!\!\bullet\!\!\text{---} \;, \tag{4.74}$$

from which it is evident that the mean field is sourced by the equal-time correlation of fluctuations while the Hartree self-energy captures the effect of the presence of a mean field.

The retarded and statistical Fock self-energies are more involving and obtained from the second term on the right-hand side of equation (4.70). Diagrammatically, the retarded Fock self-energy on the equations of motion is given by

$$\mathrm{i}\,\Sigma^{\mathrm{F}}_{ab} = -\tfrac{1}{2}\;\text{---}\!\bigcirc\!\text{---}\; -\tfrac{1}{2}\;\text{---}\!\bigcirc\!\text{---}\; -\tfrac{1}{2}\;\text{---}\!\bigcirc\!\text{---}\;, \tag{4.75}$$

and the statistical Fock self-energy on the equations of motion reads

$$\Pi_{ab} = -\tfrac{1}{2}\;\text{---}\!\bigcirc\!\text{---}\; -\tfrac{1}{2}\;\text{---}\!\bigcirc\!\text{---}\; -\tfrac{1}{2}\;\text{---}\!\bigcirc\!\text{---}\; -\tfrac{1}{2}\;\text{---}\!\bigcirc\!\text{---}\;. \tag{4.76}$$

These capture the effect of the non-linear coupling of fluctuations and in general non-local in time.

In chapter 6 the Dyson–Schwinger equations are truncated by keeping the full structure of the one- and two-point correlation functions while setting higher-order 1PI correlation function to their corresponding bare functions. This truncation is a natural extension of the 1PI one-loop approximation studied in section 4.3 and called self-consistent one-loop approximation or Hartree–Fock approximation.

4.5 The functional renormalisation group

Another non-perturbative method is the functional renormalisation group. The basic idea is to regulate the generating function (4.13) by altering the bare action to include a term which is bilinear in the fields and suppresses fluctuations within the functional integral. More explicitly consider the regulated generating functional

$$Z_k[J, \hat{J}] := \int \mathcal{D}\psi \int \mathcal{D}\hat{\psi} \, e^{-S_k + J_A\psi_A + \hat{J}_A\hat{\psi}_A} \,, \tag{4.77}$$

where the regulated bare action is given by

$$S_k := S + \tfrac{1}{2} \, \psi_{\boldsymbol{A}} R_{k,\boldsymbol{AB}} \, \psi_{\boldsymbol{B}} \,. \tag{4.78}$$

The regulator $R_{k,\boldsymbol{AB}}$ depends on the renormalisation group scale k and is build such that it suppresses fluctuations within the functional integral, either in the infrared or ultraviolet (or both).[13] This can be achieved by suppressing fluctuations in the initial state or altering the dynamics to suppress the propagation of fluctuations. In the following applications the former option is employed although the functional renormalisation group is not restricted to this case.

Analogous to before, one defines the generating functional of connected correlation functions W_k and the flowing 1PI effective action as the modified Legendre transform

$$\Gamma_k[\Psi, \hat{\Psi}; R] := \sup_J [J_{\boldsymbol{A}}\Psi_{\boldsymbol{A}} - W_k] - \tfrac{1}{2} \Psi_{\boldsymbol{A}} R_{k,\boldsymbol{AB}} \Psi_{\boldsymbol{B}} \,. \tag{4.79}$$

The term bilinear in the fields is added for later convenience but vanishes in the limit $R_{k,\boldsymbol{AB}} \to 0$ where one obtains the full 1PI effective action $\Gamma_k \to \Gamma$.

One can study how the generating functionals change when altering the renormalisation group scale by calculating the partial derivative with respect to the renormalisation group scale k. The renormalisation group flow equation for the generating functional of connected correlation functions then reads

$$\partial_k W_k = -\tfrac{1}{2} \operatorname{Tr}\left[\left(W_k^{(2)} + W_k^{(1)} \otimes W_k^{(1)}\right) \cdot \partial_k R_k\right]. \tag{4.80}$$

where the Kronecker product $\otimes$ is taken with respect to the physical and response fields, time and space and in the current context it is the analogue of Polchinski's equation [129]. Applying the modified Legendre transform (4.79) one is left with the flow equation

$$\partial_k \Gamma_k = \tfrac{1}{2} \operatorname{Tr}\left[\left[\Gamma_k^{(2)} + R_k\right]^{-1} \cdot \partial_k R_k\right], \tag{4.81}$$

which is Wetterich's equation [53] in the present context and the flow equation used in the following.

---

[13]When dealing with the functional renormalisation group wave vectors arguments of correlation functions are denoted usually by $\boldsymbol{q}$ to distinguish these from the renormalisation group scale k.

Applying functional derivatives with respect to the mean fields one obtains flow equations for 1PI correlation functions. The flow of the one-point function is given by

$$\partial_k \Gamma^{(1)}_{k,\boldsymbol{A}} = -\tfrac{1}{2} \operatorname{Tr}\left[W^{(2)}_k \cdot \Gamma^{(3)}_{k,\boldsymbol{A}} \cdot W^{(2)}_k \cdot \partial_k R_k \right] , \qquad (4.82)$$

while the flow of the two-point function reads

$$\partial_k \Gamma^{(2)}_{k,\boldsymbol{AB}} = \tfrac{1}{2} \operatorname{Tr}\left[W^{(2)}_k \cdot \Gamma^{(3)}_{k,\boldsymbol{A}} \cdot W^{(2)}_k \cdot \Gamma^{(3)}_{k,\boldsymbol{B}} \cdot W^{(2)}_k \cdot \partial_k R_k \right] + (\boldsymbol{A} \leftrightarrow \boldsymbol{B}) \\ - \tfrac{1}{2} \operatorname{Tr}\left[W^{(2)}_k \cdot \Gamma^{(4)}_{k,\boldsymbol{AB}} \cdot W^{(2)}_k \cdot \partial_k R_k \right] , \qquad (4.83)$$

and the flow of the three-point function is

$$\partial_k \Gamma^{(3)}_{k,\boldsymbol{ABC}} = -\tfrac{1}{2} \operatorname{Tr}\left[W^{(2)}_k \cdot \Gamma^{(3)}_{k,\boldsymbol{A}} \cdot W^{(2)}_k \cdot \Gamma^{(3)}_{k,\boldsymbol{B}} \cdot W^{(2)}_k \cdot \Gamma^{(3)}_{k,\boldsymbol{C}} \cdot W^{(2)}_k \cdot \partial_k R_k \right] \\ + (\text{perm. } (\boldsymbol{A}, \boldsymbol{B}, \boldsymbol{C})) \\ + \tfrac{1}{2} \operatorname{Tr}\left[W^{(2)}_k \cdot \Gamma^{(4)}_{k,\boldsymbol{AB}} \cdot W^{(2)}_k \cdot \Gamma^{(3)}_{k,\boldsymbol{C}} \cdot W^{(2)}_k \cdot \partial_k R_k \right] \qquad (4.84) \\ + (\text{perm. } (\boldsymbol{A}, \boldsymbol{B}, \boldsymbol{C})) \\ - \tfrac{1}{2} \operatorname{Tr}\left[W^{(2)}_k \cdot \Gamma^{(5)}_{k,\boldsymbol{ABC}} \cdot W^{(2)}_k \cdot \partial_k R_k \right] .$$

Very similar to the Dyson–Schwinger equation the functional renormalisation group involves an infinite tower of coupled flow equations and needs to be truncated in an appropriate way. To this end, various expansion and truncation schemes have been developed most importantly the vertex and derivative expansion which are applied in chapter 7.

In the following a regulator which suppresses ultraviolet fluctuations in the initial state is employed [35–38]. To this end the regulator is written as

$$R_{k,\boldsymbol{AB}} = \delta(\tau - \tau_{\mathrm{in}})\, \delta(\tau' - \tau_{\mathrm{in}}) \left[C^{\mathrm{in}}_{k,ab}(\boldsymbol{x} - \boldsymbol{x}') - C^{\mathrm{in}}_{ab}(\boldsymbol{x} - \boldsymbol{x}') \right] \begin{pmatrix} 0 & 0 \\ 0 & 1 \end{pmatrix} , \qquad (4.85)$$

where the power spectral density is regulated by

$$P^{\mathrm{in}}_{k,ab}(\boldsymbol{q}) := r_k(q)\, P^{\mathrm{in}}_{ab}(\boldsymbol{q}) , \qquad (4.86)$$

for a shape function which in the following is chosen to be $r_k(q) = \theta(k/q - 1)$.[14] Due to the choice of regulator and definition of the flowing effective action, one then has the limits

$$\lim_{k \to 0} \Gamma_k = S , \qquad \lim_{k \to \infty} \Gamma_k = \Gamma . \qquad (4.87)$$

---

[14]It has been criticised that for the regulator (4.85) the flow equation (4.81) simply describes initial power spectrum variations rather than truly capturing the effects of coarse-gaining [130]. While it is true that modes which are initially absent can (and will) be dynamically generated, the flow equation (4.81) is not restricted to these types of regulators. In principle, the dynamical part of the bare action (4.14) can also be regulated such that the propagation of modes on scales $q > k$ is essentially absent.

which can be used as an initial condition of the flow in the infrared in order to flow to the physical limit in the ultraviolet. The choice of a sensible regulator heavily depends on the problem at hand and the behaviour of the system in the infrared and ultraviolet. In the context of cosmology, where corrections to the bare action arise due to initial state fluctuations, the question of a sensible regulator is related to the scaling of the initial power spectrum. For a power law dark matter density contrast power spectrum, $P_{\delta\delta}^{\text{in}}(q) \propto q^n$, corrections are finite in the infrared for $n > -1$ and in the ultraviolet for $n < -3$ to all orders in standard perturbation theory [90, 91, 131–133].[15] Realistic power spectra of the ΛCDM concordance model avoid divergences in both limits due to the scaling shown in chapter (3) in equation (3.12).

To study the flow equations it is useful to introduce a diagrammatic representation of the regulator,

$$G_{k,a\bar{a}}^{\text{R}}(\tau,\tau_{\text{in}},\boldsymbol{q})\,\partial_k P_{k,\bar{a}\bar{b}}^{\text{in}}(\boldsymbol{q})\,G_{k,\bar{b}b}^{\text{A}}(\tau_{\text{in}},\tau',\boldsymbol{q}) = \quad \text{—}\!\otimes\!\text{—} \quad . \tag{4.88}$$

The flow equations of the 1PI one-point function is then given by

$$\partial_k \Gamma_{k,A}^{(0,1)} = \tfrac{1}{2} \quad \text{} \quad , \tag{4.89}$$

the inverse propagator flow is given by

$$\partial_k \Gamma_{k,AB}^{(1,1)} = -\tfrac{1}{2} \quad \text{} \quad -\tfrac{1}{2} \quad \text{} \quad +\tfrac{1}{2} \quad \text{} \quad , \tag{4.90}$$

and the 1PI statistical two-point function flow is given by

$$\partial_k \Gamma_{k,AB}^{(0,2)} = -\tfrac{1}{2} \quad -\tfrac{1}{2} \quad -\tfrac{1}{2} \quad -\tfrac{1}{2} \quad -\tfrac{1}{2} \quad -\tfrac{1}{2} \quad +\tfrac{1}{2} \quad . \tag{4.91}$$

In chapter 5 the flow equations of the two-point functions is closed using Ward identities related to extended Galilean invariance studied in the next section. In chapter 7 the functional renormalisation group is solved by truncating the theory space using an ansatz for the effective action that corresponds to dynamics that are local in time.

4.6 Extended symmetries and related Ward identities

In this section symmetries of the bare action (4.14) are investigated in order to understand the general structure of the effective action Γ_k and derive related generalised Ward identities [134]. The studied symmetries correspond to (infinitesimal)

---

[15]Even for finite corrections at all orders the perturbative series is only asymptotic and therefore does not need to converge [43].

affine field transformations

$$\delta_\epsilon \psi_{\boldsymbol{A}} = L_{\epsilon,\boldsymbol{AB}} \, \psi_{\boldsymbol{A}} + T_{\epsilon,\boldsymbol{A}} \, , \tag{4.92}$$

where L_ϵ is a linear operator and T_ϵ a translation in field space. In this context, a transformation that leaves the action invariant is called a true symmetry, while an extended symmetry changes the action by terms that are at most linear in the fields [135]. Since a change of integration variables must leave the generating functional (4.13) unaltered, one obtains the Ward identity

$$\Gamma_k^{(1)} \cdot \delta_\epsilon \Psi = \delta_\epsilon S[\Psi] + \mathrm{Tr}\left[L_\epsilon \cdot W_k^{(2)} \cdot R_k\right] . \tag{4.93}$$

The first term on the right-hand side only contributes for extended symmetries, while the second term vanishes if the regulator respects the symmetry transformation.[16] Since the employed regulator (4.85) only alters the initial power spectrum, the flowing action (4.79) respects the same symmetries as the bare action (4.14) so that the second term on the right-hand side of the Ward identity (4.93) vanishes.

4.6.1 Conservation of mass

Conservation of mass is ensured at the level of the bare action (4.14) by the continuity equation. This extends to the effective action and is related to a time-gauged density contrast response field shift, $\delta_\epsilon \hat{\delta}(\tau, \boldsymbol{x}) = \epsilon(\tau)$, which changes the bare action by a term linear in the fields,

$$\delta_\epsilon S = -\mathrm{i} \int_{\tau,\boldsymbol{x}} \epsilon(\tau) \, \partial_\tau \delta(\tau,\boldsymbol{x}) + \int_{\boldsymbol{x},\boldsymbol{x}'} \epsilon(\tau_{\mathrm{in}}) \, C^{\mathrm{in}}_{\delta a}(\boldsymbol{x}-\boldsymbol{x}') \, \hat{\Psi}_a(\tau_{\mathrm{in}},\boldsymbol{x}') \, , \tag{4.94}$$

where the second term on the right-hand side vanishes for the type of initial power spectra considered here since it is proportional to $P^{\mathrm{in}}_{ab}(\boldsymbol{0})$.[17] Since $\epsilon(\tau)$ is an (infinitesimal) arbitrary function of time, one obtains the Ward identity

$$\int_{\boldsymbol{x}} \Gamma_{k,\delta}^{(0,1)}(\tau,\boldsymbol{x}) = -\mathrm{i} \int_{\boldsymbol{x}} \partial_\tau \delta(\tau,\boldsymbol{x}) \, , \tag{4.95}$$

which encodes that the effective equations of motion of the density contrast field are of conservative form. The Ward identity may equivalently be written in Fourier space as

$$\Gamma_{k,\delta}^{(0,1)}(\tau,\boldsymbol{0}) = -\mathrm{i} \, \partial_\tau \delta(\tau,\boldsymbol{0}) \, . \tag{4.96}$$

Here and in the following, specific mean fields are denoted by the same symbols as their fluctuation counterpart for a clearer notation.

---

[16]Additionally, it is assumed that the functional integral measure is invariant under the symmetry transformation, i.e. in the absence of an anomaly, which is the case for the two symmetries studied in this section.

[17]Due to the periodic boundary conditions imposed in the functional integral, the space integral over the total derivative term in the continuity equation vanishes.

4.6.2 Extended Galilean invariance

In the following, the Galilean invariance [90, 92, 93, 136] studied in section 2.4.5 of chapter 2 is used to derive generalised Ward identities. Remember that the cumulants of the distribution function transform as

$$c_{i_1 \dots i_n}^{(n)}(\tau, \boldsymbol{x}) \mapsto c_{i_1 \dots i_n}^{(n)}(\tau, \boldsymbol{x} - \boldsymbol{v}\,T) + \delta_{n1} v_{i_1} \dot{T} \,, \tag{4.97}$$

so that only the velocity field is non-trivially shifted. The equations of motion (2.88) are invariant under this transformation up to a time-dependent shift in the velocity field equation. While this shift is compensated for by the transformation of the gravitational potential [90]

$$\partial_i \phi(\tau, \boldsymbol{x}) \mapsto \partial_i \phi(\tau, \boldsymbol{x} - \boldsymbol{v}\,T) + v_i T \dot{\mathcal{H}} \,, \tag{4.98}$$

the symmetry is no longer apparent when the gravitational potential is eliminated by solving Poisson's equation. Indeed, Galilean invariance is no longer manifest since integrating Poisson's equation in terms of the operator (4.4) fixes a frame with respect to which expectation values are computed.[18] In this sense the Galilean transformation (2.96) is already an extended symmetry that changes the bare action (4.14) by terms linear in the velocity response field.

The transformation (2.96) extends to a time-gauged symmetry of the effective action for the infinitesimal field transformations

$$\begin{aligned}\delta_\epsilon \psi_a(\tau, \boldsymbol{x}) &= -\epsilon_i(\tau)\,\partial_i \psi_a(\tau, \boldsymbol{x}) + \delta_{au_i} \dot{\epsilon}_i(\tau) \,, \\ \delta_\epsilon \hat{\psi}_a(\tau, \boldsymbol{x}) &= -\epsilon_i(\tau)\,\partial_i \hat{\psi}_a(\tau, \boldsymbol{x}) \,.\end{aligned} \tag{4.99}$$

Under these transformations all terms in the bare action (4.14) are invariant except for the term involving the time derivative and the Hubble drag term of the velocity field, giving rise to

$$\delta_\epsilon S = -\mathrm{i} \int_{\tau, \boldsymbol{x}} \hat{u}_i(\tau, \boldsymbol{x}) \Big[\ddot{\epsilon}_i(\tau) + \mathcal{H}\dot{\epsilon}_i(\tau) \Big] \,. \tag{4.100}$$

Since the right-hand side is linear in fields, this corresponds to an extended symmetry. The corresponding Ward identity reads

$$\int_{\boldsymbol{x}} \Big[\Psi_a(\tau, \boldsymbol{x})\,\partial_i - \delta_{au_i}\,\partial_\tau \Big] \Gamma_{k,a}^{(1,0)}(\tau, \boldsymbol{x}) + \int_{\boldsymbol{x}} \hat{\Psi}_a(\tau, \boldsymbol{x})\,\partial_i \Gamma_{k,a}^{(0,1)}(\tau, \boldsymbol{x})$$
$$= -\mathrm{i} \int_{\boldsymbol{x}} \Big[\partial_\tau^2 - \mathcal{H}\partial_\tau - \dot{\mathcal{H}} \Big] \hat{u}_i(\tau, \boldsymbol{x}) \,, \tag{4.101}$$

and entails that, apart from the velocity field's time derivative and Hubble drag term which are not renormalised, the effective action is invariant under time-gauged Galilean transformations.

---

[18] Equivalently, one can keep the gravitational potential and Poisson's equation at the expense of introducing another response field so that Galilean invariance corresponds to a true symmetry, as shown in the next section.

Applying field derivatives to the Ward identity (4.101) yields related identities such that for $m + n > 1$ one obtains in Fourier space

$$\left[\sum_{l=1}^{m} \theta(\tau - \tau_l)\,\mathrm{i}\,q_{l,i} + \sum_{\bar{l}=1}^{n} \theta(\tau - \tau'_{\bar{l}})\,\mathrm{i}\,q'_{\bar{l},i}\right] \Gamma^{(m,n)}_{k,a_1...b_n}(\tau_1, \boldsymbol{q}_1; ... ; \tau'_n, \boldsymbol{q}'_n)$$
$$= \Gamma^{(m+1,n)}_{k,u_i a_1...b_n}(\tau, \boldsymbol{0}; \tau_1, \boldsymbol{q}_1; ... ; \tau'_n, \boldsymbol{q}'_n)\,. \tag{4.102}$$

The Ward identities (4.102) impose linear relations between 1PI correlation functions of order $(m+1, n)$ at vanishing wave vector for a velocity field and 1PI correlation functions of lower order (m, n).

4.6.3 Non-renormalisation of the gravitational sector

Instead of eliminating the gravitational potential by solving Poisson's equation (2.85), one can equivalently use a gravitational response field $\hat{\phi}(\tau, \boldsymbol{x})$ in order to enforce Poisson's equation. Constraint equations are introduced into the generating functional (4.13) in the same manner as field equations so that the bare action in this setting reads

$$\begin{aligned}
S = &-\mathrm{i}\int_{\tau,\boldsymbol{x},\boldsymbol{x}'} \hat{\psi}_a(\tau, \boldsymbol{x})\Big[\partial_\tau \delta_{ab}\,\delta(\boldsymbol{x} - \boldsymbol{x}') + \Omega'_{ab}(\tau, \boldsymbol{x} - \boldsymbol{x}')\Big]\psi_b(\tau, \boldsymbol{x}') \\
&-\mathrm{i}\int_{\tau,\boldsymbol{x},\boldsymbol{x}',\boldsymbol{x}''} \hat{\psi}_a(\tau, \boldsymbol{x})\,\gamma_{abc}(\boldsymbol{x} - \boldsymbol{x}', \boldsymbol{x} - \boldsymbol{x}'')\,\psi_b(\tau, \boldsymbol{x}')\,\psi_c(\tau, \boldsymbol{x}'') \\
&+\int_{\boldsymbol{x},\boldsymbol{x}'} \hat{\psi}_a(\tau_{\mathrm{in}}, \boldsymbol{x})\Big[\mathrm{i}\,\delta(\boldsymbol{x} - \boldsymbol{x}')\Psi^{\mathrm{in}}_a + \tfrac{1}{2}\,C^{\mathrm{in}}_{ab}(\boldsymbol{x} - \boldsymbol{x}')\,\hat{\psi}_b(\tau_{\mathrm{in}}, \boldsymbol{x}')\Big] \\
&-\mathrm{i}\int_{\tau,\boldsymbol{x}} \hat{u}_i(\tau, \boldsymbol{x})\,\partial_i \phi(\tau, \boldsymbol{x}) \\
&-\mathrm{i}\int_{\tau,\boldsymbol{x}} \hat{\phi}(\tau, \boldsymbol{x})\Big[\partial_i \partial_i \phi(\tau, \boldsymbol{x}) - \tfrac{3}{2}\,\mathcal{H}^2\,\Omega_{\mathrm{m}}\delta(\tau, \boldsymbol{x})\Big]\,.
\end{aligned} \tag{4.103}$$

Here, Ω'_{ab} is the upper triangular part of the matrix Ω_{ab} given in equation (4.3), that is the velocity-density component due to integrating out the gravitational potential is removed. This has the advantage that no non-analyticities are present in the bare action since Ω'_{ab} only acts through spatial gradients.

The gravitational sector of the theory is particularly simple since there are two extended symmetries related to the (infinitesimal) time- and space-gauged field shifts $\delta_\epsilon \phi(\tau, \boldsymbol{x}) = \epsilon(\tau, \boldsymbol{x})$ and $\delta_\epsilon \hat{\phi}(\tau, \boldsymbol{x}) = \epsilon(\tau, \boldsymbol{x})$. These yield the Ward identities

$$\Gamma^{(1,0)}_{k,\phi}(\tau, \boldsymbol{x}) = \mathrm{i}\left[\partial_i \hat{u}_i(\tau, \boldsymbol{x}) - \partial_i \partial_i \hat{\phi}(\tau, \boldsymbol{x}')\right]\,, \tag{4.104}$$

and

$$\Gamma^{(0,1)}_{k,\phi}(\tau, \boldsymbol{x}) = -\mathrm{i}\left[\partial_i \partial_i \phi(\tau, \boldsymbol{x}) - \tfrac{3}{2}\,\mathcal{H}^2\,\Omega_{\mathrm{m}}\delta(\tau, \boldsymbol{x})\right]\,, \tag{4.105}$$

which encode that the whole gravitational sector is not renormalised and the dependence on the gravitational fields is the same for the bare and effective action.

In this setting Galilean invariance can be realised as a true symmetry using the transformations (4.99) in addition to

$$
\begin{aligned}
\delta_\epsilon \phi(\tau, \boldsymbol{x}) &= -\epsilon_i(\tau)\,\partial_i \phi_a(\tau, \boldsymbol{x}) - x_i[\ddot{\epsilon}_i(\tau) + \mathcal{H}\dot{\epsilon}_i(\tau)]\ , \\
\delta_\epsilon \widehat{\phi}(\tau, \boldsymbol{x}) &= -\epsilon_i(\tau)\,\partial_i \widehat{\phi}_a(\tau, \boldsymbol{x})\ .
\end{aligned}
\tag{4.106}
$$

In the case where the gravitational potential is integrated out using Poisson's equation (2.85),

$$
\partial_i \phi(\tau, \boldsymbol{x}) = \int_{\boldsymbol{x}'} O_i(\tau, \boldsymbol{x} - \boldsymbol{x}')\,\delta(\tau, \boldsymbol{x}') + C_i(\tau, \boldsymbol{x})\ ,
\tag{4.107}
$$

where the operator O_i is defined in equation (4.4), one has a residual gauge symmetry due to the constant of integration C_i, which is a divergence-less vector field. By choosing C_i appropriately, any bulk velocity terms appearing due to a Galilean transformation (4.99) can be eliminated. Since the constant of integration is fixed to $C_i = 0$ in the equations of motion (4.2), Galilean invariance is no longer manifest. This should be understood as 'gauge fixing' to the frame in which the velocity mean field is vanishing.[19]

---

[19]Within the functional integral representation (4.13) a specific velocity mean field can be forced by evaluating expectation values at a non-vanishing response field source current or by adding a 'frame-fixing' term to the bare action [92]. Similar to local gauge symmetries the choice of frame can be gauge fixed using the Faddeev–Popov method so that one obtains a Becchi–Rouet–Stora symmetry and a related Slavnov–Taylor identity instead of an extended Galilean symmetry [137, 138].

5 Large wave number sector of the functional renormalisation group

In this chapter the large external wave number limit of the 1PI two-point correlation function's flow equations is investigated. Using the Ward identities (4.102) related to extended Galilean invariance, the flow equations can be (formally) closed in this limit, at least in the absence of higher-order velocity cumulants. The procedure presented here is closely related to the large external wave number limit studied in the context of fluid turbulence [139–141], although being in a non-stationary setting in cosmology.

5.1 Large external wave limit

To derive the large external wave number limit of the flow equations (4.90) and (4.91), the first diagram of the inverse propagator flow (4.90) is considered as an illustrative example. It is given by

$$
\begin{aligned}
= -\mathrm{i}\,\delta(\boldsymbol{q}+\boldsymbol{q}') \int_{\substack{\bar{\tau},\bar{\tau}' \\ \tilde{\tau},\tilde{\tau}'}} \int_{\boldsymbol{l}} \hat{\Gamma}^{(2,1)}_{k,cea}(\tilde{\tau},\boldsymbol{l};\bar{\tau},-\boldsymbol{q}-\boldsymbol{l};\tau,\boldsymbol{q}) \\
\times\, G^{\mathrm{R}}_{k,ef}(\bar{\tau},\bar{\tau}',\boldsymbol{q}+\boldsymbol{l}) \\
\times\, \hat{\Gamma}^{(2,1)}_{k,dbf}(\tilde{\tau}',-\boldsymbol{l};\tau',-\boldsymbol{q};\bar{\tau}',\boldsymbol{q}+\boldsymbol{l}) \\
\times\, \hat{\partial}_k P^{\mathrm{I}}_{k,dc}(\tilde{\tau}',\tilde{\tau},\boldsymbol{l})\,,
\end{aligned}
\tag{5.1}
$$

where the circumflex denotes that an overall wave vector conserving delta function has been extracted from the 1PI three-point functions. Further, the abbreviation

$$
P^{\mathrm{I}}_{k,ab}(\tau,\tau',\boldsymbol{q}) = G^{\mathrm{R}}_{k,a\bar{a}}(\tau,\tau_{\mathrm{in}},\boldsymbol{q})\,P^{\mathrm{in}}_{k,\bar{a}\bar{b}}(\boldsymbol{q})\,G^{\mathrm{A}}_{k,\bar{b}b}(\tau_{\mathrm{in}},\tau',\boldsymbol{q})\,,
\tag{5.2}
$$

is used and the derivative

$$
\hat{\partial}_k = \int_{\boldsymbol{q}} \partial_k P^{\mathrm{in}}_{k,ab}(\boldsymbol{q})\,\frac{\delta}{\delta P^{\mathrm{in}}_{k,ab}(\boldsymbol{q})}\,,
\tag{5.3}
$$

only acts on the regulated initial power spectrum.

The internal wave vector $\boldsymbol{l}$ running through the loop of the diagram (5.1) is restricted to $|\boldsymbol{l}| = k$ due to the regulator (4.85). In the limit $q \to \infty$ the internal wave vector $\boldsymbol{l}$ is therefore small in magnitude compared to $\boldsymbol{q}$ and may be set to zero

within the 1PI three-point functions.[1] In the case where the vanishing wave vector is assigned to a velocity mode the Ward identity (4.102) can be used to relate the 1PI three-point function to a 1PI two-point function.

A priori it is not clear why the vanishing wave vector should be assigned to velocity modes since the loop naturally runs over all degrees of freedom included in the field content (4.1). In the following, it is argued that in the absence of velocity dispersion and higher-order velocity cumulants it is expected that in the limit $q \to \infty$ the leading contribution is due to the velocity-velocity sector of the regulator. More specifically, it is shown that in the large external wave number limit the diagram (5.1) is given by

$$
\text{-} \hspace-2mm \bigotimes \hspace-2mm \text{-} \sim -\mathrm{i}\,\delta(\boldsymbol{q}+\boldsymbol{q}') \int_{\substack{\bar{\tau},\bar{\tau}' \\ \tilde{\tau},\tilde{\tau}'}} \hat{\varGamma}^{(2,1)}_{k,u_i e a}(\tilde{\tau},\boldsymbol{0};\bar{\tau},-\boldsymbol{q};\tau,\boldsymbol{q})\,G^{\mathrm{R}}_{k,ef}(\bar{\tau},\bar{\tau}',\boldsymbol{q})
$$
$$
\times\,\hat{\varGamma}^{(2,1)}_{k,u_j b f}(\tilde{\tau}',\boldsymbol{0};\tau',-\boldsymbol{q};\bar{\tau}',\boldsymbol{q}) \qquad (5.4)
$$
$$
\times\,\hat{\partial}_k \int_{\boldsymbol{l}} P^{\mathrm{I}}_{k,u_j u_i}(\tilde{\tau}',\tilde{\tau},\boldsymbol{l})\,,
$$

at least *perturbatively* to all orders. The line of argument presented here is very similar to the classification of digrams in renormalised perturbation theory [18, 19].

Consider the diagram (5.1) and amputate the regulator $\hat{\partial}_k P^{\mathrm{I}}_{k,cd}$. At lowest order in standard perturbation theory the leading contribution in the limit $q \to \infty$ is given by

$$
\overset{c \qquad\quad d}{a \,\text{-}\text{-}\hspace-1mm\bullet\hspace-1mm\text{-}\hspace-1mm\circ\hspace-1mm\text{-}\hspace-1mm\bullet\hspace-1mm\text{-}\, b} \;\sim\; q^2\,g^{\mathrm{R}}_{ab}(\tau,\tau',\boldsymbol{q})\,\delta_{cu_i}\delta_{du_j}\times(q\text{-ind.})\,. \qquad (5.5)
$$

The limit makes use of the fact that the wave vector $\boldsymbol{l}$ is bounded in magnitude due to the regulator and thus negligible compared to $\boldsymbol{q}$. The leading contribution is then due to the scaling of the linear propagator

$$
g^{\mathrm{R}}_{ab}(\tau,\tau',\boldsymbol{q}) \sim \begin{pmatrix} 1 & q_j \\ q_i/q^2 & \delta_{ij} \end{pmatrix} \times (q\text{-ind.})\,, \qquad (5.6)
$$

and the structure of the bare vertices.

At the next higher order in perturbation theory two types of diagrams need to be distinguished. In the language of renormalised perturbation theory one can realise that every perturbative diagram has a *principle path* that connects the ingoing and outgoing mode with a chain of linear retarded propagators. Diagrams can be organised according to how many interactions (via bare vertices) are along this

---

[1]Strictly speaking, this is only possible if the correlation functions are analytic in wave vectors. The non-gradient dependence due to the operator (4.4) implies non-analyticity of the (inverse) propagator in the velocity-density component. The corresponding infrared divergence is associated with homogeneous mass density shifts and is usually treated by regularising gravitational interactions at large scales and related to the *Jeans swindle* [27, 142]. In the following, the tacit assumption is made that no other non-analyticities develop in the presence of a regulator.

path. Since for each bare vertex that is passed along the principal path a factor q is picked up in the large external wave number limit, the leading contribution is due to diagrams where all interactions are on that path.

As an example consider the contributions where one vertex of the diagram (5.5) is evaluated at one-loop. These consist of diagrams of the type

$$\mathrm{D}_1 = \quad \text{} \quad , \tag{5.7}$$

and

$$\mathrm{D}_2 = \quad \text{} \quad , \tag{5.8}$$

Similarly, evaluating the retarded propagator in diagram (5.5) at one-loop one obtains

$$\mathrm{D}_3 = \quad \text{} \quad . \tag{5.9}$$

The leading contribution of the diagrams is obtained by counting the vertices along the principal path such that one obtains

$$
\begin{aligned}
\mathrm{D}_1 &\sim q^3 \, g^{\mathrm{R}}_{ab}(\tau, \tau', \boldsymbol{q}) \, \delta_{du_i} \times (q\text{-ind.}) \,, \\
\mathrm{D}_{2,3} &\sim q^4 \, g^{\mathrm{R}}_{ab}(\tau, \tau', \boldsymbol{q}) \, \delta_{cu_i} \delta_{du_j} \times (q\text{-ind.}) \,.
\end{aligned}
\tag{5.10}
$$

This argument extends to any perturbative order and can be applied to all diagrams entering the flow equations (4.90) and (4.91). In turn only the velocity-velocity part of the regulator $\hat{\partial}_k P^{\mathrm{I}}_{k, u_j u_i}$ enters into the expression (5.4), at least to leading order.

Although the presented argument holds to all orders in perturbation theory, there is no rigorous justification why it should hold non-perturbatively. More specifically, in the presence of non-perturbative scales the line of argument presented here cannot be straight forwardly extended to full propagators and vertices.

Further, the presented argument no longer holds in the presence of higher-order velocity cumuants, e.g. velocity dispersion. Indeed, considering again the lowest order contribution (5.5) in the presence of velocity dispersion and taking into account the allowed vertices due to the non-linear terms in equation (4.2), one finds the leading contribution to the first diagram of the velocity-velocity inverse propagator flow to be

$$\text{} \quad \sim \quad q^2 \, g^{\mathrm{R}}_{\delta\sigma}(\tau, \tau', \boldsymbol{q}) \, \delta_{c\sigma} \delta_{d\sigma} \times (q\text{-ind.}) \,, \tag{5.11}$$

where tensorial structures are suppressed on the right-hand side. This contribution dominates in the limit $q \to \infty$ over the one given in equation (5.5) due to the scaling

$$g^{\mathrm{R}}_{\delta\sigma_{ij}}(\tau, \tau', \boldsymbol{q}) \sim q_i q_j \times (q\text{-ind.}) \,. \tag{5.12}$$

The justification that the vanishing wave vector is assigned to a velocity mode therefore relies on the following two assumptions:

- The emergence of non-perturbative scales does not invalidate the classification of leading contributions described before.

- Higher-order velocity cumulants are absent or at least subdominant.

Under these assumptions the limit (5.4) holds and the 1PI three-point vertices can be replaced using the Ward identity (4.102). This can be done for all diagrams entering the flow equations (4.90) and (4.91). More precisely, the three-point functions are replaced by

$$
\begin{aligned}
\widehat{\Gamma}^{(2,1)}_{k,u_i ba}(\tau'', \boldsymbol{0}; \tau', -\boldsymbol{q}; \tau, \boldsymbol{q}) &= -\mathrm{i}\, q_i \big[\theta(\tau'' - \tau') - \theta(\tau'' - \tau)\big] \\
&\qquad\qquad \times \widehat{\Gamma}^{(1,1)}_{k,ba}(\tau', -\boldsymbol{q}; \tau, \boldsymbol{q}) \,, \\
\widehat{\Gamma}^{(1,2)}_{k,u_i ba}(\tau'', \boldsymbol{0}; \tau', -\boldsymbol{q}; \tau, \boldsymbol{q}) &= -\mathrm{i}\, q_i \big[\theta(\tau'' - \tau') - \theta(\tau'' - \tau)\big] \\
&\qquad\qquad \times \widehat{\Gamma}^{(0,2)}_{k,ba}(\tau', -\boldsymbol{q}; \tau, \boldsymbol{q}) \,,
\end{aligned}
\tag{5.13}
$$

whereas the four-point functions are replaced using

$$
\begin{aligned}
\widehat{\Gamma}^{(3,1)}_{k,u_i u_j ba}(\tau''', \boldsymbol{0}; \tau'', \boldsymbol{0}; \tau', -\boldsymbol{q}; \tau, \boldsymbol{q}) &= -q_i q_j \big[\theta(\tau''' - \tau') - \theta(\tau''' - \tau)\big] \\
&\qquad \times \big[\theta(\tau'' - \tau') - \theta(\tau'' - \tau)\big] \\
&\qquad \times \widehat{\Gamma}^{(1,1)}_{k,ba}(\tau', -\boldsymbol{q}; \tau, \boldsymbol{q}) \,, \\
\widehat{\Gamma}^{(2,2)}_{k,u_i u_j ba}(\tau''', \boldsymbol{0}; \tau'', \boldsymbol{0}; \tau', -\boldsymbol{q}; \tau, \boldsymbol{q}) &= -q_i q_j \big[\theta(\tau''' - \tau') - \theta(\tau''' - \tau)\big] \\
&\qquad \times \big[\theta(\tau'' - \tau') - \theta(\tau'' - \tau)\big] \\
&\qquad \times \widehat{\Gamma}^{(0,2)}_{k,ba}(\tau', -\boldsymbol{q}; \tau, \boldsymbol{q}) \,.
\end{aligned}
\tag{5.14}
$$

Substituting the relations (5.13) and (5.14) into the inverse propagator flow (4.90) one obtains

$$
\begin{aligned}
\partial_k D^{\mathrm{R}}_{k,ab}(\tau, \tau', \boldsymbol{q}) = q^2 \int_{\bar{\tau}, \bar{\tau}'} D^{\mathrm{R}}_{k,ae}(\tau, \bar{\tau}, \boldsymbol{q})\, G^{\mathrm{R}}_{k,ef}(\bar{\tau}, \bar{\tau}', \boldsymbol{q})\, D^{\mathrm{R}}_{k,fb}(\bar{\tau}', \tau', \boldsymbol{q}) \\
\times \hat{\partial}_k I_k(\tau, \bar{\tau}; \bar{\tau}', \tau') \\
- \frac{q^2}{2}\, D^{\mathrm{R}}_{k,ab}(\tau, \tau', \boldsymbol{q})\, \hat{\partial}_k I_k(\tau, \tau'; \tau, \tau') \,,
\end{aligned}
\tag{5.15}
$$

and similarly for the statistical two-point function flow (4.91)

$$
\begin{aligned}
\partial_k H_{k,ab}(\tau,\tau',\boldsymbol{q}) = q^2 \int_{\bar{\tau},\bar{\tau}'} \Big[&D^{\mathrm{R}}_{k,ae}(\tau,\bar{\tau},\boldsymbol{q})\, P_{k,ef}(\bar{\tau},\bar{\tau}',\boldsymbol{q})\, D^{\mathrm{A}}_{k,fb}(\bar{\tau}',\tau',\boldsymbol{q}) \\
&- D^{\mathrm{R}}_{k,ae}(\tau,\bar{\tau},\boldsymbol{q})\, G^{\mathrm{R}}_{k,ef}(\bar{\tau},\bar{\tau}',\boldsymbol{q})\, H_{k,fb}(\bar{\tau}',\tau',\boldsymbol{q}) \\
&- H_{k,ae}(\tau,\bar{\tau},\boldsymbol{q})\, G^{\mathrm{A}}_{k,ef}(\bar{\tau},\bar{\tau}',\boldsymbol{q})\, D^{\mathrm{A}}_{k,fb}(\bar{\tau}',\tau',\boldsymbol{q}) \Big] \\
&\hspace{4cm}\times \hat{\partial}_k I_k(\tau,\bar{\tau};\tau',\bar{\tau}') \\
-\frac{q^2}{2}\, H_{k,ab}&(\tau,\tau',\boldsymbol{q})\, \hat{\partial}_k I_k(\tau,\tau';\tau,\tau') \\
+ \delta&(\tau-\tau_{\mathrm{in}})\,\delta(\tau'-\tau_{\mathrm{in}})\, \hat{\partial}_k P^{\mathrm{in}}_{k,ab}(\boldsymbol{q})\,,
\end{aligned}
\tag{5.16}
$$

where the function I_k is given by

$$
I_k(\tau,\tau';\bar{\tau},\bar{\tau}') = \frac{1}{3}\int_{\tau'}^{\tau}\mathrm{d}\tau''\int_{\bar{\tau}'}^{\bar{\tau}}\mathrm{d}\bar{\tau}''\int_{\boldsymbol{q}} P^{\mathrm{I}}_{k,u_i u_i}(\tau'',\bar{\tau}'',\boldsymbol{q})\,.
\tag{5.17}
$$

As a concrete example the first diagram of the inverse propagator flow (4.90) is computed and the other diagrams follow similarly. The first flow diagram of equation (4.90) is given by

$$
\begin{aligned}
\text{[diagram]} = -\mathrm{i}\,\delta(\boldsymbol{q}+\boldsymbol{q}') \int_{\substack{\bar{\tau},\bar{\tau}' \\ \tilde{\tau},\tilde{\tau}'}} \int_{\boldsymbol{l}} &\widehat{\Gamma}^{(2,1)}_{k,cea}(\tilde{\tau},\boldsymbol{l};\bar{\tau},-\boldsymbol{q}-\boldsymbol{l};\tau,\boldsymbol{q}) \\
&\times G^{\mathrm{R}}_{k,ef}(\bar{\tau},\bar{\tau}',\boldsymbol{q}+\boldsymbol{l}) \\
&\times \widehat{\Gamma}^{(2,1)}_{k,dbf}(\tilde{\tau}',-\boldsymbol{l};\tau',-\boldsymbol{q};\bar{\tau}',\boldsymbol{q}+\boldsymbol{l}) \\
&\hspace{2cm}\times \hat{\partial}_k P^{\mathrm{I}}_{k,dc}(\tilde{\tau}',\tilde{\tau},\boldsymbol{l}) \\
\sim -\mathrm{i}\,\delta(\boldsymbol{q}+\boldsymbol{q}') \int_{\substack{\bar{\tau},\bar{\tau}' \\ \tilde{\tau},\tilde{\tau}'}} &\widehat{\Gamma}^{(2,1)}_{k,u_j ea}(\tilde{\tau},\boldsymbol{0};\bar{\tau},-\boldsymbol{q};\tau,\boldsymbol{q})\, G^{\mathrm{R}}_{k,ef}(\bar{\tau},\bar{\tau}',\boldsymbol{q}) \\
&\times \widehat{\Gamma}^{(2,1)}_{k,u_i bf}(\tilde{\tau}',\boldsymbol{0};\tau',-\boldsymbol{q};\bar{\tau}',\boldsymbol{q}) \\
&\hspace{2cm}\times \hat{\partial}_k \int_{\boldsymbol{l}} P^{\mathrm{I}}_{k,u_i u_j}(\tilde{\tau}',\tilde{\tau},\boldsymbol{l}) \\
= -\mathrm{i}\,\delta(\boldsymbol{q}+\boldsymbol{q}') \int_{\bar{\tau},\bar{\tau}'} &D^{\mathrm{R}}_{k,ae}(\tau,\bar{\tau},\boldsymbol{q})\, G^{\mathrm{R}}_{k,ef}(\bar{\tau},\bar{\tau}',\boldsymbol{q})\, D^{\mathrm{R}}_{k,fb}(\bar{\tau}',\tau',\boldsymbol{q}) \\
&\times \frac{q^2}{3}\int_{\tilde{\tau},\tilde{\tau}'}\big[\theta(\tilde{\tau}-\bar{\tau})-\theta(\tilde{\tau}-\tau)\big] \\
&\hspace{1cm}\times \big[\theta(\tilde{\tau}'-\tau')-\theta(\tilde{\tau}'-\bar{\tau}')\big] \\
&\hspace{2cm}\times \hat{\partial}_k \int_{\boldsymbol{l}} P^{\mathrm{I}}_{k,u_i u_i}(\tilde{\tau}',\tilde{\tau},\boldsymbol{l}) \\
= -\mathrm{i}\,\delta(\boldsymbol{q}+\boldsymbol{q}')\, q^2 \int_{\bar{\tau},\bar{\tau}'} &D^{\mathrm{R}}_{k,ae}(\tau,\bar{\tau},\boldsymbol{q})\, G^{\mathrm{R}}_{k,ef}(\bar{\tau},\bar{\tau}',\boldsymbol{q}) \\
&\times D^{\mathrm{R}}_{k,fb}(\bar{\tau}',\tau',\boldsymbol{q})\, \hat{\partial}_k I_k(\tau,\bar{\tau};\bar{\tau}',\tau')
\end{aligned}
\tag{5.18}
$$

where the second equality holds in the limit $q \to \infty$ under the assumptions discussed. The third equality makes use of the Ward identity (5.13) and statistical isotropy implies

$$q_i q_j \int_{\boldsymbol{l}} P^{\mathrm{I}}_{k,u_i u_j}(\tau, \tau', \boldsymbol{l}) = \frac{q^2}{3} \int_{\boldsymbol{l}} P^{\mathrm{I}}_{k,u_i u_i}(\tau, \tau', \boldsymbol{l}) \,. \tag{5.19}$$

Finally, the last equality uses definition (5.17) to rewrite the expression.

The flow equations (5.15) and (5.16) are (formally) closed at the level of two-point functions, although involving connected and 1PI correlation functions. The flow of the propagator and power spectrum can be obtained from relation (4.34) and read

$$\partial_k G^{\mathrm{R}}_{k,ab}(\tau, \tau', \boldsymbol{q}) = - \int_{\bar{\tau}, \bar{\tau}'} G^{\mathrm{R}}_{k,a\bar{a}}(\tau, \bar{\tau}, \boldsymbol{q}) \, \partial_k D^{\mathrm{R}}_{k,\bar{a}\bar{b}}(\bar{\tau}, \bar{\tau}', \boldsymbol{q}) \, G^{\mathrm{R}}_{k,\bar{b}b}(\bar{\tau}', \tau', \boldsymbol{q}) \,, \tag{5.20}$$

and

$$\partial_k P_{k,ab}(\tau, \tau', \boldsymbol{q}) = \int_{\bar{\tau}, \bar{\tau}'} \partial_k \left[G^{\mathrm{R}}_{k,a\bar{a}}(\tau, \bar{\tau}, \boldsymbol{q}) \, H_{k,\bar{a}\bar{b}}(\bar{\tau}, \bar{\tau}', \boldsymbol{q}) \, G^{\mathrm{A}}_{k,\bar{b}b}(\bar{\tau}', \tau', \boldsymbol{q}) \right] \,. \tag{5.21}$$

Using the flow equations (5.15) and (5.16) one finally arrives at the rather simple equation for the retarded propagator

$$\partial_k G^{\mathrm{R}}_{k,ab}(\tau, \tau', \boldsymbol{q}) = -\tfrac{1}{2} \, q^2 \, \hat{\partial}_k I_k(\tau, \tau'; \tau, \tau') \, G^{\mathrm{R}}_{k,ab}(\tau, \tau', \boldsymbol{q}) \,, \tag{5.22}$$

and the power spectrum

$$\partial_k P_{k,ab}(\tau, \tau', \boldsymbol{q}) = -\tfrac{1}{2} \, q^2 \, \hat{\partial}_k I_k(\tau, \tau'; \tau, \tau') \, P_{k,ab}(\tau, \tau', \boldsymbol{q}) + \hat{\partial}_k P^{\mathrm{I}}_{k,ab}(\tau, \tau', \boldsymbol{q}) \,. \tag{5.23}$$

Note that the function I_k defined in equation (5.17) vanishes at equal times of either of the two time argument pairs due to the Heaviside unit step functions appearing in the identities (5.13) and (5.14) as well as being localised at the renormalisation group scale k due to the regulator. This implies in particular that the first term on the right-hand side of equation (5.23) vanishes for the equal-time power spectrum.

Although the equations (5.15) and (5.16) are formally closed, the function I_k involves knowledge of the propagator at $q = k$ which is the opposite limit to what was assumed in the derivation, at least in some regions of the renormalisation group flow trajectories.

While the function I_k is non-universal, the fact that the propagator and power spectrum have a Gaussian suppression in wave number q in the limit $q \to \infty$ is universal and a direct results of the possibility to close the flow equations at the level of two-point functions. As was remarked before, this holds as long as dark matter is described by the single-stream approximation in the absence of non-perturbative scales and other effects due to e.g. velocity dispersion are not present. In turn, any violation from this scaling has to be due to the emergence of non-perturbative scales or due to higher-order velocity cumulants and is regarded as an interesting possible signature for such non-perturbative effects.

5.2 Sweeping effect

A simple approximation that allows to solve the flow equations (5.22) and (5.23) analytically is given by evaluating the propagators in the expression $\hat{\partial}_k P_{k,ab}^{\mathrm{I}}$ at linear level so that $\hat{\partial}_k P_{k,ab}^{\mathrm{L}}$ is the regulator entering the flow equations. This is justified for a renormalisation group flow deep in the infrared, where gravitational dynamics is well described by linear theory. There, one obtains

$$I_k(\tau, \tau'; \tau, \tau') = \frac{[D_+(\tau) - D_+(\tau')]^2}{D_+(\tau_{\mathrm{in}})^2}\, \sigma_{\mathrm{v},k}^2\ , \tag{5.24}$$

for growing mode initial conditions,

$$u_i^{\mathrm{L}}(\tau, \boldsymbol{q}) = \frac{\mathrm{i}\, q_i}{q^2}\, \frac{\dot{D}_+(\tau)}{D_+(\tau)}\, \delta^{\mathrm{L}}(\tau, \boldsymbol{q})\ , \tag{5.25}$$

where D_+ is the standard linear growing mode of density fluctuations in the single-stream approximation, here normalised to unity at $a = 1$, corresponding to today. Further, $\sigma_{\mathrm{v},k}$ is the initial root mean square velocity,

$$\sigma_{\mathrm{v},k}^2 = \frac{1}{3}\, C_{k,u_i u_i}^{\mathrm{in}}(\boldsymbol{0}) \Big/ \frac{\dot{D}_+(\tau_{\mathrm{in}})^2}{D_+(\tau_{\mathrm{in}})^2} = \frac{1}{6\pi^2} \int_0^k \mathrm{d}q\, q^2\, P_{u_i u_i}^{\mathrm{in}}(\boldsymbol{q}) \Big/ \frac{\dot{D}_+(\tau_{\mathrm{in}})^2}{D_+(\tau_{\mathrm{in}})^2}\ , \tag{5.26}$$

up to a factor of $\dot{D}_+(\tau_{\mathrm{in}})^2/D_+(\tau_{\mathrm{in}})^2$. The flow equation for the propagator is then solved by

$$G_{k,ab}^{\mathrm{R}}(\tau, \tau', \boldsymbol{q}) = g_{ab}^{\mathrm{R}}(\tau, \tau', \boldsymbol{q})\, \mathrm{e}^{-\frac{1}{2} q^2 \sigma_{\mathrm{v},k}^2 [D_+(\tau) - D_+(\tau')]^2 / D_+(\tau_{\mathrm{in}})^2}\ , \tag{5.27}$$

and similar for the power spectrum,

$$P_{k,ab}(\tau, \tau', \boldsymbol{q}) = P_{k,ab}^{\mathrm{L}}(\tau, \tau', \boldsymbol{q})\, \mathrm{e}^{-\frac{1}{2} q^2 \sigma_{\mathrm{v},k}^2 [D_+(\tau) - D_+(\tau')]^2 / D_+(\tau_{\mathrm{in}})^2}\ . \tag{5.28}$$

In this setting the propagator and the unequal-time power spectrum feature a Gaussian suppression factor due to the *linear* root mean square velocity field.

In the following it is shown that a random background flow, associated to a velocity mean field, has the same effect on the linear response function and is related to the *sweeping effect* previously discussed in the context of fluid turbulence [143]. To this end consider the cumulant evolution equations (2.88) on a background flow $v_i(\tau)$. It is assumed that the background flow evolves proportional to some function $\dot{\mu}(\tau)$ so that $v_i(\tau) = \dot{\mu}(\tau)\, v_i$, where v_i is a zero-mean normal distributed multivariate random variable.[2] The linear response function is the Green's function of the linear equations of motion (4.2) which are modified in the presence of a background flow to

$$\partial_\tau \psi_a(\tau, \boldsymbol{x}) + \int_{\boldsymbol{x}'} \Omega_{ab}(\tau, \boldsymbol{x} - \boldsymbol{x}')\, \psi_b(\tau, \boldsymbol{x}') + v_i(\tau)\, \partial_i \psi_a(\tau, \boldsymbol{x}) = 0\ . \tag{5.29}$$

---

[2]For a velocity field decaying with the Hubble expansion one simply has $\dot{\mu}(\tau) \propto a(\tau)^{-1}$.

The corresponding linear response function is then given in Fourier space by

$$g_{ab}^{\mathrm{R}}(\tau, \tau', \boldsymbol{q}) \, \mathrm{e}^{-\mathrm{i}\boldsymbol{q}\cdot\boldsymbol{v}[\mu(\tau)-\mu(\tau')]} \ , \tag{5.30}$$

where $g_{ab}^{\mathrm{R}}(\tau, \tau', \boldsymbol{q})$ is the linear response in the absence of a background flow. The mean linear response function is then given by averaging over the distribution of v_i such that one obtains [143]

$$G_{ab}^{\mathrm{R}}(\tau, \tau', \boldsymbol{q}) = g_{ab}^{\mathrm{R}}(\tau, \tau', \boldsymbol{q}) \, \mathrm{e}^{-\frac{1}{2}q^2 v_{\mathrm{rms}}^2 [\mu(\tau)-\mu(\tau')]^2} \ , \tag{5.31}$$

where v_{rms} is the root mean square background velocity.

This analysis shows that the Gaussian suppression factor in the propagator (5.31) is not related to a true loss of memory due to relaxation processes but rather to the random advection of small-scale structures due to a large-scale flow also know as sweeping effect [28, 29, 144, 145].

One can now notice that the large wave number limit propagator (5.27) is of a similar form as the response function on a random background flow. In the infrared of the renormalisation group flow the suppression is due to the linear root mean square velocity, suggesting that it does not truly capture the effect of memory loss associated with relaxation towards equilibrium but rather describes the sweeping of small-scale structure due to an effective random large-scale advection. In contrast, the flow equations (5.22) and (5.23) are more general since the function I_k includes non-linear information beyond the sweeping effect.

The propagator (5.27) was first obtained in the framework of renormalised perturbation theory [19]. Interestingly enough, this form of the propagator is actually exact in the Zeldovich approximation [29], whereas for more realistic approximations, such as the adhesion model, the propagator is already much more complicated [144, 145].

6 Truncated Dyson–Schwinger equations

In this chapter the dynamics of dark matter in terms of a kinetic theory description beyond the single-stream approximation is investigated with the Dyson–Schwinger equation. While the extension of the kinetic theory description enables to go beyond the shell-crossing regime, the Dyson–Schwinger equation allows for a non-perturbative calculation of the correlation functions of the underlying field theory. Combining the extension of the kinetic theory description with the non-perturbative Dyson–Schwinger equation overcomes the main limitations of standard perturbation theory in the single-stream approximation and allows to probe small-scale physics.

In section 6.1 the field content which is used to describe dark matter is fixed and the employed truncations of the Dyson–Schwinger equation discussed. Subsequently, in sections 6.2 and 6.3 two truncations of the Dyson–Schwinger equation are studied in greater detail.

6.1 Field content and evolution equations

In the following, dark matter is described in the kinetic theory picture discussed in chapter 2. To this end, the cumulant expansion of the phase-space distribution function is *cum grano salis* truncated after the second order such that the relevant degrees of freedom are parametrised by the density contrast δ, the velocity vector u_i and the velocity dispersion tensor σ_{ij}. The latter two are decomposed into irreducible components according to equations (3.20) and (3.24) and only the scalar velocity dispersion modes are kept in the following. While it would in principle be interesting to also include the vector and tensor velocity dispersion modes, this enlarges the field content by another four degrees of freedom making numerical solutions even more time consuming than they already are.

The relevant field content is in this case given by

$$\psi_a = \left(\delta, \quad -\frac{\theta}{f\mathcal{H}}, \quad \frac{k^2\sigma}{(f\mathcal{H})^2}, \quad \frac{k^2\vartheta}{(f\mathcal{H})^2}, \quad \frac{\omega_i}{f\mathcal{H}} \right), \tag{6.1}$$

where prefactors of k and $f\mathcal{H}$ are chosen such that the fields are of the same dimension. The equations of motion (4.2) are most conveniently written with respect to the time evolution parameter $\eta := \ln(D_+)$ and take the form

$$\partial_\eta \psi_a(\eta, \boldsymbol{k}) + \Omega_{ab}(\eta)\, \psi_b(\eta, \boldsymbol{k}) + \int_{\boldsymbol{q}} \gamma_{abc}(\boldsymbol{q}, \boldsymbol{k} - \boldsymbol{q})\, \psi_b(\eta, \boldsymbol{q})\, \psi_c(\eta, \boldsymbol{k} - \boldsymbol{q}) = 0 \,. \tag{6.2}$$

The matrix specifying the linear part is given by

$$\Omega_{ab}(\eta) = \begin{pmatrix} 0 & -1 & 0 & 0 & 0 \\ -\frac{3}{2}\frac{\Omega_{\mathrm{m}}}{f^2} & \frac{3}{2}\frac{\Omega_{\mathrm{m}}}{f^2} - 1 & 1 & 1 & 0 \\ 0 & 0 & 3\frac{\Omega_{\mathrm{m}}}{f^2} - 2 & 0 & 0 \\ 0 & 0 & 0 & 3\frac{\Omega_{\mathrm{m}}}{f^2} - 2 & 0 \\ 0 & 0 & 0 & 0 & \frac{3}{2}\frac{\Omega_{\mathrm{m}}}{f^2} - 1 \end{pmatrix} , \qquad (6.3)$$

where the transverse projector of the component Ω_{55} has been amputated and the bare vertices γ_{abc} are listed in appendix C. The matrix Ω_{ab} is wave number independent and straight forwardly allows to work in the approximation $\Omega_{\mathrm{m}}/f^2 = 1$, where the linear equations of motion are time-translation invariant.

In contrast to the single-stream approximation the field content (6.1) features a non-vanishing mean field,

$$\langle \psi_a(\eta, \boldsymbol{k}) \rangle = \delta_{a3}\,\dirac\delta(\boldsymbol{k})\,\frac{k^2\bar\sigma(\eta)}{f(\eta)^2 \mathcal{H}(\eta)^2} =: \delta_{a3}\,\dirac\delta(\boldsymbol{k})\,k^2\tilde\sigma(\eta) , \qquad (6.4)$$

where the second equality defines the rescaled mean field $\tilde\sigma$ and it is remarked that due to the wave number factors appearing in the field content (6.1) an overall $k^2\dirac\delta(\boldsymbol{k})$ needs to be removed when dealing with the mean field.

In the following, the dynamics of the connected one- and two-point correlation functions is studied. The evolution of the mean field is determined by the effective equation of motion

$$\partial_\eta\tilde\sigma(\eta) + \left(3\frac{\Omega_{\mathrm{m}}}{f^2} - 2\right)\tilde\sigma(\eta) = \delta(\eta - \eta_{\mathrm{in}})\,\tilde\sigma^{\mathrm{in}} + Q(\eta) , \qquad (6.5)$$

where the source term is simply denoted as Q. The propagator equation (4.36) takes the form

$$\begin{aligned} \left[\partial_\eta\delta_{ab} + \Omega_{ab}(\eta) - \Sigma^{\mathrm{H}}_{ab}(\eta, k)\right] G^{\mathrm{R}}_{bc}(\eta, \eta', k) & \\ - \int_{\eta'}^{\eta}\mathrm{d}\xi\,\Sigma^{\mathrm{F}}_{ab}(\eta, \xi, k)\,G^{\mathrm{R}}_{bc}(\xi, \eta', k) &= \delta_{ac}\delta(\eta - \eta') , \end{aligned} \qquad (6.6)$$

while the power spectrum equation (4.37) reads

$$\begin{aligned} \left[\partial_\eta\delta_{a\bar a} + \Omega_{a\bar a}(\eta) - \Sigma^{\mathrm{H}}_{ab}(\eta, k)\right] P_{\bar a b}(\eta, \eta', k) - \int_{\eta_{\mathrm{in}}}^{\eta}\mathrm{d}\xi\,\Sigma^{\mathrm{F}}_{a\bar a}(\eta, \xi, k)\,P_{\bar a b}(\xi, \eta', k) & \\ = \delta(\eta - \eta')\,G^{\mathrm{R}}_{b\bar b}(\eta', \eta_{\mathrm{in}}, k)\,P^{\mathrm{in}}_{a\bar b}(k) + \int_{\eta_{\mathrm{in}}}^{\eta'}\mathrm{d}\xi\,G^{\mathrm{R}}_{b\bar b}(\eta', \xi, k)\,\Pi_{a\bar b}(\eta, \xi, k) & , \end{aligned} \qquad (6.7)$$

where the advanced propagator was eliminated in favour of the retarded one using relation (4.22).

The evolution equations (6.5), (6.6) and (6.7) are exact up to here and have only been rewritten in terms of a source term and the self-energies. These can be

determined by the Dyson–Schwinger equation as discussed in section 4.4 of chapter 4 and are given by equations (4.74), (4.75) and (4.76). Since the latter two depend on the 1PI three-point function, one needs to find an appropriate approximation to close the Dyson–Schwinger hierarchy. This is achieved here by keeping the full structure of the one- and two-point functions and setting the 1PI three-point function to its bare form.

The source term and Hartree self-energy stay exact in this truncation,

$$\mathrm{i}\,Q = \tfrac{1}{2}\ \text{}\quad,\qquad \mathrm{i}\,\Sigma^{\mathrm{H}}_{ab} = \ \text{}\quad,\qquad\qquad (6.8)$$

while the Fock self-energies reduce to

$$\mathrm{i}\,\Sigma^{\mathrm{F}}_{ab} = -\tfrac{1}{2}\ \text{}\ -\tfrac{1}{2}\ \text{}\quad,\qquad \Pi_{ab} = -\tfrac{1}{2}\ \text{}\quad.\qquad (6.9)$$

In quantum field theories a similar truncation is known as *Hartree–Fock approximation* [146–148] or *self-consistent one-loop* since the full two-point correlation functions enter in the loops of the self-energies.

More explicitly, the source is given by

$$Q(\eta) = \frac{1}{6\pi^2} \int_0^\infty \mathrm{d}q\, \left[2P_{42}(\eta,\eta,q) - P_{32}(\eta,\eta,q) \right] ,\qquad (6.10)$$

and shows that the velocity dispersion mean field is sourced by the back-reaction of velocity-velocity dispersion cross-correlations.[1] As long as $2P_{42}(\eta,\eta,q)$ is larger than $P_{32}(\eta,\eta,q)$ the source term is positive and enhances the velocity dispersion mean field. Since there is *a priori* no reason why isotropic velocity dispersion fluctuations should be much larger than anisotropic fluctuations, one expects the mean field to grow in time.

The Hartree self-energy is given by

$$\Sigma^{\mathrm{H}}_{ab}(\eta,k) = \begin{pmatrix} 0 & 0 & 0 & 0 & 0 \\ -k^2\tilde{\sigma} & 0 & 0 & 0 & 0 \\ 0 & \tfrac{2}{3}k^2\tilde{\sigma} & 0 & 0 & 0 \\ 0 & \tfrac{4}{3}k^2\tilde{\sigma} & 0 & 0 & 0 \\ 0 & 0 & 0 & 0 & 0 \end{pmatrix} ,\qquad (6.11)$$

and describes the influence of the mean field on the evolution of fluctuations. The effect of the source term (6.10) and Hartree self-energy (6.11) is investigated in section 6.2 in order to understand how these interplay.

---

[1]In principle also the cross-spectrum of the velocity and velocity dispersion vectorial modes enters into the source term (6.10). This contribution is absent since the latter is neglected in the here employed approximation.

Finally, the Fock self-energies are given by

$$\Sigma_{ab}^{\mathrm{F}}(\eta,\eta',k) = 4\int_{\boldsymbol{q}} \gamma_{ace}(\boldsymbol{q},\boldsymbol{k}-\boldsymbol{l})\, G_{ef}^{\mathrm{R}}(\eta,\eta',|\boldsymbol{k}-\boldsymbol{q}|)\, \gamma_{fdb}(-\boldsymbol{q},\boldsymbol{k})\, P_{cd}(\eta,\eta',q)\;, \quad (6.12)$$

and

$$\begin{aligned} \Pi_{ab}(\eta,\eta',k) = 2\int_{\boldsymbol{q}} \gamma_{ace}(\boldsymbol{q},\boldsymbol{k}-\boldsymbol{q})\, P_{ef}(\eta,\eta',|\boldsymbol{k}-\boldsymbol{q}|)\, \gamma_{bfd}(-\boldsymbol{k}+\boldsymbol{q},-\boldsymbol{q}) \\ \times\, P_{cd}(\eta,\eta',q)\;, \end{aligned} \quad (6.13)$$

and describe the non-local effects of correlations on the evolution of fluctuations.

Since the equations (6.5), (6.6) and (6.7) are in general coupled, they need to be solved simultaneously. From a technical point of view the evolution equations ban be classified as a system of non-linear Volterra–Fredholm integro-differential equations of second kind in time and non-linear Fredholm integral equations of second kind in wave number. To solve these numerically, the Runge–Kutta–Cash–Karp method [149–151] adapted to Volterra integro-differential equations [152] is employed for the time evolution while a finite element method using B-splines of order one as basis functions is used for the wave number interpolation. The details of the implementation are given in appendix D.

6.2 Hartree approximation

As a first approximation the Fock self-energies (6.12) and (6.13) are neglected to understand the interplay between the mean field and the fluctuations. In this setting the mean field is still sourced by the correlation of fluctuations which in turn evolve in the presence of the mean field. The propagator equation (6.6) then simplifies to

$$\left[\partial_\eta \delta_{ab} + \Omega_{ab}(\eta) - \Sigma_{ab}^{\mathrm{H}}(\eta,k)\right] G_{bc}^{\mathrm{R}}(\eta,\eta',k) = \delta_{ac}\delta(\eta-\eta')\;, \quad (6.14)$$

and the power spectrum equation (6.7) is solved by

$$P_{ab}(\eta,\eta',k) = G_{a\bar{a}}^{\mathrm{R}}(\eta,\eta_{\mathrm{in}},k)\, G_{b\bar{b}}^{\mathrm{R}}(\eta',\eta_{\mathrm{in}},k)\, P_{\bar{a}\bar{b}}^{\mathrm{in}}(k)\;, \quad (6.15)$$

due to the absence of the statistical self-energy.

6.2.1 Growth factors and free-streaming scale

To simplify the following analysis the approximation $\Omega_{\mathrm{m}}/f^2 = 1$ is employed, effectively mapping the ΛCDM cosmology onto an Einstein–de Sitter cosmology. In this case the linear equations of motion are time-translation invariant and the linear propagator can be calculated using Laplace transforms.[2] Explicitly, the linear

---

[2]A thorough discussion of the Laplace transform is given in chapter 7.

retarded propagator reads

$$g_{ab}^{\mathrm{R}}(\eta - \eta') = \Big[A_{ab}\, \mathrm{e}^{\eta - \eta'} + B_{ab}\, \mathrm{e}^{-\frac{3}{2}(\eta - \eta')} + C_{ab}\, \mathrm{e}^{-(\eta - \eta')}$$
$$+ D_{ab}\, \mathrm{e}^{-\frac{1}{2}(\eta - \eta')} \Big]\, \theta(\eta - \eta')\,, \tag{6.16}$$

where the matrices characterising the different independent solutions are given by

$$A = \frac{1}{5} \begin{pmatrix} 3 & 2 & -1 & -1 & 0 \\ 3 & 2 & -1 & -1 & 0 \\ 0 & 0 & 0 & 0 & 0 \\ 0 & 0 & 0 & 0 & 0 \\ 0 & 0 & 0 & 0 & 0 \end{pmatrix}\,, \quad B = \frac{1}{5} \begin{pmatrix} 2 & -2 & -4 & -4 & 0 \\ -3 & 3 & 6 & 6 & 0 \\ 0 & 0 & 0 & 0 & 0 \\ 0 & 0 & 0 & 0 & 0 \\ 0 & 0 & 0 & 0 & 0 \end{pmatrix}\,, \tag{6.17}$$

and

$$C = \begin{pmatrix} 0 & 0 & 1 & 1 & 0 \\ 0 & 0 & -1 & -1 & 0 \\ 0 & 0 & 1 & 0 & 0 \\ 0 & 0 & 0 & 1 & 0 \\ 0 & 0 & 0 & 0 & 0 \end{pmatrix}\,, \quad D = \begin{pmatrix} 0 & 0 & 0 & 0 & 0 \\ 0 & 0 & 0 & 0 & 0 \\ 0 & 0 & 0 & 0 & 0 \\ 0 & 0 & 0 & 0 & 0 \\ 0 & 0 & 0 & 0 & 1 \end{pmatrix}\,. \tag{6.18}$$

The eigenvalues of the matrix $-\Omega_{ab}$ characterise the growth properties of the independent solutions of the linear propagator and are referred to as *growth factors*. The first two terms of the linear propagator (6.16) correspond to the growing and decaying modes of the single-stream approximation (3.37), whereas the third and fourth term correspond to decaying modes associated with the velocity dispersion and vorticity degrees of freedom, respectively.

The propagator equation (6.14) is more general in the sense that it describes the mean linear response in the presence of a mean field and is no longer time-translation invariant. Nonetheless, the eigenvalues and -vectors of the matrix $-\Omega_{ab} + \Sigma_{ab}^{\mathrm{H}}$ determine the (time-dependent) growth properties of the corresponding solutions. The growth factors are then the roots of the characteristic polynomial

$$\chi(s) = \Big[s^3 + \tfrac{3}{2}\, s^2 + (3k^2\tilde{\sigma} - 1)s + k^2\tilde{\sigma} - \tfrac{3}{2} \Big](s + 1)(s + \tfrac{1}{2})\,, \tag{6.19}$$

which only depend on the dimensionless combination $k^2\tilde{\sigma}$. In the limit $k^2\tilde{\sigma} \to 0$ these approach the growth factors of the linear propagator (6.16).

The standard growing and decaying modes of the single-stream approximation correspond to the roots

$$s_{\mathrm{g}} = 1 + \mathcal{O}(k^2\tilde{\sigma})\,, \qquad s_{\mathrm{d}} = -\frac{3}{2} + \mathcal{O}(k^2\tilde{\sigma})\,, \tag{6.20}$$

while the decaying modes associated with the velocity dispersion degrees of freedom are characterised by

$$s_{\mathrm{d}}^* = -1 + \mathcal{O}(k^2\tilde{\sigma})\,, \qquad s_{\mathrm{d}}^{**} = -1\,, \tag{6.21}$$
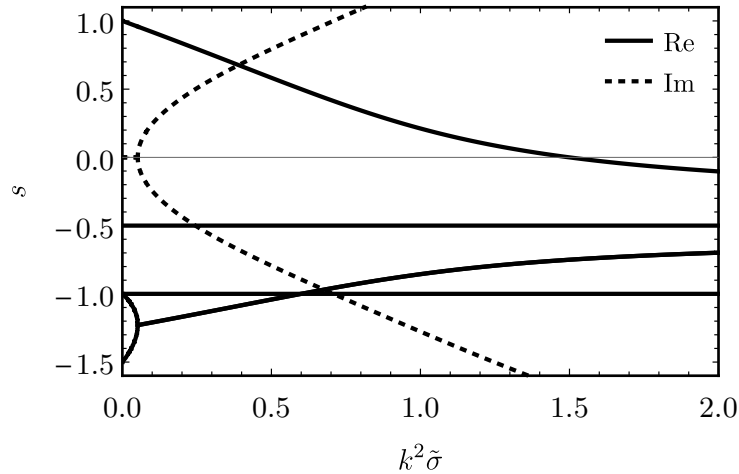
Figure 6.1: Roots of the characteristic polynomial (6.19) as a function of $k^2\tilde{\sigma}$. The real parts (solid curves) correspond to growing or decaying contributions for positive or negative values, respectively, while the imaginary parts (dotted curves) are responsible for oscillatory behaviour of the corresponding solutions.

and become degenerate in the limit $k^2\tilde{\sigma} \to 0$. Finally, the vectorial growth factor characterising the linear decay of the vorticity field is given by $s_{\mathrm{v}} = -1/2$.

While the growth factors s_{d}^{**} and s_{v} are constant, the other three are determined by the roots of the cubic polynomial in the square brackets of equation (6.19). From the discriminant criterion one finds that the roots are all real for $k^2\tilde{\sigma} \lesssim 0.051$ while for larger values two roots are complex conjugate. The real and imaginary parts of the growth factors are displayed in figure 6.1 as a function of $k^2\tilde{\sigma}$.

The complex conjugate roots are identified as being the decaying mode growth factors s_{d} and s_{d}^* which have a negative real part for all $k^2\tilde{\sigma}$ and in the limit $k^2\tilde{\sigma} \to \infty$ approach $\mathrm{Re}(s_{\mathrm{d}}) \to -7/12$ while the imaginary part is diverging. The real root is the growing mode growth factor s_{g} which features a zero-crossing at $k^2\tilde{\sigma} = 3/2$ and stays negative for larger values while approaching $s_{\mathrm{g}} \to -1/3$ in the limit $k^2\tilde{\sigma} \to \infty$.

The zero-crossing of s_{g} is related to the *free-streaming wave number* [12]

$$k_{\mathrm{fs}}(\eta) := \sqrt{\frac{3}{2\,\tilde{\sigma}(\eta)}} \quad , \tag{6.22}$$

above which all growth factors are negative. The free-streaming wave number sets the length scale below which the growth of structure is damped or even completely stalled due to the free-streaming of dark matter particles. From a formal point of view the mechanism is very similar to the Jeans instability [153] that describes the gravitational collapse of a gas cloud. In this case the thermal pressure is responsible

for the suppression of small-scale structures and the same formula (6.22) applies for the Jeans wave number, where the velocity dispersion mean field is replaced by the speed of sound squared.

To fully characterise the growth properties of the solutions, one also needs to study the eigenvectors of the matrix $-\Omega_{ab} + \Sigma_{ab}^{\mathrm{H}}$. The only one relevant in the following is the growing mode eigenvector which is given by

$$w_{\mathrm{g}}(k^2\tilde{\sigma}) = (1\,,1\,,0\,,0\,,0) + \mathcal{O}(k^2\tilde{\sigma})\,, \tag{6.23}$$

and implies the standard growing mode relation $\delta^{\mathrm{L}} = -\theta^{\mathrm{L}}/(f\mathcal{H})$ for the single-stream approximation. In what follows, it is assumed that the fluctuations deep within the matter dominated era of the Universe are sufficiently well described by the growing mode of the single-stream approximation. With this assumption the initial power spectrum is chosen to be

$$P_{ab}^{\mathrm{in}}(k) = w_{\mathrm{g},a}(0)\,w_{\mathrm{g},b}(0)\,P_{\delta\delta}^{\mathrm{in}}(k)\,, \tag{6.24}$$

implying the absence of initial velocity dispersion and vorticity fluctuations.

While the initial power spectrum (6.24) corresponds to cold initial conditions, one could also study an initial power spectrum build out of the full scale-dependent eigenvector $w_{\mathrm{g},b}(k^2\tilde{\sigma}^{\mathrm{in}})$ by specifying an initial velocity dispersion mean field $\tilde{\sigma}^{\mathrm{in}}$. This would introduce a non-trivial suppression in the ultraviolet of the initial power spectrum as is typical for warm dark matter models. In the following investigations it is chosen to dynamically generate the suppression associated with velocity dispersion degrees of freedom starting from cold initial conditions for the fluctuations together with a non-vanishing mean field $\tilde{\sigma}^{\mathrm{in}}$.

To study the response of fluctuations, it is convenient to define the reduced propagator

$$G_a^{\mathrm{R}}(\eta, k) := G_{ab}^{\mathrm{R}}(\eta, \eta_{\mathrm{in}}, k)\,w_{\mathrm{g},a}(0)\,, \tag{6.25}$$

quantifying the mean linear response of initial conditions that are proportional to $w_{\mathrm{g},a}(0)$. Since only the density contrast and velocity-divergence fields are initialised, the velocity dispersion response is dynamically generated. The vectorial mode is absent at all times since it cannot be sourced in the Hartree approximation.

6.2.2 Linear mean field

Before turning to the full Hartree approximation it is useful to study an approximation that can be solved with analytical methods. To this end, the source term Q is neglected such that the mean field evolves linearly and decays due to the Hubble expansion,

$$\tilde{\sigma}(\eta) = \tilde{\sigma}^{\mathrm{in}}\,\mathrm{e}^{-(\eta-\eta_{\mathrm{in}})}\,. \tag{6.26}$$

The propagator equation (6.14) can then be reduced to a third-order differential equation for the reduced density contrast propagator,

$$\partial_\eta^3 G_1^{\mathrm{R}}(\eta, k) + \tfrac{3}{2}\,\partial_\eta^2 G_1^{\mathrm{R}}(\eta, k) + [3k^2\tilde{\sigma}(\eta) - 1]\partial_\eta G_1^{\mathrm{R}}(\eta, k) - \tfrac{3}{2}\,G_1^{\mathrm{R}}(\eta, k) = 0\,. \tag{6.27}$$
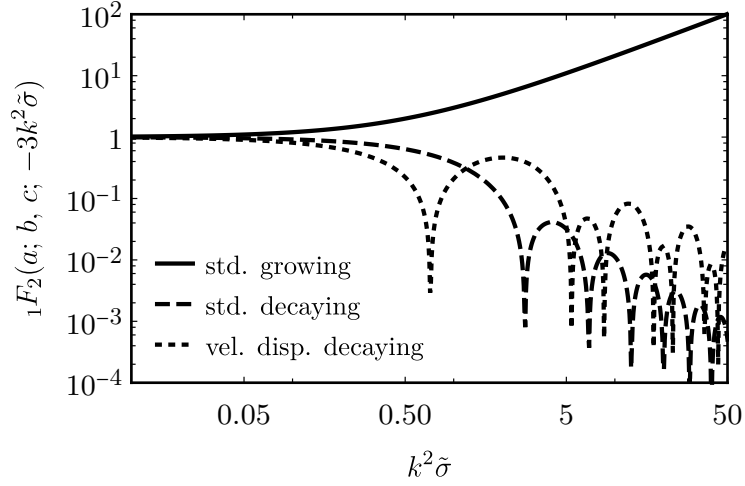
Figure 6.2: Hypergeometric functions appearing in the solutions (6.28) as a function of $k^2\tilde{\sigma}$. The growing mode (solid curve) is enhanced at non-vanishing $k^2\tilde{\sigma}$, whereas the decaying modes (dashed and dotted curves) are suppressed and oscillate with increasing frequency and decaying amplitude. The latter behaviour can be directly attributed to the corresponding growth factors displayed in figure 6.1.

The general solution to this equation is build out of the three independent solutions

$$
\begin{aligned}
F_{\mathrm{g}}(\eta, k) &= \mathrm{e}^{\eta} \, {}_1F_2\!\left(-1; -1, -\tfrac{3}{2}; -3k^2\tilde{\sigma}\right), \\
F_{\mathrm{d}}(\eta, k) &= \mathrm{e}^{-\frac{3}{2}\eta} \, {}_1F_2\!\left(\tfrac{3}{2}; \tfrac{3}{2}, \tfrac{7}{2}; -3k^2\tilde{\sigma}\right), \\
F_{\mathrm{d}}^{*}(\eta, k) &= \mathrm{e}^{-\eta} \, {}_1F_2\!\left(1; \tfrac{1}{2}, 3; -3k^2\tilde{\sigma}\right),
\end{aligned}
\tag{6.28}
$$

where ${}_1F_2$ are generalised hypergeometric functions that are displayed in figure 6.2. The two solutions F_{g} and F_{d} are related to the growing and decaying modes with growth factors (6.20) while the solution F_{d}^{*} is the decaying mode associated with the growth factors (6.21). In the limit $k^2\tilde{\sigma} \to 0$ the hypergeometric functions approach unity and one obtains the solutions related to the first three terms of the linear propagator (6.16). Notice, that going to larger $\tilde{\sigma}$ at constant k^2 implies going backwards in time in this approximation since the mean field (6.26) is decaying in time.

The growing mode is enhanced at non-vanishing $k^2\tilde{\sigma}$, whereas the decaying modes are damped due to oscillations of increasing frequency and decaying amplitude. The suppression of the decaying modes can be traced back to the increasing imaginary part and decreasing real part of the growth factors s_{d} and s_{d}^{*} displayed in figure 6.1. On the other hand the enhancement of the growing mode cannot be explained solely by the growth factor s_{g}, but depends on information encoded in the corresponding eigenvector as well. Nonetheless, the growing mode does not feature any oscillations which is due to the fact that the growth factor s_{g} is always real.

6.2.3 Sourced mean field

Restoring the source term Q and the dependence on Ω_{m}/f^2, qualitatively does not change the influence of the mean field on the fluctuating fields. What does change is that the back-reaction of fluctuations now sources the mean field and as such they are coupled. Since the results from the last section suggest that all fluctuation power spectra are suppressed at wave numbers larger than k_{fs} in the presence of a mean field, one expects the dominant contributions to the source term (6.10) to be from wave numbers below the free-streaming wave number.

Since the mean field and the fluctuations are coupled in the Hartree approximation, they need to be solved with numerical methods. The wave number interpolation is done over finite elements which naturally introduce an infrared and ultraviolet cut-off. The solutions are computed with $N_k = 500$ interpolation points, an infrared cut-off $k_{\mathrm{min}} = 10^{-5}$ h/Mpc and an ultraviolet cut-off corresponding to the initial free-streaming wave number of the dark matter model. It has been checked that the results do not vary to much when increasing the ultraviolet cut-off confirming the conjecture that the dominant contributions to the source term Q are from wave numbers smaller than k_{fs}.

For a numerical solution the initial power spectrum (6.24) and an initial mean field $\tilde{\sigma}^{\mathrm{in}}$ need to be supplied. The initial density contrast power spectrum is generated deep within the matter dominated era of the Universe at redshift $z_{\mathrm{in}} = 99$ and on scales 10^{-5} $h/\mathrm{Mpc} \lesssim k \lesssim 20$ h/Mpc for a ΛCDM cosmology with parameters from Planck 2015 [161] using the CLASS code [157] and extrapolated into the ultraviolet using the fitting formula $\alpha \log(\beta k)^2 k^{n_{\mathrm{s}}-4}$ with parameters α and β.

Typical values for the velocity dispersion mean field of non-relativistic dark matter that decouples thermally in the early Universe are roughly of the order of $\bar{\sigma}^{\mathrm{eq}} \sim 10^5$ $\mathrm{km}^2/\mathrm{s}^2$ for sterile neutrinos with a mass of 1 keV and $\bar{\sigma}^{\mathrm{eq}} \sim 10^{-7}$ $\mathrm{km}^2/\mathrm{s}^2$ for weakly interacting massive particles with a mass of 100 GeV at radiation-matter equality [154]. These values can be extrapolated to $z_{\mathrm{in}} = 99$ using the linear decay due to the Hubble expansion, at least as long as the source term can be neglected. Since the evolution is throughout the matter dominated era of the Universe, one can safely assume an Einstein–de Sitter cosmology such that $\bar{\sigma} \propto a^{-2}$. Computing the radiation-matter equality using the cosmic microwave background temperature $T_{\mathrm{CMB}} \approx 2.73$ K [158] one obtains the values $\bar{\sigma}^{\mathrm{in}} \sim 10^2$ $\mathrm{km}^2/\mathrm{s}^2$ and $\bar{\sigma}^{\mathrm{in}} \sim 10^{-10}$ $\mathrm{km}^2/\mathrm{s}^2$ for sterile neutrinos and weakly interacting massive particles, respectively.

To cover different models, numerical solutions of the evolution equations are computed for various initial values of the velocity dispersion mean field ranging from $\bar{\sigma}^{\mathrm{in}} = 10^{-10}$ $\mathrm{km}^2/\mathrm{s}^2$ to $\bar{\sigma}^{\mathrm{in}} = 10^5$ $\mathrm{km}^2/\mathrm{s}^2$. Four of these numerical solutions for the velocity dispersion mean field are shown in figure 6.3.

For all initial conditions studied the mean fields follow the linear decay due to the Hubble expansion initially, justifying the extrapolation from radiation-matter equality up to redshift $z_{\mathrm{in}} = 99$. In the subsequent evolution the source term (6.10) grows to the point where it leads to a turnover from decay to growth of the mean
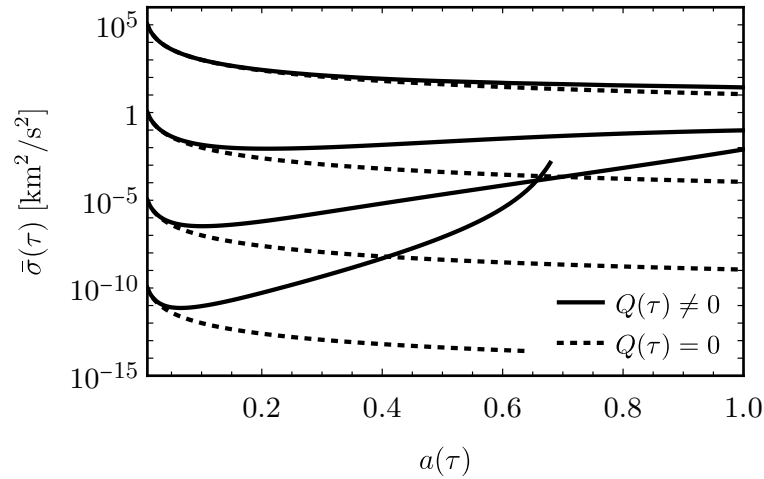
Figure 6.3: Time evolution of the velocity dispersion mean field as a function of the scale factor. Solutions which are sourced by correlations (solid curves) grow in time compared to those decaying linearly (dotted curves) due to the Hubble expansion. Smaller initial values correspond to larger free-streaming wave numbers and lead to a stronger late-time growth.

field. The time of this turnover depends on the warmness of the dark matter model and happens earlier for colder and later for warmer models. This is attributed to the free-streaming wave number which is much larger for the colder models and in turn allows correlations from smaller scales to contribute to Q. This is most notable for the coldest candidate investigated here which undergoes a phase of extreme growth for $z \lesssim 0.5$ to the point where it seems that the back-reaction of fluctuations blows up the mean field [7, 8].

For a complete picture, the power spectra (6.15) are needed which in the Hartree approximation are directly related to the reduced propagators (6.25). Numerical solutions of the latter are shown in figure 6.4 at redshift $z = 0$ and for the initial conditions $\bar{\sigma}^{\text{in}} = 1 \text{ km}^2/\text{s}^2$ and $\bar{\sigma}^{\text{in}} = 10^{-5} \text{ km}^2/\text{s}^2$. It is emphasised that the abscissas do not coincide for the two dark matter models since these start from different initial mean fields.

The reduced density and velocity-divergence propagators are in the growing mode of the single-stream approximation for small $k^2 \tilde{\sigma}^{\text{in}}$ while the reduced velocity dispersion propagator has a near to power law scaling in $k^2 \tilde{\sigma}^{\text{in}}$. For larger $k^2 \tilde{\sigma}^{\text{in}}$ the reduced propagators exhibit oscillations with a decaying amplitude for the density and velocity-divergence and a near to constant amplitude for the velocity dispersion. These appear at scales that are related to the (time-dependent) free-streaming wave number which in turn is set by the mean field. The colder dark matter model has a ratio of $\tilde{\sigma}/\tilde{\sigma}^{\text{in}} \approx 9.0 \cdot 10^5$ compared to the warmer model with $\tilde{\sigma}/\tilde{\sigma}^{\text{in}} \approx 11$ at redshift
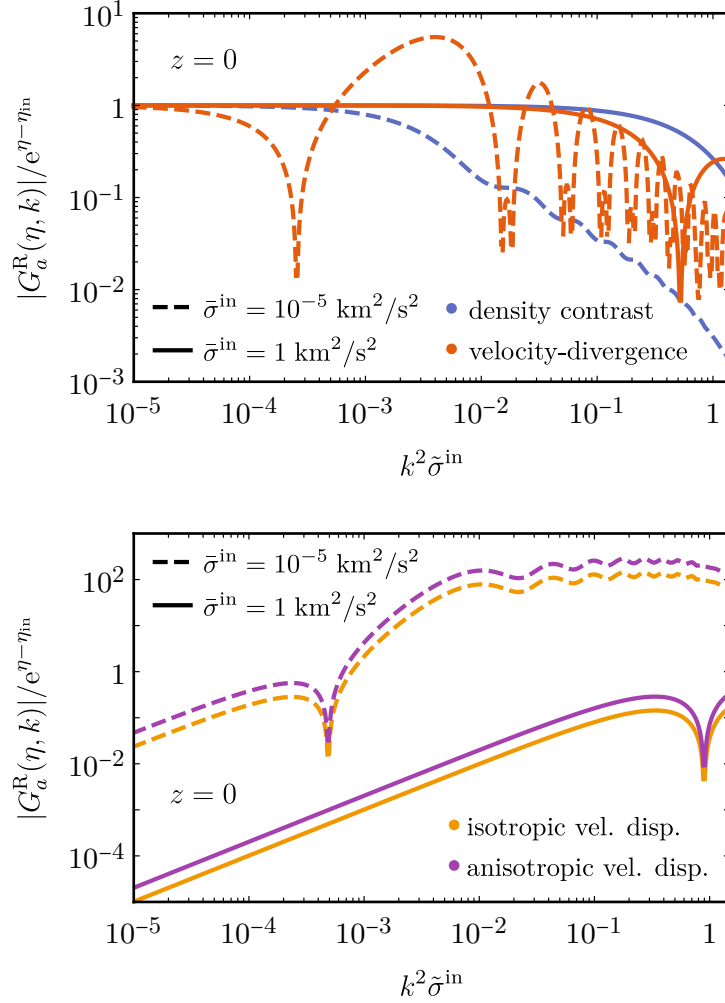
Figure 6.4: The reduced density contrast (blue curves), velocity-divergence (red curves) and the isotropic (yellow curves) and anisotropic (violet curves) velocity dispersion propagators normalised to the standard growing mode as a function of $k^2\tilde{\sigma}^{\mathrm{in}}$. They are shown for the two initial velocity dispersion mean fields 1 km^2/s^2 (solid curves) and 10^{-5} km^2/s^2 (dashed curves). The damping scale responsible for the oscillations is set by the corresponding mean field shown in figure 6.3 and is at much smaller $k^2\tilde{\sigma}^{\mathrm{in}}$ for the colder dark matter model due to its stronger growth in time.

$z = 0$.[3] Correspondingly, the scale of oscillatory behaviour is at much smaller $k^2 \tilde{\sigma}^{\mathrm{in}}$ for the colder dark matter model.

To conclude this section the most important insights from the Hartree approximation are summarised as follows:

- The back-reaction of velocity-velocity dispersion cross-correlations leads to an enhancement the velocity dispersion mean field.

- Fluctuations evolving in the presence of the velocity dispersion mean field are damped on scales smaller than the free-streaming length.

6.3 Hartree–Fock approximation

Having studied the Hartree approximation, one can now reinstall the Fock self-energies (6.12) and (6.13) to solve for the full one-loop self-consistent Hartree–Fock approximation. Since in this case the non-local effect of correlations is included, the full system of equations (6.5), (6.6) and (6.7) needs to be solved simultaneously.

6.3.1 Large external wave number limit

Before turning to the full numerical solutions, it is useful to study a limit in which at least some analytical insight can be obtained. In the limit of large external wave numbers the propagator equation can be much simplified and solved in an approximation without the mean field. This can be seen as a complementary investigation to chapter 5, where the same limit was studied with the functional renormalisation group.

The inclusion of the retarded Fock self-energy Σ^{F}_{ab} introduces a new scale dependence in the propagator due to the non-linear coupling of modes. As long as the velocity dispersion degrees of freedom are comparably small, one expects the dominant non-linear contribution to be due to the sweeping effect studied in chapter 5. To isolate this contribution and investigate how it appears in the Hartree–Fock approximation, the large external wave number limit is studied in the absence of velocity dispersion degrees of freedom.

In the limit $k \to \infty$ the leading-order contribution to the retarded Fock self-energy (6.12) is calculated to be

$$\Sigma^{\mathrm{F}}_{ab}(\eta, \eta', k) \sim -k^2 J(\eta, \eta')^2 \, G^{\mathrm{R}}_{ab}(\eta, \eta', k) \;, \tag{6.29}$$

where

$$J(\eta, \eta')^2 := \frac{1}{6\pi^2} \int_0^\infty \mathrm{d}q \left[P_{22}(\eta, \eta', q) + 2 P_{55}(\eta, \eta', q) \right] . \tag{6.30}$$

Notice that in the equal-time limit $J(\eta, \eta)^2$ is equal to the root mean square velocity $C_{u_i u_i}(\eta, \eta, 0)/3$ up to a factor of $(f\mathcal{H})^2$. Since $J(\eta, \eta')$ depends on the full velocity

---

[3]Notice that the physical velocity dispersion mean field $\bar{\sigma}$ is displayed in figure 6.3 while the free-streaming wave number is set by the redefined mean field $\tilde{\sigma} = \bar{\sigma}/(f\mathcal{H})^2$.

power spectrum, the general solution involves solving the power spectrum equation (6.7). To avoid this complication, the full velocity power spectrum is approximated by the linear one. In this case one obtains

$$J(\eta, \eta')^2 = e^{\eta - \eta_{\text{in}}} \, e^{\eta' - \eta_{\text{in}}} \, \sigma_v^2 \, , \tag{6.31}$$

where

$$\sigma_v^2 := \frac{1}{6\pi^2} \int_0^\infty \mathrm{d}q \, P_{22}^{\text{in}}(q) \, , \tag{6.32}$$

is often interpreted as a one-dimensional velocity dispersion in the sense of a mean square velocity. The propagator equation (6.6) then reduces to

$$
\left[\partial_\eta \delta_{ab} + \Omega_{ab}\right] G_{bc}^{\text{R}}(\eta, \eta', k) + (k\sigma_v)^2 \int_{\eta'}^\eta \mathrm{d}\xi \, e^{\eta + \xi - 2\eta_{\text{in}}} \, G_{ab}^{\text{R}}(\eta, \xi, k) \, G_{bc}^{\text{R}}(\xi, \eta', k)
$$
$$
= \delta_{ac} \delta(\eta - \eta') \, . \tag{6.33}
$$

Before investigating the solutions to this equation, the connection to the large external wave number limit of the functional renormalisation group studied in chapter 5 is drawn. As was already pointed out, the above limit assumes the absence of velocity dispersion degrees of freedom which would contribute terms to the self-energy (6.29) that dominate over those of order k^2. This was completely analogous in the limit of the functional renormalisation group, where velocity dispersion degrees of freedom were assumed to be absent. Further, $J(\eta, \eta')$ in general involves the full velocity power spectrum very similar to the function (5.17). Finally, to solve the two-point function flow equation and obtain an explicit solution for the propagator, a similar approximation in terms of the linear power spectrum was assumed. In the current notation the propagator obtained from the functional renormalisation group calculation reads

$$G_{ab}^{\text{R}}(\eta, \eta', k) = g_{ab}^{\text{R}}(\eta, \eta') \, \exp\left(-\tfrac{1}{2} \, k^2 \sigma_v^2 \big[e^{\eta - \eta_{\text{in}}} - e^{\eta' - \eta_{\text{in}}}\big]^2\right) \, . \tag{6.34}$$

Returning to equation (6.33), one can studied the 1PI one-loop approximation which is given by evaluating the propagator stemming from the self-energy (6.29) at linear level. The resulting equation is linear in the full propagator and can be solved by Laplace transforms to give [28]

$$G_{ab}^{\text{R}}(\eta, \eta', k) = g_{ab}^{\text{R}}(\eta, \eta') \cos\big(k\sigma_v \big[e^{\eta - \eta_{\text{in}}} - e^{\eta' - \eta_{\text{in}}}\big]\big) \, . \tag{6.35}$$

Similarly, equation (6.33) can actually also be solved via Laplace transforms in the case where both full propagators are kept and reads [28, 31]

$$G_{ab}^{\text{R}}(\eta, \eta', k) = g_{ab}^{\text{R}}(\eta, \eta') \, \frac{J_1\big(2k\sigma_v \big[e^{\eta - \eta_{\text{in}}} - e^{\eta' - \eta_{\text{in}}}\big]\big)}{k\sigma_v \big[e^{\eta - \eta_{\text{in}}} - e^{\eta' - \eta_{\text{in}}}\big]} \, , \tag{6.36}$$

where J_1 is the first-order Bessel function of first kind.[4]

---

[4]The Laplace transform of the two propagators (6.35) and (6.36) is studied in detail in chapter 7.
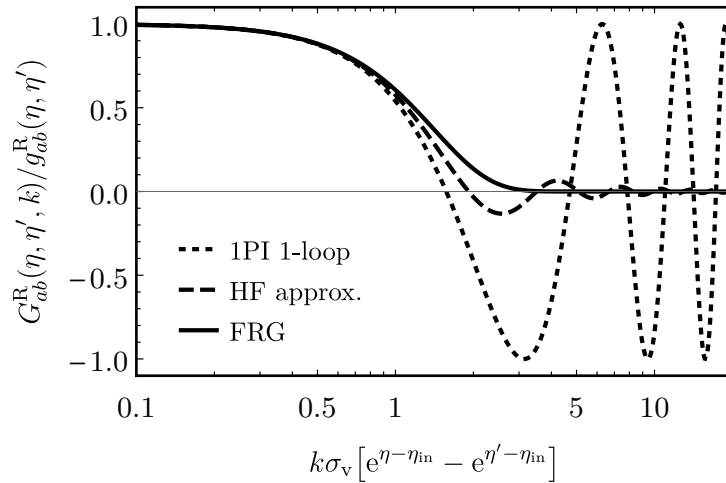
Figure 6.5: The propagators (6.34), (6.35) and (6.36) normalised to the linear propagator as a function of $k\sigma_{\mathrm{v}}\left[\mathrm{e}^{\eta-\eta_{\mathrm{in}}} - \mathrm{e}^{\eta'-\eta_{\mathrm{in}}}\right]$. While the functional renormalisation group (FRG) propagator (solid curve) shows a Gaussian suppression, the Hartree–Fock (HF) approximation (dashed curve) and the 1PI one-loop approximation (dotted curve) feature oscillations related to the different partial resummations of the perturbative series.

The large external wave number limit propagators (6.34), (6.35) and (6.36) can all be written as the linear retarded propagator multiplied by a correction factor that only depends on the dimensionless combination $k\sigma_{\mathrm{v}}\left[\mathrm{e}^{\eta-\eta_{\mathrm{in}}} - \mathrm{e}^{\eta'-\eta_{\mathrm{in}}}\right]$ and are shown in figure 6.5.

The propagator obtained from the functional renormalisation group calculation (6.34) is suppressed by a Gaussian factor while the 1PI one-loop and Hartree–Fock approximation propagators feature oscillations which in the former case are suppressed at larger $k\sigma_{\mathrm{v}}\left[\mathrm{e}^{\eta-\eta_{\mathrm{in}}} - \mathrm{e}^{\eta'-\eta_{\mathrm{in}}}\right]$. The characteristic scale of suppression respectively the frequency of the oscillations is determined by the *non-linear wave number*

$$k_{\mathrm{nl}}(\eta) := \frac{1}{\sigma_{\mathrm{v}}\,\mathrm{e}^{\eta-\eta_{\mathrm{in}}}}\ , \tag{6.37}$$

or more precisely by the difference of the inverse of two non-linear wave numbers at the two times of the propagator.

The difference of the propagators is due to the different resummation schemes underlying the approximations in which they were derived. While the three methods are all non-perturbative in the sense that they resum the perturbative series to infinite order, they correspond to different infinite partial resummations. This is best understood in the language of renormalised perturbation theory [18], where the propagator (6.34) can be obtained as a systematic resummation of the perturbative series.

Loop order	1	2	3	4	5	...	ℓ
1PI 1-loop	1	1	1	1	1	...	1
HF approx.	1	2	5	14	42	...	$(2\ell)!/((\ell+1)!\ell!)$
FRG	1	3	15	105	945	...	$(2\ell-1)!!$

Table 6.1: Number of diagrams included at loop order ℓ in the different resummation schemes. While the 1PI one-loop approximation captures only a single diagram at each loop order, the Hartree–Fock approximation improves on this, but captures only a subset those diagrams resummed in the functional renormalisation group (FRG).

The Gaussian suppression factor entering the propagator (6.34) can be written as the series

$$\mathrm{e}^{-\frac{1}{2}X^2} = \sum_{\ell=0}^{\infty} \frac{(2\ell-1)!!}{(2\ell)!} \left(-X^2\right)^\ell , \tag{6.38}$$

where $X := k\sigma_{\mathrm{v}}\left[\mathrm{e}^{\eta-\eta_{\mathrm{in}}} - \mathrm{e}^{\eta'-\eta_{\mathrm{in}}}\right]$ and !! is the double factorial. Here, $(2\ell-1)!!$ are the number of diagrams contributing to the propagator at perturbative loop order ℓ while the factor $1/(2\ell)!$ is due to all time integrations within a diagram [19]. It is emphasised that these are not all diagrams, but rather only a subclass of diagrams that are assumed to be dominant in the large external wave number limit. This is also clear from the functional renormalisation group calculation performed in chapter 5, where the propagator (6.34) was obtained in an approximation. As such it corresponds to an infinite partial resummation of the perturbative series.

Applying the same expansion to the propagators (6.35) and (6.36), one can find the number of diagrams contributing at each loop order. For the 1PI one-loop approximation the expansion of the cosine reads

$$\cos(X) = \sum_{\ell=0}^{\infty} \frac{1}{(2\ell)!} \left(-X^2\right)^\ell , \tag{6.39}$$

while for the Hartree–Fock approximation one finds

$$\frac{J_1(2X)}{X} = \sum_{\ell=0}^{\infty} \left[\frac{(2\ell)!}{(\ell+1)!\ell!}\right] \frac{1}{(2\ell)!} \left(-X^2\right)^\ell . \tag{6.40}$$

The number of diagrams contributing at each loop order to the different resummation schemes is summarised in table 6.1. It is noteworthy that in the direct-interaction approximation similar results for the propagator hold in turbulence [155, 156].

The different partial resummations can also be obtained from topological arguments. Consider the contributions to the propagator contained in the resummation of renormalised perturbation theory up to two-loop order. At zero and one-loop

order there is only a single diagram which is captured by all resummation schemes. At two-loop order though there are the three diagrams

$$
\text{(diagram)}^{(1)} + \text{(diagram)}^{(2)} + \text{(diagram)}^{(3)} . \tag{6.41}
$$

While the 1PI one-loop approximation can only capture diagram (1) topologically, the Hartree–Fock approximation contains the diagrams (1) and (2) due to its self-consistent one-loop structure. Finally, the functional renormalisation group calculation of chapter 5 captures all three diagrams (1), (2) and (3).

Based on the large external wave number limit two approximation schemes interpolating between the perturbative small wave number and non-perturbative large wave number sector haven been developed. In renormalised perturbation theory the propagator (6.34) is used for the interpolation [19] while in the direct-interaction approximation the propagator (6.36) is utilised [31]. In the next section the numerical solution of the full propagator equation (6.6) is compared to these interpolation schemes which in the following are referred to as 'CS' and 'TH' approximations, respectively.

6.3.2 Numerical solutions

In this section the full system of equations (6.5), (6.6) and (6.7) is solved with numerical methods in the Hartree–Fock approximation. The equations are solved in the single-stream approximation as well as for the field content (6.1) and are compared to N-body simulations that are discussed in the following.

N-body simulations

Since N-body simulations can only simulate a representative finite region of the Universe, one typically has to decide whether one wants to accurately reproduce large-scale structures, requiring a fairly large simulation volume, or is interested in resolving small-scale physics, which requires a rather high number density of particles. To test the performance of the Hartree–Fock approximation, numerical solutions are compared to the Horizon Run 2 (HR2) N-body simulation [166] featuring a very large simulation volume as well as to a N-body simulation of Buehlmann & Hahn (BH19) [169] featuring a comparably high number density of particles. The cosmological parameters and codes used for the simulations as well as the number of particles N_p, the box side length L_box and the initial redshift z_in are summarised in table 6.2.

Three snapshots of the BH19 N-body simulation [169] were kindly provided by the authors M. Buehlmann and O. Hahn. The datasets contain estimates for the density, velocity and isotropic velocity dispersion interpolated on a 1024^3-mesh at redshifts $z = 2.165$, $z = 0.994$ and $z = 0$. The density field was estimated using the

Simulation	Cosmology	Code	N_{p}	L_{box} [Mpc/h]	z_{in}
HR2 [166]	WMAP5 [159]	GOTPM [163]	6000^3	7200	32
BH19 [169]	Planck 2015 [161]	GADGET-2 [164]	1024^3	300	99

Table 6.2: Details of the *N*-body simulations used as comparison to the numerical solutions of the Hartree–Fock approximation.

cloud-in-cell deposition algorithm [170] while the velocity and velocity dispersion fields were obtained from the Lagrangian tessellation method [171, 172].

To derive an estimate for the power spectra, the fields are discretely Fourier transformed on a three-dimensional grid with fundamental wave number $k_{\mathrm{f}} := 2\pi/L_{\mathrm{box}}$ and $N_{\mathrm{grid}} = 1024$ grid points per dimension. Further, the density field is deconvolved using the cloud-in-cell window function [173]

$$W(\boldsymbol{n}) = \prod_{i=1}^{3} \mathrm{sinc}\left(\frac{\pi n_i}{N_{\mathrm{grid}}}\right)^2 , \tag{6.42}$$

where $n_i \in \{1, \dots, N_{\mathrm{grid}}\}$. The power spectrum estimate $\hat{P}_{ab}(k)$ is then obtained from the spatial average of two fields over the simulation volume and an angular average of modes within spherical shells of thickness k_{f} and radius $k = nk_{\mathrm{f}}$ for $n \in \{1, \dots, N_{\mathrm{grid}}\}$. Finally, the statistical error is estimated as [174]

$$\Delta\hat{P}_{ab}(k) := \frac{1}{\sqrt{2\pi n}}\left[\hat{P}_{ab}(k) + \left(\frac{L_{\mathrm{box}}}{N_{\mathrm{grid}}}\right)^3\right] , \tag{6.43}$$

where the first term on the right-hand side is the sample variance while the second term is the Poisson shot noise.

It is emphasised that the power spectrum and its error estimate should be taken with caution for small wave numbers due to systematic uncertainties related to the relatively small box size of the BH19 *N*-body simulation.

Details of the numerical solutions

To compare the Hartree–Fock approximation to the HR2 and BH19 *N*-body simulations, two sets of numerical solutions are computed. These account for the different cosmological parameters and initial redshifts listed in table 6.2. The initial power spectrum is generated by the CLASS code [157] on scales 10^{-5} h/Mpc $\lesssim k \lesssim 20$ h/Mpc and extrapolated into the ultraviolet using the fitting formula $\alpha \log(\beta k)^2 k^{n_{\mathrm{s}}-4}$. The wave number interpolation is done on a grid with an infrared cut-off $k_{\mathrm{min}} = k_{\mathrm{f}}$ and an ultraviolet cut-off $k_{\mathrm{max}} = nk_{\mathrm{Ny}}$ equal to a multiple of the Nyquist wave number $k_{\mathrm{Ny}} := \pi N_{\mathrm{grid}}/L_{\mathrm{box}}$. For the HR2 simulation these are given by $k_{\mathrm{f}} \approx 8.7 \cdot 10^{-4}$ h/Mpc and $k_{\mathrm{Ny}} \approx 2.6$ h/Mpc while for the BH19 simulation they

are $k_{\mathrm{f}} \approx 2.1 \cdot 10^{-2} \ h/\mathrm{Mpc}$ and $k_{\mathrm{Ny}} \approx 11 \ h/\mathrm{Mpc}$. More specifically, when comparing to the HR2 simulation the cut-off is chosen as $k_{\mathrm{max}} \approx 5.2 \cdot 10^{-2} \ h/\mathrm{Mpc}$ while when comparing to the BH19 simulation the cut-off is varied between $k_{\mathrm{max}} \approx 11 \ h/\mathrm{Mpc}$ and $k_{\mathrm{max}} \approx 43 \ h/\mathrm{Mpc}$.[5]

In the following, numerical solutions are computed in the single-stream approximation as well as for the field content (6.1). In the former case a wave number grid with $N_k = 100$ interpolation points is chosen and in the latter case $N_k = 50$. While it would be desirable to increase the number of interpolation points, it considerably slows down the solving algorithm since the arrays storing the Fock self-energies (6.12) and (6.13) scale cubic in N_k.[6]

Single-stream approximation

To gain more insight into the general properties of the Hartree–Fock approximation, the system of equations (6.5), (6.6) and (6.7) is first solved in the single-stream approximation where the field content (6.1) reduces to the density and velocity-divergence only. The density contrast propagator and power spectrum have also been studied in the single-stream approximation with the two-particle irreducible method [27–30] and in closure theory [31–33] which yield the same evolution equations as the Hartree–Fock approximation. In the following, the focus lies in identifying how well the Hartree–Fock approximation captures non-linearities as well as to find where the single-stream approximation fails.

Propagator: In figure 6.6 the density contrast and velocity-divergence reduced propagators are shown for $k \approx 2 \ h/\mathrm{Mpc}$ (upper panel) and $z = 0$ (lower panel). The numerical solution of the Hartree–Fock approximation is near to identical with the TH approximation. A slight deviation for wave numbers $k \gtrsim k_{\mathrm{nl}}(\eta)$ is observed, which is not to surprising since the TH approximation interpolates between the small and large wave number sector. As was already discussed in section 6.3.1, the observed oscillations are not associated with physical phenomena but rather with the partial resummation of the full perturbative series.

Density contrast equal-time auto-spectrum: In figure 6.7 the dimensionless density contrast equal-time auto-spectrum normalised to the linear one is shown at redshifts $z = 2$ (upper panel) and $z = 0$ (lower panel). At large wave numbers, the Hartree–Fock approximation does not overestimate the N-body power spectrum as bad as the standard perturbation theory one-loop prediction. While the deviation from the N-body power spectrum is fairly small at redshift $z = 2$ it grows towards

---

[5] While numerical solutions computed in the single-stream approximation are percent-accurate for $k_{\mathrm{max}} \gtrsim 5 \ h/\mathrm{Mpc}$ [31], this changes dramatically when including velocity dispersion degrees of freedom since the mean field source term (6.10) is sensitive to small-scale physics.

[6] The self-energy arrays also scale with the sixth power in the field content which is the reason why the vector and tensor velocity dispersion modes were neglected.
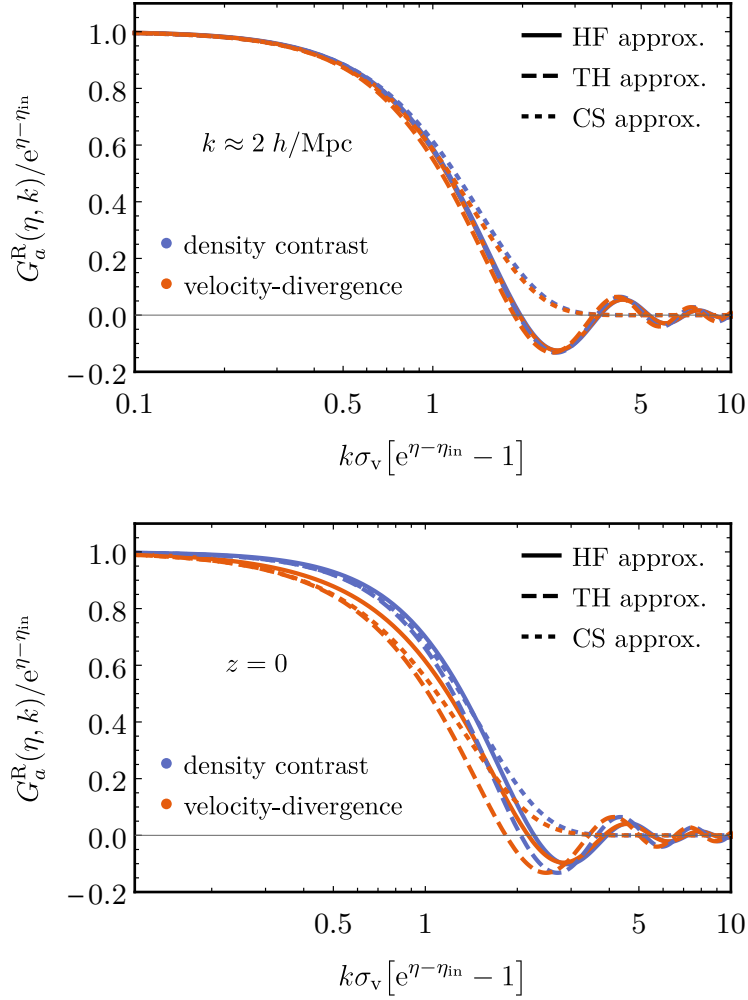
Figure 6.6: Density contrast (blue curves) and velocity-divergence (red curves) reduced propagators for $k \approx 2\,h/\mathrm{Mpc}$ (upper panel) and $z = 0$ (lower panel). The numerical solution of the Hartree–Fock (HF) approximation (solid curves) is compared to the TH (dashed curves) and CS (dotted curves) approximation. The Hartree–Fock and TH approximations are near to identical since the latter is based on the large wave number limit of the former.
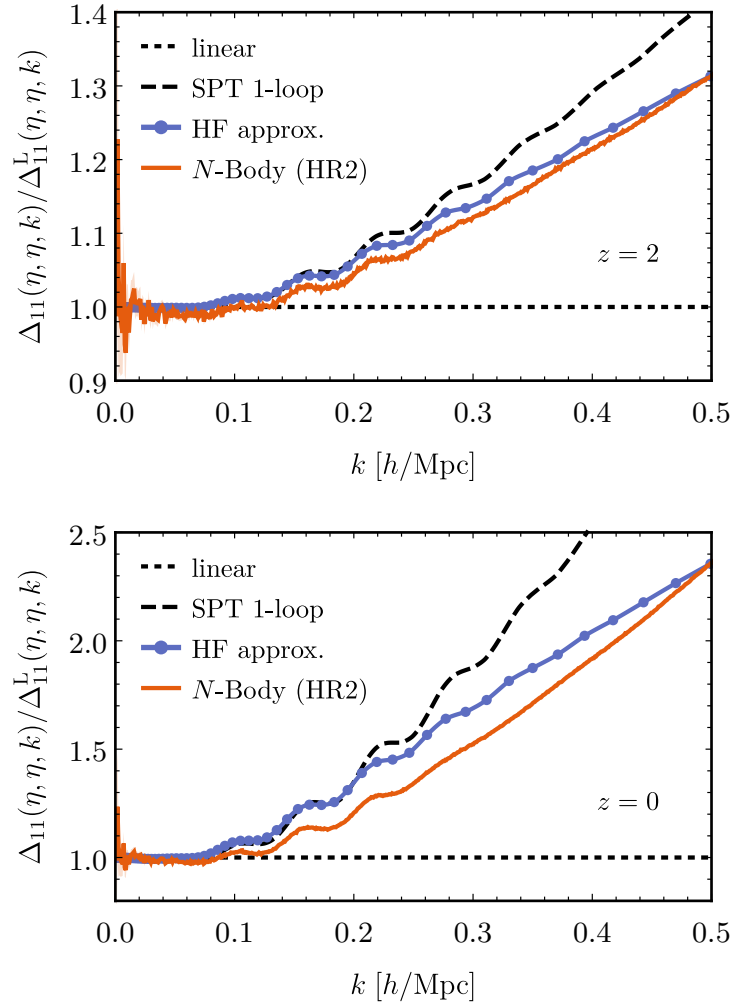
Figure 6.7: Dimensionless density contrast equal-time auto-spectrum normalised to the linear one (black dotted curves) at redshifts $z = 2$ (upper panel) and $z = 0$ (lower panel). The numerical solution of the Hartree–Fock (HF) approximation (blue solid curves) is compared to the standard perturbation theory (SPT) one-loop prediction (black dashed curves) and data from the HR2 N-body simulation (red solid curves). While the Hartree–Fock approximation shows better convergence properties at larger wave numbers, it overestimates the power spectrum at smaller wave numbers.
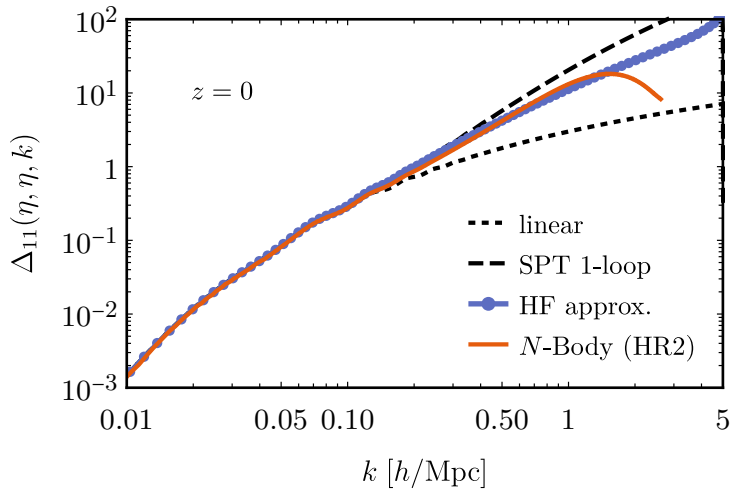
Figure 6.8: Dimensionless density contrast equal-time auto-spectrum at redshift $z = 0$. The Hartree–Fock approximation captures the general shape of the non-linear power spectrum obtained from N-body simulations much better than the standard perturbation theory one-loop predication.

redshift $z = 0$. Especially for wave numbers $k \lesssim 0.2 \ h/\mathrm{Mpc}$ the Hartree–Fock approximation seems to follow the standard perturbation theory one-loop prediction. Since the full 1PI three-point functions are set to their bare form in the Hartree–Fock approximation, it is likely that vertex corrections are needed to accurately capture the mildly non-linear regime.

In figure 6.8 the dimensionless density contrast equal-time auto-spectrum is shown for a larger range of wave numbers at redshift $z = 0$. The Hartree–Fock approximation shows a much better convergence towards the N-body power spectrum compared to the standard perturbation theory one-loop prediction that badly overestimates the power spectrum. The drop of the N-body power spectrum at wave numbers near the Nyquist wave number is due to finite box size effects and should not be trusted.

Velocity-divergence equal-time auto-spectrum: In figure 6.9 the dimensionless density contrast (upper panel) and velocity-divergence (lower panel) equal-time auto-spectra are shown at redshift $z = 0$. The density contrast power spectrum is shown for the sake of completeness and similar to the one shown in figure 6.8 but computed with different cosmological parameters and cut-offs since it is compared with the BH19 N-body simulation. The better performance of the standard perturbation theory one-loop predication is attributed to the missing of large-scale modes due to the comparably large infrared cut-off $k_{\min} \approx 2.1 \cdot 10^{-2} \ h/\mathrm{Mpc}$, suppressing the overestimation observed in figure 6.8.

Neither the Hartree–Fock nor the standard perturbation theory one-loop predication can capture the sharp drop of the velocity-divergence power spectrum at
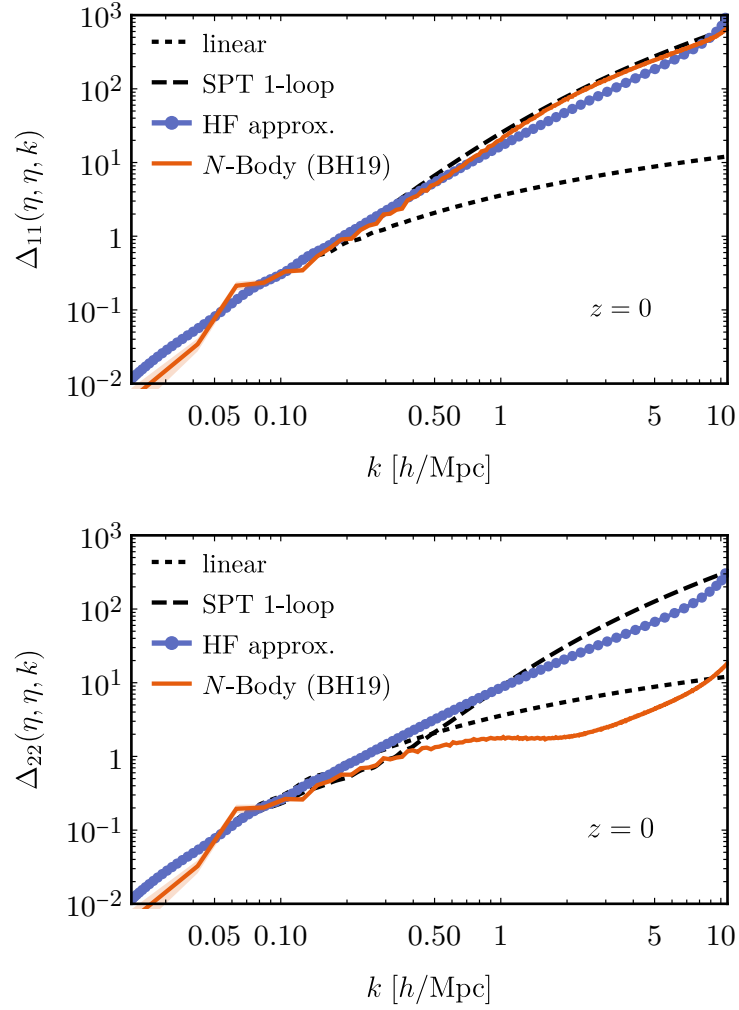
Figure 6.9: Dimensionless density contrast (upper panel) and velocity-divergence (lower panel) equal-time auto-spectrum at redshift $z = 0$. The numerical solution of the Hartree–Fock (HF) approximation (blue solid curves) is compared to the standard perturbation theory (SPT) one-loop prediction (black dashed curves) and data from the BH19 N-body simulation (red solid curve). The Hartree–Fock approximation badly overestimates the N-body velocity-divergence power spectrum even in the small wave number regime. This is due to the fact that the drop of the velocity-divergence power spectrum is associated with effects beyond the single-stream approximation.

small scales. Even worse, the Hartree–Fock approximation even fails to reproduce the power spectrum at relatively small wave numbers where the standard perturbation theory one-loop predication can capture at least the onset of the suppression. Indeed, the drop is associated with the energy transfer into vorticity modes [168] and thus beyond the single-stream approximation. This is discussed in detail when studying the Hartree–Fock approximation including velocity dispersion degrees of freedom.

Unequal-time auto-spectra and equal-time cross-spectra: In figure 6.9 the dimensionless density contrast unequal-time auto-spectrum (upper panel) at redshifts $z = 0$ and $z' = 2.165$ as well as the dimensionless velocity-divergence-density contrast equal-time cross-spectrum (lower panel) at redshift $z = 0$ are shown. The oscillatory suppression of the unequal-time power spectrum is qualitatively captured by the Hartree–Fock approximation due to the non-perturbative self-consistent resummation of the propagators contrary to the standard perturbation theory one-loop prediction. While the *N*-body power spectrum seems to indicate an almost constant amplitude, the Hartree–Fock approximation features a decaying amplitude which is directly related to the in amplitude decaying oscillations shown in figure 6.6.

More interesting and important for the investigations that include velocity dispersion degrees of freedom is the cross-spectrum. The *N*-body power spectrum stays close to the linear prediction up to $k \approx 1.0 \; h/\mathrm{Mpc}$ above which a sign change is observed. This is interpreted as a turnover from matter inflow to outflow and associated with shell-crossing [167, 169]. Naturally, this cannot be captured in the single-stream approximation and explains why the Hartree–Fock approximation is unable to capture the *N*-body power spectrum.

Summary:

- The propagators are to very good approximation described by the large wave number limit (6.36), at least if the initial and final times are sufficiently far apart.

- The density contrast equal-time auto-spectrum converges well at small scales but fails to accurately capture the physics at mildly non-linear scales. This is most likely due to neglecting corrections to the bare vertex.

- The drop of the velocity-divergence equal-time auto-spectrum cannot be captured since it is associated to the energy transfer into vorticity modes.

- The oscillatory suppression of unequal-time auto-spectra is qualitatively captured due to the non-perturbative resummation of the propagators.

- The sign change in the velocity-divergence-density contrast equal-time cross-spectrum cannot be captured since it is associated with shell-crossing.
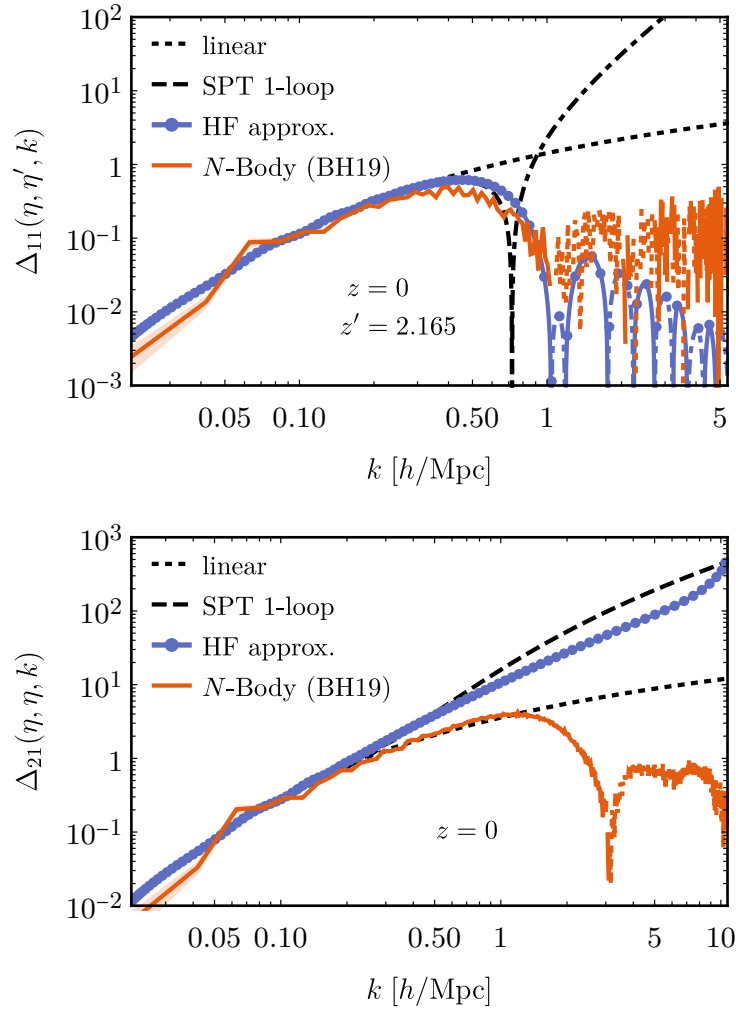
Figure 6.10: Dimensionless density contrast unequal-time auto-spectrum (upper panel) at redshifts $z = 0$ and $z' = 2.165$ as well as velocity-divergence-density contrast equal-time cross-power spectrum (lower panel) at redshift $z = 0$. The numerical solution of the Hartree–Fock (HF) approximation (blue solid curves) is compared to the standard perturbation theory (SPT) one-loop prediction (black dashed curves) and data from the BH19 N-body simulation (red solid curve). The oscillatory suppression is of the unequal-time power spectrum is qualitatively captured by the Hartree–Fock approximation due to the non-perturabtive resummation of propagators. The sign change observed in the equal-time cross-spectrum cannot be captured since it is associated with shell-crossing.

Including velocity dispersion degrees of freedom

Having seen the limitations of the single-stream approximation in the last section, the Hartree–Fock approximation is now studied for the field content (6.1) including the vorticity and velocity dispersion fields. In this case, the free-streaming of dark matter seen in the Hartree approximation as well as the non-linear coupling of modes encoded in the Fock self-energies contribute. To take both effects correctly into account, the two scales associated with them, namely the free-streaming wave number k_{fs} and the non-linear wave number k_{nl}, need to be resolved. Numerically this is rather challenging for cold dark matter candidates since these scales are separated by several orders of magnitudes. Since the propagators are suppressed on small scales the adaptive Runge–Kutta method takes smaller times steps as one solves at later times. The larger the ultraviolet cut-off wave number is, the more time steps are necessary to keep the errors under control. To obtain results in a sensible amount of time, but at the same time capture the effects of non-vanishing velocity dispersion in the following rather warm dark matter candidates are studied. More specifically the initial velocity dispersion mean field is taken to be between $\bar{\sigma}^{in} = 10^2$ km^2/s^2 and $\bar{\sigma}^{in} = 10^5$ km^2/s^2. The ultraviolet cut-off is varied between $k_{max} = k_{Ny}$ and $k_{max} = 4k_{Ny}$ to see the effect of including smaller scales.

Velocity dispersion mean field: In figure 6.11 the velocity dispersion mean field for different ultraviolet cut-offs is shown. Here the different initial conditions are colour-coded which is also used in the figures following to distinguish the different solutions. All numerical solution have been performed for an ultraviolet cut-off $k_{max} = k_{Ny}$ and $k_{max} = 2k_{Ny}$ as well as for $k_{max} = 4k_{Ny}$ for the coldest candidate studied here, with an initial velocity dispersion mean field of $\bar{\sigma}^{in} = 10^2$ km^2/s^2. As can be seen, as long as the free-streaming wave number is below or of the order of the ultraviolet cut-off the numerical solutions are well converged and insensitive to a larger ultraviolet cut-off. This is best seen for the warmest candidate with an initial mean field of $\bar{\sigma}^{in} = 10^5$ km^2/s^2 which has a growing free-streaming wave number starting at $k_{fs} \approx 2.1$ h/Mpc at $z = 99$ to $k_{fs} \approx 6.2$ h/Mpc at $z = 0$, both well below the ultraviolet cut-off. One can clearly observer how colder initial conditions naturally need a larger ultraviolet cut-off to capture the small-scale power which sources the growth of the mean field. Most drastically this is seen for the coldest candidate where the free-streaming wave number at the point of turnover from decay to growth is roughly of the order $k_{fs} \approx 210$ h/Mpc which is way above the largest ultraviolet cut-off $k_{max} = 4k_{Ny} \approx 43$ h/Mpc used here. This naturally extends to colder candidates. The velocity dispersion mean field can be computed from the three snapshots of the BH19 *N*-body simulations as the spatial average of the velocity dispersion tensor trace. These are also shown and it is evident that the velocity dispersion mean field is even larger than the rather warm dark matter candidates studied here. One could conjecture that if it would be computationally manageable to start out with a very cold dark matter candidate, such as a weakly interacting particle with $\bar{\sigma}^{in} \sim 10^{-10}$ km^2/s^2, an early growth could lead to the
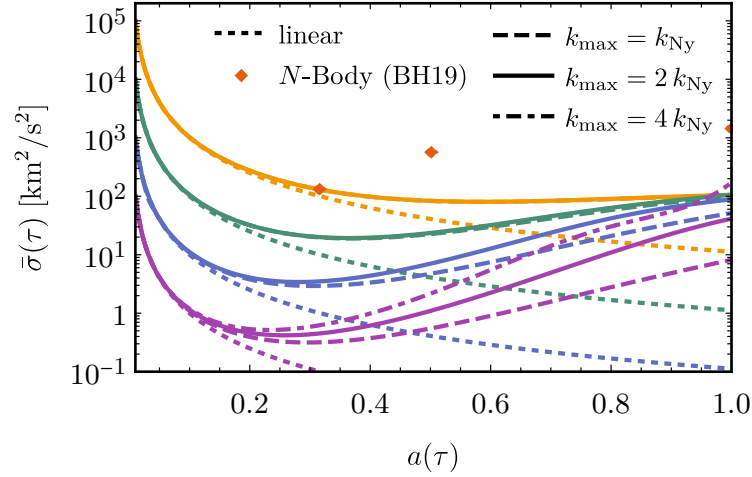
Figure 6.11: Evolution of the velocity dispersion mean field in the Hartree–Fock approximation for different ultraviolet cut-offs that are multiples of $k_{\mathrm{Ny}} \approx 11\ h/\mathrm{Mpc}$. Shown as the numerical solutions which are colour coded for differential initial conditions (violet, blue, green and yellow from coldest to warmest), the linearly decaying mean field (dotted curves) and the three snapshots from data of the BH19 N-body simulation (red diamonds). For warmer dark matter where the free-streaming wave number is below the cut-off the results are well converged while for colder dark matter with a larger free-streaming wave number this is no longer the case.
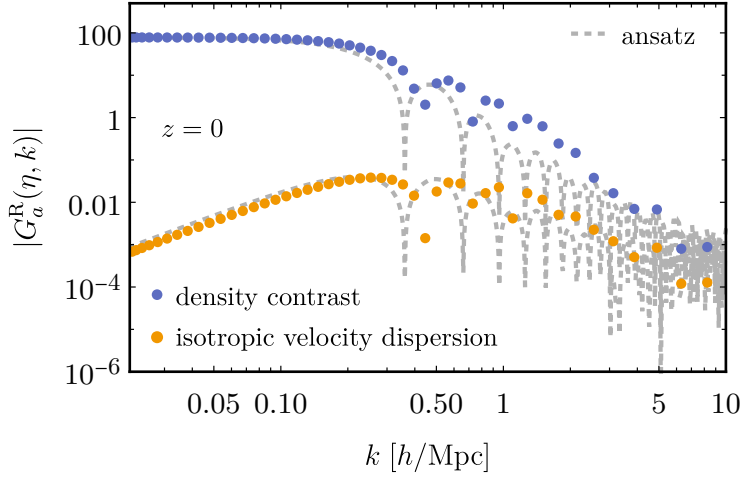
Figure 6.12: Density contrast and isotropic velocity dispersion reduced propagators for the dark matter model with $\bar{\sigma}^{\mathrm{in}} = 10^5 \mathrm{\ km}^2/\mathrm{s}^2$ at redshift $z = 0$. Also shown is the ansatz (6.44) superposing the free-streaming effect found in the Hartree approximation (6.28) and the large wave number limit (6.36). Qualitatively, the ansatz captures the numerical solution of the Hartree–Fock approximation which naturally captures both effects.

observed values. Due to the above mentioned computational limitations it was not possible to verify this.

Propagator: In figure 6.12 the density contrast and isotropic velocity dispersion reduced propagators for the dark matter model with $\bar{\sigma}^{\mathrm{in}} = 10^5 \mathrm{\ km}^2/\mathrm{s}^2$ are shown at redshift $z = 0$. To see how the effects of the Hartree and retarded Fock self-energy combine, both have been superposed with the ansatz

$$G_{ab}^{\mathrm{R}}(\eta, \eta', k) = \tilde{G}_{ab}^{\mathrm{R}}(\eta - \eta', k^2 \tilde{\sigma}) \frac{J_1\left(2k\sigma_{\mathrm{v}}\left[\mathrm{e}^{\eta - \eta_{\mathrm{in}}} - \mathrm{e}^{\eta' - \eta_{\mathrm{in}}}\right]\right)}{k\sigma_{\mathrm{v}}\left[\mathrm{e}^{\eta - \eta_{\mathrm{in}}} - \mathrm{e}^{\eta' - \eta_{\mathrm{in}}}\right]} \ , \qquad (6.44)$$

where $\tilde{G}_{ab}^{\mathrm{R}}(\eta - \eta', k^2 \tilde{\sigma})$ is the retarded propagator that is obtained in the Hartree approximation for a linear mean field and can be reconstructed from the solutions (6.28). This naïve ansatz qualitatively captures the Hartree–Fock approximation and reproduces the superposition of oscillations from free-streaming encoded in the Hartree self-energy and of the decaying oscillations due to the coupling of modes encoded in the retarded Fock self-energy.[7] Although not shown here, the performance of the ansatz (6.44) worsens when compared to colder dark matter models. Since

---

[7]It is again emphasised that the oscillations due to the retarded Fock self-energy are a consequence of the employed truncation of the Dyson–Schwinger hierarchy and can be understood as an infinite but partial resummation of standard perturbation theory.

the propagator $\tilde{G}_{ab}^{\mathrm{R}}(\eta - \eta', k^2\tilde{\sigma})$ is strictly speaking only valid for a decaying mean field, it fails to capture the effect of a strongly growing mean field as is the case for the colder dark matter models.

Density and velocity equal-time auto-spectra: Although only initially rather warm dark matter candidates are studied, the question arises whether the approximation including velocity dispersion degrees of freedom can overcome the shortcomings of the single-stream approximation. To see the impact on non-vanishing velocity dispersion, the dimensionless density contrast and velocity-divergence equal-time auto-spectrum is shown in figure 6.13. The solutions corresponding to different velocity dispersion mean field initial conditions are colour coded in the same way as in figure 6.11. Additionally, the free-streaming scales related to the corresponding velocity dispersion mean field are displayed. Since the numerical solutions all have a mean field of the same order at redshift $z = 0$, and therefore a similar free-streaming wave number, only a single free-streaming wave number is indicated here. It is clearly visible that the dark matter models starting out with a warmer initial condition show a large suppression in the density contrast as well as in the velocity-divergence power spectrum. Interestingly, one can observe that although the velocity dispersion is of similar order at redshift $z = 0$, the dark matter models starting out comparably cold show near to no suppression in the density contrast power spectrum and match the *N*-body data rather well. Comparing with the evolution of the mean field shown in figure 6.11, it seems that if the mean field obtains a large value only at late times one does not see a suppression in the density contrast power spectrum. In contrast, consider the warmest dark matter model shown that is warm for a large part of its time evolution. Although the final mean field is even below the final mean field of the initially colder model, a significant suppression is observed in the density contrast power spectrum. This suggest that indeed the dark matter model should start out with a small velocity dispersion mean field in to match the observed power spectrum. On the other hand, this also implies that a late-time large velocity dispersion mean field does not necessarily imply the power spectrum to be suppressed.

Velocity dispersion equal-time auto-spectra: In figure 6.14 the time (upper panel) and wave number (lower panel) dependencies of the dimensionless isotropic velocity dispersion equal-time auto-spectrum are shown at constant wave number $k \approx 0.5 \ h/\mathrm{Mpc}$ and redshift $z = 0$, respectively. Displayed is the time dependence of the power spectrum at constant wave number $k \approx 0.5 \ h/\mathrm{Mpc}$ which grows in time and does so more strongly for the initially colder dark matter models, very similar to the velocity dispersion mean field. Also depicted are the corresponding three snapshots of the *N*-body simulations of BH19 which seem to exhibit a stronger growth at late times, roughly scaling $\propto D_+^8$. Also shown is the wave number dependence compared to the data from the BH19 *N*-body simulations. One can clearly see a near to power law scaling of the power spectrum in the infrared up to some
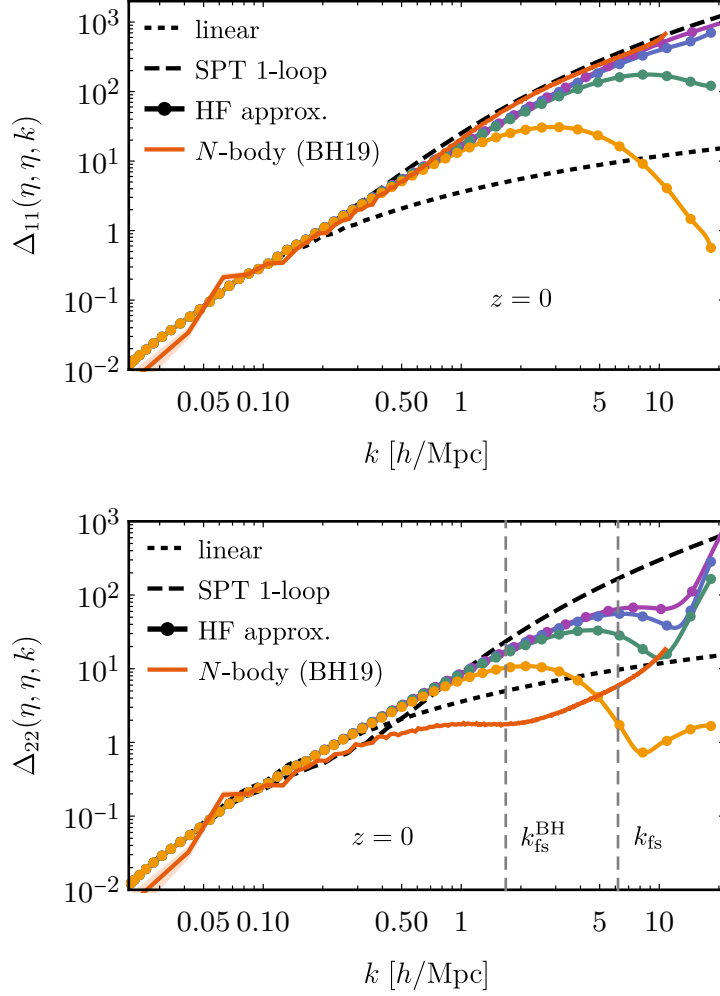
Figure 6.13: Dimensionless density contrast (upper panel) and velocity-divergence (lower panel) equal-time auto-spectrum at redshift $z = 0$. The numerical solutions of the Hartree–Fock (HF) approximation are colour coded according to the respective mean fields shown in figure 6.11. They are compared to the linear power spectrum (black dotted curves), the standard perturbation theory (SPT) one-loop prediction (black dashed curves) and data from the BH19 N-body simulation (red solid curve). Both spectra are suppressed for warmer dark matter models, although the velocity-divergence power spectrum shows a much stronger suppression.
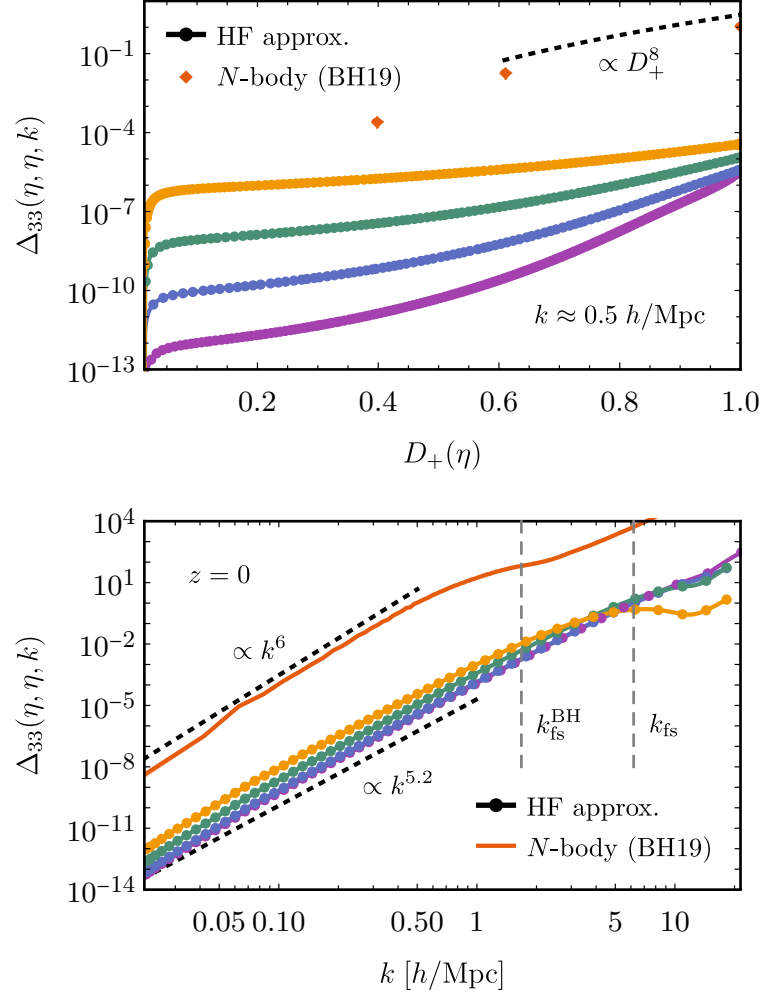
Figure 6.14: Time (upper panel) and wave number (lower panel) dependence of the dimensionless isotropic velocity dispersion equal-time auto-spectrum at constant wave number $k \approx 0.5 \ h/\mathrm{Mpc}$ and redshift $z = 0$, respectively. The numerical solutions of the Hartree–Fock (HF) approximation are colour coded according to the respective mean fields shown in figure 6.11. Three snapshots from data of the BH19 N-body simulation (red diamonds and red solid curves) as well as power law scalings (black dotted lines) are also shown. The velocity dispersion of colder dark matter candidates grows faster in time but all candidates show a near to power law scaling in wave number at redshift $z = 0$ corresponding to a spectral index $n_\sigma \approx -1.8$ up to the free-streaming wave number.

wave number above which the power spectrum drops. Later analysis and *N*-body simulations [167, 169] seem to indicate that is scale is related to shell-crossing and the largest collapsed structures. In the current framework this is in turn related to the velocity dispersion mean field and the free-streaming scale as indicated. That is, one can clearly see that for wave numbers above the linear free-streaming scale the power spectrum drops. The spectral index observed in *N*-body simulations is roughly $n_\sigma \approx -1$ [169] and corresponds to the indicated scaling $\Delta_{33} \propto k^6$.[8] The numerical solutions show a slightly less step power spectrum which scales roughly as $\Delta_{33} \propto k^{5.2}$ in the infrared, before dropping on wave numbers above the free-streaming scale.

Velocity- and velocity dispersion-density equal-time cross-spectra: In figure 6.15 the dimensionless velocity-divergence- and velocity dispersion-density contrast equal-time cross-spectra at redshift $z = 0$ are shown. It has been seen in figure 6.10 that the single-stream approximation badly fails to describe the velocity-divergence-density contrast equal-time cross-spectrum. This was related to the fact that the observed sign change in *N*-body data is related to shell-crossing which cannot be described by the single-stream approximation. In contrast, when including velocity dispersion degrees of freedom the effect is captured. Both cross-spectra shown in figure 6.15 carry a signature of shell-crossing, related to the sign change in correlation. It is also evident that the scale of shell-crossing is related to the free-streaming wave number (the sign change occurs roughly at $2k_{\text{fs}}$) and thus to the velocity dispersion mean field. It is clear that the numerical solutions presented here show a sign change at a higher wave number compared to the since the *N*-body simulations since the corresponding mean field is smaller. Nonetheless, one can see that including velocity dispersion degrees of freedom into the description actually allows to describe effects associated with shell-crossing.

Vorticity equal-time auto-spectra: In figure 6.16 the time (upper panel) and wave number (lower panel) dependencies of the dimensionless vorticity equal-time auto-spectrum are shown at constant wave number $k \approx 0.5 \ h/\text{Mpc}$ and redshift $z = 0$, respectively. It is emphasised that vorticity is initially absent and can also not be sourced by the mean field alone, which is why it is also absent the Hartree approximations studied in section 6.2. But it can be sourced by non-linear terms of the fluctuations and is thus naturally generated in the Hartree–Fock approximation due to the mode coupling of the 1PI statistical self-energy. One can observe the late-time scaling D_+^7 [88, 167] in the BH19 *N*-body data and finds that the numerical solutions growth similar, although depending on the specific dark matter model. More interesting is the wave number dependence. As indicated and seen in various *N*-body simulations [88, 167, 168] one finds a spectral index $n_\omega \approx 2.5$ in the infrared corresponding to the scaling $\Delta_{55} \propto k^{5.5}$ of the dimensionless vorticity power spectrum, before dropping on scales smaller than the free-streaming scale. The nu-

---

[8]Remember that $\Delta_{33} \propto k^3 P_{33} \propto k^7 P_{\sigma\sigma}$ due to the rescaling in the field content (6.1).
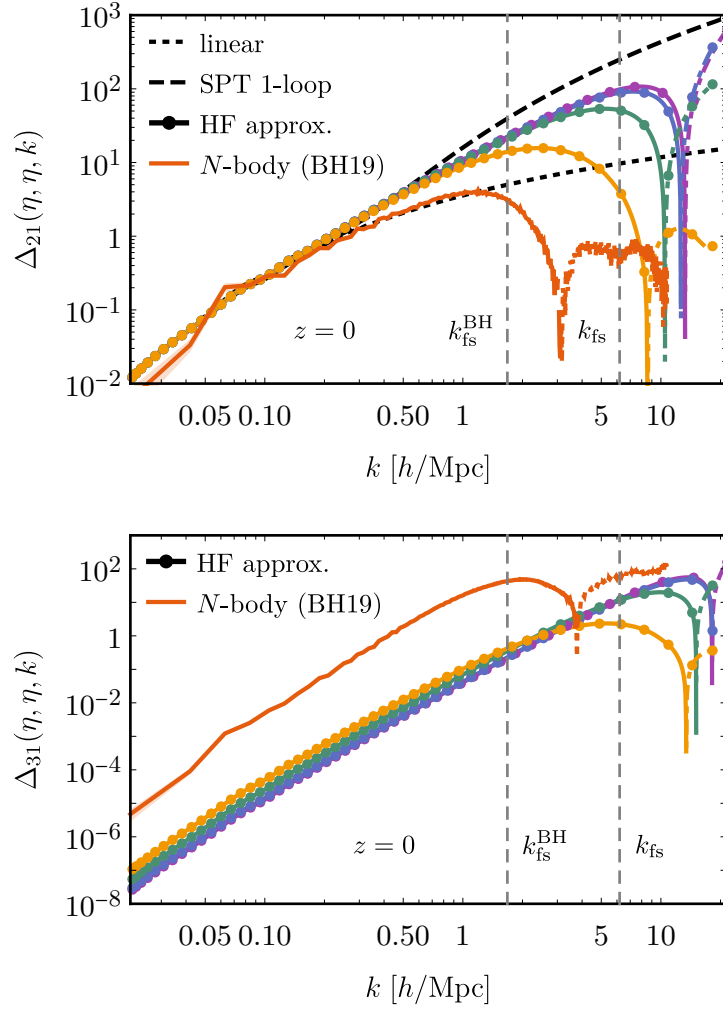
Figure 6.15: Dimensionless velocity-divergence- (upper panel) and velocity dispersion-density contrast (lower panel) equal-time cross-power spectrum $z = 0$. The numerical solutions of the Hartree–Fock (HF) approximation are colour coded according to the respective mean fields shown in figure 6.11. They are compared to the linear power spectrum (black dotted curves), the standard perturbation theory (SPT) one-loop prediction (black dashed curves) and data from the BH19 N-body simulation (red solid curve). The sign change of the cross-spectra is associated with shell-crossing and captured by the Hartree–Fock approximation in both power spectra.
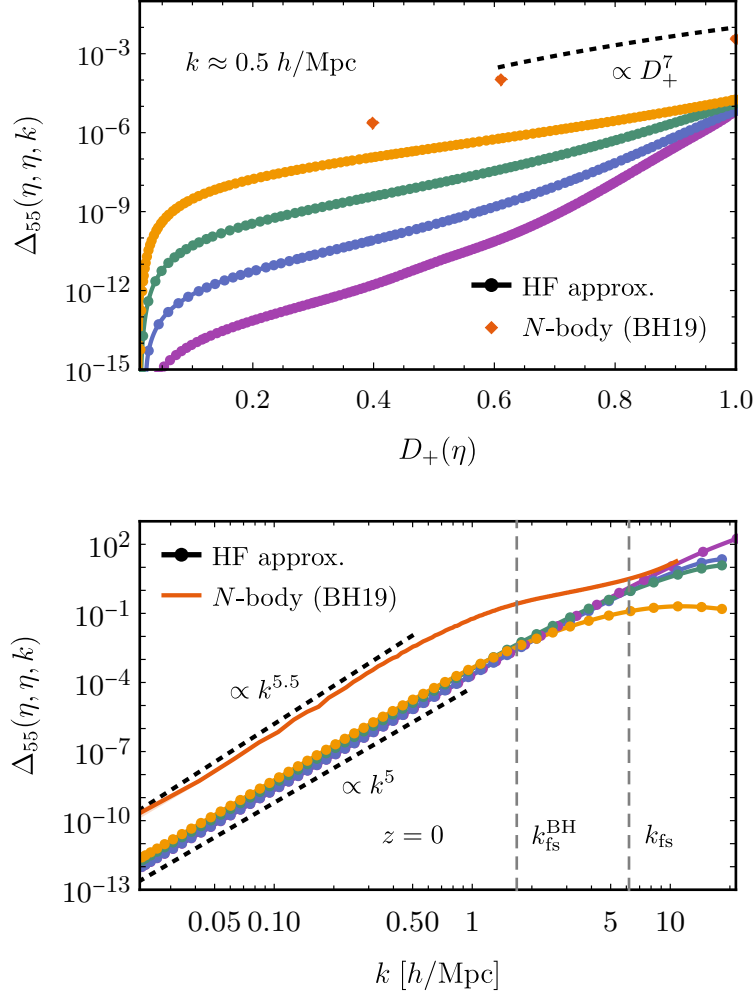
Figure 6.16: Time (upper panel) and wave number (lower panel) dependence of the dimensionless isotropic velocity dispersion equal-time auto-spectrum at constant wave number $k \approx 0.5 \ h/\mathrm{Mpc}$ and redshift $z = 0$, respectively. The numerical solutions of the Hartree–Fock (HF) approximation are colour coded according to the respective mean fields shown in figure 6.11. Three snapshots from data of the BH19 N-body simulation (red diamonds and red solid curves) as well as power law scalings (black dotted lines) are also shown. The vorticity of colder dark matter candidates grows faster in time but all candidates show a near to power law scaling in wave number at redshift $z = 0$ corresponding to a spectral index $n_\omega \approx 2$ up to the free-streaming wave number.

merical solution shows a spectral index of almost exact $n_\omega \approx 2$.[9] Indeed, there are arguments that if vorticity is absent initially, one expects the power spectrum to actually scale with a spectral index $n_\omega = 2$. Since the position space covariance function has only has finite support due to causality, the Fourier transform needs to be analytic [175]. Since the vorticity mode is transverse, the power spectrum carries an additional transverse projector $P_{ij}(\boldsymbol{k})$ such that the simplest scaling required for analyticity is given by $n_\omega = 2$. Precisely such a scaling is observed in the infrared of the Hartree–Fock approximation. It has been argued [168] that a deviation from this scaling observed in *N*-body simulations could be due to missing contributions of large scales due to the finite box size, rendering the *N*-body power spectrum to steep. Along similar lines one could argue that the deviation between the isotropic velocity dispersion equal-time auto-spectrum shown in figure 6.14 is due to this finite size effect.

It is remarked here, that although the infrared is perturbative in the sense that fluctuations are small and the density contrast power spectrum is well described by perturbation theory, the generation of vorticity and velocity dispersion is a highly non-perturbative effect. This is also the reason why perturbative methods do not correctly capture the scaling of the vorticity power spectrum, see e.g. [11,176]. Also it is interesting to realise that the drop of the velocity-divergence auto-spectrum happens at the rise of the vorticity auto-spectrum, with the lowest point of the former corresponding to the peak of the latter. This is interpreted as consequence of angular momentum conservation converting power from the velocity-divergences to vorticity modes, preventing the further infall of matter [168].

---

[9]Notice here that the spectrum P_{55} differs from the vorticity spectrum only by wave number independent factors such that the spectral index is the same.

7 Time-local effective dynamics with the functional renormalisation group

In this chapter a description for dark matter that features time-local effective dynamics is investigated with the functional renormalisation group. To this end, the structure of the (inverse) propagators corresponding to local and non-local dynamics are investigated using Laplace transforms. Following, an ansatz for the effective action is studied which can be understood as a combination of a vertex and derivative expansion up to the order of the bare action. The relevant coefficients needed to capture the sweeping effect studied in chapter 5 are found and the flow equations are solved for them. The corresponding propagators are computed and compared to those obtained in the large wave number limit. Finally, the density and velocity-divergence power spectra are computed using the non-perturbative propagators obtained before and compared to data from N-body simulations.

Laplace transform

In the following, it is convenient to work with the Laplace transform taking a time variable t to the complex frequency s. For a suitable function or distribution $f(t)$ with support on the positive real line the Laplace transform is defined as

$$f(s) := \int_0^\infty \mathrm{d}t \, \mathrm{e}^{-st} f(t) \, . \tag{7.1}$$

Within the region of absolute convergence the Laplace transform is analytic and can be inverted using the Bromwich integral

$$f(t) = \lim_{\sigma \to \infty} \int_{c-\mathrm{i}\sigma}^{c+\mathrm{i}\sigma} \frac{\mathrm{d}s}{2\pi \mathrm{i}} \, \mathrm{e}^{st} f(s) \, , \tag{7.2}$$

where c is real and to the right of all singularities of the integrand.

7.1 Local and non-local dynamics

Consider the retarded propagator equation

$$\int_{\eta'}^{\eta} \mathrm{d}\xi \, D_{ab}^{\mathrm{R}}(\eta, \xi, q) \, G_{bc}^{\mathrm{R}}(\xi, \eta', q) = \delta_{ac} \delta(\eta - \eta') \, . \tag{7.3}$$

For a generic inverse propagator the equation is naturally non-local in time and includes memory effects. In the case where the inverse propagator has support for

$\eta = \eta'$ only, such as in the linear case (4.5) or for the bare inverse propagator (4.46), the dynamics are local in time.

Consider the Laplace transform of the retarded inverse propagator with respect to $\Delta\eta = \eta - \eta'$,

$$D_{k,ab}^{\mathrm{R}}(\eta, q; s) = \int_0^\infty \mathrm{d}\Delta\eta \, \mathrm{e}^{-s\Delta\eta} \, D_{k,ab}^{\mathrm{R}}(\eta, \eta - \Delta\eta, q) \,, \tag{7.4}$$

taking its natural support $\Delta\eta \geq 0$ into account.[1] For a time-translation invariant system the inverse propagator only depends on $\Delta\eta$ and the propagator can be obtained by inverting the matrix structure of equation (7.4) and subsequently inverting the Laplace transform. For a generic system that is not time translation invariant this is no longer possible and equation (7.3) needs to be solved with other methods.

To investigate local and non-local dynamics it is convenient to expand the inverse propagator in terms of a Laurent series,

$$D_{k,ab}^{\mathrm{R}}(\eta, q; s) = \sum_{n=-\infty}^{\infty} D_{k,ab}^{(n)}(\eta, q) \, (s - s_*)^n \,, \tag{7.5}$$

around some complex frequency s_*.[2]

Local dynamics

In the case where s_* is non-singular the principal part of the series vanishes and one obtains an ordinary Taylor series. Provided that the series terminates at some finite order N, the corresponding dynamics are local and of Nth-order since inverting the Laplace transform results in a local derivative expansion. In the case of local first-order dynamics one obtains

$$D_{k,ab}^{\mathrm{R}}(\eta, \eta', q) = \left[D_{k,ab}^{(0)}(\eta, q) + D_{k,ab}^{(1)}(\eta, q) \, (\partial_\eta - s_*) \right] \delta(\eta - \eta') \,, \tag{7.6}$$

which captures the linear retarded inverse propagator of the cosmological field theory introduced in chapter 4. To summarise, local dynamics necessarily correspond to an inverse propagator that is a polynomial in complex frequency.

Non-local dynamics

If the series does not terminate at finite order, the self-energy generally does not correspond to local dynamics.[3] If s_* is a singularity, one naturally obtains non-local

---

[1] Since the initial conditions are given at some finite η_{in}, the time difference $\Delta\eta$ can maximally be $\eta - \eta_{\mathrm{in}}$. The Laplace transform (7.4) should be understood as the limit $\eta_{\mathrm{in}} \to -\infty$ where the initial conditions are pushed infinitely far into the past. This can also be understood as integrating out the linear dynamics within the functional integral such that the initial conditions do not explicitly enter into the bare action [29].

[2] For any complex frequency s_* that is no branch point and in the region of absolute convergence the series exists in some annulus around s_*.

[3] Consider e.g. a self-energy of the form $\Sigma_{k,ab}^{\mathrm{R}}(\eta, q; s) \propto \mathrm{e}^{-as}$ which corresponds to a delayed impulse response $\Sigma_{k,ab}^{\mathrm{R}}(\eta, \eta', q) \propto \delta(\eta - \eta' - a)$.

terms from the non-vanishing principal part of the Laurent series. Consider e.g. an affine term and an isolated simple pole, that is the Laurent series features only the $n = \pm 1$ terms. In this case one obtains

$$D^{\mathrm{R}}_{k,ab}(\eta, \eta', q) = D^{(1)}_{k,ab}(\eta, q)\,(\partial_\eta - s_*)\,\delta(\eta - \eta') + D^{(-1)}_{k,ab}(\eta, q)\,\mathrm{e}^{s_*(\eta - \eta')}\,\theta(\eta - \eta')\,, \quad (7.7)$$

naturally leading to memory integrals in the equations of motion.[4]

Classifying the large wave number limit propagators

Consider the ansatz

$$G^{\mathrm{R}}_{k,ab}(\eta, \eta', q) = g^{\mathrm{R}}_{ab}(\eta - \eta')\,F_k(\mathrm{e}^\eta - \mathrm{e}^{\eta'}, q)\,, \quad (7.8)$$

which captures the various large wave number limits discussed in chapter 6, at least when employing the approximation $\Omega_{\mathrm{m}}/f^2 = 1$ such that the linear dynamics are time-translation invariant. To obey the boundary conditions of the propagator one should impose $F_k(0, q) = 1 = F_k(\mathrm{e}^\eta - \mathrm{e}^{\eta'}, 0)$.

Using the ansatz (7.8) as well as the equations of motion (7.3) and projecting onto the single-stream growing mode using $w_a = (1, 1)$, one obtains the evolution equation

$$\partial_\eta F_k(\mathrm{e}^\eta - \mathrm{e}^{\eta'}, q) - \int_{\eta'}^\eta \mathrm{d}\xi\,\mathrm{e}^{\eta + \xi}\,\bar{\Sigma}^{\mathrm{R}}_k(\mathrm{e}^\eta - \mathrm{e}^\xi, q)\,F_k(\mathrm{e}^\xi - \mathrm{e}^{\eta'}, q) = 0\,, \quad (7.9)$$

where it is assumed that

$$\bar{\Sigma}^{\mathrm{R}}_k(\mathrm{e}^\eta - \mathrm{e}^{\eta'}, q) := \mathrm{e}^{-2\eta}\,\tfrac{1}{2}\,w_a w_b \Sigma^{\mathrm{R}}_{k,ab}(\eta, \eta', q)\,, \quad (7.10)$$

captures the time dependence of the self-energy.[5] Taking the Laplace transform with respect to $\mathrm{e}^\eta - \mathrm{e}^{\eta'}$ one arrives at

$$\left[s - \bar{\Sigma}^{\mathrm{R}}_k(s, q)\right] F_k(s, q) = 1\,. \quad (7.12)$$

To understand the structure of the self-energy, one needs to invert the Laplace transform of $s - 1/F_k(s, q)$.

It is straightforward to verify that the three large wave number limit cases discussed in 6 do not correspond to local dynamics since their inverse propagator is no

---

[4]This is for example the case for the 1PI one-loop self-energy which lead to the oscillatory propagator (6.35).

[5]Obviously, this is most generally not the case. But considering the large wave number limit of the Hartree–Fock approximation as derived in chapter 6 one has

$$\bar{\Sigma}^{\mathrm{R}}_k(\mathrm{e}^\eta - \mathrm{e}^{\eta'}, q) = -q^2 \sigma^2_{\mathrm{v},k}\,\mathrm{e}^{-2\eta_{\mathrm{in}}}\,F_k(\mathrm{e}^\eta - \mathrm{e}^{\eta'}, q)\,\theta(\eta - \eta')\,, \quad (7.11)$$

and similarly without the factor additional factor F_k on the right-hand side for the 1PI one-loop approximation.

polynomial in frequency. More explicitly, with $\omega_k(q) = q\sigma_{\mathrm{v},k}\,\mathrm{e}^{-\eta_{\mathrm{in}}}$ one finds that the 1PI one-loop approximation (6.35) corresponds to

$$F_k(s,q) = \frac{s}{s^2 + \omega_k^2}\;, \tag{7.13}$$

the Hartree–Fock approximation (6.36) to

$$F_k(s,q) = \frac{-s + \sqrt{s^2 + 4\omega_k^2}}{2\omega_k^2}\;, \tag{7.14}$$

and the functional renormalisation group result (6.34) to

$$F_k(s,q) = \sqrt{\frac{\pi}{2\omega_k^2}}\,\exp\left\{\frac{s^2}{2\omega_k^2}\right\}\mathrm{erfc}\left\{\sqrt{\frac{s^2}{2\omega_k^2}}\right\}\;, \tag{7.15}$$

where $\mathrm{erfc}(\,\cdot\,)$ is the complementary error function.

Finally, consider the case where the dynamics is actually local and of first order. In this case one has

$$F_k(s,q) = \frac{A_k(q)}{s - \omega_k(q)}\;, \tag{7.16}$$

and consequently

$$F_k(\mathrm{e}^\eta - \mathrm{e}^{\eta'},q) = A_k(q)\exp\left\{\omega_k(q)\left(\mathrm{e}^\eta - \mathrm{e}^{\eta'}\right)\right\}\;. \tag{7.17}$$

It should be clear that this is only a special case of the more general equation (7.3) since here the ansatz (7.8) is already rather restrictive. Nonetheless it captures the spirit of local dynamics, as is seen in the following sections.

7.2 Effective action with local dynamics

7.2.1 Truncation scheme and ansatz

The effective action can be (formally) expanded as

$$\Gamma_k[\Psi,\hat{\Psi}] = \sum_{n\in\mathbb{N}} g_{k,n}\cdot\mathcal{O}_n[\Psi,\hat{\Psi}]\;, \tag{7.18}$$

for a functional basis of operators $\mathcal{O}_n[\Psi,\hat{\Psi}]$ and generalised couplings $g_{k,n}$ where the dot symbolises the summation and integration over all internal structures, such as time and space arguments. This quite general form is not to helpful in real applications and one usually decides on a set of operators which are assumed to be suited. A common expansion scheme is the vertex expansion, where one chooses the operators to be monomials in the fields

$$\mathcal{O}_{A_1\dots A_m B_1\dots B_n} = \prod_{i=1}^{m}\Psi_{A_i}\prod_{j=1}^{n}\hat{\Psi}_{B_j}\;. \tag{7.19}$$

Truncating the expansion at finite order allows to actually close the infinite hierarchy of flow equations derived in chapter 4.

Since a general truncation of the vertex expansion is still rather general, the ansatz used in the following is further restricted. That is, the ansatz is taken to only feature operators which are already present in the bare action and which respect the symmetries, that is statistical isotropy and homogeneity as well as mass conservation and extended Galilean invariance. Further, only operators are allowed that describe local first-order dynamics, that is the same kind of equations that describe the effective cosmological fluid. More specifically, the ansatz considered can be written as

$$
\begin{aligned}
\Gamma_k[\Psi, \hat{\Psi}] = {}& -\mathrm{i} \int_{\eta, \boldsymbol{q}} \hat{\Psi}_a(\eta, -\boldsymbol{q}) \big[\partial_\eta \delta_{ab} + \Omega_{k,ab}(\eta, \boldsymbol{q})\big] \Psi_b(\eta, \boldsymbol{q}) \\
& -\mathrm{i} \int_{\eta, \boldsymbol{q}, \boldsymbol{q}'} \hat{\Psi}_a(\eta, -\boldsymbol{q}) \, \gamma_{k,abc}(\eta, \boldsymbol{q}', \boldsymbol{q} - \boldsymbol{q}') \, \Psi_b(\eta, \boldsymbol{q}') \, \Psi_c(\eta, \boldsymbol{q} - \boldsymbol{q}') \\
& +\mathrm{i} \int_\eta \hat{\Psi}_a(\eta, \boldsymbol{0}) \big[\delta(\eta - \eta_{\mathrm{in}}) \, \Psi_a^{\mathrm{in}} + Q_{k,a}(\eta)\big] \\
& +\tfrac{1}{2} \int_{\eta, \eta', \boldsymbol{q}} \hat{\Psi}_a(\eta, -\boldsymbol{q}) \Big[\delta(\eta - \eta_{\mathrm{in}}) \, \delta(\eta' - \eta_{\mathrm{in}}) \, P_{ab}^{\mathrm{in}}(\boldsymbol{q}) \\
& \hspace{6cm} + \Pi_{k,ab}(\eta, \eta', \boldsymbol{q})\Big] \hat{\Psi}_b(\eta', \boldsymbol{q}) \,.
\end{aligned}
\tag{7.20}
$$

Here $\Omega_{k,ab}$ and $\gamma_{k,abc}$ are scale-dependent generalisations of their bare counterparts and should be chosen to not violate the symmetries studied in section 4.6 of chapter 4. The source term $Q_{k,a}$ and statistical self-energy $\Pi_{k,ab}$ are completely general for now.

The dynamical part of the action is described by first-order local dynamics. More specifically, the inverse retarded propagator reads on the equations of motion

$$
D_{k,ab}^{\mathrm{R}}(\eta, \eta', q) = \big[\partial_\eta \delta_{ab} + \Omega_{k,ab}(\eta, q) + 2\gamma_{k,abc}(\eta, \boldsymbol{q}, \boldsymbol{0}) \, \Psi_c(\eta)\big] \delta(\eta - \eta') \,.
\tag{7.21}
$$

Similarly, the three-point function is local in time

$$
\begin{aligned}
\Gamma_{k,bca}^{(2,1)}(\eta', \boldsymbol{q}'; \eta'', \boldsymbol{q}''; \eta, \boldsymbol{q}) = {}& -2\,\mathrm{i}\, \delta(\eta - \eta') \, \delta(\eta - \eta'') \, \bar{\delta}(\boldsymbol{q} + \boldsymbol{q}' + \boldsymbol{q}'') \\
& \times \gamma_{k,abc}(\eta, \boldsymbol{q}', \boldsymbol{q}'') \,.
\end{aligned}
\tag{7.22}
$$

7.2.2 Flow equations

Since the ansatz (7.20) only includes 1PI correlation functions up to third order, the corresponding functional renormalisation group flow equations are closed and read diagrammatically for the source term

$$
\mathrm{i}\,\partial_k Q_{k,a} = \tfrac{1}{2} \; \text{-- } \!\!\bullet\!\!\bigcirc\!\!\otimes \quad ,
\tag{7.23}
$$

for the inverse propagator

$$\mathrm{i}\,\partial_k \Sigma^{\mathrm{R}}_{k,ab} = -\frac{1}{2} \text{<image>} - \frac{1}{2} \text{<image>} \quad , \tag{7.24}$$

and for the 1PI statistical two-point function

$$\partial_k \Pi_{k,ab} = -\frac{1}{2} \text{<image>} - \frac{1}{2} \text{<image>} \quad , \tag{7.25}$$

and similarly for the 1PI three-point function flow which is not explicitly shown here. These can be written in an explicit manner to read

$$\partial_k Q_{k,a}(\eta) = -\int_l \gamma_{k,abc}(\eta, \boldsymbol{l}, -\boldsymbol{l})\, G^{\mathrm{R}}_{k,c\bar{c}}(\eta, \eta_{\mathrm{in}}, l)\, \partial_k P^{\mathrm{in}}_{k,\bar{c}\bar{d}}(l)\, G^{\mathrm{A}}_{k,\bar{d}d}(\eta_{\mathrm{in}}, \eta, l)\ , \tag{7.26}$$

for the source term,

$$\begin{aligned}
\partial_k \Sigma^{\mathrm{R}}_{k,ab}(\eta, \eta', q) = 4\int_l \gamma_{k,ace}(\eta, \boldsymbol{l}, \boldsymbol{q}-\boldsymbol{l})\, G^{\mathrm{R}}_{k,ef}(\eta, \eta', |\boldsymbol{q}-\boldsymbol{l}|)\, \gamma_{k,fdb}(\eta', -\boldsymbol{l}, \boldsymbol{q}) \\
\times\, G^{\mathrm{R}}_{k,d\bar{d}}(\eta', \eta_{\mathrm{in}}, l)\, \partial_k P^{\mathrm{in}}_{k,\bar{d}\bar{c}}(l)\, G^{\mathrm{A}}_{k,\bar{c}c}(\eta_{\mathrm{in}}, \eta, l)\ ,
\end{aligned} \tag{7.27}$$

for the inverse propagator self-energy,

$$\begin{aligned}
\partial_k \Pi_{k,ab}(\eta, \eta', q) = 4\int_l \gamma_{k,ace}(\eta, \boldsymbol{l}, \boldsymbol{q}-\boldsymbol{l})\, P_{k,ef}(\eta, \eta', |\boldsymbol{q}-\boldsymbol{l}|) \\
\times\, \gamma_{k,bfd}(\eta', -\boldsymbol{q}+\boldsymbol{l}, -\boldsymbol{l}) \\
\times\, G^{\mathrm{R}}_{k,d\bar{d}}(\eta', \eta_{\mathrm{in}}, l)\, \partial_k P^{\mathrm{in}}_{k,\bar{d}\bar{c}}(l)\, G^{\mathrm{A}}_{k,\bar{c}c}(\eta_{\mathrm{in}}, \eta, l)\ ,
\end{aligned} \tag{7.28}$$

for the 1PI statistical self-energy.

7.2.3 Projection onto local ansatz

An obvious problem is that the flow equation for the inverse propagator is non-local in time, opposed to the ansatz (7.20). This reflects that the ansatz is not self-consistent and the renormalisation group flow naturally evolves away from the theory subspace spanned by the effective action ansatz. To project the non-local flow onto the local ansatz the prescription developed in reference [37] is employed. This prescription maps the non-local self-energy flow onto the local ansatz using Laplace transforms which essentially matches the corresponding growth factors of the inverse propagators.

Here the projection prescription developed in reference [37] is reviewed, since it is thereafter used. The idea behind the projection can be understood by considering the simple case of a time-translation invariant system

$$G^{\mathrm{R}}_{ab}(\eta-\eta', q) = \int_{c-\mathrm{i}\infty}^{c+\mathrm{i}\infty} \frac{\mathrm{d}s}{2\pi\,\mathrm{i}}\, \mathrm{e}^{s(\eta-\eta')} \left[D^{\mathrm{R}}(q; s) \right]^{-1}_{ab}\ , \tag{7.29}$$

where c is a real number that is to the right of all singularities. In the case where the integrand has isolated poles only, the integral (7.2) can be computed using Cauchy's residue theorem and the poles determine the growth properties of the propagator. That is, the zeros of the inverse propagator's determinant are of interest. These are precisely the growth factors also studied in chapter 6. In the non-stationary setting equation (7.29) can no longer be used to compute the propagator, but rather the general equation (7.3) needs to be solved using other methods. To project the non-local flow onto the local ansatz, the corresponding zeros of the inverse propagator's determinant are matched. Specifically, consider

$$\det\bigl(D_k^{\mathrm{R}}(\eta, q; s)\bigr) = 0 \ , \tag{7.30}$$

having zeros $s_k(\eta, q)$. Using Jacobi's formula, one can compute the flow equation for the zero-crossing to be [37]

$$\partial_k s_k(\eta, q) = -\frac{\operatorname{tr}\bigl(D_k^{\mathrm{R}}(\eta, q; s)^{-1} \cdot \partial_k D_k^{\mathrm{R}}(\eta, q; s)\bigr)}{\operatorname{tr}\bigl(D_k^{\mathrm{R}}(\eta, q; s)^{-1} \cdot \partial_s D_k^{\mathrm{R}}(\eta, q; s)\bigr)}\Bigg|_{s=s_k(\eta, q)} \ . \tag{7.31}$$

The right-hand side can now be computed using the local ansatz

$$D_{k,ab}^{\mathrm{R}}(\eta, q; s) = s\delta_{ab} + \Omega_{k,ab}(\eta, q) + 2\gamma_{k,abc}(\eta, \boldsymbol{q}, \boldsymbol{0})\, \Phi_c(\eta) \ , \tag{7.32}$$

as well as using the flow equation (7.27) in order to match the zero-crossings. This is how the non-local flow is projected onto a local ansatz in the following.

7.3 Propagator

To reduce the complexity and understand general properties of such a local ansatz, the single-stream approximation is considered. This simplifies matters extremely due to the absence of mean fields. The field content is set to

$$\psi_a(\eta, \boldsymbol{q}) = \left(\delta, \quad -\frac{\theta}{f\mathcal{H}}\right) \ , \tag{7.33}$$

and further the approximation $\Omega_{\mathrm{m}}/f^2 = 1$ is employed such that

$$\Omega_{ab} = \begin{pmatrix} 0 & -1 \\ -\frac{3}{2} & \frac{1}{2} \end{pmatrix} \ . \tag{7.34}$$

Since the ansatz (7.20) is still quite general, the aim is to find only a few flow parameters which sufficiently well describe the effective dynamics of cosmic structure formation. To this end, the vertex is set to its bare form and only ansätze of the form

$$\Omega_{k,ab}(\eta, q) = \Omega_{ab} + \lambda_{k,ab}\, \mathrm{e}^{\kappa_k \eta}\, q^2 \ , \tag{7.35}$$

are considered and it is shown *a posteriori* that these kind of ansätze, if chosen appropriately, capture the dominant wave number and time behaviour obtained

from other approximations. That is, the dynamics are corrected due to gradients in the linear part and should be understood as a derivative expansion. Note here, that although only corrections up to order q^2 are taken into account, this is at the level of the inverse propagator and thus by the virtue of the 1PI resummation scheme leads to a non-perturbative propagator to all orders in q. The exponential dependence on the time evolution parameter η is motivated by the one-loop result which features such a time dependence.

Due to the structure of the ansatz one has the zero-crossings

$$s_{\text{g},k}(\eta, q) = 1 + \mathcal{O}(q^2) , \qquad s_{\text{d},k}(\eta, q) = -\frac{3}{2} + \mathcal{O}(q^2) , \qquad (7.36)$$

which smoothly connect to the standard single-stream approximation growth factors studied in chapter 6. Since the projection (7.31) is rather complicated in full form, the zero-crossing flow is only solved up to order q^2 in the spirit of the derivative expansion. That is, using that the self-energy vanishes in the limit $q \to 0$ for this ansatz, the zero-crossing flow at order q^2 is given by

$$\partial_{q^2} \partial_k s_k(\eta, 0) = \frac{1}{4s+1} \, \text{tr}\left(\begin{pmatrix} 2s+1 & 2 \\ 3 & 2s \end{pmatrix} \cdot \partial_{q^2} \partial_k \Sigma_k^{\text{R}}(\eta, 0; s) \right) \Bigg|_{s=s_k(\eta, 0)} . \qquad (7.37)$$

In the following, this is abbreviated at order q^2 as

$$\begin{aligned} \text{Flow}_{\text{g},k}(\eta) &:= \frac{1}{5} \, \text{tr}\left(\begin{pmatrix} 3 & 2 \\ 3 & 2 \end{pmatrix} \cdot \partial_{q^2} \partial_k \Sigma_k^{\text{R}}(\eta, q; 1) \Big|_{q^2=0} \right) , \\ \text{Flow}_{\text{d},k}(\eta) &:= -\frac{1}{5} \, \text{tr}\left(\begin{pmatrix} -2 & 2 \\ 3 & -3 \end{pmatrix} \cdot \partial_{q^2} \partial_k \Sigma_k^{\text{R}}(\eta, q; -\tfrac{3}{2}) \Big|_{q^2=0} \right) , \end{aligned} \qquad (7.38)$$

for the growing mode $s_{\text{g},k}(\eta, 0) = 1$ and decaying mode $s_{\text{d},k}(\eta, 0) = -3/2$, respectively. It should be noted that there might be more zero-crossings due to the non-local structure of the full non-perturbative self-energy. Here only those are taking into account that smoothly connect to the linear growing and decaying mode.

Although the ansatz (7.35) can in principal be solved using numerical methods, it is preferred here to find an ansatz that can be solved analytically, at least to some extent. To this end, the question arises what kind of coefficients are necessary to capture the dominant physics. Reference [37] has studied the case where

$$\lambda_k = \begin{pmatrix} 0 & 0 \\ \lambda_{\text{s},k} & \lambda_{\nu,k} \end{pmatrix} , \qquad (7.39)$$

where the coefficients $\lambda_{\text{s},k}$ and $\lambda_{\nu,k}$ are interpreted as effective sound velocity and viscosity, respectively, thereby mapping the non-local flow onto a viscous fluid theory. The main deficit of the approach is that the corresponding density propagator fails to reproduce the characteristic suppressions on small scales, associated with the sweeping effect as is later shown.

The reason for this is, as already mentioned, that the sweeping effect causes this suppression. In order to capture it, one would need coefficients in each equation of motion coupling to the field that carries the time derivative. That is, these are terms that live on the diagonal of λ_{ab} and can be interpreted as an effective convective derivative in the sense that the coefficient acts similar to a velocity background. In the viscous ansatz (7.39) such a coefficient exists for the velocity-divergence field but not for the density contrast field, leading to a suppression in the velocity propagator and near to no suppression in the density propagator. To overcome this, two ansätze are studied, one where a single coefficient is included and a second one allowing for more dependence in the flow, where two coefficients are included.

7.3.1 One-loop approximation

For the one-loop approximation, the propagators and power spectrum on the right-hand side of the flow equation (7.27) are set to their linear form, such that the equation has a perturbative one-loop structure. In this case one obtains for the order q^2 self-energy

$$\partial_{q^2}\partial_k \Sigma_k^{\mathrm{R}}(\eta, q; s)\Big|_{q^2=0} = -\frac{\mathrm{e}^{2(\eta-\eta_{\mathrm{in}})}\,\sigma_{\mathrm{v},k}^2}{2s^2+5s}\begin{pmatrix} 2s-3 & 4/5 \\ 9 & 2s+8 \end{pmatrix}, \tag{7.40}$$

and thus finds the flows

$$\mathrm{Flow}_{\mathrm{g},k}(\eta) = -\frac{187}{175}\,\mathrm{e}^{2(\eta-\eta_{\mathrm{in}})}\,\sigma_{\mathrm{v},k}^2\,, \qquad \mathrm{Flow}_{\mathrm{d},k}(\eta) = -\frac{29}{25}\,\mathrm{e}^{2(\eta-\eta_{\mathrm{in}})}\,\sigma_{\mathrm{v},k}^2\,. \tag{7.41}$$

Since both growth factors are corrected by a negative term, the growth of modes is suppressed due to non-linearities. These values are used for the two ansätze studied in the following section to initialise the flow at some large infrared scale.

7.3.2 One-coefficient ansatz

As a first example, the ansatz

$$\lambda_{k,ab} = \lambda_k \delta_{ab}\,, \tag{7.42}$$

is considered. The corresponding propagator can be solved for analytically and reads

$$G_{k,ab}^{\mathrm{R}}(\eta, \eta', q) = g_{ab}^{\mathrm{R}}(\eta-\eta')\exp\left\{-\frac{\lambda_k}{\kappa_k}\,q^2\left[\mathrm{e}^{\kappa_k\eta}-\mathrm{e}^{\kappa_k\eta'}\right]\right\}, \tag{7.43}$$

where the single-stream approximation linear retarded propagator $g_{ab}^{\mathrm{R}}(\eta-\eta')$ is given by the upper left (2×2)-block of equation (6.16) given in chapter 6. Notice here the close relation to the simplified version (7.17) of a local dynamics ansatz although a more general time dependence is allowed here due to the coefficient κ_k.

The zero-crossings of the ansatz are then given by

$$s_k^{(1)}(\eta, q) = 1 - \lambda_k\,\mathrm{e}^{\kappa_k\eta}\,q^2\,, \qquad s_k^{(2)}(\eta, q) = -\frac{3}{2} - \lambda_k\,\mathrm{e}^{\kappa_k\eta}\,q^2\,. \tag{7.44}$$

To match the renormalisation group flow to the coefficients, one still has the freedom how to do so since there are two flow equations. Since one expects that the growing mode determines most of the late-time structure formation, here it is chosen to compute the flow of the zero-crossings using only the flow of $s_k^{(1)}(\eta, q)$.[6] Then the relevant flow equation reads

$$\partial_k(\lambda_k \, e^{\kappa_k \eta}) = -\text{Flow}_{\text{g},k}(\eta) \,. \tag{7.45}$$

Since the time dependence of the flow is not completely captured by the ansatz, one further needs to specify how to project to the two coefficients. This is done by applying a time derivative and evaluating the flow at some (arbitrary) projection time η_*. By doing so one obtains the two flow equations

$$\partial_k\lambda_k = e^{-\kappa_k \eta_*} \left[\eta_*\text{Flow}'_{\text{g},k}(\eta_*) - (1 + \kappa_k\eta_*)\,\text{Flow}_{\text{g},k}(\eta_*) \right] \,, \tag{7.46}$$

and

$$\partial_k\kappa_k = \frac{e^{-\kappa_k \eta_*}}{\lambda_k} \left[\kappa_k\text{Flow}_{\text{g},k}(\eta_*) - \text{Flow}'_{\text{g},k}(\eta_*) \right] \,, \tag{7.47}$$

where the time derivative of the flow is abbreviated as $\text{Flow}'_{\text{g},k}(\eta) := \partial_\eta\text{Flow}_{\text{g},k}(\eta)$. One should check that the time dependence on η_* is weak, otherwise indicating that the ansatz does not capture the dominant time dependence. An explicit formula for $\text{Flow}'_{\text{g},k}(\eta)$ is given in appendix E.

For the numerical solutions of the flow equations (7.46) and (7.47) an initial power spectrum is taken from the Eisenstein & Hu fitting formula [177] at $z = 99$ and the Planck 2018 parameters [162]. The flow is then initialised at $k_{\text{in}} = 10^{-3} \, h/\text{Mpc}$ with the one-loop values,

$$\lambda_k = \frac{187}{175} \, \sigma_{\text{v},k}^2 \,, \qquad \kappa_k = 2 \,, \tag{7.48}$$

although these are also varied in order to check the robustness of the flows and fixed points. The flow of the amplitude coefficient λ_k and exponent characterising the time dependence κ_k for a projection time $\eta_* = 0$ corresponding to today, are shown in figure 7.1. Both coefficients initially follow the one-loop result as the amount of fluctuations allowed by the regulator is small and a perturbative treatment is applicable. Around the scale $k \approx 0.05 \, h/\text{Mpc}$ the full flow equation starts to deviate from the one-loop prediction, at least when the projection time is close to today. For a projection time chosen at earlier times the flow approaches the one-loop result, which is not to surprising since at earlier times perturbation theory is applicable at smaller scales.

The corresponding reduced propagator normalised to the linear one at the fixed point is shown in figure 7.2. Since the density and velocity-divergence reduced propagators are the same in this approximation, only one propagator is shown here. Shown is also the functional renormalisation group result obtained in chapter 5

---

[6]Additionally, the region of convergence of the self-energy Laplace transform is given by $\text{Re}(s) > 0$. Using the decaying mode might involve analytically continuing the flow numerically as done in the next section.
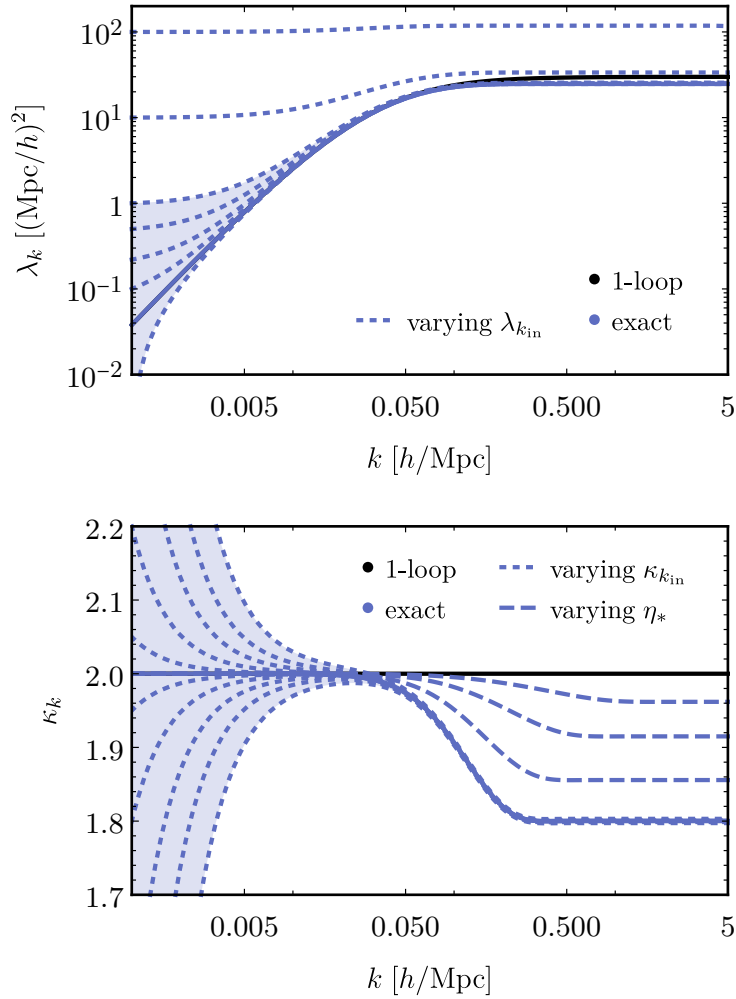
Figure 7.1: Renormalisation group flow of the coefficients λ_k (upper panel) and κ_k (lower panel) for a projection time $\eta_* = 0$ corresponding to today. Shown is the one-loop result (black solid curves), varying initial conditions (dotted blue curves) as well as also different projection times (dashed blue curves). It is clearly visible that the coefficients approach a fixed point near to independent of the initial condition. Varying the amplitude coefficient by several orders of magnitude shifts the respective fixed point. Changing the projection time also shifts the fixed point, between the values attained at a projection time $\eta_* = 0$ and $\eta_* = \eta_{\text{in}}$, where the fixed point coincides with the one-loop result.
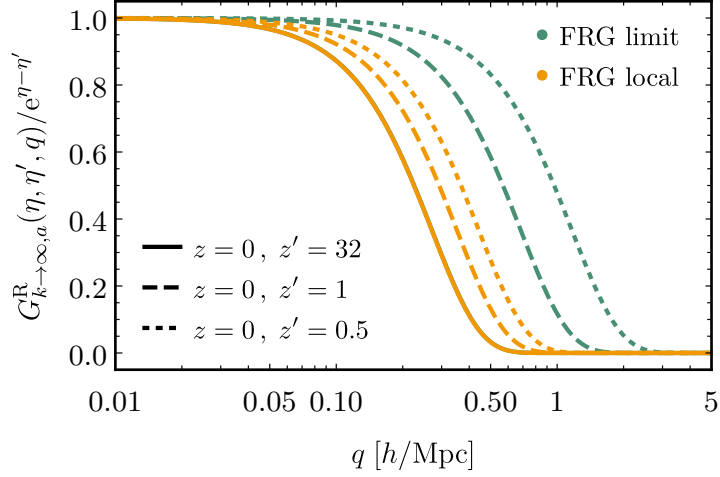
Figure 7.2: Reduced propagator at the fixed point for the local-time ansatz (yellow curves) in the single-stream approximation with coefficients λ_k and κ_k. Also shown is the reduced propagator obtained from the large wave number limit (green curves). For large time differences the propagators nearly coincide while for small time differences they differ. This can be directly attributed to the time-local ansatz of the inverse propagator.

which features the Gaussian suppression factor. As is evident, the propagators nearly coincide at large time differences, whereas at small time differences they show different suppression scales. This is clear from the analytical result (7.43) which leads to a much slower 'opening' of the propagator when the time difference is lowered due to the different time dependencies $(\mathrm{e}^{\kappa_k \eta} - \mathrm{e}^{\kappa_k \eta'})$ and $(\mathrm{e}^\eta - \mathrm{e}^{\eta'})^2$. From the perspective of the Laplace transform this can be understood as follows. As was discussed at the beginning of this chapter, the local ansatz corresponds to a Taylor expansion in complex frequency, very similar to a derivative expansion in gradients. Naturally, this only accounts for small frequencies corresponding to large time differences. Therefore this sector should be captured well while the short time difference sector is dominated by the principal part of the Laurent series and corresponds to memory effects.

It is emphasised that the Gaussian suppression factor obtained in the large wave number limit of the functional renormalisation group flow is also obtain in an approximation for the function I_k which determined the flow equations, see also equation (5.27), and in general it is not clear whether the full non-perturbative propagator really shows such a Gaussian suppression in the time difference $(\mathrm{e}^\eta - \mathrm{e}^{\eta'})^2$.

7.3.3 Two-coefficient ansatz

To improve the ansatz and allow for more dependence in the flow, the more general ansatz

$$\lambda_{k,ab} = \begin{pmatrix} \lambda_{1,k} & 0 \\ 0 & \lambda_{2,k} \end{pmatrix} , \tag{7.49}$$

is considered. Structurally, the ansatz still features coefficients which describe corrections that involve to the fields that carry the time derivative, but allow the amplitude of these terms to be different. In this case the propagator is build from the growing solution

$$F_{\mathrm{g},k}(\eta, q) = \mathrm{e}^\eta \, \mathrm{e}^{-\frac{\lambda_{1,k}}{\kappa_k} q^2 \mathrm{e}^{\kappa_k \eta}} \, {}_1F_1\!\left(\tfrac{1}{\kappa_k} \, ; \, 1 + \tfrac{5}{2\kappa_k} \, ; \, -\tfrac{\lambda_{2,k} - \lambda_{1,k}}{\kappa_k} q^2 \, \mathrm{e}^{\kappa_k \eta} \right) , \tag{7.50}$$

and decaying solution

$$F_{\mathrm{d},k}(\eta, q) = \mathrm{e}^{-\frac{3}{2}\eta} \, \mathrm{e}^{-\frac{\lambda_{1,k}}{\kappa_k} q^2 \mathrm{e}^{\kappa_k \eta}} \, {}_1F_1\!\left(-\tfrac{3}{2\kappa_k} \, ; \, 1 - \tfrac{5}{2\kappa_k} \, ; \, -\tfrac{\lambda_{2,k} - \lambda_{1,k}}{\kappa_k} q^2 \, \mathrm{e}^{\kappa_k \eta} \right) , \tag{7.51}$$

where ${}_1F_1$ is Kummer's confluent hypergeometric function. Using the matrix

$$U_k(\eta, q) = \begin{pmatrix} F_{\mathrm{g},k}(\eta, q) & F_{\mathrm{d},k}(\eta, q) \\ \left[\partial_\eta + \lambda_{1,k} \, \mathrm{e}^{\kappa_k \eta} \, q^2 \right] F_{\mathrm{g},k}(\eta, q) & \left[\partial_\eta + \lambda_{1,k} \, \mathrm{e}^{\kappa_k \eta} \, q^2 \right] F_{\mathrm{d},k}(\eta, q) \end{pmatrix} , \tag{7.52}$$

the propagator can then be reconstructed as

$$G^{\mathrm{R}}_{k,ac}(\eta, \eta', q) = U_{k,ab}(\eta, q) \, U_{k,bc}(\eta', q)^{-1} \, \theta(\eta - \eta') . \tag{7.53}$$

In this case the flow is already more complicated and the corresponding inverse propagator's zero-crossings need to be expanded. Up to order q^2 these are given by

$$\begin{aligned} s_{\mathrm{g},k}(\eta, q) &= 1 - \left[\tfrac{3}{5}\lambda_{1,k} + \tfrac{2}{5}\lambda_{2,k} \right] \mathrm{e}^{\kappa_k \eta} \, q^2 + \mathcal{O}(q^4) , \\ s_{\mathrm{d},k}(\eta, q) &= -\tfrac{3}{2} - \left[\tfrac{2}{5}\lambda_{1,k} + \tfrac{3}{5}\lambda_{2,k} \right] \mathrm{e}^{\kappa_k \eta} \, q^2 + \mathcal{O}(q^4) . \end{aligned} \tag{7.54}$$

To study the flow of the two amplitude coefficients independently, the flow of both zero-crossings must be taken into account,

$$\begin{aligned} \partial_k \left[\lambda_{1,k} \, \mathrm{e}^{\kappa_k \eta} \right] &= -3 \, \mathrm{Flow}_{\mathrm{g},k}(\eta) + 2 \, \mathrm{Flow}_{\mathrm{d},k}(\eta) , \\ \partial_k \left[\lambda_{2,k} \, \mathrm{e}^{\kappa_k \eta} \right] &= 2 \, \mathrm{Flow}_{\mathrm{g},k}(\eta) - 3 \, \mathrm{Flow}_{\mathrm{d},k}(\eta) . \end{aligned} \tag{7.55}$$

As before, the flow is projected to some time η_* and the flow of the coefficient κ_k describing the time evolution is again computed from the flow of the growing mode

zero-crossing only. One then finds

$$
\begin{aligned}
\partial_k \lambda_{1,k} = \frac{\mathrm{e}^{-\kappa_k \eta_*}}{3\lambda_{1,k} + 2\lambda_{2,k}} \Big[& 5\lambda_{1,k}\eta_* \,\mathrm{Flow}_{\mathrm{g},k}'(\eta_*) \\
& - (9\lambda_{1,k} + 6\lambda_{2,k} + 5\lambda_{1,k}\kappa_k\eta_*) \,\mathrm{Flow}_{\mathrm{g},k}(\eta_*) \\
& + (6\lambda_{1,k} + 4\lambda_{2,k}) \,\mathrm{Flow}_{\mathrm{d},k}(\eta_*) \Big] , \\
\partial_k \lambda_{2,k} = \frac{\mathrm{e}^{-\kappa_k \eta_*}}{3\lambda_{1,k} + 2\lambda_{2,k}} \Big[& 5\lambda_{2,k}\eta_* \,\mathrm{Flow}_{\mathrm{g},k}'(\eta_*) \\
& + (6\lambda_{1,k} + 4\lambda_{2,k} - 5\lambda_{2,k}\kappa_k\eta_*) \,\mathrm{Flow}_{\mathrm{g},k}(\eta_*) \\
& - (9\lambda_{1,k} + 6\lambda_{2,k}) \,\mathrm{Flow}_{\mathrm{d},k}(\eta_*) \Big] , \\
\partial_k \kappa_k = \frac{5\,\mathrm{e}^{-\kappa_k \eta_*}}{3\lambda_{1,k} + 2\lambda_{2,k}} \Big[& \kappa_k \,\mathrm{Flow}_{\mathrm{g},k}(\eta_*) - \mathrm{Flow}_{\mathrm{g},k}'(\eta_*) \Big] .
\end{aligned}
\tag{7.56}
$$

A problem occurring in a description with two coefficient is that the flow involves the self-energy evaluated at the decaying mode zero-crossing, which is negative. Since the Laplace transform only has a region of convergence $\mathrm{Re}(s) > 0$ and cannot be performed analytically due to the rather involving propagator (7.53), the self-energy needs to be analytically continued by numerical methods. There is no obvious way how to do this in general and one would therefore rather prefer to work in an approximation which allows to perform the Laplace transformation explicitly. To this end the hypergeometric functions within the propagator (7.53) are expanded using the generalised hypergeometric series expansion

$$
{}_1F_1\left(a; b; z\right) = \sum_{n=0}^{\infty} \frac{a^{(n)} z^n}{b^{(n)} n!} ,
\tag{7.57}
$$

where $a^{(n)}$ and $b^{(n)}$ denote the rising factorial for any real number a and b. It is noted that this expansion is still non-perturbative in the wave number q^2 due to the exponential decaying prefactors in the propagator (7.53). Also note that the suppression in the exponential prefactor, as written in equation (7.53), is due to the coefficient $\lambda_{1,k}$. This must not necessarily be the case, since it can be exchange with the coefficient $\lambda_{2,k}$ using Kummer's transformation

$$
{}_1F_1\left(a; b; z\right) = \mathrm{e}^z \,{}_1F_1\left(b - a; b; -z\right) .
\tag{7.58}
$$

Applying this transformation first and then using the series expansion (7.57) allows to keep either of the two amplitude coefficients as suppression factor.

In the following, only the terms $n = 0, 1$ of the expansion (7.57) are taken into account. Effectively this gives a flow of the order k^2, up to an overall non-perturbative prefactor

$$
\propto \exp\!\left(-\frac{2\lambda_{i,k}}{\kappa_k} \, k^2 \, \mathrm{e}^{\kappa_k \eta} \right) ,
\tag{7.59}
$$

due to the two propagators attached to the regulator in equation (7.27). These are evaluated at a loop wave number of magnitude k and where $i = 1, 2$, depending

on which coefficient is extracted. Due to this fact, the flow equations should be treated with care for renormalisation group scales $k^2 \lambda_{i,k} \gtrsim 1$. The explicit forms of $\mathrm{Flow}_{\mathrm{g},k}(\eta_*)$ and $\mathrm{Flow}_{\mathrm{d},k}(\eta_*)$ in this approximation, in the following referred to as 'leading-order' approximation, are again listed in appendix E.

The flow is initialised at $k_{\mathrm{in}} = 10^{-3} \ h/\mathrm{Mpc}$ with the one-loop values,

$$\lambda_{1,k} = \frac{31}{35} \, \sigma_{\mathrm{v},k}^2 \ , \qquad \lambda_{2,k} = \frac{47}{35} \, \sigma_{\mathrm{v},k}^2 \ , \qquad \kappa_k = 2 \ , \tag{7.60}$$

which are also varied to check the robustness of the flow. Additionally, the self-energy is also numerically analytically continued using the Schlessinger Point Method (SPM) [178, 179] to verify that the leading-order approximation is indeed justified. Since performing the analytical continuation numerically is quite time intensive, it is only computed for a single set of initial conditions.

The flow of the amplitude coefficients $\lambda_{1,k}$ and $\lambda_{2,k}$ for a projection time $\eta_* = 0$ are shown in figure 7.3 and of the coefficient κ_k in figure 7.4. Similar to the case with one coefficient these approach fixed points in the ultraviolet which are robust against changing the initial conditions, at least if not changing them by several orders of magnitude. The flow is solved for two cases, namely by extracting the $\lambda_{1,k}$ or the $\lambda_{2,k}$ coefficient as in the prefactor (7.59). Indeed, it is seen that only the latter choice gives a stable renormalisation group flow while the former choice leads to a blow up at finite renormalisation group scale. Also shown is the full numerically analytically continued result which coincides with the leading-order approximation that uses $\lambda_{2,k}$, at least up to the scale shown. After this scale it becomes numerically rather challenging to solve the analytically continued flow since it seems to become stiff. Nonetheless, the flow seems to be already in the fixed point at this renormalisation group scale, indicating that the leading-order approximation using $\lambda_{2,k}$ describes the flow sufficiently well.

The corresponding reduced propagators at the fixed point are shown for the density contrast in figure 7.5 and for the velocity-divergence in figure 7.6. As a comparison also shown are the propagators obtained when employing the mapping onto a viscous theory studied in reference [37]. The density contrast reduced propagator for the time-local ansatz is similar to the propagator with only one coefficient shown in figure 7.2. A sight difference can be seen when considering the largest time difference which is due to the more general dependence of the ansatz. Compared to the viscous propagators it is clearly visible that the time-local ansatz is much stronger suppressed at small scales. As was mentioned before, this is due to the fact that there is no coefficient in the continuity equation that can account for the non-linear coupling of modes and suppress the density response. The suppression observed is solely due to the viscous coefficients entering Euler's equations and seem to suppress the density response only at much smaller scales. The velocity-divergence reduced propagators show similar suppression behaviour and the characteristic 'slower opening' of the propagator when compared to the propagators obtained from the large wave number limit.
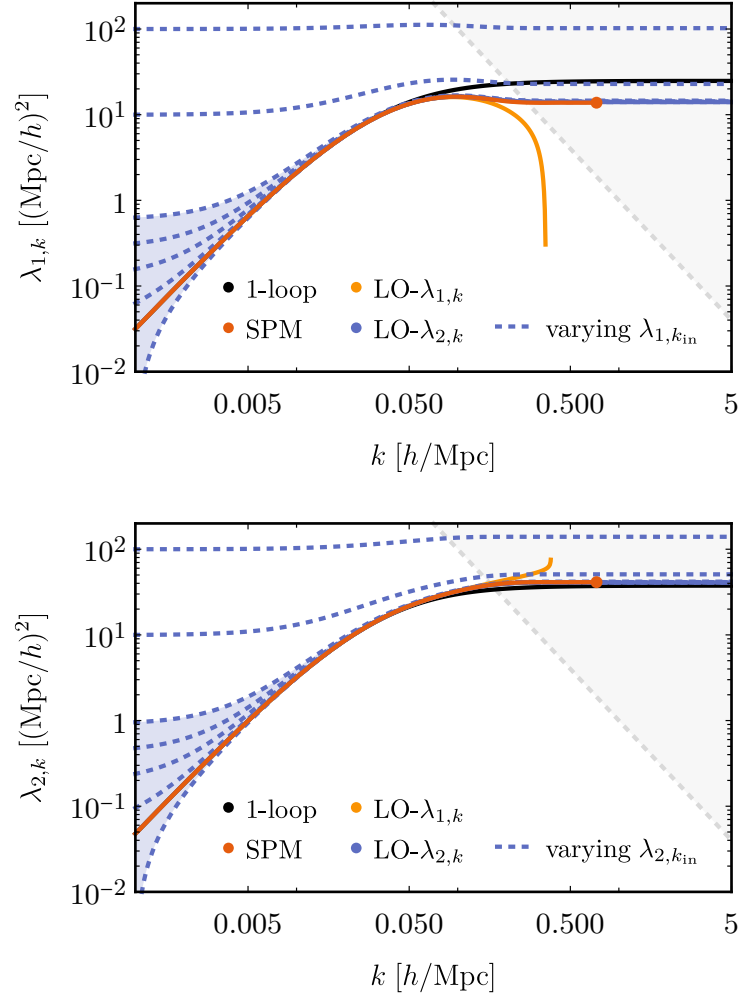
Figure 7.3: The flow of the coefficients $\lambda_{1,k}$ and $\lambda_{2,k}$ for a projection time $\eta_* = 0$. The flow is solved at one-loop (black curves), using the leading-order approximation (blue and yellow curves) and with the SPM (red curve). The leading-order approximation based on the coefficient $\lambda_{2,k}$ is stable and coincides with the SPM while using the coefficient $\lambda_{1,k}$ leads to a blow up at finite renormalisation group scale. The grey shaded region indicates where $k^2\lambda_{i,k} \leq 1$.
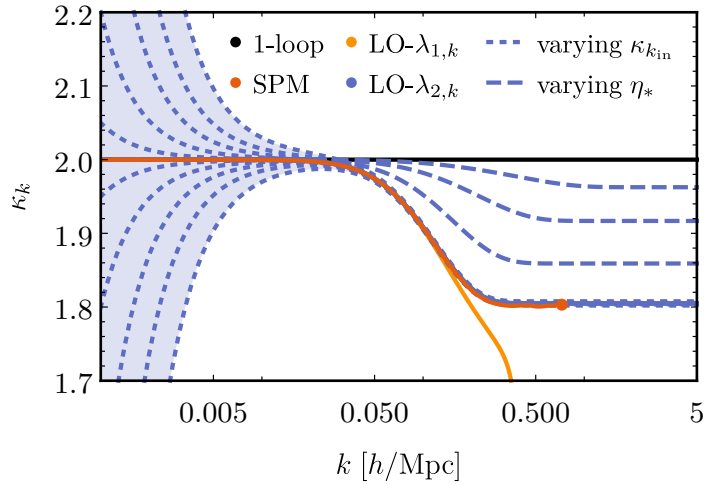
Figure 7.4: The flow of the coefficient κ_k for a projection time $\eta_* = 0$. The flow is solved at one-loop (black curves), using the leading-order approximation (blue and yellow curves) and with the SPM (red curve). The leading-order approximation based on the coefficient $\lambda_{2,k}$ is stable and coincides with the SPM while using the coefficient $\lambda_{1,k}$ leads to a blow up at finite renormalisation group scale.

Simulation	Cosmology	Code	N_{grid}	L_{box} [Mpc/h]	z_{in}
HR2 [166]	WMAP5 [159]	GOTPM [163]	6000	7200	32
HAA15 [167]	WMAP7 [160]	L-GADGET-3 [165]	1024	1000	100

Table 7.1: Details of the *N*-body simulations that are used as comparison to the functional renormalisation group results.

7.4 Power spectrum

As a first application of the renormalisation group to the power spectrum, the 1PI statistical self-energy flow (7.28) is solved at one-loop level and used to compute the power spectrum using the formula (4.38) and the full propagators obtained from the large wave number limit as well as those from the time-local ansatz. Although it would be interesting to solve the full flow equation (7.28), this is more involving since the power spectrum itself enters into the equation and is therefore left for future work.

In the following numerical solutions for the the power spectra are shown and compared to data from *N*-body simulations. To this end, the numerical solutions are computed with an infrared cut-off corresponding to the fundamental wave number of the simulation box size, $k_{\text{f}} = 2\pi/L_{\text{box}}$. The initial power spectra are generated
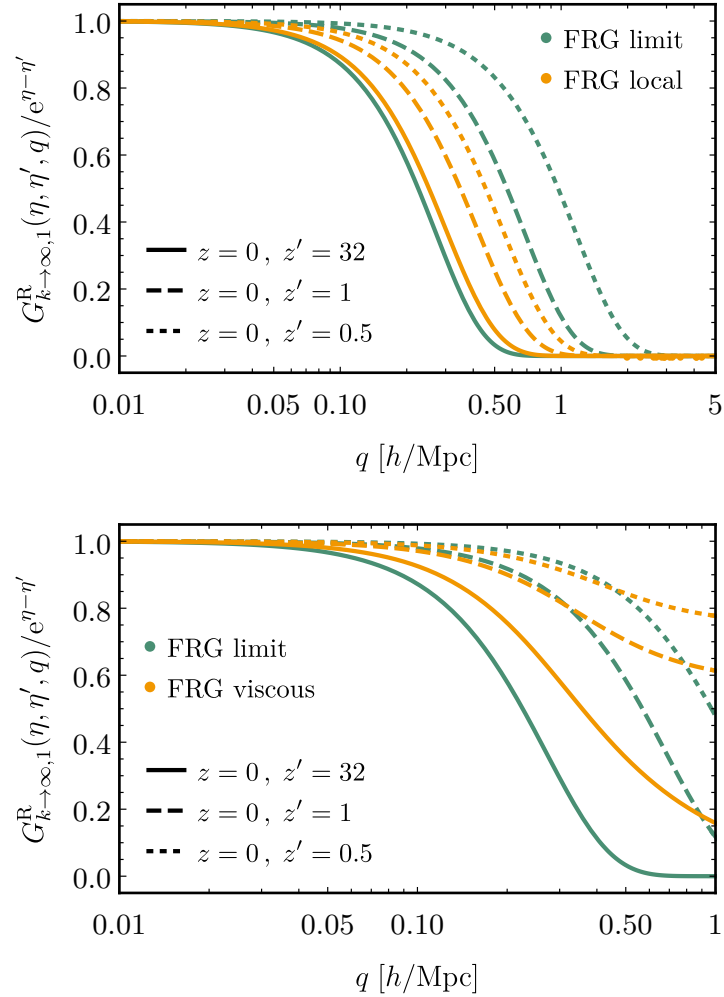
Figure 7.5: Reduced density contrast propagator obtained from the ansatz (7.49) (upper panel) and for the viscous ansatz (7.39) (lower panel) at the fixed point for the local-time ansatz (yellow curves) in the single-stream approximation. Also shown is the reduced propagator obtained from the large wave number limit (green curves). It is clearly visible that the density propagator obtained from mapping to a viscous theory is much less suppressed at small scales due to the absence of a coefficient in the continuity equation.
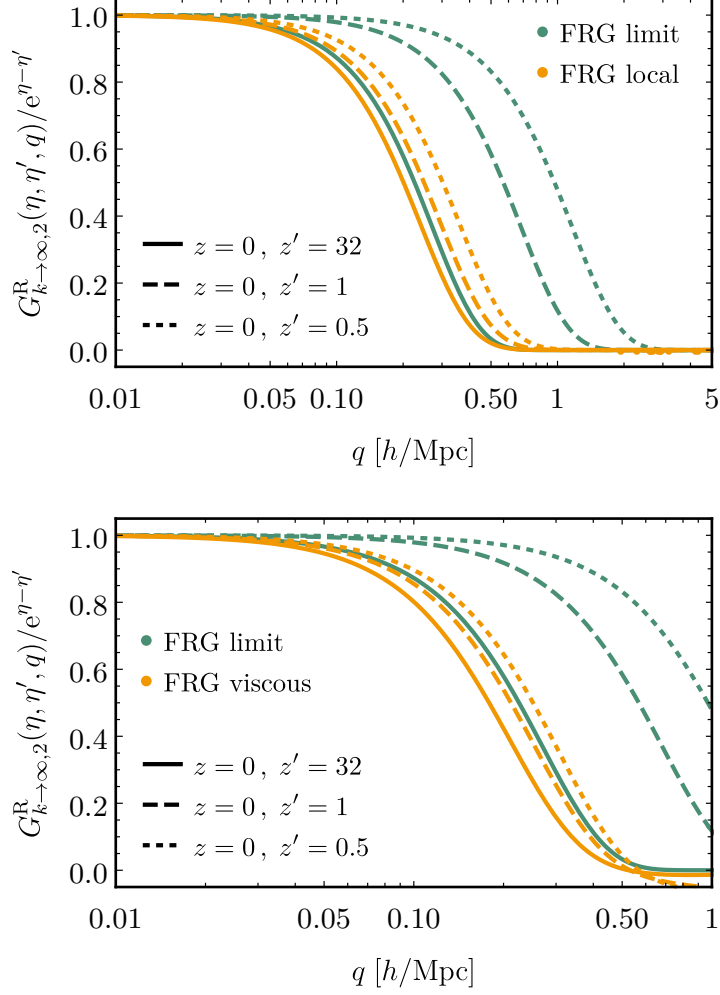
Figure 7.6: Reduced velocity-divergence propagator obtained from the ansatz (7.49) (upper panel) and for the viscous ansatz (7.39) (lower panel) at the fixed point for the local-time ansatz (yellow curves) in the single-stream approximation. Also shown is the reduced propagator obtained from the large wave number limit (green curves). The propagators behave similarly, with minor difference such as that the viscous velocity-divergence propagator also obtains negative values.
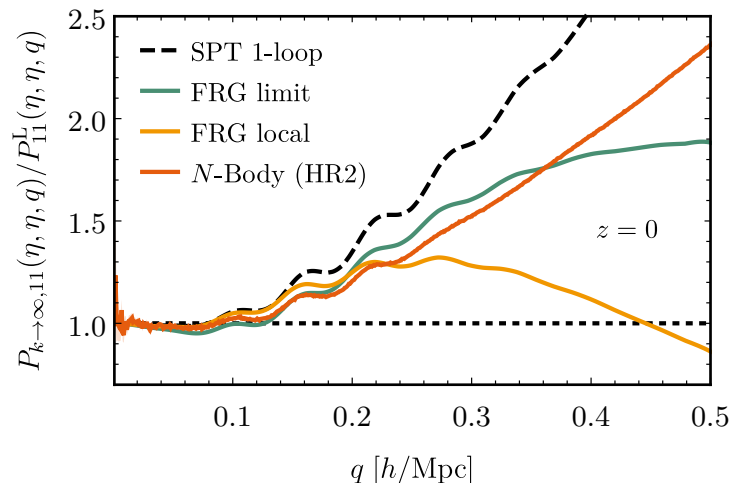
Figure 7.7: Density contrast auto-spectrum at the fixed point normalised to the linear one. Shown is the standard perturbation theory one-loop prediction (black dashed curve), the functional renormalisation group (FRG) calculation using the large wave number limit (green solid curve) as well as the time-local ansatz (yellow solid curve) propagator and data from the HR2 *N*-body simulation (red solid curve).

at a redshift z_{in} listed in table 7.1, using the CLASS code [157] and for cosmological parameters from the Wilkinson Microwave Anisotropy Probe, either from the five-year (WMAP5) [159] or seven-year (WMAP7) [160] mission. The density contrast auto-spectrum is compared to data from the Horizon Run 2 (HR2) *N*-body simulations [166] while the velocity-divergence-density contrast cross-power spectrum as well as the velocity-divergence auto-spectrum is compared to the *N*-body data fit of Hahn, Angulo & Abel (HAA) [167]. This is summarised in table 7.1.

In figure 7.7 the density contrast auto-spectrum is shown at redshift $z = 0$. The density-contrast power spectrum obtained from the time-local and large wave number propagator both perform better than the standard perturbation theory one-loop prediction and are close to the *N*-body power spectrum up to scales $k \approx 0.2\ h/\text{Mpc}$. The result obtained when using the large wave number propagator is slightly more accurate for small wave numbers while the result obtained from the time-local ansatz seems to follow the standard perturbative result at very small wave numbers, before underestimating the *N*-body power spectrum badly. One could conjecture that this is due to neglecting vertex corrections in the time-local ansatz studied here, although this is not completely clear.

In figure 7.8 the velocity-divergence-density contrast cross- and velocity-divergence auto-spectrum are shown at redshift $z = 0$. Both power spectra are much better captured by the time-local ansatz than with the large wave number limit propagator. For the velocity-divergence auto-spectrum the results using the time-local ansatz
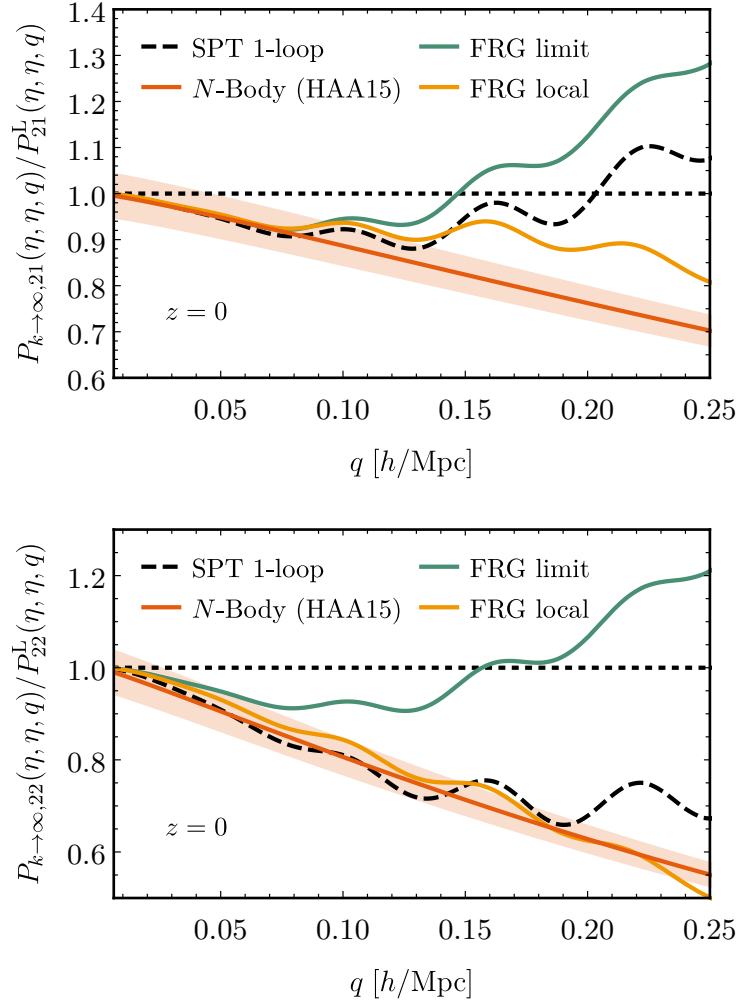
Figure 7.8: Velocity-divergence-density contrast cross-spectrum (upper panel) and velocity-divergence auto-spectrum (lower panel) at the fixed point normalised to the linear one. Shown is the standard perturbation theory one-loop prediction (black dashed curve), the functional renormalisation group (FRG) calculation using the large wave number limit (green solid curve) as well as the time-local ansatz (yellow solid curve) propagator and data from the HR2 *N*-body simulation (red solid curve).

even captures the power spectrum within the error up to $k \approx 0.2 \ h/\text{Mpc}$. While this is an improvement over the standard perturbative result it is emphasised that in chapter 6 it was shown that a major contribution to the drop in the velocity-divergence auto-spectrum is due to the transfer of power to vorticity modes. This typically happens at much smaller scales and the onset of the suppression seen here seem to be due to the non-linear coupling of modes. This seems to be captured much better by the time-local ansatz than the large wave number limit propagator.

8 Discussion and outlook

In this thesis the gravitational dynamics of dark matter have been studied in a kinetic theory approach that is extending the perfect pressureless fluid description. Moreover, correlation functions that quantify the statistical properties of dark matter have been calculated with non-perturbative functional methods that allow predictions in the non-linear regime of cosmic structure formation.

In chapter 2 it has been motivated that an extension of the perfect pressureless fluid description of dark matter is necessary to account for small-scale physical phenomena such as shell-crossing. While the inclusion of the velocity dispersion tensor into the dark matter description cannot account for such phenomena microscopically, it captures these effects in terms of an effective theory description. Although the Vlasov hierarchy is not closed under a truncation of the cumulant expansion after the first order, it has been motivated that a truncation including the velocity dispersion tensor can be sensible for a description of late-time dark matter dynamics.

Building on earlier work [27, 28, 35, 37], a statistical field theory formulation for dark matter gravitational dynamics was introduced in chapter 4 which in particular treated the inclusion of non-vanishing mean fields such as needed for a dark matter description that includes velocity dispersion degrees of freedom. Various expansion and approximation schemes of the statistical field theory were studied and the Dyson–Schwinger equation and the functional renormalisation group were obtained. Finally, Ward identities of the effective action that are related to mass conservation and an extended version of Galilean invariance were derived.

In chapter 5 the Ward identities that are related to extended Galilean invariance were used to solve the large wave number sector of the functional renormalisation group in the single-stream approximation. The Ward identities allow to (formally) close the flow equations of the two-point correlation functions such that these can in principle be solved. In an approximation where only the linear power spectrum acts as the regulator the flow equations were solved to obtain explicit expressions for the propagator and the unequal-time power spectrum. These are suppressed on smaller scales due to an effect known as sweeping effect in fluid turbulence. This can be understood as the random advection of small-scale structures due to an effective large-scale velocity background.

In chapter 6 a dark matter description that includes velocity dispersion degrees of freedom was studied in a self-consistent one-loop approximation of the Dyson–Schwinger equations where the full structure of the one- and two-point correlation functions was kept and the 1PI three-point correlation functions were set to their bare form. The resulting closed system of evolution equations for the one- and two-point correlation functions was studied in great detail and solved in different

approximations. It has been seen that a mean field for the isotropic velocity dispersion naturally emerges due to the back-reaction of fluctuations onto the background. In turn, the fluctuating fields evolve in the presence of the velocity dispersion mean field which introduces a new scale k_{fs} associated to the free-streaming of dark matter particles. This leads to a characteristic suppression of the power spectra typically associated with warm dark matter. It has been seen that the velocity dispersion mean field is sourced stronger if initially smaller, leading to the fact that even if dark matter starts out as been cold it naturally gets warmer over the course of time. In particular, it has been seen that the velocity dispersion mean field can be quite large at late-times without leaving a signature in the density contrast power spectrum. This is only the case for the dark matter models that start out cold and attain a large velocity dispersion due to a strong back-reaction of the fluctuations. This is compatible with the observed power spectrum which usually excludes warm dark matter models due to a missing suppression of small scales structures. The signature of shell-crossing observed in velocity and density cross-correlations was shown to be qualitatively captured by including velocity dispersion degrees of freedom as well as the transfer of power to vorticity modes leading to a drop in the velocity-divergence auto-spectrum. Further, a non-perturbative determination of the velocity dispersion and vorticity power spectrum was obtained from first principles. The corresponding spectral indices are given by $n_\sigma \approx -1.8$ and $n_\omega \approx 2$, close to the values obtained from N-body simulations [167–169].

In chapter 7 time-local effective dynamics for dark matter were investigated using the functional renormalisation group. To this end, a combination of a vertex and derivative expansion of the effective action of the same order as the bare action was employed. Since the renormalisation group flow equations are generically non-local in time, they needed to be projected onto the local ansatz. To this end the prescription developed in reference [37] was employed and the Laplace transform of inverse propagators for local and non-local dynamics was studied. By mapping the non-local flow equations onto the time-local ansatz of the effective action, the relevant flow coefficients that capture the suppression associated with the sweeping effect investigated in chapter 5 were identified. These lead to propagators that exhibit the same wave number dependence that was obtained in the large wave number limit of the functional renormalisation group. Due to the nature of the ansatz the time dependence is naturally different than the one obtained in the approximate solution of the large wave number limit which correspond to non-local dynamics. Finally, the density and velocity-divergence power spectra were computed using the propagators obtained in the large wave number limit and from the time-local ansatz. These perform better than standard perturbation theory, although giving different results at smaller scales. While the large wave number propagator captures the density contrast power spectrum to a better degree, the velocity-divergence power spectrum is better captured by the time-local ansatz.

The kinetic theory dark matter description as well as the functional methods developed and investigated in this thesis can be used for further studies extending the results obtained here. On the one hand one could investigate the inclusion of

a collision term in the Vlasov equation in order to account for dark matter self-interactions. With an appropriate ansatz for the collision term an extension of the methods employed throughout this thesis should work in a very similar manner. On the other hand it would also be interesting to include higher-order velocity cumulants into the dark matter description to investigate the stability of the cumulant truncation employed in this thesis and understand the limits of such truncations better.

It was shown that the Hartree–Fock approximation studied in chapter 6 qualitatively captures the physics that are observed in *N*-body simulations, ranging from the shell-crossing signature in cross-spectra to the drop of the velocity-divergence auto-spectrum associated with transfer of power to vorticity modes. The limitations that were encountered are of pure computational nature due to the large separation of the free-streaming and non-linear scale for cold dark matter. It would be most interesting to develop an algorithm which can also solve the Hartree–Fock approximation for colder dark matter models. Since this requires to cover a larger range of wave numbers while resolving the free-streaming and non-linear scale, one could work with an adaptive finite element method or try to use spectral methods.

Having investigated the inclusion of dark matter velocity dispersion with the Dyson–Schwinger equation, it would be most interesting to investigate the inclusion of velocity dispersion also with the functional renormalisation group. Using a time-local ansatz for the effective action similar to the one studied in chapter 7, one could use the insights gained from the solutions in the Hartree–Fock approximation to find appropriate flow coefficients that capture the growth of the velocity dispersion mean field as well as the suppression in the propagator due to free-streaming. A complication in this setting is that one also needs to compute the running of the 1PI one- and three-point functions, naturally leading to a more complex system of flow equations. Nonetheless, it would be interesting to investigate whether an effective time-local ansatz can account for the signatures of shell-crossing seen in the Hartree–Fock approximation, also because the renormalisation group flow equations are numerically not as involving.

A Irreducible representations of the translation and rotation group

The main text is mostly concerned with the decomposition of vector and symmetric second-order tensor fields on three-dimensional Euclidean space. For a sufficiently fast decaying vector field $v_i(\boldsymbol{x})$, one often utilises the Helmholtz decomposition [180],

$$v_i = \partial_i \hat{v} + \hat{v}_i \ , \tag{A.1}$$

resolving the vector field into an irrotational vector field $\partial_i \hat{v}(\boldsymbol{x})$ and a solenoidal vector field $\hat{v}_i(\boldsymbol{x})$.[1]

Similarly, a symmetric second-order tensor field $s_{ij}(\boldsymbol{x})$ can be resolved using the Lifschitz decomposition [181]

$$s_{ij} = \delta_{ij} t + (\partial_i \partial_j - \tfrac{1}{3} \delta_{ij} \Delta) \, \hat{s} + \partial_{(i} \hat{s}_{j)} + \hat{s}_{ij} \ , \tag{A.2}$$

where $t(\boldsymbol{x})$ and $\hat{s}(\boldsymbol{x})$ are functions and $\hat{s}_i(\boldsymbol{x})$ and $\hat{s}_{ij}(\boldsymbol{x})$ are a solenoidal vector and tensor field, respectively.

More generally, the decomposition of a nth-order symmetric tensor field can be organised in terms of irreducible representations of the Euclidean translation and rotation group and is discussed in detail in the following sections.

A.1 Representations of the translation and special orthogonal group

A.1.1 Translation group

The three-dimensional translation group $\mathrm{T}(3, \mathbb{R})$ is an abelian real non-compact Lie group and as such all irreducible complex representations are one-dimensional. Since it is a non-compact Lie group, the infinite-dimensional unitary representation on the space of square-integrable functions can only be decomposed in terms of a direct integral [182],

$$L^2(\mathbb{R}^3) \cong \int_{\mathbb{R}^3}^{\oplus} H_{\boldsymbol{x}} \, \mathrm{d}\mu(\boldsymbol{x}) \ , \tag{A.3}$$

---

[1]Given suitable boundary conditions, the decomposition is unique in simply connected and contractible regions of $\mathbb{R}^3$. In multiple connected regions an irrotational vector field is not necessarily conservative and in non-contractible regions a solenoidal vector field is not necessarily the curl of a vector potential.

where $H_{\boldsymbol{x}} \cong \mathbb{C}$ for all $\boldsymbol{x} \in \mathbb{R}^3$ and μ is the standard Lebesgue measure on three-dimensional Euclidean space. This can be understood from the point of view of harmonic analysis as the decomposition of a function $f \in L^2(\mathbb{R}^3)$ into plane waves,

$$f(\boldsymbol{x}) = \int_{\boldsymbol{k}} \widehat{f}(\boldsymbol{k}) \, \mathrm{e}^{\mathrm{i}\boldsymbol{k}\cdot\boldsymbol{x}} \ , \tag{A.4}$$

where the $\mathrm{e}^{\mathrm{i}\boldsymbol{k}\cdot\boldsymbol{x}}$ span the one-dimensional irreducible unitary representations $H_{\boldsymbol{x}}$.

A.1.2 Special orthogonal group

The special orthogonal group $\mathrm{SO}(n, \mathbb{R})$ is a real compact Lie group which is abelian for $n \leq 2$ and non-abelian for $n \geq 3$. In the following only the cases $n = 2$ and $n = 3$ are of interest.

For $n = 2$ the special orthogonal group is abelian and thus all irreducible complex representations are one-dimensional and may be labelled by an integer $m \in \mathbb{Z}$. All non-trivial irreducible real representations are two-dimensional and may be labelled by a positive integer $m \in \mathbb{N}$ which is related to two (one-dimensional) conjugate irreducible complex representations.

For $n = 3$ the special orthogonal group has $(2\ell+1)$-dimensional irreducible real and complex representations for all $\ell \in \mathbb{N}_0$, in the following denoted as V_ℓ. These can be realised on different vector spaces, the one relevant in the following is the vector space of traceless and symmetric ℓth-order tensors.

True and pseudovector representation

The orthogonal group $\mathrm{O}(3, \mathbb{R})$ is isomorphic to the internal direct procuct $\mathrm{SO}(3, \mathbb{R}) \times \mathbb{Z}_2$ and as such each irreducible representation of $\mathrm{SO}(3, \mathbb{R})$ can be lifted to two distinct irreducible representations of $\mathrm{O}(3, \mathbb{R})$. These are the three-dimensional defining or *vector* representation which lifts to the *true vector* representation transforming in the alternating representation of $\mathbb{Z}_2$ and the *pseudovector* representation transforming in the trivial representation of $\mathbb{Z}_2$.[2]

A.1.3 Tensor products

Generally, one can consider tensor products of representations and these naturally can also be decomposed into irreducible representations.

In the following, the decomposition of tensor products of finite-dimensional representations of the rotation group into irreducibles is considered. The tensor product of two irreducible representations of $\mathrm{SO}(3, \mathbb{R})$ can be decomposed into a direct sum

---

[2]In fact, the true vector representation is the defining representation while the pseudovector representation is the adjoint representation of $\mathrm{O}(3, \mathbb{R})$. These descend to identical representations of $\mathrm{SO}(3, \mathbb{R})$.

according to the Clebsch–Gordan decomposition [183],

$$V_{\ell_1} \otimes V_{\ell_2} \cong \bigoplus_{\ell=|\ell_1-\ell_2|}^{\ell_1+\ell_2} V_\ell \ . \tag{A.5}$$

This can be iterated to the case of a tensor product of n representations, such that the tensor power of the defining represenstation decomposes as

$$V_1^{\otimes n} \cong \bigoplus_{j=0}^{n} V_{n-j}^{\oplus m_{n,n-j}} \ , \tag{A.6}$$

with multiplicities [184]

$$m_{n,j} = \sum_{k=0}^{\lfloor (n-j)/3 \rfloor} (-1)^k \binom{n}{k} \binom{2n-3k-j-2}{n-2} \ . \tag{A.7}$$

Along similar line one can decompose the symmetric power of the defining representation into the direct sum,

$$\mathrm{Sym}^n(V_1) \cong \bigoplus_{j=0}^{\lfloor n/2 \rfloor} V_{n-2j} \ . \tag{A.8}$$

A.2 Decomposition of symmetric three-tensor fields

A symmetric nth-order three-tensor field transforms as

$$T_{i_1 \dots i_n}(\boldsymbol{x}) \mapsto R_{i_1 j_1} \dots R_{i_n j_n} T_{j_1 \dots j_n}(R^{-1} \cdot \boldsymbol{x}) \ , \tag{A.9}$$

for all rotations $R \in \mathrm{SO}(3, \mathbb{R})$ and as

$$T_{i_1 \dots i_n}(\boldsymbol{x}) \mapsto T_{i_1 \dots i_n}(\boldsymbol{x} + \boldsymbol{a}) \ , \tag{A.10}$$

for all translations $\boldsymbol{a} \in \mathbb{R}^3$.

Assuming suitable decay conditions the tensor field can be decompose into irreducible unitary representations of the translation group by a Fourier transformation,

$$T_{i_1 \dots i_n}(\boldsymbol{x}) = \int_{\boldsymbol{k}} \mathrm{e}^{\mathrm{i}\boldsymbol{k}\cdot\boldsymbol{x}} \hat{T}_{i_1 \dots i_n}(\boldsymbol{k}) \ . \tag{A.11}$$

The tensor $\hat{T}_{i_1 \dots i_n}(\boldsymbol{k})$ transforms in the nth symmetric power of the defining representation of the three-dimensional rotation group and can be decomposed into irreducible representations according to formula (A.8). This decomposition can be explicitly realised as [185],

$$\hat{T}_{i_1 \dots i_n}(\boldsymbol{k}) = \sum_{j=0}^{\lfloor n/2 \rfloor} \mathcal{T}_{(i_1 \dots i_{n-2j}}^{(n-2j)}(\boldsymbol{k}) \, \delta_{i_{n-2j+1} i_{n-2j+2}} \dots \delta_{i_{n-1} i_n)} \ , \tag{A.12}$$

where the tensors $\mathcal{T}^{(\ell)}_{i_1 \ldots i_\ell}(\boldsymbol{k})$ are traceless and symmetric.[3] By restricting to the subgroup of rotations in the plane perpendicular to the wave vector $\boldsymbol{k}$ the irreducible representations of $\mathrm{SO}(3, \mathbb{R})$ break up into irreducilbe representations of $\mathrm{SO}(2, \mathbb{R})$. Explicitly, this can be written as,

$$\mathcal{T}^{(\ell)}_{i_1 \ldots i_\ell}(\boldsymbol{k}) = \sum_{m=0}^{\ell} \mathcal{T}^{(\ell,m)}_{i_1 \ldots i_m}(\boldsymbol{k}) \, \widehat{k}_{i_{m+1} \ldots i_\ell} \, , \tag{A.13}$$

where the tensors $\mathcal{T}^{(\ell,m)}_{i_1 \ldots i_m}(\boldsymbol{k})$ are transverse, traceless and symmetric and $\widehat{k}_{i_1 \ldots i_m}$ are longitudinal, traceless and symmetric tensors. Finally, the full decomposition reads

$$T_{i_1 \ldots i_n}(\boldsymbol{x}) = \int_{\boldsymbol{k}} \mathrm{e}^{\mathrm{i} \boldsymbol{k} \cdot \boldsymbol{x}} \sum_{j=0}^{\lfloor n/2 \rfloor} \sum_{m=0}^{n-2j} \mathcal{T}^{(n-2j,m)}_{(i_1 \ldots i_m}(\boldsymbol{k}) \, \widehat{k}_{i_{m+1} \ldots i_{n-2j}} \, \delta_{i_{n-2j+1} i_{n-2j+2}} \cdots \delta_{i_{n-1} i_n)} \, . \tag{A.14}$$

Explicitly a vector field is decomposed as

$$v_i(\boldsymbol{x}) = \int_{\boldsymbol{k}} \mathrm{e}^{\mathrm{i} \boldsymbol{k} \cdot \boldsymbol{x}} \left[\widehat{v}_i(\boldsymbol{k}) + \mathrm{i} \, k_i \widehat{v}(\boldsymbol{k}) \right] \, , \tag{A.15}$$

and a symmetric second-order tensor field is decomposed

$$s_{ij}(\boldsymbol{x}) = \int_{\boldsymbol{k}} \mathrm{e}^{\mathrm{i} \boldsymbol{k} \cdot \boldsymbol{x}} \left[\widehat{s}_{ij}(\boldsymbol{k}) + \mathrm{i} \, k_i \widehat{s}_j(\boldsymbol{k}) + \mathrm{i} \, k_j \widehat{s}_i(\boldsymbol{k}) - \tfrac{3}{2} \left(k_i k_j - \tfrac{1}{3} \delta_{ij} k^2 \right) \widehat{s}(\boldsymbol{k}) + \delta_{ij} \widehat{t}(\boldsymbol{k}) \right] \, , \tag{A.16}$$

where prefactors are inserted for convenience to invert the Fourier transformation. Inverting the Fourier transformation one obtains the decompositions (A.1) and (A.2). Often one also writes a solenoidal vector field as the curl of a vector potential,

$$\widehat{v}_i(\boldsymbol{k}) = \epsilon_{ijk} \, \mathrm{i} \, k_j \widehat{A}_k(\boldsymbol{k}) \, , \qquad v_i(\boldsymbol{x}) = \epsilon_{ijk} \partial_j A_k(\boldsymbol{x}) \, , \tag{A.17}$$

where the vector potential now transforms in the pseudovector representation.

---

[3]This decomposition is easily generalised to a non-symmetric nth-order tensor field by using the decomposition (A.6).

B Langevin dynamics with stochastic initial conditions

In this section the Martin–Siggia–Rose/Janssen–de Dominicis formalism [120–123] is reviewed in the (1+0)-dimensional setting with some applications for a cubic interaction term in the action which is structurally speaking the closest to the equations of motion studied in cosmology.

B.1 Existence and uniqueness

Consider the first-order ordinary differential equation

$$\frac{\mathrm{d}\phi(t)}{\mathrm{d}t} + F(\phi(t)) = 0 \; , \tag{B.1}$$

where it is assumed that $F(\phi)$ is locally Lipschitz continuous. Given some initial condition $\phi(t^{\mathrm{in}}) = \phi^{\mathrm{in}}$ the Picard–Lindelöf theorem [186, 187] guarantees the existence and uniqueness of a solution $\phi^{\mathrm{sol}}(t)$ on an interval $[t^{\mathrm{in}} - T, t^{\mathrm{in}} + T]$ for some $T > 0$ although T may depend on ϕ^{in}.

As a practical example through this section, the Riccati equation with constant coefficients is studied. That is, $F(\phi) = -\mu\phi + g\phi^2$ where $\mu, g > 0$ without loss of generality. Structurally speaking, this is also the closest to the cosmological setting studied in the main text, that is one deal with linear and quadratic terms in the equations of motion.[1] For any initial condition ϕ^{in} one can find the (locally unique) solution

$$\phi^{\mathrm{sol}}(t) = \frac{\mathrm{e}^{\mu(t-t^{\mathrm{in}})}\,\phi^{\mathrm{in}}}{1 + \frac{g}{\mu}\phi^{\mathrm{in}}\big[\mathrm{e}^{\mu(t-t^{\mathrm{in}})} - 1\big]} \; . \tag{B.2}$$

The solution has a (possible) finite escape time $t = t^{\mathrm{in}} + t_*$ with

$$t_*(\phi^{\mathrm{in}}) = \frac{1}{\mu}\ln\left(1 - \frac{\mu}{g\phi^{\mathrm{in}}}\right) \; , \tag{B.3}$$

provided $\mu/(g\phi^{\mathrm{in}}) > 1$. That is, for $\phi^{\mathrm{in}} > 0$ there is a (possible) blow-up at some time $t < t^{\mathrm{in}}$ while for $\phi^{\mathrm{in}} > 0$ there is a (definite) blow-up at some time $t > t^{\mathrm{in}}$ and for $\phi^{\mathrm{in}} = 0$ there is the a global trivial vanishing solution.

---

[1]It is emphasised that in the cosmological setting studied in chapter 4 the equations of motion are a system of non-linear hyperbolic-elliptic partial differential equations and thus the results derived here cannot simply be transferred to there.

B.2 Response functions

To study the response of a system described by equation (B.1), one supplies a source current

$$\frac{\mathrm{d}\phi(t)}{\mathrm{d}t} + F(\phi(t)) = \hat{K}(t) \,, \tag{B.4}$$

where $\hat{K}(t)$ is interpreted as an input impulse of a system.[2] Interpreting the solution as the response of the system, one can expand the solution as a Volterra series [188]

$$\phi_K^{\mathrm{sol}}(t) = \sum_{n=0}^{\infty} \frac{1}{n!} \int_{t^{\mathrm{in}}}^{t^{\mathrm{fi}}} \mathrm{d}t_1 \dots \int_{t^{\mathrm{in}}}^{t^{\mathrm{fi}}} \mathrm{d}t_n \, R^{(n)}(t, t_1, \dots, t_n) \, \hat{K}(t_1) \dots \hat{K}(t_n) \,, \tag{B.5}$$

where

$$R^{(0)}(t) = \phi^{\mathrm{sol}}(t) \,, \tag{B.6}$$

is the solution in the absence of a source current and the Volterra kernels for $n > 0$

$$R^{(n)}(t, t_1, \dots, t_n) = \left. \frac{\delta^n \phi_K^{\mathrm{sol}}(t)}{\delta \hat{K}(t_1) \dots \delta \hat{K}(t_n)} \right|_{\hat{K}(t)=0} \,, \tag{B.7}$$

can be regarded as generalised non-linear response functions. Since the response of an impulse is causal, the response functions only have support for $t > t_i$ for all $i \in \{1, \dots, n\}$. In the case of a generic non-linear $F(\phi)$, the Volterra kernels are non-vanishing and the series expansion has a finite radius of convergence depending on the explicit form of $F(\phi)$.

As an illustrative example consider the linear case $F(\phi) = -\mu\phi$ with the solution

$$\phi_K^{\mathrm{sol}}(t) = \mathrm{e}^{\mu(t-t^{\mathrm{in}})} \, \phi^{\mathrm{in}} + \int_{t^{\mathrm{in}}}^{t} \mathrm{d}t' \, \mathrm{e}^{\mu(t-t')} \, \hat{K}(t') \,. \tag{B.8}$$

This obviously gives

$$R^{(0)}(t) = \mathrm{e}^{\mu(t-t^{\mathrm{in}})} \, \phi^{\mathrm{in}} \,, \qquad R^{(1)}(t, t') = \theta(t-t') \, \mathrm{e}^{\mu(t-t')} \,, \tag{B.9}$$

while all higher-order responses vanish, as expected for a linear system. In particular, notice that the linear response function is causal.

Although no explicit solution to the Riccati equation with a time-dependent source current can be given, the Volterra series exists, provided the solution does not blow up, within some characteristic radius of convergence of the source currents. More specifically, for $F(\phi)$ an analytic function (such as the examples studied here) and no finite escape time, a Volterra series exists and converges uniformly and absolutely on any finite time interval within a characteristic radius of convergence (possibly depending on the length of the time interval) for sufficiently smooth and bounded source currents [189,190] and can also be extended to system with finite escape time at least on time intervals before the blow-up [191]. Often, the Volterra kernels and source currents are of more general type such as tempered distributions [192,193].

---

[2]The presence of a (continuous) source current does not alter the local existence and uniqueness of a solution.

B.3 Random initial conditions

In the following the initial conditions are assumed to be random variables that follow a distribution characterised by the probability density function $P(\phi^{\mathrm{in}})$. One is then interested in expectation values,

$$\langle \mathcal{O}(\phi^{\mathrm{in}}) \rangle_{\mathrm{in}} := \int_{\mathbb{R}} \mathrm{d}\phi^{\mathrm{in}} \, \mathcal{O}(\phi^{\mathrm{in}}) \, P(\phi^{\mathrm{in}}) \,, \tag{B.10}$$

where the operator $\mathcal{O}$ is typically taken to be a monomial in the solution, in order to compute moments of the (time-dependent) field $\phi^{\mathrm{sol}}(t)$, such as the mean field or the covariance of two fields (possibly at unequal times). That is, due to the random initial conditions, the field $\phi^{\mathrm{sol}}(t)$ is a stochastic process and moreover its distribution can vary from the initial one for any non-linear $F(\phi)$.

In the following the distribution function is mostly taken to be a normal distribution with mean Φ^{in} and variance C^{in},

$$P(\phi^{\mathrm{in}}) = \frac{1}{\sqrt{2\pi C^{\mathrm{in}}}} \exp\left\{ -\frac{1}{2} \frac{(\phi^{\mathrm{in}} - \Phi^{\mathrm{in}})^2}{C^{\mathrm{in}}} \right\} \,. \tag{B.11}$$

Going back to the exemplary Riccati equation with solution, one can realise that expectation values such as the mean or the covariance function are not well-defined on any fixed time interval from t^{in} to t^{fi}. That is, in order to compute the expectation values, one has to average over all initial conditions ϕ^{in} and in particular over all negative initial conditions. Since each initial condition on the negative line is associated to a (finite) blow-up time, there is no definite time interval on which solutions to *all* initial conditions exist. In particular this implies that the mean field and unequal-time covariance is not defined while the equal-time covariance function diverges.

From a physical point of view one would argue that at large enough field values some mechanism comes to rescue before the finite blow-up time. A rather simple extension would be $F(\phi) = -\mu\phi + g\phi^2 + \epsilon\phi^3$ with $\epsilon > 0$ such that solutions stay finite.

B.4 Asymptotic expansions

Finally one can compute expectation values perturbatively. That is, the solution is expanded in terms of its initial condition and expectation values are computed order by order.[3] More explicitly that is,

$$\phi^{\mathrm{sol}}(t) = \sum_{n=0}^{\infty} \frac{1}{n!} \left. \frac{\partial^n \phi^{\mathrm{sol}}(t)}{\partial(\phi^{\mathrm{in}})^n} \right|_{\phi^{\mathrm{in}}=0} (\phi^{\mathrm{in}})^n \,, \tag{B.12}$$

---

[3]One can also work perturbatively in couplings, although here it is preferred to not do so.

similar to the Volterra series for response functions. The series expansion naturally has a radius of convergence within which the series convergence absolutely and uniformly.

Computing expectation values perturbatively is usually done as an asymptotic series, that is e.g. for the mean field

$$\langle \phi^{\mathrm{sol}}(t) \rangle_{\mathrm{in}} \sim \sum_{n=0}^{\infty} \frac{1}{n!} \frac{\partial^n \phi^{\mathrm{sol}}(t)}{\partial (\phi^{\mathrm{in}})^n} \bigg|_{\phi^{\mathrm{in}}=0} \langle (\phi^{\mathrm{in}})^n \rangle_{\mathrm{in}} . \tag{B.13}$$

Since the series expansion convergence absolutely and uniformly only within the radius of convergence, taking the series expansion and taking expectation value in general cases does not commute. Nevertheless the expectation values can be understood as an asymptotic series, in the sense that for a distribution which is strongly peaked within the radius of convergence might actually provide a sufficient good approximation to the true expectation value.

An extreme example would be a degenerate distribution which is localised within the region of convergence. Smoothing the degenerate distribution to a normal distribution (again strongly peaked within the radius of convergence) naturally cannot be exact since one averages over values outside the region of convergence. Nevertheless, it might give a reasonable approximation taking only a finite amount of terms into account. Generally, one usually has an optimal amount of terms which leads to the smallest error compared to the exact result.

Returning to the Riccati equation example one encounters another peculiarity which one should be aware of. The expansion reads

$$\phi^{\mathrm{sol}}(t) = \mathrm{e}^{\mu(t-t^{\mathrm{in}})} \sum_{n=0}^{\infty} (-1)^n \left(\frac{g}{\mu} \right)^n \left[\mathrm{e}^{\mu(t-t^{\mathrm{in}})} - 1 \right]^n (\phi^{\mathrm{in}})^{n+1} , \tag{B.14}$$

and it is easy to see that the radius of convergence is given by

$$|\phi^{\mathrm{in}}| < \frac{\mu}{g} \left[\mathrm{e}^{\mu(t-t^{\mathrm{in}})} - 1 \right]^{-1} , \tag{B.15}$$

for all $t^{\mathrm{in}} \leq t < t^{\mathrm{in}} + t_*(\phi^{\mathrm{in}})$. The limit $g \to 0$ and $t = t^{\mathrm{in}}$ naturally are the cases with an infinite radius of convergence, while for all finite times and an interacting theory one naturally has a finite radius of convergence. As was already pointed out, odd moments of the field are undefined while even moments are simply divergent. This is a direct consequence of the finite escape time. Nonetheless, the series expansion (B.14) is valid within the region of convergence (B.15). Computing the average of equation (B.14) one obtains an asymptotic series for the mean field, although the left-hand side is not well-defined. Using the asymptotic series, one can now actually compute the mean field and covariance function, although the exact results is not even existent or simple divergent. That is, while the asymptotic series can provide a suitable way of approximating expectation values, it should be treated with care.

B.5 Stochastic processes

In order to build up the Martin–Siggia–Rose/Janssen–de Dominicis formalism one has to discretise the evolution equation. That is, consider the partition $t \in \{t_n : n \in \{1, \dots, N\}\}$ where $t_n = t^{\text{in}} + (n-1)\epsilon$ with $\epsilon = (t^{\text{fi}} - t^{\text{in}})/(N-1)$ and abbreviate $\phi_n = \phi(t_n)$ and $F_n = F(\phi(t_n))$. Then one can express the dynamical evolution of the fields together with the initial conditions as

$$\Delta_\epsilon \phi_n + (1-\lambda)F_{n-1} + \lambda F_n = (1-\lambda)\hat{K}_{n-1} + \lambda \hat{K}_n + \frac{\delta_{n1}}{\epsilon}\phi^{\text{in}} , \qquad (\text{B.16})$$

with the forward finite difference derivative

$$\Delta_\epsilon \phi_n = \frac{\phi_n - \phi_{n-1}}{\epsilon} , \qquad (\text{B.17})$$

for $n \in \{1, \dots, N\}$ with $\lambda \in [0,1]$ and $\phi_0 = 0$ as well as $\hat{K}_0 = 0$. For $n = 1$ this yields

$$\phi^{\text{sol}}_{K,1} = \phi^{\text{in}} + \mathcal{O}(\epsilon) , \qquad (\text{B.18})$$

which recovers the initial conditions in the continuum limit $\epsilon \to 0$. The corresponding continuum limit is given by

$$\frac{\mathrm{d}\phi(t)}{\mathrm{d}t} + F(\phi(t)) = \hat{K}(t) + \delta(t - t^{\text{in}})\,\phi^{\text{in}} , \qquad (\text{B.19})$$

which in this context is a Langevin equation [194] where the noise term is localised at initial time. That is, in contrast to equation (B.1) the initial condition are forced within the equations of motion.

Consider the linear case $F(\phi) = -\mu\phi$. In this case the linear recursion relation (B.16) is uniquely solved by

$$\phi^{\text{sol}}_{\hat{K},n} = \frac{c^n}{1 - \epsilon\lambda\mu}\phi^{\text{in}} + \frac{\epsilon}{1 - \epsilon\lambda\mu}\sum_{m=0}^{n-1} c^{n-m-1}\Big[(1-\lambda)\hat{K}_m + \lambda\hat{K}_{m+1}\Big] , \qquad (\text{B.20})$$

where

$$c = \frac{1 + \epsilon(1-\lambda)\mu}{1 - \epsilon\lambda\mu} . \qquad (\text{B.21})$$

It is now easy to verify that in the continuum limit $\epsilon \to 0$ one obtains the solution (B.8) using

$$\mathrm{e}^x = \lim_{N\to\infty}\left(1 + \frac{x}{N}\right)^N . \qquad (\text{B.22})$$

Further one can now make sense of the discretised linear response function as

$$R^{(1)}_{nm} := \frac{\partial \phi^{\text{sol}}_{\hat{K},n}}{\epsilon\partial\hat{K}_m} = \begin{cases} \dfrac{c^{n-m}}{(1 - \epsilon\lambda\mu)(1 + \epsilon(1-\lambda)\mu)} & \text{for } n > m \\[2ex] \dfrac{\lambda}{1 - \epsilon\lambda\mu} & \text{for } n = m \\[2ex] 0 & \text{for } n < m \end{cases} , \qquad (\text{B.23})$$

which in the continuum limit $\epsilon \to 0$ leads to

$$R^{(1)}(t,t') = \begin{cases} e^{\mu(t-t')} & \text{for } t > t' \\ \lambda & \text{for } t = t' \\ 0 & \text{for } t < t' \end{cases} . \tag{B.24}$$

That is, the stochastic differential equation depends on the discretisation procedure and amounts to the prescription $\theta(0) = \lambda$. In the following we employ the Itô convention $\lambda = 0$.

B.6 Martin–Siggia–Rose/Janssen–de Dominicis formalism

The construction is loosely based on the review [127]. Writing $\hat{K}_n = i\,\hat{J}_n$ for later convenience, the relevant moment-generating function is given by [120–123, 195, 196]

$$Z(J, \hat{J}) = \langle e^{\epsilon J_n \phi^{\text{sol}}_{\hat{J},n}} \rangle_{\text{in}} = \int_{\mathbb{R}} d\phi^{\text{in}} \, P(\phi^{\text{in}}) \, e^{\epsilon J_n \phi^{\text{sol}}_{\hat{J},n}} \, , \tag{B.25}$$

where factors of ϵ are conveniently introduced in order to take the continuum limit at the end and double appearing indices are summed over.[4] This can be rewritten using delta functions to

$$Z(J, \hat{J}) = \int_{\mathbb{R}} d\phi^{\text{in}} \, P(\phi^{\text{in}}) \int_{\mathbb{R}^N} d^N \phi \left[\prod_{\bar{n}=1}^{N} \delta(\phi_{\bar{n}} - \phi^{\text{sol}}_{\hat{J},\bar{n}}) \right] e^{\epsilon J_n \phi_n} \, . \tag{B.26}$$

Then one uses the delta function identity (and thereby assumes a unique solution)

$$\prod_{n=1}^{N} \delta(\phi_n - \phi^{\text{sol}}_{\hat{J},n}) = |\det(\mathcal{J})| \prod_{n=1}^{N} \delta(E_n) \, , \tag{B.27}$$

where

$$E_n = \Delta_\epsilon \phi_n + (1-\lambda)F_{n-1} + \lambda F_n - (1-\lambda)\hat{K}_{n-1} - \lambda\hat{K}_n - \frac{\delta_{n1}}{\epsilon} \phi^{\text{in}} \, , \tag{B.28}$$

are the discretised evolution equations and the Jacobian is given by

$$\mathcal{J}_{mn} := \frac{\partial E_m}{\partial \phi_n} = \frac{\delta_{mn} - \delta_{m(n-1)}}{\epsilon} + (1-\lambda)F'_{n-1}\delta_{m(n-1)} + \lambda F'_n \delta_{mn} \, , \tag{B.29}$$

where $F'(\phi) := \partial F(\phi)/\partial \phi$. Since the Jacobian is of upper triangular form, the determinant is given by

$$\det(\mathcal{J}) = \frac{1}{\epsilon^N} \prod_{n=1}^{N} (1 + \epsilon \lambda F'_n) \, , \tag{B.30}$$

---

[4]It is assumed that the moment-generating functional exists, that is the solution exists in the time interval for all initial conditions and the distribution function is 'nice' enough.

and since the second term can be made as small as desired by choosing ϵ small enough, the determinant can be assumed to be positive without loss of generality. Understanding the delta functions as a tempered distribution it can be expressed in terms of its Fourier transform as

$$\delta(E_n) = \epsilon^N \int_{\mathbb{R}^N} \frac{\mathrm{d}^N\hat{\phi}}{(2\pi)^N} \, \mathrm{e}^{\mathrm{i}\epsilon\hat{\phi}_n E_n} \ , \tag{B.31}$$

such that equation the delta functions can be written as

$$\prod_{n=1}^{N} \delta(\phi_n - \phi_{\hat{J},n}^{\mathrm{sol}}) = |\det(\epsilon\mathcal{J})| \int_{\mathbb{R}^N} \frac{\mathrm{d}^N\hat{\phi}}{(2\pi)^N} \, \mathrm{e}^{\mathrm{i}\epsilon\hat{\phi}_n E_n} \ . \tag{B.32}$$

Here one can already see, that using equation (B.30) lead to the determinant being unity for Itô discretisation, $\lambda = 0$. For a general discretisation one can exponentiate the determinant using the Faddeev–Popov method by introducing two Grassmann variables, θ_n and $\bar{\theta}_n$. Explicitly, this reads

$$\det(\epsilon\mathcal{J}) = \int_{\Lambda^N} \mathrm{d}^N\theta \int_{\Lambda^N} \mathrm{d}^N\bar{\theta} \, \mathrm{e}^{\epsilon\bar{\theta}_n[\Delta_\epsilon\theta_n + (1-\lambda)F'_{n-1}\theta_{n-1} + \lambda F'_n\theta_n]} \tag{B.33}$$

where $\theta_0 := 0$. Plugging all of the above together one obtains the final result

$$\begin{aligned}
Z(J,\hat{J}) = {} & \int_{\mathbb{R}} \mathrm{d}\phi^{\mathrm{in}} \, P(\phi^{\mathrm{in}}) \int_{\mathbb{R}^N} \mathrm{d}^N\phi \int_{\mathbb{R}^N} \frac{\mathrm{d}^N\hat{\phi}}{(2\pi)^N} \int_{\Lambda^N} \mathrm{d}^N\theta \int_{\Lambda^N} \mathrm{d}^N\bar{\theta} \\
& \times \exp\left\{ \mathrm{i}\,\epsilon\hat{\phi}_n \left[\Delta_\epsilon\phi_n + (1-\lambda)F_{n-1} + \lambda F_n - \frac{\delta_{n1}}{\epsilon}\phi^{\mathrm{in}} \right] \right\} \\
& \times \exp\left\{ \epsilon\bar{\theta}_n[\Delta_\epsilon\theta_n + (1-\lambda)F'_{n-1}\theta_{n-1} + \lambda F'_n\theta_n] \right\} \\
& \times \exp\left\{ \epsilon J_n\phi_n + \epsilon\left[(1-\lambda)\hat{J}_{n-1} + \lambda\hat{J}_n\right]\hat{\phi}_n \right\} \ ,
\end{aligned} \tag{B.34}$$

where the second line is the dynamical part, the third line is the ghost part due to the discretisation of stochastic differential equation and the last line are the source currents. In the case of Gaussian initial conditions the integral over the initial fields can be performed explicitly to arrive at

$$Z(J,\hat{J}) = \int_{\mathbb{R}^N} \mathrm{d}^N\phi \int_{\mathbb{R}^N} \frac{\mathrm{d}^N\hat{\phi}}{(2\pi)^N} \int_{\Lambda^N} \mathrm{d}^N\theta \int_{\Lambda^N} \mathrm{d}^N\bar{\theta} \, \mathrm{e}^{-S-S_{\mathrm{FP}}} \, \mathrm{e}^{\mathrm{sources}} \ , \tag{B.35}$$

with the Martin–Siggia–Rose/Janssen–de Dominicis action

$$S(\phi,\hat{\phi}) = -\mathrm{i}\,\epsilon\hat{\phi}_n[\Delta_\epsilon\phi_n + (1-\lambda)F_{n-1} + \lambda F_n] + \mathrm{i}\,\hat{\phi}_1\Phi^{\mathrm{in}} + \tfrac{1}{2}\,\hat{\phi}_1 C^{\mathrm{in}}\hat{\phi}_1 \ , \tag{B.36}$$

and the Faddeev–Popov action

$$S_{\mathrm{FP}}(\phi,\theta,\bar{\theta}) = -\epsilon\bar{\theta}_n[\Delta_\epsilon\theta_n + (1-\lambda)F'_{n-1}\theta_{n-1} + \lambda F'_n\theta_n] \ , \tag{B.37}$$

and the sources

$$\text{sources} = \epsilon J_n \phi_n + \epsilon \Big[(1-\lambda)\hat{J}_{n-1} + \lambda \hat{J}_n\Big]\hat{\phi}_n \; . \tag{B.38}$$

To take the continuum limit, provided it exists in some sensible way, one should specify the function space that is integrated over in order to take care of issues such as boundary conditions. One then obtains

$$Z[J,\hat{J}] = \int \mathcal{D}\phi \int \mathcal{D}\hat{\phi} \int \mathcal{D}\theta \int \mathcal{D}\bar{\theta} \; \mathrm{e}^{-S - S_{\mathrm{FP}}} \, \mathrm{e}^{\text{sources}} \; , \tag{B.39}$$

with the Martin–Siggia–Rose/Janssen–de Dominicis action

$$S[\phi,\hat{\phi}] = -\mathrm{i}\int_{t^{\mathrm{in}}}^{t^{\mathrm{fi}}} \mathrm{d}t\, \hat{\phi}(t)\big[\partial_t \phi(t) + F(\phi(t))\big] + \mathrm{i}\,\hat{\phi}(t^{\mathrm{in}})\,\Phi^{\mathrm{in}} + \tfrac{1}{2}\,\hat{\phi}(t^{\mathrm{in}})\,C^{\mathrm{in}}\,\hat{\phi}(t^{\mathrm{in}}) \; , \tag{B.40}$$

and the Faddeev–Popov action

$$S_{\mathrm{FP}}[\phi,\theta,\bar{\theta}] = -\int_{t^{\mathrm{in}}}^{t^{\mathrm{fi}}} \mathrm{d}t\, \bar{\theta}(t)\Big[\partial_t \theta(t) + F'(\phi(t))\,\theta(t)\Big] \; , \tag{B.41}$$

and the sources

$$\text{sources} = \int_{t^{\mathrm{in}}}^{t^{\mathrm{fi}}} \mathrm{d}t\, \Big[J(t)\,\phi(t) + \hat{J}(t)\,\hat{\phi}(t)\Big] \; . \tag{B.42}$$

In the case of Itô discretisation the ghost part can be integrate to unity and one obtains

$$Z[J,\hat{J}] = \int \mathcal{D}\phi \int \mathcal{D}\hat{\phi} \; \mathrm{e}^{-S} \, \mathrm{e}^{\text{sources}} \; , \tag{B.43}$$

which is the generating functional started off with in equation (4.13) in the main text.

C Bare vertices

The bare vertices of the field content $\psi_a(\tau, \boldsymbol{x}) = (\delta, u_i, \sigma_{ij})$ are given by

$$
\begin{aligned}
\gamma_{\delta u_i \delta}(\boldsymbol{x} - \boldsymbol{x}', \boldsymbol{x} - \boldsymbol{x}'') &= \tfrac{1}{2}\,\partial_i[\delta(\boldsymbol{x} - \boldsymbol{x}')\,\delta(\boldsymbol{x} - \boldsymbol{x}'')]\,, \\
\gamma_{u_i u_j u_k}(\boldsymbol{x} - \boldsymbol{x}', \boldsymbol{x} - \boldsymbol{x}'') &= \tfrac{1}{2}\big[\delta_{ik}\,\delta(\boldsymbol{x} - \boldsymbol{x}')\,\partial_j \delta(\boldsymbol{x} - \boldsymbol{x}'') \\
&\qquad\qquad + \delta_{ij}\,\partial_k\delta(\boldsymbol{x} - \boldsymbol{x}')\,\delta(\boldsymbol{x} - \boldsymbol{x}'')\big]\,, \\
\gamma_{u_i \sigma_{jk} \delta}(\boldsymbol{x} - \boldsymbol{x}', \boldsymbol{x} - \boldsymbol{x}'') &= \tfrac{1}{2}\,\delta_{ij}\,\delta(\boldsymbol{x} - \boldsymbol{x}')\,\partial_k\delta(\boldsymbol{x} - \boldsymbol{x}'')\,, \\
\gamma_{\sigma_{ij}\sigma_{kl} u_m}(\boldsymbol{x} - \boldsymbol{x}', \boldsymbol{x} - \boldsymbol{x}'') &= \tfrac{1}{2}\big[\delta_{ik}\delta_{jl}\partial_m\delta(\boldsymbol{x} - \boldsymbol{x}')\,\delta(\boldsymbol{x} - \boldsymbol{x}'') \\
&\qquad\qquad + \big(\delta_{ik}\delta_{jl} + \delta_{jk}\delta_{il}\big)\delta(\boldsymbol{x} - \boldsymbol{x}')\,\partial_l\delta(\boldsymbol{x} - \boldsymbol{x}'')\big]\,.
\end{aligned}
\tag{C.1}
$$

Similarly, the bare vertices of a description including higher-order velocity cumulants can be obtained from the non-linear terms of the evolution equation (2.88).

The bare vertices of the field content (6.1) used in chapter 6 are obtained by decomposing the bare vertices (C.1) using the decompositions (3.20) and (3.24). With $\boldsymbol{k} = \boldsymbol{k}_1 + \boldsymbol{k}_2$, one finds that the $\gamma_{\delta u_i \delta}$ vertex decomposes into the two vertices

$$
\begin{aligned}
\gamma_{121}(\boldsymbol{k}_1, \boldsymbol{k}_2) &= -\frac{\boldsymbol{k} \cdot \boldsymbol{k}_1}{2k_1^2}\,, \\
\gamma_{15_i 1}(\boldsymbol{k}_1, \boldsymbol{k}_2) &= -\frac{(\boldsymbol{k}_1 \times \boldsymbol{k}_2)_i}{2k_1^2}\,,
\end{aligned}
\tag{C.2}
$$

the $\gamma_{u_i u_j u_k}$ vertex into the five vertices

$$
\begin{aligned}
\gamma_{222}(\boldsymbol{k}_1, \boldsymbol{k}_2) &= -\frac{k^2\,(\boldsymbol{k}_1 \cdot \boldsymbol{k}_2)}{2k_1^2 k_2^2}\,, \\
\gamma_{225_i}(\boldsymbol{k}_1, \boldsymbol{k}_2) &= -\frac{[k_1^2 + 2(\boldsymbol{k}_1 \cdot \boldsymbol{k}_2)](\boldsymbol{k}_1 \times \boldsymbol{k}_2)_i}{2k_1^2 k_2^2}\,, \\
\gamma_{25_i 5_j}(\boldsymbol{k}_1, \boldsymbol{k}_2) &= \frac{(\boldsymbol{k}_1 \times \boldsymbol{k}_2)_i (\boldsymbol{k}_1 \times \boldsymbol{k}_2)_j}{k_1^2 k_2^2}\,, \\
\gamma_{5_i 25_j}(\boldsymbol{k}_1, \boldsymbol{k}_2) &= \frac{k_{1,i}k_{1,j} - \delta_{ij}(\boldsymbol{k} \cdot \boldsymbol{k}_1)}{2k_1^2}\,, \\
\gamma_{5_i 5_j 5_k}(\boldsymbol{k}_1, \boldsymbol{k}_2) &= \frac{[k_2^2 - k_1^2](\boldsymbol{k}_1 \times \boldsymbol{k}_2)_i \delta_{jk} - k_2^2 \epsilon_{ijl}k_l k_{1,k} - k_1^2 \epsilon_{ikl}k_l k_{2,j}}{2k_1^2 k_2^2}\,,
\end{aligned}
\tag{C.3}
$$

the $\gamma_{u_i \sigma_{jk} \delta}$ vertex into the four vertices

$$\gamma_{231}(\boldsymbol{k}_1, \boldsymbol{k}_2) = \frac{\boldsymbol{k} \cdot \boldsymbol{k}_2}{2k_1^2} ,$$

$$\gamma_{241}(\boldsymbol{k}_1, \boldsymbol{k}_2) = \frac{3(\boldsymbol{k} \cdot \boldsymbol{k}_1)(\boldsymbol{k}_1 \cdot \boldsymbol{k}_2) - k_1^2(\boldsymbol{k} \cdot \boldsymbol{k}_2)}{4k_1^4} ,$$

$$\gamma_{5_i 31}(\boldsymbol{k}_1, \boldsymbol{k}_2) = -\frac{(\boldsymbol{k}_1 \times \boldsymbol{k}_2)_i}{2k_1^2} ,$$

$$\gamma_{5_i 41}(\boldsymbol{k}_1, \boldsymbol{k}_2) = \frac{[k_1^2 + 3(\boldsymbol{k}_1 \cdot \boldsymbol{k}_2)](\boldsymbol{k}_1 \times \boldsymbol{k}_2)_i}{4k_1^4} ,$$

(C.4)

and the $\gamma_{\sigma_{ij} \sigma_{kl} u_m}$ vertex into the eight vertices

$$\gamma_{332}(\boldsymbol{k}_1, \boldsymbol{k}_2) = -\frac{3k^2(\boldsymbol{k}_1 \cdot \boldsymbol{k}_2) + 2k^2 k_2^2}{6k_1^2 k_2^2} ,$$

$$\gamma_{335_i}(\boldsymbol{k}_1, \boldsymbol{k}_2) = -\frac{k^2(\boldsymbol{k}_1 \times \boldsymbol{k}_2)_i}{2k_1^2 k_2^2} ,$$

$$\gamma_{342}(\boldsymbol{k}_1, \boldsymbol{k}_2) = \frac{k^2 k_1^2 k_2^2 - 3k^2(\boldsymbol{k}_1 \cdot \boldsymbol{k}_2)^2}{6k_1^4 k_2^2} ,$$

$$\gamma_{345_i}(\boldsymbol{k}_1, \boldsymbol{k}_2) = -\frac{k^2(\boldsymbol{k}_1 \cdot \boldsymbol{k}_2)(\boldsymbol{k}_1 \times \boldsymbol{k}_2)_i}{2k_1^4 k_2^2} ,$$

$$\gamma_{432}(\boldsymbol{k}_1, \boldsymbol{k}_2) = \frac{k^2 k_2^2 - 3(\boldsymbol{k} \cdot \boldsymbol{k}_2)^2}{3k_1^2 k_2^2} ,$$

$$\gamma_{435_i}(\boldsymbol{k}_1, \boldsymbol{k}_2) = -\frac{(\boldsymbol{k} \cdot \boldsymbol{k}_2)(\boldsymbol{k}_1 \times \boldsymbol{k}_2)_i}{k_1^2 k_2^2} ,$$

$$\gamma_{442}(\boldsymbol{k}_1, \boldsymbol{k}_2) = -\frac{18(\boldsymbol{k} \cdot \boldsymbol{k}_1)(\boldsymbol{k} \cdot \boldsymbol{k}_2)(\boldsymbol{k}_1 \cdot \boldsymbol{k}_2) + 9(\boldsymbol{k} \cdot \boldsymbol{k}_1)^2(\boldsymbol{k}_1 \cdot \boldsymbol{k}_2)}{12k_1^4 k_2^2}$$
$$+ \frac{6k^2(\boldsymbol{k}_1 \cdot \boldsymbol{k}_2)^2 + 6k_1^2(\boldsymbol{k} \cdot \boldsymbol{k}_2)^2 + 3k^2 k_1^2(\boldsymbol{k}_1 \cdot \boldsymbol{k}_2) - 2k^2 k_1^2 k_2^2}{12k_1^4 k_2^2} ,$$

$$\gamma_{445_i}(\boldsymbol{k}_1, \boldsymbol{k}_2) = -\frac{[6(\boldsymbol{k} \cdot \boldsymbol{k}_1)(\boldsymbol{k}_1 \cdot \boldsymbol{k}_2) + 3(\boldsymbol{k} \cdot \boldsymbol{k}_1)^2 - 2k^2(\boldsymbol{k}_1 \cdot \boldsymbol{k}_2)](\boldsymbol{k}_1 \times \boldsymbol{k}_2)_i}{4k_1^4 k_2^2}$$
$$+ \frac{[2k_1^2(\boldsymbol{k} \cdot \boldsymbol{k}_2) + k^2 k_1^2](\boldsymbol{k}_1 \times \boldsymbol{k}_2)_i}{4k_1^4 k_2^2} .$$

(C.5)

D Numerical implementation of the Hartree–Fock approximation

The system of equations (6.5), (6.6) and (6.7) with the source term (6.10), the Hartree self-energy (6.11) and the Fock self-energies (6.12) and (6.13) is numerically solved using the Runge–Kutta–Cash–Karp method [149–151] adapted to Volterra integro-differential equations [152]. The wave number dependence of the propagator and power spectrum is interpolated using a finite element method and described in detail below.

The wave number interval is mapped $\chi : [k_{\min}, k_{\max}) \to [-1, 1)$ with

$$\chi(k) := \left(\frac{k/k_* - k_{\min}/k_*}{1 - k/k_{\max}} - 1 \right) \bigg/ \left(\frac{k/k_* - k_{\min}/k_*}{1 - k/k_{\max}} + 1 \right) , \tag{D.1}$$

where $k_* = 0.25 \ h/\text{Mpc}$ is chosen here. The mapping (D.1) naturally allows for the limits $k_{\min} \to 0$ and/or $k_{\max} \to \infty$. An grid over the variable χ is then obtained from the Chebychev nodes

$$\chi_n = \cos\left(\frac{n + \frac{1}{2}}{N_k + 2} \pi \right) , \tag{D.2}$$

with $n \in \{0, \ldots, N_k + 1\}$ which infers a wave number grid k_n via the inverse of the mapping (D.1). The interpolation over this lattice is done with a basis of B-spines of order one which are the triangular functions

$$T_n(\chi) = \begin{cases} \dfrac{\chi - \chi_{n-1}}{\chi_n - \chi_{n-1}} & \text{if } \chi_{n-1} \leq \chi < \chi_n \\ \dfrac{\chi_{n+1} - \chi}{\chi_{n+1} - \chi_n} & \text{if } \chi_n \leq \chi < \chi_{n+1} \\ 0 & \text{elsewise} \end{cases} , \tag{D.3}$$

for $n \in \{1, \ldots, N_k\}$ which fulfil the orthogonality condition $T_n(\chi_{\bar{n}}) = \delta_{n\bar{n}}$. The propagator and power spectrum are expand in the triangular basis functions as

$$\begin{aligned} G_{ab}^{\text{R}}(\eta, \eta', k) &= \sum_{n=1}^{N_k} G_{n,ab}^{\text{R}}(\eta, \eta') \, T_n(\chi(k)) , \\ P_{ab}(\eta, \eta', k) &= \sum_{n=1}^{N_k} P_{n,ab}(\eta, \eta') \, T_n(\chi(k)) . \end{aligned} \tag{D.4}$$

The source term (6.10) can then be written as

$$Q(\eta) = \sum_{n=1}^{N_k} A^Q_{n,ab} P_{n,ab}(\eta, \eta) \tag{D.5}$$

while the Fock self-energies (6.12) and (6.13) are

$$\Sigma^{\mathrm{F}}_{ab}(\eta, \eta', k_n) = \sum_{\bar{n}=1}^{N_k} \sum_{\tilde{n}=1}^{N_k} A^{\mathrm{F}}_{n\bar{n}\tilde{n},acefdb} P_{\bar{n},cd}(\eta, \eta') G^{\mathrm{R}}_{\tilde{n},ef}(\eta, \eta') \,,$$
$$\Pi_{ab}(\eta, \eta', k_n) = \sum_{\bar{n}=1}^{N_k} \sum_{\tilde{n}=1}^{N_k} A^{\Pi}_{n\bar{n}\tilde{n},acebfd} P_{\bar{n},cd}(\eta, \eta') P_{\tilde{n},ef}(\eta, \eta') \,. \tag{D.6}$$

The array which stores the source term is given by

$$A^Q_{n,ab} = \int_{\boldsymbol{q}} \gamma_{3ab}(\boldsymbol{q}, -\boldsymbol{q}) T_n(\chi(q)) \,, \tag{D.7}$$

while the retarded Fock self-energy is stored in

$$A^{\mathrm{F}}_{n\bar{n}\tilde{n},acefdb} = 4 \int_{\boldsymbol{q}} \gamma_{ace}(\boldsymbol{q}, \boldsymbol{k} - \boldsymbol{q}) T_{\tilde{n}}(\chi(|\boldsymbol{k} - \boldsymbol{q}|)) \gamma_{fdb}(-\boldsymbol{q}, \boldsymbol{k}) T_{\bar{n}}(\chi(q)) \,,$$
$$A^{\Pi}_{n\bar{n}\tilde{n},acebfd} = 2 \int_{\boldsymbol{q}} \gamma_{ace}(\boldsymbol{q}, \boldsymbol{k} - \boldsymbol{q}) T_{\tilde{n}}(\chi(|\boldsymbol{k} - \boldsymbol{q}|)) \gamma_{bfd}(-\boldsymbol{k} + \boldsymbol{q}, -\boldsymbol{q}) T_{\bar{n}}(\chi(q)) \,, \tag{D.8}$$

where $|\boldsymbol{k}| = k_n$. To compute the arrays (D.7) and (D.8) the integration is shifted to $\boldsymbol{q}' = \boldsymbol{q} - \boldsymbol{k}/2$ and evaluated using the elliptical coordinates [28, 32]

$$\boldsymbol{q}' = \frac{k}{2} \begin{pmatrix} \sinh(\chi) \sin(\theta) \cos(\varphi) \\ \sinh(\chi) \sin(\theta) \sin(\varphi) \\ \cosh(\chi) \cos(\theta) \end{pmatrix} \,, \tag{D.9}$$

where $\chi \in [0, \infty)$, $\theta \in [0, \pi)$ and $\varphi \in [0, 2\pi)$. The integration over the azimuthal angle φ can be preformed to give a factor of 2π and with the substitutions $X = \cosh(\chi)$ and $Y = \cos(\theta)$ one finally arrive at

$$\int_{\mathbb{R}^3} \frac{\mathrm{d}^3 q}{(2\pi)^3} = \frac{k^3}{32\pi^2} \int_1^\infty \mathrm{d}X \int_{-1}^1 \mathrm{d}Y \, (X^2 - Y^2) \,, \tag{D.10}$$

where $X \in [1, \infty)$ and $Y \in [-1, 1)$. The integrals are further restricted due to the compact support of the triangular basis functions (D.3) to

$$\int_{\Omega_{\bar{n}\tilde{n}}(\boldsymbol{k})} \frac{\mathrm{d}^3 q}{(2\pi)^3} = \frac{k^3}{32\pi^2} \int_{X^{\min}_{\bar{n}\tilde{n}}}^{X^{\max}_{\bar{n}\tilde{n}}} \mathrm{d}X \int_{Y^{\min}_{\bar{n}\tilde{n}}(X)}^{Y^{\max}_{\bar{n}\tilde{n}}(X)} \mathrm{d}Y \, (X^2 - Y^2) \,, \tag{D.11}$$

with the domain

$$\Omega_{\bar{n}\tilde{n}}(\boldsymbol{k}) = \left\{ \boldsymbol{q} \in \mathbb{R}^3 : k_{\bar{n}-1} \leq |\boldsymbol{q}| < k_{\bar{n}+1} \,, \; k_{\tilde{n}-1} \leq |\boldsymbol{k} - \boldsymbol{q}| < k_{\tilde{n}+1} \right\} \,. \tag{D.12}$$

The limits of the Y integration are

$$
Y_{\bar{n}\tilde{n}}^{\min}(X) = \min\left\{1 \ , \ \max\left\{-1 \ , \ \frac{2k_{\bar{n}-1}}{k} - X \ , \ X - \frac{2k_{\tilde{n}+1}}{k}\right\}\right\} \ ,
$$
$$
Y_{\bar{n}\tilde{n}}^{\max}(X) = \max\left\{-1 \ , \ \min\left\{1 \ , \ \frac{2k_{\bar{n}+1}}{k} - X \ , \ X - \frac{2k_{\tilde{n}-1}}{k}\right\}\right\} \ ,
$$
(D.13)

and of the X integration

$$
X_{\bar{n}\tilde{n}}^{\min} = \max\left\{1 \ , \ \frac{k_{\bar{n}-1} + k_{\tilde{n}-1}}{k}\right\} \ ,
$$
$$
X_{\bar{n}\tilde{n}}^{\max} = \max\left\{1 \ , \ \frac{k_{\bar{n}+1} + k_{\tilde{n}+1}}{k}\right\} \ .
$$
(D.14)

The integration of the (X, Y)-plain is done using the trapezoidal rule with 100 points in each variable keeping the error around the percent level [32].

E Renormalisation group flow equations for time-local dynamics

The flow equations are numerically solved using the dimensionless coefficients $\widetilde{\lambda}_{i,k} = k^2\lambda_{i,k}$ and 'flow time' $t = \ln(k/k_*)$ for some arbitrary reference scale k_* here chosen to be $k_* = 10^{-3}$ h/Mpc.

E.1 One-coefficient ansatz

In the ansatz with one coefficient (7.42) the flow of the growing mode zero-crossing at order q^2 is given by

$$\text{Flow}_{g,k}(\eta) = e^{2(\eta-\eta_{\text{in}})} \, e^{-\frac{2\lambda_k}{\kappa_k} \, k^2 e^{\kappa_k \eta}} \, \sigma^2_{\text{v},k}\left[-\frac{187}{175} + \frac{2(137 + 46\kappa_k) \, e^{\kappa_k \eta} \, k^2\lambda_k}{35(1 + \kappa_k)(7 + 2\kappa_k)}\right]. \quad \text{(E.1)}$$

E.2 Two-coefficient ansatz

For the ansatz with two coefficients with the coefficient $\lambda_{2,k}$ extracted in the leading-order approximation one has the growing mode zero-crossing at order q^2

$$\begin{aligned}
\text{Flow}_{g,k}(\eta) = \,& e^{2(\eta-\eta_{\text{in}})} \, \sigma^2_{\text{v},k} \, e^{-X} \\
& \times \left[-\frac{187}{175} + \frac{2X[(3927 + 3\kappa_k(2775 + 2\kappa_k(799 + 158\kappa_k)))]\lambda_{1,k}}{175(1 + \kappa_k)(5 + 2\kappa_k)(7 + 2\kappa_k)\lambda_{2,k}} \right. \\
& \left. \quad - \frac{2X[(3927 + 2\kappa_k(2450 + \kappa_k(1137 + 244\kappa_k)))]\lambda_{2,k}}{175(1 + \kappa_k)(5 + 2\kappa_k)(7 + 2\kappa_k)\lambda_{2,k}}\right],
\end{aligned} \quad \text{(E.2)}$$

and the decaying mode zero-crossing at order q^2

$$\begin{aligned}
\text{Flow}_{d,k}(\eta) = \,& e^{2(\eta-\eta_{\text{in}})} \, \sigma^2_{\text{v},k} \, e^{-X} \\
& \times \left[-\frac{29}{25} + \frac{X[(-522 + \kappa_k(-705 + 226\kappa_k + 232\kappa_k^2)]\lambda_{1,k}}{25(1 + \kappa_k)(-3 + 2\kappa_k)(5 + 2\kappa_k)\lambda_{2,k}} \right. \\
& \left. \quad + \frac{X[(522 + 2\kappa_k(155 - 2\kappa_k(155 - 2\kappa_k(173 + 96\kappa_k))))]\lambda_{2,k}}{25(1 + \kappa_k)(-3 + 2\kappa_k)(5 + 2\kappa_k)\lambda_{2,k}}\right],
\end{aligned} \quad \text{(E.3)}$$

where $X = 2\lambda_{2,k} \, k^2 \, e^{\kappa_k \eta} / \kappa_k$. To solve the flow equation only the $n = 0, 1$ terms of the series expansion (7.57) are included.

Bibliography

[1] P. J. E. Peebles & B. Ratra, *The cosmological constant and dark energy*, Rev. Mod. Phys. **75** (2003) 559.

[2] E. W. Kolb & M. S. Turner, *The Early Universe*, Addison-Wesley Publishing Company (1990).

[3] A. R. Liddle & D. H. Lyth, *Cosmological Inflation and Large-Scale Structure*, Cambridge University Press (2000).

[4] V. Springel et al., *Simulations of the formation, evolution and clustering of galaxies and quasars*, Nature **435** (2005) 629.

[5] P. J. E. Peebles, *The Large-Scale Structure of the Universe*, Princeton University Press (1980).

[6] T. Buchert & A. Domínguez, *Modeling multi-stream flow in collisionless matter: approximations for large-scale structure beyond shell-crossing*, Astron. Astrophys. **335** (1998) 395.

[7] P. McDonald, *How to generate a significant effective temperature for cold dark matter, from first principles*, J. Cosmol. Astropart. Phys. **04** (2011) 032.

[8] A. Erschfeld & S. Floerchinger, *Evolution of dark matter velocity dispersion*, J. Cosmol. Astropart. Phys. **06** (2019) 039.

[9] M. Pietroni, G. Mangano, N. Saviano & M. Viel, *Coarse-grained cosmological perturbation theory*, J. Cosmol. Astropart. Phys. **01** (2012) 019.

[10] O. F. Piattella, D. C. Rodrigues, J. C. Fabris & J. A. de Freitas Pacheco, *Evolution of the phase-space density and the Jeans scale for dark matter derived from the Vlasov-Einstein equation*, J. Cosmol. Astropart. Phys. **11** (2013) 002.

[11] A. Aviles, *Dark matter dispersion tensor in perturbation theory*, Phys. Rev. D **93** (2016) 063517.

[12] P. Valageas, *Impact of a warm dark matter late-time velocity dispersion on large-scale structures*, Phys. Rev. D **86** (2012) 123501.

[13] S. V. Tassev, *The Helmholtz Hierarchy: phase space statistics of cold dark matter*, J. Cosmol. Astropart. Phys. **10** (2011) 022.

[14] P. McDonald & Z. Vlah, *Large-scale structure perturbation theory without losing stream crossing*, Phys. Rev. D **97** (2018) 023508.

[15] L. M. Widrow & N. Kaiser, *Using the Schrödinger Equation to Simulate Collisionless Matter*, Astrophys. J. Lett. **416** (1993) L71.

[16] C. Uhlemann, *Finding closure: approximating Vlasov-Poisson using finitely generated cumulants*, J. Cosmol. Astropart. Phys. **10** (2018) 030.

[17] F. Bernardeau, S. Colombi, E. Gaztañaga & R. Scoccimarro, *Large-scale structure of the Universe and cosmological perturbation theory*, Phys. Rep. **367** (2002) 1.

[18] M. Crocce & R. Scoccimarro, *Renormalized cosmological perturbation theory*, Phys. Rev. D **73** (2006) 063519.

[19] M. Crocce & R. Scoccimarro, *Memory of initial conditions in gravitational clustering*, Phys. Rev. D **73** (2006) 063520.

[20] M. Crocce & R. Scoccimarro, *Nonlinear evolution of baryon acoustic oscillations*, Phys. Rev. D **77** (2008) 023533.

[21] F. Bernardeau, M. Crocce & R. Scoccimarro, *Multipoint propagators in cosmological gravitational instability*, Phys. Rev. D **78** (2008) 103521.

[22] M. Pietroni, *Flowing with time: a new approach to non-linear cosmological perturbations*, J. Cosmol. Astropart. Phys. **10** (2008) 036.

[23] S. Anselmi, S. Matarrese & M. Pietroni, *Next-to-leading resummations in cosmological perturbation theory*, J. Cosmol. Astropart. Phys. **06** (2011) 015.

[24] S. Anselmi & M. Pietroni, *Nonlinear power spectrum from resummed perturbation theory: a leap beyond the BAO scale*, J. Cosmol. Astropart. Phys. **12** (2012) 013.

[25] F. Bernardeau, N. Van de Rijt & F. Vernizzi, *Resummed propagators in multicomponent cosmic fluids with the eikonal approximation*, Phys. Rev. D **85** (2012) 063509.

[26] F. Bernardeau, N. Van de Rijt & F. Vernizzi, *Power spectra in the eikonal approximation with adiabatic and nonadiabatic modes*, Phys. Rev. D **87** (2013) 043530.

[27] P. Valageas, *A new approach to gravitational clustering: A path-integral formalism and large-N expansions*, Astron. Astrophys. **421** (2004) 23.

[28] P. Valageas, *Large-N expansions applied to gravitational clustering*, Astron. Astrophys. **465** (2007) 725.

[29] P. Valageas, *Using the Zeldovich dynamics to test expansion schemes*, Astron. Astrophys. **476** (2007) 31.

[30] P. Valageas, *Expansion schemes for gravitational clustering: computing two-point and three-point functions*, Astron. Astrophys. **484** (2008) 79.

[31] A. Taruya & T. Hiramatsu, *A Closure Theory for Nonlinear Evolution of Cosmological Power Spectra*, Astrophys. J. **674** (2008) 617.

[32] T. Hiramatsu & A. Taruya, *Chasing the nonlinear evolution of matter power spectrum with a numerical resummation method: Solution of closure equations*, Phys. Rev. D **79** (2009) 103526.

[33] A. Taruya, T. Nishimichi, S. Saito & T. Hiramatsu, *Nonlinear evolution of baryon acoustic oscillations from improved perturbation theory in real and redshift spaces*, Phys. Rev. D **80** (2009) 123503.

[34] P. McDonald, *Dark matter clustering: A simple renormalization group approach*, Phys. Rev. D **75** (2007) 043514.

[35] S. Matarrese & M. Pietroni, *Resumming cosmic perturbations*, J. Cosmol. Astropart. Phys. **06** (2007) 026.

[36] S. Matarrese & M. Pietroni, *Baryonic Acoustic Oscillations via the Renormalization Group*, Mod. Phys. Lett. A **23** (2008) 25.

[37] S. Floerchinger, M. Garny, N. Tetradis & U. A. Wiedemann, *Renormalization-group flow of the effective action of cosmological large-scale structures*, J. Cosmol. Astropart. Phys. **01** (2017) 048.

[38] S. Floerchinger, M. Garny, A. Katsis, N. Tetradis & U. A. Wiedemann, *The dark matter bispectrum from effective viscosity and one-particle irreducible vertices*, J. Cosmol. Astropart. Phys. **09** (2019) 047.

[39] D. Baumann, A. Nicolis, L. Senatore & M. Zaldarriaga, *Cosmological non-linearities as an effective fluid*, J. Cosmol. Astropart. Phys. **07** (2012) 051.

[40] J. J. M. Carrasco, M. P. Hertzberg & L. Senatore, *The effective field theory of cosmological large scale structures*, J. High Energy Phys. **09** (2012) 082.

[41] R. A. Porto, L. Senatore & M. Zaldarriaga, *The Lagrangian-space Effective Field Theory of large scale structures*, J. Cosmol. Astropart. Phys. **05** (2014) 022.

[42] D. Blas, S. Floerchinger, M. Garny, N. Tetradis & U. A. Wiedemann, *Large scale structure from viscous dark matter*, J. Cosmol. Astropart. Phys. **11** (2015) 049.

[43] D. Blas, M. Garny & T. Konstandin, *Cosmological perturbation theory at three-loop order*, J. Cosmol. Astropart. Phys. **01** (2014) 010.

[44] D. Blas, M. Garny, M. M. Ivanov & S. Sibiryakov *Time-sliced perturbation theory for large scale structure I: general formalism*, J. Cosmol. Astropart. Phys. **07** (2016) 052.

[45] D. Blas, M. Garny, M. M. Ivanov & S. Sibiryakov *Time-sliced perturbation theory II: baryon acoustic oscillations and infrared resummation*, J. Cosmol. Astropart. Phys. **07** (2016) 028.

[46] C. Viermann, F. Fabis, E. Kozlikin, R. Lilow & M. Bartelmann, *Nonequilibrium statistical field theory for classical particles: Basic kinetic theory*, Phys. Rev. E **91** (2015) 062120.

[47] M. Bartelmann et al., *A microscopic, non-equilibrium, statistical field theory for cosmic structure formation*, New J. Phys. **18** (2016) 043020.

[48] M. Bartelmann et al., *Cosmic Structure Formation with Kinetic Field Theory*, Ann. Phys. (Berl.) **531** (2019) 1800446.

[49] J. Zinn-Justin, *Quantum Field Theory and Critical Phenomena*, Oxford University Press (1989).

[50] F. J. Dyson, *The S Matrix in Quantum Electrodynamics*, Phys. Rev. **75** (1949) 1736.

[51] J. Schwinger, *On the Green's functions of quantized fields. I*, Proc. Natl. Acad. Sci. U.S.A. **37** (1951) 452.

[52] J. Schwinger, *On the Green's functions of quantized fields. II*, Proc. Natl. Acad. Sci. U.S.A. **37** (1951) 455.

[53] C. Wetterich, *Exact evolution equation for the effective potential*, Phys. Lett. B **301** (1993) 90.

[54] J. Berges, N. Tetradis & C. Wetterich, *Non-perturbative renormalization flow in quantum field theory and statistical physics*, Phys. Rep. **363** (2002) 223.

[55] N. Dupuis et al., *The nonperturbative functional renormalization group and its applications*, Phys. Rep. **910** (2021) 1.

[56] C. W. Misner, K. S. Thorne & J. A. Wheeler, *Gravitation*, W. H. Freeman and Company (1973).

[57] A. Einstein, *Die Grundlage der allgemeinen Relativitätstheorie*, Ann. Phys. (Berl.) **354** (1916) 769.

[58] O. Sarbach and T. Zannias, *The geometry of the tangent bundle and the relativistic kinetic theory of gases*, Class. Quantum Gravity **31** (2014) 085013.

[59] C. Cercignani & G. M. Kremer, *The Relativistic Boltzmann Equation: Theory and Applications*, Birkhäuser Verlag (2002).

[60] H. Grad, *On the Kinetic Theory of Rarefied Gases*, Commun. Pure Appl. Math. **2** (1949) 331.

[61] I. Müller, *Zum Paradoxon der Wärmeleitungstheorie*, Z. Phys. **198** (1967) 329.

[62] W. Israel & J. M. Stewart, *Thermodynamics of nonstationary and transient effects in a relativistic gas*, Phys. Lett. A **58** (1976) 213.

[63] W. Israel, *Nonstationary Irreversible Thermodynamics: A Causal Relativistic Theory*, Ann. Phys. (N.Y.) **100** (1976) 310.

[64] W. Israel & J. M. Stewart, *Transient Relativistic Thermodynamics and Kinetic Theory*, Ann. Phys. (N.Y.) **118** (1979) 341.

[65] R. Baier, P. Romatschke, D. T. Son, A. O. Starinets & M. A. Stephanov, *Relativistic viscous hydrodynamics, conformal invariance, and holography*, J. High Energy Phys. **04** (2008) 100.

[66] G. S. Denicol, H. Niemi, E. Molnár & D. H. Rischke, *Derivation of transient relativistic fluid dynamics from the Boltzmann equation*, Phys. Rev. D **85** (2012) 114047; *Erratum*: Phys. Rev. D **91** (2015) 039902.

[67] A. Erschfeld, S. Floerchinger & M. Rupprecht, *General relativistic nonideal fluid equations for dark matter from a truncated cumulant expansion*, Phys. Rev. D **102** (2020) 063520.

[68] M. Lachièze-Rey & J.-P. Luminet, *Cosmic topology*, Phys. Rep. **254** (1995) 135.

[69] A. Friedman, *Über die Krümmung des Raumes*, Z. Phys. **10** (1922) 377.

[70] J. Ehlers, P. Geren & R. K. Sachs, *Isotropic Solutions of the Einstein–Liouville Equations*, J. Math. Phys. **9** (1968) 1344.

[71] R. Treciokas & G. F. R. Ellis, *Isotropic Solutions of the Einstein-Boltzmann Equations*, Commun. Math. Phys. **23** (1971) 1.

[72] W. R. Stoeger, R. Maartens & G. F. R. Ellis, *Proving Almost-Homogeneity of the Universe: an Almost Ehlers-Geren-Sachs Theorem*, Astrophys. J. **443** (1995) 1.

[73] S. D. Maharaj & R. Maartens, *General Solution of Liouville's Equation in Robertson–Walker Space-Times*, Gen. Relativ. Gravit. **19** (1987) 1217.

[74] R. Maartens & S. D. Maharaj, *Invariant Solutions of Liouville's Equation in Robertson–Walker Space-Times*, Gen. Relativ. Gravit. **19** (1987) 1223.

[75] J. M. Bardeen, *Gauge-invariant cosmological perturbations*, Phys. Rev. D **22** (1980) 1882.

[76] G. F. R. Ellis & M. Bruni, *Covariant and gauge-invariant approach to cosmological density fluctuations*, Phys. Rev. D **40** (1989) 1804.

[77] M. Bruni, P. K. S. Dunsby & G. F. R. Ellis, *Cosmological Perturbations and the Physical Meaning of Gauge-invariant Variables*, Astrophys. J. **395** (1992) 34.

[78] L. Bombelli, W. E. Couch & R. J. Torrence, *Perfect fluid perturbations of cosmological spacetimes in Stewart's variables*, Class. Quantum Gravity **11** (1994) 139.

[79] V. F. Mukhanov, H. A. Feldman & R. H. Brandenberger, *Theory of cosmological perturbations*, Phys. Rep. **215** (1992) 203.

[80] C.-P. Ma & E. Bretschinger, *Cosmological Perturbation Theory in the Synchronous and Conformal Newtonian Gauges*, Astrophys. J. **455** (1995) 7.

[81] J. W. York, *Conformally invariant orthogonal decomposition of symmetric tensors on Riemannian manifolds and the initial-value problem of general relativity*, J. Math. Phys. **14** (1973) 456.

[82] H. Kodama & M. Sasaki, *Cosmological Perturbation Theory*, Prog. Theor. Phys. Supp. **78** (1984) 1.

[83] J. M. Stewart, *Perturbations of Friedmann–Robertson–Walker cosmological models*, Class. Quantum Gravity **7** (1990) 1169.

[84] C. Eckart, *The Thermodynamics of Irreversible Processes III. Relativistic Theory of the Simple Fluid*, Phys. Rev. **58** (1940) 919.

[85] L. D. Landau & E. M. Lifschitz, *Fluid Mechanics*, Pergamon Press (1959).

[86] M. Davis & P. J. E. Peebles, *On the integration of the BBGKY equations for the development of strongly nonlinear clustering in an expanding universe*, Astrophys. J. Suppl. Ser. **34** (1977) 425.

[87] C. Uhlemann & M. Kopp *Coarse-grained cosmological perturbation theory: Stirring up the dust model*, Phys. Rev. D **91** (2015) 084010.

[88] S. Pueblas & R. Scoccimarro, *Generation of vorticity and velocity dispersion by orbit crossing*, Phys. Rev. D **80** (2009) 043504.

[89] J. Binney & S. Tremaine, *Galactic Dynamics*, Princeton University Press (1987).

[90] R. Scoccimarro & J. Frieman, *Loop Corrections in Nonlinear Cosmological Perturbation Theory*, Astrophys. J. Suppl. Ser. **105** (1996) 37.

[91] R. Scoccimarro & J. A. Frieman, *Loop Corrections in Nonlinear Cosmological Perturbation Theory. II. Two-Point Statistics and Self-Similarity*, Astrophys. J. **473** (1996) 620.

[92] M. Peloso & M. Pietroni, *Galilean invariance and the consistency relation for the nonlinear squeezed bispectrum of large scale structure*, J. Cosmol. Astropart. Phys. **05** (2013) 031.

[93] P. Creminelli, J. Noreña, M. Simonović & F. Vernizzi, *Single-field consistency relations of large scale structure*, J. Cosmol. Astropart. Phys. **12** (2013) 025.

[94] R. J. Adler, *The Geometry of Random Fields*, John Wiley & Sons (1981).

[95] P. Watts & P. Coles, *Statistical cosmology with quadratic density fields*, Mon. Not. R. Astron. Soc. **338** (2003) 806.

[96] J. M. Bardeen, J. R. Bond, N. Kaiser & A. S. Szalay, *The Statistics of Peaks of Gaussian Random Fields*, Astrophys. J. **304** (1986) 15.

[97] G. E. Uhlenbeck & L. S. Ornstein, *On the Theory of the Brownian Motion*, Phys. Rev. **36** (1930) 823.

[98] R. Scoccimarro et al., *Nonlinear Evolution of the Bispectrum of Cosmological Perturbations*, Astrophys. J. **496** (1998) 586.

[99] A. H. Guth, *Inflationary universe: A possible solution to the horizon and flatness problems*, Phys. Rev. D **23** (1981) 347.

[100] A. D. Linde, *A new inflationary universe scenario: A possible solution of the horizon, flatness, homogeneity, isotropy and primordial monopole problems*, Phys. Lett. B **108** (1981) 389.

[101] A. Albrecht & P. J. Steinhardt, *Cosmology for Grand Unified Theories with Radiatively Induced Symmetry Breaking*, Phys. Rev. Lett. **48** (1982) 1220.

[102] E. R. Harrison, *Fluctuations at the Threshold of Classical Cosmology*, Phys. Rev. D **1** (1970) 2726.

[103] Ya. B. Zeldovich, *A Hypothesis, Unifying the Structure and the Entropy of the Universe*, Mon. Not. R. Astron. Soc. **160** (1972) 1.

[104] S. W. Hawking, *The development of irregularities in a single bubble inflationary universe*, Phys. Lett. B **115** (1982) 295.

[105] A. H. Guth & S.-Y. Pi, *Fluctuations in the New Inflationary Universe*, Phys. Rev. Lett. **49** (1982) 1110.

[106] A. A. Starobinsky, *Dynamics of phase transition in the new inflationary universe scenario and generation of perturbations*, Phys. Lett. B **117** (1982) 175.

Bibliography

[107] J. M. Bardeen, P. J. Steinhardt & M. S. Turner, *Spontaneous creation of almost scale-free density perturbations in an inflationary universe*, Phys. Rev. D **28** (1983) 679.

[108] P. Mészáros, *The Behaviour of Point Masses in an Expanding Cosmological Substratum*, Astron. Astrophys. **37** (1974) 225.

[109] V. Silveira & I. Waga, *Decaying Λ cosmologies and power spectrum*, Phys. Rev. D **50** (1994) 4890.

[110] H. Martel & W. Freudling, *Second-Order Perturbation Theory in $\Omega \neq 1$ Friedmann Models*, Astrophys. J. **371** (1991) 1.

[111] R. Juszkiewicz, *On the evolution of cosmological adiabatic perturbations in the weakly non-linear regime*, Mon. Not. R. Astron. Soc. **197** (1981) 931.

[112] E. T. Vishniac, *Why weakly non-linear effects are small in a zero-pressure cosmology*, Mon. Not. R. Astron. Soc. **203** (1983) 345.

[113] Y. Suto & M. Sasaki *Quasinonlinear Theory of Cosmological Self-Gravitating Systems*, Phys. Rev. Lett. **66** (1991) 264.

[114] N. Makino, M. Sasaki & Y. Suto, *Analytic approach to the perturbative expansion of nonlinear gravitational fluctuations in cosmological density and velocity fields*, Phys. Rev. D **46** (1992) 585.

[115] L. Isserlis, *On a Formula for the Product-Moment Coefficient of any Order of a Normal Frequency Distribution in any Number of Variables*, Biometrika **12** (1918) 134.

[116] G. C. Wick, *The Evaluation of the Collision Matrix*, Phys. Rev. **80** (1950) 268.

[117] M. McQuinn & M. White, *Cosmological perturbation theory in 1+1 dimensions*, J. Cosmol. Astropart. Phys. **01** (2016) 043.

[118] R. Scoccimarro, *A New Angle on Gravitational Clustering*, Ann. N. Y. Acad. Sci. **927** (2001) 13.

[119] R. Scoccimarro, *Transients from initial conditions: a perturbative analysis*, Mon. Not. R. Astron. Soc. **299** (1998) 1097.

[120] P. C. Martin, E. D. Siggia & H. A. Rose, *Statistical Dynamics of Classical Systems*, Phys. Rev. A **8** (1973) 423.

[121] C. de Dominicis, *Techniques de renormalisation de la théorie des champs et dynamique des phénomènes critiques*, J. Phys. Colloq. **37** (1976) C1-247.

[122] H.-K. Janssen, *On a Lagrangean for Classical Field Dynamics and Renormalization Group Calculations of Dynamical Critical Properties*, Z. Phys. B **23** (1976) 377.

[123] C. de Dominicis & L. Peliti, *Field-theory renormalization and critical dynamics above T_c: Helium, antiferromagnets, and liquid-gas systems*, Phys. Rev. B **18** (1978) 353.

[124] J. Schwinger, *Brownian Motion of a Quantum Oscillator*, J. Math. Phys. **2** (1961) 407.

[125] L. V. Keldysh, *Diagram technique for nonequilibrium processes*, Sov. Phys. JETP **20** (1965) 1018. [Zh. Eksp. Teor. Fiz. **47** (1964) 1515].

[126] D. Hochberg, C. Molina-París, J. Pérez-Mercader & M. Visser, *Effective action for stochastic partial differential equations*, Phys. Rev. E **60** (1999) 6343.

[127] J. A. Hertz, Y. Roudi & P. Sollich, *Path integral methods for the dynamics of stochastic and disordered systems*, J. Phys. A **50** (2017) 033001.

[128] L. Canet, H. Chaté & B. Delamotte, *General framework of the non-perturbative renormalization group for non-equilibrium steady states*, J. Phys. A **44** (2011) 495001.

[129] J. Polchinski, *Renormalization and effective lagrangians*, Nucl. Phys. B **231** (1984) 269.

[130] O. J. Rosten, *A comment on the path integral approach to cosmological perturbation theory*, J. Cosmol. Astropart. Phys. **01** (2008) 029.

[131] M. H. Goroff, B. Grinstein, S.-J. Rey & M. B. Wise, *Coupling of modes of cosmological mass density fluctuations*, Astrophys. J. **311** (1986) 6.

[132] B. Jain & E. Bertschinger, *Self-similar Evolution of Gravitational Clustering: Is $n = -1$ Special?*, Astrophys. J. **456** (1996) 43.

[133] D. Blas, M. Garny & T. Konstandin, *On the non-linear scale of cosmological perturbation theory*, J. Cosmol. Astropart. Phys. **09** (2013) 024.

[134] E. V. Teodorovich, *A hydrodynamic generalization of Ward's identity*, Appl. Math. Mech. **53** (1989) 340.

[135] L. Canet, B. Delamotte & N. Wschebor, *Fully developed isotropic turbulence: Symmetries and exact identities*, Phys. Rev. E **91** (2015) 053004.

[136] A. Kehagias & A. Riotto, *Symmetries and consistency relations in the large scale structure of the universe*, Nucl. Phys. B **873** (2013) 514.

[137] A. Berera & D. Hochberg, *Gauge Symmetry and Slavnov-Taylor Identities for Randomly Stirred Fluids*, Phys. Rev. Lett. **90** (2007) 254501.

[138] A. Berera & D. Hochberg, *Gauge fixing, BRS invariance and Ward identities for randomly stirred flows*, Nucl. Phys. B **814** (2009) 522.

[139] L. Canet, B. Delamotte & N. Wschebor, *Fully developed isotropic turbulence: Nonperturbative renormalization group formalism and fixed-point solution*, Phys. Rev. E **93** (2016) 063101.

[140] L. Canet, V. Rossetto, N. Wschebor & G. Balarac, *Spatiotemporal velocity-velocity correlation function in fully developed turbulence*, Phys. Rev. E **95** (2017) 023107.

[141] M. Tarpin, L. Canet & N. Wschebor, *Breaking of scale invariance in the time dependence of correlation functions in isotropic and homogeneous turbulence*, Phys. Fluids **30** (2018) 055102.

[142] M. K.-H. Kiessling, *The "Jeans swindle" A true story—mathematically speaking*, Adv. Appl. Math. **31** (2003) 132.

[143] R. H. Kraichnan, *Kolmogorov's Hypotheses and Eulerian Turbulence Theory*, Phys. Fluids **7** (1964) 1723.

[144] F. Bernardeau & P. Valageas, *Eulerian and Lagrangian propagators for the adhesion model (Burgers dynamics)*, Phys. Rev. D **81** (2010) 043516.

[145] F. Bernardeau & P. Valageas, *Exact results for propagators in the geometrical adhesion model*, Phys. Rev. D **85** (2012) 023516.

[146] D. R. Hartree, *The Wave Mechanics of an Atom with a Non-Coulomb Central Field. Part II. Some Results and Discussion*, Math. Proc. Camb. Philos. Soc. **24** (1928) 111.

[147] V. Fock, *Näherungsmethode zur Lösung des quantenmechanischen Mehrkörperproblems*, Z. Phys. **61** (1930) 126.

[148] D. R. Hartree & W. Hartree, *Self-Consistent Field, with Exchange, for Beryllium*, Proc. R. Soc. Lond. A **150** (1935) 9.

[149] C. Runge, *Ueber die numerische Auflösung von Differentialgleichungen*, Math. Ann. **46** (1895) 167.

[150] W. Kutta, *Beitrag zur näherungsweisen Integration totaler Differentialgleichungen*, Z. Math. Phys. **46** (1901) 435.

[151] J. R. Cash & A. H. Karp, *A Variable Order Runge-Kutta Method for Initial Value Problems with Rapidly Varying Right-Hand Sides*, ACM Trans. Math. Softw. **16** (1990) 201.

[152] C. Lubich, *Runge-Kutta Theory for Volterra Integrodifferential Equations*, Numer. Math. **40** (1982) 119.

[153] J. H. Jeans, *The Stability of a Spherical Nebula*, Philos. Trans. R. Soc. A **199** (1902) 1.

[154] D. Boyanovsky & J. Wu, *Small scale aspects of warm dark matter: Power spectra and acoustic oscillations*, Phys. Rev. D **83** (2011) 043524.

[155] R. H. Kraichnan, *Dynamics of Nonlinear Stochastic Systems*, J. Math. Phys. **2** (1961) 124.

[156] R. H. Kraichnan, *Decay of Isotropic Turbulence in the Direct-Interaction Approximation*, Phys. Fluids **7** (1964) 1030.

[157] D. Blas, J. Lesgourgues & T. Tram, *The Cosmic Linear Anisotropy Solving System (CLASS). Part II: Approximation schemes*, J. Cosmol. Astropart. Phys. **07** (2011) 034.

[158] D. J. Fixsen, *The Temperature of the Cosmic Microwave Background*, Astrophys. J. **707** (2009) 916.

[159] E. Komatsu et al., *Five-Year Wilkinson Microwave Anisotropy Probe* Observations: Cosmological Interpretation*, Astrophys. J. Suppl. Ser. **180** (2009) 330.

[160] E. Komatsu et al., *Seven-Year Wilkinson Microwave Anisotropy Probe (WMAP*) Observations: Cosmological Interpretation*, Astrophys. J. Suppl. Ser. **192** (2011) 18.

[161] Planck Collaboration, *Planck 2015 results XIII. Cosmological parameters*, Astron. Astrophys. **594** (2016) A13.

[162] Planck Collaboration, *Planck 2018 results VI. Cosmological parameters*, Astron. Astrophys. **641** (2020) A6.

[163] J. Dubinski, J. Kim, C. Park & R. Humble, *GOTPM: a parallel hybrid particle-mesh treecode*, New Astron. **9** (2004) 111.

[164] V. Springel, *The cosmological simulation code* GADGET-2, Mon. Not. R. Astron. Soc. **364** (2005) 1105.

[165] R. E. Angulo et al., *Scaling relations for galaxy clusters in the Millennium-XXL simulation*, Mon. Not. R. Astron. Soc. **426** (2012) 2046.

[166] J. Kim, C. Park, G. Rossi, S. M. Lee & J. R. Gott III, *The New Horizon Run Cosmological N-Body Simulations*, J. Korean Astron. Soc. **44** (2011) 217.

[167] O. Hahn, R. E. Angulo & T. Abel, *The properties of cosmic velocity fields*, Mon. Not. R. Astron. Soc. **454** (2015) 3920.

[168] G. Jelic-Cizmek, F. Lepori, J. Adamek & R. Durrer, *The generation of vorticity in cosmological N-body simulations*, J. Cosmol. Astropart. Phys. **09** (2018) 006.

[169] M. Buehlmann & O. Hahn, *Large-scale velocity dispersion and the cosmic web*, Mon. Not. R. Astron. Soc. **487** (2019) 228.

[170] R. W. Hockney & J. W. Eastwood, *Computer Simulation Using Particles*, McGraw-Hill (1981).

[171] S. Shandarin, S. Habib & K. Heitmann, *Cosmic web, multistream flows, and tessellations*, Phys. Rev. D **85** (2012) 083005.

[172] T. Abel, O. Hahn & R. Kaehler, *Tracing the dark matter sheet in phase space*, Mon. Not. R. Astron. Soc. **427** (2012) 61.

[173] Y. P. Jing, *Correcting for the Alias Effect When Measuring the Power Spectrum Using a Fast Fourier Transform*, Astrophys. J. **620** (2005) 559.

[174] D. Jeong & E. Komatsu, *Perturbation Theory Reloaded. II. Nonlinear Bias, Baryon Acoustic Oscillations, and Millennium Simulation in Real Space*, Astrophys. J. **691** (2009) 569.

[175] R. Durrer & C. Caprini, *Primordial magnetic fields and causality*, J. Cosmol. Astropart. Phys. **11** (2003) 010.

[176] G. Cusin, V. Tansella & R. Durrer, *Vorticity generation in the Universe: A perturbative approach*, Phys. Rev. D **95** (2017) 063527.

[177] D. J. Eisenstein & W. Hu, *Power Spectra for Cold Dark Matter and its Variants*, Astrophys. J. **511** (1999) 5.

[178] L. Schlessinger, *Use of Analyticity in the Calculation of Nonrelativistic Scattering Amplitudes*, Phys. Rev. **167** (1968) 1411.

[179] R.-A. Tripolt, P. Gubler, M. Ulybyshev & L. von Smekal, *Numerical analytic continuation of Euclidean data*, Comput. Phys. Commun. **237** (2019) 129.

[180] H. Helmholtz, *Über Integrale der hydrodynamischen Gleichungen, welche den Wirbelbewegungen entsprechen*, J. Reine Angew. Math. **55** (1858) 25.

[181] E. Lifshitz, *On the gravitational stability of the expanding universe*, J. Phys. (USSR) **10** (1946) 116.

[182] M. Sugiura, *Unitary Representations and Harmonic Analysis: An Introduction*, Kodansha, Tokyo (1975).

[183] I. M. Gel'fand, R. A. Minlos & Z. Ya. Shapiro, *Representations of the rotation and Lorentz groups and their applications*, Pergamon Press, Oxford (1963).

[184] V. V. Mihailov, *Addition of arbitrary number of identical angular momenta*, J. Phys. A **10** (1977) 147.

[185] A. J. M. Spencer, *A note on the decomposition of tensors into traceless symmetric tensors*, Int. J. Eng. Sci. **8** (1970) 475.

[186] É. Picard, *Sur l'application des méthodes d'approximations successives à l'étude de certaines équations différentielles ordinaires*, J. Math. Pures Appl. **9** (1893) 217.

[187] E. Lindelöf, *Sur l'application de la méthode des approximations successives aux équations différentielles ordinaires du premier ordre*, C. R. Hebd. Séances Acad. Sci. **118** (1894) 454.

[188] V. Volterra, *Theory of Functionals and of Integral and Integro-Differential Equations*, Blackie & Son (1930).

[189] R. W. Brockett, *Volterra Series and Geometric Control Theory*, Automatica **12** (1976) 167; *An Addendum*: Automatica **12** (1976) 635.

[190] E. G. Gilbert, *Functional Expansions for the Response of Nonlinear Differential Systems*, IEEE Trans. Automat. Contr. **22** (1977) 909.

[191] C. Lesiak & A. J. Krener, *The Existence and Uniqueness of Volterra Series for Nonlinear Systems*, IEEE Trans. Automat. Contr. **23** (1978) 1090.

[192] I. W. Sandberg, *Volterra-Like Expansions for Solutions of Nonlinear Integral Equations and Nonlinear Differential Equations*, IEEE Trans. Circuits Syst. **30** (1983) 68.

[193] S. Boyd, L. O. Chua & C. A. Desoer, *Analytical Foundations of Volterra Series*, IMA J. Math. Control Inf. **1** (1984) 243.

[194] P. Langevin, *Sur la théorie du mouvement brownien*, C. R. Hebd. Séances Acad. Sci. **146** (1908) 530.

[195] R. Phythian, *The functional formalism of classical statistical dynamics*, J. Phys. A **10** (1977) 777.

[196] R. V. Jensen, *Functional Integral Approach to Classical Statistical Dynamics*, J. Stat. Phys. **25** (1981) 183.

Danksagung

Zuerst und im Besonderen bedanke ich mich bei meinem Doktorvater Priv.-Doz. Dr. Stefan Flörchinger für seine exzellente Betreuung über die letzten Jahre hinweg. Seine Anregungen haben wesentlich zum Gelingen dieser Dissertation beigetragen.

Ebenso bedanke ich mich bei Prof. Dr. Matthias Bartelmann für die Übernahme des Zweitgutachtens dieser Dissertation und die damit verbundenen Mühen.

Weiterhin waren die zahllosen Gespräche mit den Kollegen vom Institut für Theoretische Physik Heidelberg eine große Unterstützung. Unter anderen danke ich hierfür Paul Wittmer, Lennert Thormählen, Johannes Hölck, Jan Horak, Eduardo Grossi, Natalia Sanchez-Kuntz und Tobias Haas.

Mein ganz besonderer Dank gilt außerdem meinen Eltern und Sophie Radecker, die mich stets auf meinem Weg unterstützt haben.

Der Konrad-Adenauer-Stiftung möchte ich für die Förderung meines Dissertationsvorhabens danken.